E-ISSN 1305-3612

Diagnostic and Interventional Radiology

TSR 1924
TURKISH SOCIETY OF RADIOLOGY

dirjournal.org

VOLUME 32
ISSUE 6
November 2026

Diagnostic and Interventional Radiology

Official Journal of the Turkish Society of Radiology

E-ISSN: 1305-3612

www.dirjournal.org

Editor-in-Chief

Şükrü Mehmet Ertürk, MD

Department of Radiology, İstanbul University Faculty of Medicine, İstanbul, Türkiye

E-mail: smerturk@gmail.com

Section Editors and Scientific Editorial Board

Abdominal Imaging

Sonay Aydın, MD

Department of Radiology, Erzincan Binali Yıldırım University Mengücek Gazi Training and Research Hospital, Erzincan, Türkiye

E-mail: sonay.aydin@erzincan.edu.tr

Nurullah Dağ, MD

Department of Radiology, İnönü University Faculty of Medicine, Malatya, Türkiye

E-mail: nurullah.dag@inonu.edu.tr
drndag@icloud.com

Oğuz Dicle, MD

Department of Radiology, Dokuz Eylül University Faculty of Medicine, İzmir, Türkiye

E-mail: odicle59@gmail.com

İlkay S. İdilman, MD

Department of Radiology, Hacettepe University Faculty of Medicine, Ankara, Türkiye

E-mail: ipolater@yahoo.com

Artificial Intelligence and Informatics

Tuğba Akıncı D'Antonoli, MD

Division of Diagnostic and Interventional Neuroradiology, Department of Radiology, University Hospital Basel, Basel, Switzerland

Department of Pediatric Radiology, University Children's Hospital Basel, Basel, Switzerland

E-mail: tugba.akincidantonoli@unibas.ch

Ulaş Bağcı, PhD

Department of Radiology, Northwestern University Faculty of Medicine, Chicago, United States of America

E-mail: ulas.bagci@northwestern.edu

Görkem Durak, MD

Department of Radiology, Northwestern University Faculty of Medicine, Chicago, United States of America

E-mail: gorkem.durak@northwestern.edu

İsmail Meşe, MD

Department of Radiology, Üsküdar State Hospital, İstanbul, Türkiye

E-mail: ismail_mese@yahoo.com

Breast Imaging

Işıl Başara Akın, MD

Department of Radiology, Dokuz Eylül University Faculty of Medicine, İzmir, Türkiye

E-mail: isilbasara@gmail.com

Serap Gültekin, MD

Department of Radiology, Gazi University Faculty of Medicine, Ankara, Türkiye

E-mail: sergultekin@yahoo.com

Chest and Cardiovascular Imaging

Serçin Özkök, MD, PhD

Department of Radiology, University of Health Sciences Türkiye, Başakşehir Çam and Sakura City Hospital, İstanbul, Türkiye

E-mail: sercinbas2005@gmail.com

Gamze Durhan, MD

Department of Radiology, Hacettepe University Faculty of Medicine, Ankara, Türkiye

E-mail: gamzedurhan@gmail.com

Furkan Ufuk, MD

Department of Radiology, The University of Chicago, Chicago, United States of America

E-mail: furkan.ufuk@hotmail.com

Emergency Radiology

Francesca Iacobellis, MD

Department of General and Emergency Radiology, Antonio Cardarelli Hospital, Naples, Italy

E-mail: iacobellisf@gmail.com

Hybrid Imaging and Nuclear Medicine

Zeynep Gözde Özkan, MD

Department of Internal Medicine, İstanbul University Faculty of Medicine, Division of Nuclear Medicine, İstanbul, Türkiye

E-mail: zeynep.ozkan@istanbul.edu.tr

zgozdeozkan@yahoo.com

Interventional Radiology

Barbaros Çil, MD, FCIRSE

Department of Radiology, Koç University School of Medicine, İstanbul, Türkiye

E-mail: bcil@ku.edu.tr

Osman Öcal, MD

Department of Diagnostic and Interventional Radiology, Heidelberg University Hospital, Heidelberg, Germany

E-mail: osman.oecal@med.uni-heidelberg.de

Onur Taydaş, MD

Department of Radiology, Sakarya University Faculty of Medicine, Sakarya, Türkiye

E-mail: onurtaydas@sakarya.edu.tr,
taydasonur@gmail.com

Bahri Üstünsöz, MD

Department of Radiology, LSUHSC (Louisiana State University Health Science Center) School of Medicine, New Orleans, United States of America

E-mail: bustunsoz2000@yahoo.com

Musculoskeletal Imaging

Zeynep Maraş Özdemir, MD

Department of Radiology, Güven Hospital, Ankara, Türkiye

E-mail: zynpmaras@yahoo.com

Hayri Oğul, MD

Department of Radiology, İstanbul Medipol University Faculty of Medicine, İstanbul, Türkiye

E-mail: drhogul@gmail.com

Adalet Elçin Yıldız, MD

Department of Radiology, Hacettepe University Faculty of Medicine, Ankara, Türkiye

E-mail: aelcindr@gmail.com

Neuroradiology

Gökçen Çoban Çiftçi, MD

Department of Radiology, Hacettepe University Faculty of Medicine, Ankara, Türkiye

E-mail: drgokcencoban@gmail.com

Erkan Gökçe, MD

Department of Radiology, Tokat Gaziosmanpaşa University Faculty of Medicine, Tokat, Türkiye

E-mail: drerkangokce@gmail.com

Elif Günay Bulut, MD

Department of Radiology/Neuroradiology, Hacettepe University Faculty of Medicine, Ankara, Türkiye

E-mail: drelifbulut@yahoo.com

Suzan Şaylısoy, MD

Department of Radiology, Eskişehir Osmangazi University Faculty of Medicine, Eskişehir, Türkiye

E-mail: ssaylisoy@ogu.edu.tr

Oncologic and General Radiology

Afak Durur Karakaya, MD, PhD

Department of Radiology, Koç University Faculty of Medicine, İstanbul, Türkiye

E-mail: afakdurur@yahoo.com

İnci Kızıldağ Yırgın, MD

Department of Radiology, İstanbul University Faculty of Medicine, İstanbul, Türkiye

E-mail: inci.kizildag@gmail.com

Pediatric Radiology

Evrim Özmen, MD

Department of Radiology, Koç University Hospital, İstanbul, Türkiye

E-mail: evrimkilicdr@gmail.com

Diagnostic and Interventional Radiology

Official Journal of the Turkish Society of Radiology

E-ISSN: 1305-3612
www.dirjournal.org

Ultrasound and Interventional Radiology
Halit Nahit Şendur, MD
Department of Radiology, Gazi University Faculty of Medicine, Ankara, Türkiye
E-mail: hsendur@gmail.com

Editorial Consultant to Editor-in-Chief
Mehmet Ruhi Onur, MD
Department of Radiology, Hacettepe University Faculty of Medicine, Ankara, Türkiye
E-mail: ruhionur@yahoo.com

Publication Coordinator
Nermin Tunçbilek, MD
Department of Radiology, Trakya University Faculty of Medicine, Edirne, Türkiye
E-mail: drtuncbilek@hotmail.com

Biostatistical Consultant
İlker Ercan, PhD
Department of Biostatistics, Uludağ University School of Medicine, Bursa, Türkiye
E-mail: iercan@msn.com

Social Media Leads
Sıtkı Safa Taflan, MD
İstanbul University, İstanbul Faculty of Medicine, Department of Radiology, İstanbul, Türkiye
Sıla Atacan, MD
İstanbul University Faculty of Medicine, Department of Radiology, İstanbul, Türkiye
Gursel Karacaoglu, MD
İstanbul Medeniyet University, Department of Radiology, İstanbul, Türkiye
Mahmut Bilal Doğan, MD
Marmara University Faculty of Medicine, Department of Radiology, İstanbul, Türkiye

Publication Services
Galenos Publishing, İstanbul, Türkiye

Past Editors
Editors-in-Chief
Mehmet Ruhi Onur, MD (2023-2026)
Mustafa Seçil, MD (2016-2023)
Nevzat Karabulut, MD (2011-2016)
Üstün Aydıngöz, MD (2010-2011)
Okan Akhan, MD (2001-2010)
Ferhun Balkancı, MD (1999-2001)
Aytekin Besim, MD (1994-1999)*
* Dr. Aytekin Besim actually served as the General Coordinator. His work in this capacity, however, was in effect that of an Editor-in-Chief.

Editors
Ayşenur Cila, MD (2001-2002)
Suat Kemal Aytaç, MD (1997-2001)
Erhan Ilgıt, MD (1994-2001)
Okan Akhan, MD (1994-2001)
Ferhun Balkancı, MD (1994-2000)
Serdar Akyar, MD (1994-1997)

Section Editors
Section Editorship was established in 2002 at the tenure of Dr. Okan Akhan, Editor-in-Chief.

Abdominal Imaging
Bengi Gürses, MD (2020-2023)
Mehmet Ruhi Onur, MD (2016-2023)
Barış Türkbey, MD (2014-2020)
Mustafa N. Özmen, MD (2012-2018)
Murat Acar, MD (2015-2016)
Mustafa Seçil, MD (2011-2016)
Ahmet Tuncay Turgut, MD (2011)
Deniz Akata, MD (2007-2011)
Ayşe Erden, MD (2002-2011)
Okan Akhan, MD (2002-2010)
Hakan Özdemir, MD (2002-2010)

Artificial Intelligence and Informatics
Burak Koçak, MD (2023-2026)
Barış Türkbey, MD (2020-2023)

Breast Imaging
Mustafa Erkin Arıbal, MD (2016-2023)
Sibel Kul, MD (2015-2018)
Ayşenur Oktay, MD (2009-2014)
Ayşegül Özdemir, MD (2004-2009)

Cardiovascular Imaging
Uğur Bozlar, MD (2016-2023)
Muşturay Karçaaltıncaba, MD (2007-2010)
Mecit Kantarcı, MD (2010-2016)

Chest Imaging
Nevzat Karabulut, MD (2010-2014)
Çetin Atasoy, MD (2007-2010)
Macit Arıyürek, MD (2002-2007)
Figen Demirkazık, MD (2014-2018)

General Radiology
Ersin Öztürk, MD (2014-2017)
Utku Şenol, MD (2010-2013)
Oğuz Dicle, MD (2007-2010)

Interventional Radiology
James Milburn, MD (2023-2026)
Cüneyt Aytekin, MD (2016-2023)
Bora Peynircioğlu, MD (2012-2015)
Levent Oğuzkurt, MD (2011-2014)
Fatih Boyvat, MD (2007-2010)
İsmail Oran, MD (2015-2019)

Musculoskeletal Imaging
Hatice Tuba Sanal, MD (2016-2023)
Fatih Kantarcı, MD (2014-2016)
Ayşenur Oktay, MD (2011-2013)
Üstün Aydıngöz, MD (2002-2011)
Berna Dirim Mete (2016-2017)

Neuroradiology and Head & Neck Imaging
Gülgün Yılmaz Ovalı, MD (2023-2026)
Kubilay Aydın, MD (2016-2023)
Nafi Aygün, MD (2016-2023)
Kader Karlı Oğuz, MD (2011-2015)
Süleyman Men, MD (2007-2013)
Muhteşem Ağıldere, MD (2002-2011)

Nuclear Medicine
Evrim Bengi Türkbey, MD (2023-2026)
A. Cahid Civelek, MD (2016-2023)
Oktay Sarı, MD (2015)
Akın Yıldız, MD (2011-2014)
Pediatric Radiology
Meltem Ceyhan Bilgici, MD (2023-2026)
Korgün Koral, MD (2016-2023)
Murat Kocaoğlu, MD (2016-2023)
Ensar Yekeler, MD (2014-2016)
Suat Fitöz, MD (2007-2013)

Turkish Society of Radiology is one of the foremost medical specialty organizations in Türkiye. It was formed by the merger of the two main radiology societies of Türkiye, one of which was founded in 1924. The Society is based in Ankara, Türkiye.

TSR 1924
TURKISH SOCIETY OF RADIOLOGY

Diagnostic and Interventional Radiology

Official Journal of the Turkish Society of Radiology

E-ISSN: 1305-3612

www.dirjournal.org

Diagnostic and Interventional Radiology (Diagn Interv Radiol) is a bimonthly periodical of the Turkish Society of Radiology and the content of the journal is available at https://www.dirjournal.org/. It is peer-reviewed and adheres to the highest ethical and editorial standards. The editors of the journal endorse the Editorial Policy Statements Approved by the Council of Science Editors Board of Directors (https://cse.memberclicks.net/). The journal is in compliance with the Recommendations for the Conduct, Reporting, Editing and Publication of Scholarly Work in Medical Journals published by the International Committee of Medical Journal Editors (updated May 2022, www.icmje.org).

First ten volumes of Diagnostic and Interventional Radiology have been published in Turkish under the name of Tanısal ve Girişimsel Radyoloji (MEDLINE abbreviation: Tani Girisim Radyol), the current title's exact Turkish translation.

Diagnostic and Interventional Radiology is an open access publication, and the journal's publication model is based on Budapest Open Access Initiative (BOAI) declaration. All published content is available online, free of charge at https://www.dirjournal.org/. Authors retain the copyright of their published work in Diagnostic and Interventional Radiology. The journal's content is licensed under a Creative Commons Attribution-NonCommercial (CC BY-NC) 4.0 International License which permits third parties to share and adapt the content for non-commercial purposes by giving the appropriate credit to the original work.

Please refer to the journal's webpage (**https://dirjournal.org/**) for "Aims and Scope", "Instructions to Authors" and "Instructions to Reviewers".

The editorial and publication processes of the journal are shaped in accordance with the guidelines of the ICMJE, WAME, CSE, COPE, EASE, and NISO.
Diagnostic and Interventional Radiology is indexed in **SCI-Expanded, Pubmed/Medline, Pubmed Central, TUBITAK ULAKBIM TR Index, Scopus, DOAJ, EBSCO, HINARI, EMBASE, CINAHL, ProQuest, Gale and CNKI.**

The journal is published online.

Owner: Turkish Society of Radiology

Responsible Manager: Şükrü Mehmet Ertürk

Contact Information

Diagnostic and Interventional Radiology Turkish Society of Radiology

Hoşdere Cad., Güzelkent Sok., Çankaya Evleri, F/2, 06540
Ankara, Türkiye

E-mail: info@dirjournal.org

Phone: +90 (312) 442 36 53 **Fax:** +90 (312) 442 36 54

Publisher Contact

Address: Molla Gürani Mah. Kaçamak Sk.
No: 21/1 34093 İstanbul, Türkiye

Phone: +90 (530) 177 30 97

E-mail: info@galenos.com.tr/yayin@galenos.com.tr

Web: www.galenos.com.tr **Publisher Certificate Number:** 14521

Online Publication Date: November 2026

E-ISSN 1305-3612

International scientific journal published bimonthly.

TURKISH SOCIETY OF RADIOLOGY

Turkish Society of Radiology is one of the foremost medical specialty organizations in Türkiye. It was formed by the merger of the two main radiology societies of Türkiye, one of which was founded in 1924. The Society is based in Ankara, Türkiye.

Diagnostic and Interventional Radiology

Volume 32 • Issue 6

November 2026

www.dirjournal.org

Contents

EDITORIAL

732 When the radiologist remains: Reverse alignment and the final biological component. *Şükrü Mehmet Ertürk*

ABDOMINAL IMAGING

734 Original Article **Intratumoral and peritumoral radiomics based on multi-parametric magnetic resonance imaging for predicting microsatellite instability in endometrial cancer.** *Xiaoyu He, Xi Yin*

743 Letter to the Editor **Letter to the Editor: On the clinical applicability of multiparametric and multimodal approaches in the evaluation of focal liver lesions.** *Ali Kemal Sivrioglu*

745 Original Article **Global trends and hotspots of machine learning in the diagnosis of prostate cancer: a bibliometric analysis from 1997 to 2024.** *Yixiao Shi*

755 Letter to the Editor **Reply: Regarding "multiparametric magnetic resonance imaging, diffusion-weighted magnetic resonance imaging, and magnetic resonance elastography: differentiating benign and malignant liver lesions".** *İlkay S. İdilman*

ARTIFICIAL INTELLIGENCE AND INFORMATICS

757 Original Article **Predicting drainage success of peritonsillar abscesses: a radiomics-based machine learning approach using contrast-enhanced computed tomography.** *İzzet Selçuk Parlak, Bökebatur Ahmet Raşit Mendi, Alperen Özkan*

765 Letter to the Editor **Letter to the Editor: Challenges of applying large language models to image-based interpretation in abdominal radiology.** *Eren Çamur, Turay Cesur, Yasin Celal Güneş*

767 Letter to the Editor **Reply: challenges of applying large language models to image-based interpretation in abdominal radiology.** *Alperen Elek, Duygu Doğa Ekizalioğlu, Ezgi Güler*

BREAST IMAGING

769 Original Article **Peritumoral-to-tumoral apparent diffusion coefficient ratio as a marker of tumor microenvironment activity across breast cancer molecular subtypes.** *Seçil Gündoğdu, Eda Elverici, Arzu Özsoy, Leman Günbey Karabekmez, Muhammed Said Beşler, Emre Gündoğdu*

CARDIOVASCULAR IMAGING

777 Original Article **Magnetic resonance imaging evaluation of myocardial and hepatic tissue remodeling and cardiac function in sickle cell anemia.** *Serhat Başaran, Kaan Esen, Aydan Akdeniz, Hasan H. Yüksek, Yüksel Balcı*

EMERGENCY RADIOLOGY

787 Original Article **The relationship between hypostasis and gas detected in postmortem computed tomography and the postmortem interval.** *Vefa Çakmak, Abdülkadir İzci, Tuğçe Dönmez, Zeynab Zülfügarlı, Ayşe Kurtuluş Dereli, Kemalettin Acar*

GENERAL RADIOLOGY

794 Letter to the Editor **Letter to the Editor: On the role of mentorship, ethics, and quality in publication success.** *Atilla Hikmet Çilengir*

796 Letter to the Editor **Reply: On the role of mentorship, ethics, and quality in publication success.** *Ali Salbas, Ali Murat Koc*

798 Letter to the Editor **Methodological considerations regarding control preference interpretation: a comment on management of contrast media-related risk factors by Öztürk and Karabıyık.** *Franklin de Jesus Santiago Villegas, Juan Manuel Calero Canaval*

HEAD AND NECK IMAGING

800 Original Article **Semicircular canal aplasia: radiologic spectrum and clinical correlations on computed tomography and magnetic resonance imaging.** *Nisa Başpınar, Mehmet Atalar, Serdar Aktı, Adem Bora*

808 Letter to the Editor **Reply:** Letter to Editor: **Dual-energy computed tomography-based volumetric thyroid iodine quantification: correlation with thyroid hormonal status, pathologic diagnosis, and phantom validation.** *Younghen Lee*

Full text of these articles can be accessed online at www.dirjournal.org or through PubMed (https://www.ncbi.nlm.nih.gov/pmc/journals/2754/).

Diagnostic and Interventional Radiology

Volume 32 • Issue 6

November 2026

www.dirjournal.org

Contents

INTERVENTIONAL RADIOLOGY

810 Original Article **Tract embolization using absorbable gelatin sponge torpedoes following transsplenic or transhepatic access in pediatric patients.** *Mert Bayramoğlu, Yunus Emre Şentürk, Enes Muhammed Cantürk, Vügar Samadli, Levent Oğuzkurt*

818 Original Article **Image-guided, urethra-sparing transperineal radiofrequency ablation for benign prostatic hyperplasia: a prospective bicenter outpatient study.** *Thiago Franchi Nunes, Denis Szejnfeld, Públio Cesar Cavalcante Viana, Flávio Scavone Stefanini, Vinicius Adami Vayego Fornazari, Túlio Fabiano de Oliveira Leite, Alvaro Sadek Sarkis, Hugo Alexandre Socrates de Castro*

828 Original Article **Safety and efficacy of combined ethanol and bleomycin sclerotherapy via percutaneous pigtail catheter for benign cervical cystic lesions: a single-center retrospective study.** *Sang Lim Choi, Woosun Choi, Byung Kook Kwak, Jinyoung Choi*

835 Original Article **Pleural and intra-abdominal long-term drainage: comparison of a novel double-loop and a conventional single-loop catheter.** *Su Ho Kim, Jung Suk Oh, Ho Jong Chun*

841 Original Article **Reduction of hemorrhagic complications after non-focal renal biopsy with pre-procedure desmopressin administration.** *Bradford Dugan, Christine A. Welch, Asif Rahman, Michael V. Korona, Amy R. Deipolyi*

846 Original Article **Comparative evaluation of two resorbable microparticles in a porcine kidney model: angiographic and pathologic outcomes.** *Won Seok Choi, Kun Yung Kim, Chong-ho Lee, Young-Min Han, Minuk Kim, Sung-hwan Yoon, Chang Jin Yoon, Jae Hwan Lee*

852 Letter to the Editor **Letter to the Editor: Methodological considerations in the analysis of multiphase computed tomography angiography findings for outcome prediction in middle cerebral artery M1 occlusion.** *Yakup Ozbay*

854 Letter to the Editor **Letter to the Editor: Pleural tail sign in computed tomography–guided lung biopsy: insights and considerations for clinical practice.** *Andrea Carolina Munive, Nicolás Guerrero Acosta, Isabella Andrea Bolaños Bermúdez, David Fernando Torres Cortés*

856 Letter to the Editor **Reply: "Pleural tail sign in computed tomography–guided lung biopsy: insights and considerations for clinical practice".** *Jacob Jalil Hassan, Hans-Jonas Meyer*

NEURORADIOLOGY

858 Invited Commentary **Standardizing neuroradiological ancillary testing in brain death determination: a national clinical protocol from Türkiye.** *Gul Hatipoglu, Kamil Karaali, Burak Kocak, Derya Bako, Mehmet Fatih Erbay*

862 CORRIGENDUM

Full text of these articles can be accessed online at www.dirjournal.org or through PubMed (https://www.ncbi.nlm.nih.gov/pmc/journals/2754/).

Diagn Interv Radiol 2026; DOI: 10.4274/dir.2026.262809

EDITORIAL

©Copyright 2026 Author(s) - Available online at dirjournal.org.
Content of this journal is licensed under a Creative Commons Attribution-NonCommercial 4.0 International License.

When the radiologist remains: Reverse alignment and the final biological component

Şükrü Mehmet Ertürk

Editor-in-Chief

İstanbul University Faculty of Medicine, Department of Radiology, İstanbul, Türkiye

Harrison's paper on "reverse alignment" prompted this follow-up.[1] In my earlier editorial, I called the gradual adaptation of radiological practice to machine-compatible forms "mechanistic drift." I described the "final biological component" as a possible endpoint: a radiologist still reads and signs reports, yet the work around that person increasingly follows the demands of measurement, standardization, and computational systems.[2] Harrison examines a closely related danger across human practices more broadly. His account gives the original warning a wider conceptual frame, although it does not show that this change has occurred in radiology. Nguyen[3] and Velotto[4] then help clarify how the danger might arise and why formal human oversight may not be enough.

Harrison and the wider frame

The familiar alignment question asks how artificial intelligence (AI) can be made responsive to human values and goals. Harrison asks what happens in the other direction: people and institutions may adapt their practices and simplify their values to fit what computational systems can readily represent and optimize.[1] Such adaptation need not be imposed by a machine. It can emerge through the incentives, records, routines, and definitions of success that people build around it.

That is why Harrison's argument resonates with the earlier editorial. Radiology's emphasis on turnaround time, standardized reports, productivity measures, and auditable decisions did not begin with AI.[2] Harrison's examples often involve commercial platforms.[1] In radiology, throughput, reimbursement, quality assurance, and medicolegal pressures also shape the work. AI can intensify these pressures by giving machine-readable findings a direct path into triage, reporting, and evaluation, while contextual judgment may be harder to carry through the same systems. Harrison supplies a general account of the direction of this adaptation; mechanistic drift names its possible expression in radiology. The radiologist may retain responsibility while the range of judgment the workflow welcomes grows narrower.

How practice can shift

Harrison uses Nguyen's account of value capture to explain one route of reverse alignment.[1] A rich value is given a simpler representation, often a number, and the representation gradually takes the place of the value in practical decisions.[3] Turnaround time, report completeness, discrepancy rates, and AI triage scores are useful measures. Trouble arises if a department begins to treat what these measures capture as the full meaning of good radiological work. Contextual interpretation, consultation, appropriate hesitation, and justified departure from a pathway may matter greatly while remaining harder to count.

Imagine an AI-prioritized worklist paired with a turnaround-time dashboard. A radiologist spends additional time comparing an apparently routine examination with prior images and contacting the referring clinician about a subtle change. That care may register as delay, while the priority score gives the case little prominence. Both tools can be useful and correctly implemented. Their combined effect depends on whether the department recognizes the extra work as good judgment or as a deviation from the preferred path. Before and after AI deployment, a department could sample departures from worklist priorities, review their

Epub: 29.09.2026

Publication date: 02.11.2026

DOI: 10.4274/dir.2026.262809

You may cite this article as: Ertürk ŞM. When the radiologist remains: reverse alignment and the final biological component. *Diagn Interv Radiol*. 2026;32(6):732-733.

clinical justification, and track the rationale, time and evaluation costs, and whether reasons informed quality review. If justified departures become harder to record or carry greater penalties, that would be a warning sign, not proof of reverse alignment.

Velotto describes the next step: an AI output can acquire practical authority when it becomes the ordinary starting point for action, even though the system is neither a moral agent nor the formal decision-maker.[4] A worklist priority, suggested finding, or draft report can become a default that requires effort to question. The radiologist remains answerable, but the surrounding workflow influences where attention starts and when disagreement needs justification. Nguyen explains how a proxy can displace a clinical value; Velotto explains how a system's output can become authoritative in daily work. Together they give Harrison's broader concern a practical route into radiology.[1,3,4]

AI can change radiological decisions through both its accuracy and its place in the workflow. In a study of radiologists, assistance had uneven effects, and inaccurate predictions worsened performance.[5] In a veterinary radiology experiment, presenting AI advice before or after an initial judgment changed how participants used it.[6] These findings concern specific decisions. Mechanistic drift concerns what happens when such arrangements become routine and set the terms of good work.

The verdict for radiology

The question, then, is who sets those terms. I have described radiology as an epistemic system: the clinical practice through which imaging becomes actionable knowledge.[7] A radiologist can still sign every report while worklists, draft findings, and performance measures increasingly define what merits attention and which departures require justification. The practical test is whether radiologists can depart from an AI recommendation for a clinical reason, and whether the department uses those reasons to improve the workflow. An override that carries substantial time or evaluation costs offers little effective discretion. Daye and colleagues describe structures for implementing and monitoring clinical AI.[8] Those structures should also examine what worklists and dashboards reward, which outputs become defaults, and how justified departures are handled.

The final biological component is the endpoint to avoid. A radiologist remains more than a signatory only when clinical judgment can change both the decision at hand and the rules that govern the next one.

AI assistance acknowledgement

ChatGPT (OpenAI) and Claude (Anthropic) were used for critical revision, condensation, language refinement, and formatting. The author independently determined the argument, clinical interpretation, and sources; reviewed and verified all AI-assisted material and references; and accepts full responsibility. No AI system is listed as an author.

References

1. Harrison DJ. The message hidden within the pattern: a reverse alignment problem for debates in artificial intelligence. *AI Soc.* 2026;41:6335-6356. [Crossref]
2. Ertürk ŞM. The final biological component: AI and radiology's mechanistic drift. *Diagn Interv Radiol.* 2026;32(4):351-353. [Crossref]
3. Nguyen CT. Value capture. *J Ethics Soc Philos.* 2024;27(3):469-504. [Crossref]
4. Velotto G. From product to operative artefact: practical authority and operational answerability in AI ethics. *AI Ethics*. 2026;6:425. [Crossref]
5. Yu F, Moehring A, Banerjee O, Salz T, Agarwal N, Rajpurkar P. Heterogeneity and predictors of the effects of AI assistance on radiologists. *Nat Med.* 2024;30(3):837-849. [Crossref]
6. Fogliato R, Chappidi S, Lungren MP, et al. Who goes first? Influences of human-AI workflow on decision making in clinical imaging. In: Proceedings of the 2022 ACM Conference on Fairness, Accountability, and Transparency. New York (NY): Association for Computing Machinery; 2022. p. 1362-1374. [Crossref]
7. Erturk SM. Radiology is not a task: AI and the epistemic system of radiology. *Acad Radiol.* 2026. [Crossref]
8. Daye D, Wiggins WF, Lungren MP, et al. Implementation of clinical artificial intelligence in radiology: who decides and how? *Radiology.* 2022;305(3):555-563. [Crossref] Erratum in: *Radiology.* 2022;305(1):E62. [Crossref]

Diagn Interv Radiol 2026; DOI: 10.4274/dir.2026.263743

ABDOMINAL IMAGING

ORIGINAL ARTICLE

©Copyright 2026 Author(s) - Available online at dirjournal.org.
Content of this journal is licensed under a Creative Commons Attribution-NonCommercial 4.0 International License.

Intratumoral and peritumoral radiomics based on multi-parametric magnetic resonance imaging for predicting microsatellite instability in endometrial cancer

Xiaoyu He
Xi Yin

The First Affiliated Hospital, Shihezi University, Medical Imaging Center, Shihezi, China

PURPOSE

This study aimed to evaluate the utility of intratumoral and peritumoral radiomics derived from multi-parametric magnetic resonance imaging for predicting microsatellite instability (MSI) in endometrial cancer (EC).

METHODS

We retrospectively analyzed 161 patients with pathologically confirmed EC, assigning them to a training (n = 112) and a test cohort (n = 49) at a 7:3 ratio, and collected their full clinical and imaging data. We manually delineated regions of interest on axial T2-weighted imaging (T2WI), diffusion-weighted imaging (DWI), and dynamic contrast-enhanced (CE) T1-weighted imaging sequences, expanding them by 3, 5, and 7 mm to define peritumoral regions. We then extracted and selected radiomic features from both intratumoral and peritumoral areas. Using six machine learning algorithms, we developed separate radiomics models and assessed their performance via the area under the receiver operating characteristic curve (AUC). To complete the evaluation, we compared statistical differences using the DeLong test and generated calibration curves to verify predictive accuracy.

RESULTS

Clinical characteristics exhibited no significant correlation with MSI status. In single-sequence analysis, the CE model demonstrated the highest performance (training AUC: 0.912; test AUC: 0.856). The multi-parametric model (T2WI + DWI + CE) outperformed single-sequence models, achieving AUCs of 0.934 and 0.914 in the training and test cohorts, respectively. Peritumoral radiomics independently showed robust predictive value; specifically, the model derived from 3 mm peritumoral features (across DWI) yielded a training AUC of 0.898 and a test AUC of 0.790. Notably, the integration of intratumoral and peritumoral features maximized predictive accuracy. The final model, combining optimal intratumoral features (T2WI + DWI + CE) with 3 mm peritumoral DWI features, achieved the best performance with a remarkable AUC of 0.998 in the test cohort.

CONCLUSION

Peritumoral radiomics possesses strong independent predictive value and significantly enhances the performance of intratumoral models. The integration of intratumoral and peritumoral radiomics offers a precise, non-invasive method for preoperative MSI prediction, serving as a valuable tool to facilitate clinical decision-making.

CLINICAL SIGNIFICANCE

This study establishes a reliable, non-invasive radiomics approach for the preoperative assessment of MSI status.

KEYWORDS

Endometrial cancer, microsatellite instability, peritumor, radiomics, magnetic resonance imaging, diffusion-weighted imaging, predictive model

Handling editor: İlkay İdilman

Corresponding author: Xi Yin

E-mail: 1260431436@qq.com

Received 12 December 2025; revision requested 18 January 2026; last revision requested 21 February 2026; accepted 11 March 2026.

Epub: 12.05.2026

Publication date: 02.11.2026

DOI: 10.4274/dir.2026.263743

You may cite this article as: He X, Yin X. Intratumoral and peritumoral radiomics based on multi-parametric magnetic resonance imaging for predicting microsatellite instability in endometrial cancer. *Diagn Interv Radiol*. 2026;32(6):734-742.

Endometrial cancer (EC) ranks as the sixth most common cancer in women globally and stands as one of the top three gynecological malignancies. Both its incidence and mortality rates have shown a steady upward trend. In 2020, China accounted for 19.6% of global new cases of uterine malignancies and 17.1% of related deaths, underscoring the substantial burden it places on women's health.[1] Microsatellite instability (MSI), a genomic hypermutable phenotype resulting from defects in the DNA mismatch repair (MMR) system, is profoundly implicated in the progression, prognosis, and therapeutic response to anti-programmed cell death protein 1/programmed death-ligand 1 immunotherapy in EC.[2] Notably, patients with MSI-high (MSI-H) EC exhibit significantly superior responses to immunotherapy and improved prognoses compared with those with microsatellite stable (MSS) tumors.[3,4] Consequently, accurate preoperative assessment of MSI status is pivotal for tailoring individualized treatment strategies and optimizing clinical outcomes.

Currently, the gold standard for MSI detection relies on postoperative immunohistochemistry (IHC). However, this method is limited by its invasive nature, potential sampling bias, and inability to provide real-time guidance for preoperative planning.[5] As a promising non-invasive modality, magnetic resonance imaging (MRI) is widely utilized for tumor assessment due to its superior visualization of anatomical structures and tissue characteristics.[6-9] Radiomics leverages machine learning algorithms to extract high-throughput quantitative features from medical images, decoding tumor heterogeneity that is often imperceptible to visual inspection;[10] this approach has demonstrated significant value in tumor staging and therapeutic efficacy prediction.[11] Nevertheless, current radiomics investigations into EC-MSI[12-14] have predominantly focused on intratumoral features, largely overlooking the peritumoral region. The peritumoral microenvironment—characterized by inflammation, angiogenesis, and microscopic infiltration—is biologically relevant and may harbor complementary information regarding MSI status. To bridge this gap, we innovatively integrated multi-sequence MRI-based radiomic features from both intratumoral and peritumoral regions to construct a robust prediction model for MSI in EC. This study aims to establish a non-invasive, efficient method for preoperative MSI assessment, thereby providing a novel diagnostic tool to facilitate precision medicine in EC.

Main points

- Microsatellite instability (MSI) is not only significantly associated with the progression and prognosis of endometrial cancer (EC), but it also serves as a critical predictive biomarker for the efficacy of anti-programmed cell death protein 1 and anti-programmed death-ligand 1 immunotherapy.
- Accurate assessment of MSI status is a fundamental prerequisite for tailoring personalized treatment strategies and optimizing clinical outcomes in patients with EC.
- The integration of intratumoral and peritumoral imaging features offers a promising, non-invasive modality for the accurate preoperative prediction of MSI status.

Methods

Research participants

This retrospective study was approved by the Ethics Review Committee of The First Affiliated Hospital, Shihezi University (approval number: KJ2022-11-01, date: 2022.11.01), and the requirement for informed consent was waived due to the retrospective nature of the analysis. Data were collected from 161 patients with EC admitted to the study institution between January 2018 and May 2025. The cohort was randomly divided into a training set (n = 112) and a test set (n = 49) at a ratio of 7:3 using a computer-generated random number sequence. The inclusion criteria were as follows: (1) histopathologically confirmed diagnosis of EC with complete assessment of MSI status and (2) availability of standard preoperative pelvic MRI scans. Patients were excluded if they met any of the following criteria: (1) receipt of preoperative antitumor therapies, such as chemotherapy or radiotherapy, or (2) presence of significant motion artifacts or metal artifacts on MRI images that interfered with image analysis and feature extraction.

Data collection and microsatellite instability determination

Based on prior literature, the following clinical characteristics were retrieved from electronic medical records: age, body mass index (BMI), menopausal status, history of hypertension and diabetes mellitus, International Federation of Gynecology and Obstetrics stage, histological grade, deep myometrial invasion (DMI), lymphovascular space invasion (LVSI), and lymph node metastasis (LNM). MSI status was determined via IHC in strict adherence to the expert consensus guidelines on MSI detection techniques.[15] IHC staining was performed to evaluate the expression of four MMR proteins: MLH1, MSH2, MSH6, and PMS2. Tumors exhibiting loss of nuclear expression in one or more (≥ 1) of these proteins were classified as MSI-H. Conversely, tumors demonstrating intact expression of all four proteins were classified as MSS or MSI-low.

Magnetic resonance imaging acquisition protocols

Before the examination, all patients were screened for and instructed to remove metallic objects to ensure safety. To minimize intestinal motion and susceptibility artifacts, a bowel preparation protocol was implemented: Patients ingested two sachets of polyethylene glycol electrolyte powder (137.15 g per sachet dissolved in 2,000 mL of warm water) 4 hours before the scan, consuming the entire volume within 1 hour to achieve complete colonic cleansing. Following bowel preparation, patients were instructed to drink 500–800 mL of water 1 hour before imaging to maintain moderate bladder distension. An intravenous catheter was inserted into the antecubital vein for contrast administration. Patients were positioned supine, head-first, with arms raised above the head, and were trained in breath-holding techniques or instructed to breathe naturally to minimize respiratory motion artifacts.

Images were acquired using a Siemens 3.0 T magnetic resonance scanner (Siemens Healthineers, Erlangen, Germany) equipped with an 8-channel phased-array body coil. The protocol included conventional pelvic MRI sequences and dynamic contrast-enhanced (CE) MRI. Detailed scanning parameters are summarized in Table 1.

Regions of interest segmentation and feature extraction

MRI scans in Digital Imaging and Communications in Medicine format were retrieved from the Picture Archiving and Communication System and imported into the uAI research platform (Version 20250130, Shanghai United Imaging Intelligence Co., Ltd.) for analysis. Regions of interest (ROIs) were manually delineated layer-by-layer on the axial T2-weighted imaging (T2WI), diffusion-weighted imaging (DWI), and the third or fourth phase of DCE T1-weighted imaging sequences. The segmentation was performed by a radiologist with 10 years of experience in gynecological MRI, who was blinded to the patients' clinical and patho-

logical information. The detailed workflow of this study is illustrated in Figure 1.

To evaluate inter-observer reproducibility, two radiologists with 10 and 15 years of experience in gynecologic imaging, who were blinded to clinical information, independently performed tumor ROI segmentation on 50 randomly selected cases from the training cohort. To assess intra-observer reproducibility, one of the radiologists repeated the segmentation on the same images after a washout period of 4 weeks. The intraclass correlation coefficient (ICC) was calculated for all extracted features. Only features demonstrating high stability (ICC > 0.80) were considered robust and retained for subsequent analysis.

Peritumoral ROIs were generated by dilating the manual tumor ROI boundaries by 3, 5, and 7 mm and subsequently subtracting the original intratumoral volume. Before feature extraction, images underwent standardization, resampling, and N4 bias field correction to ensure data consistency. Radiomic features were extracted from three distinct regions: the intratumoral ROI, the peritumoral ROI, and the combined (tumor + peritumoral) ROI. The extracted feature set included morphological features, first-order statistics, and texture features derived from the Gray Level Co-occurrence Matrix, Gray Level Run Length Matrix, Gray Level Size Zone Matrix, Gray Level Dependence Matrix, and Neighboring Gray Tone Difference Matrix. Data were normalized using Z-score standardization. To address overfitting, dimensionality reduction was performed using Pearson correlation analysis followed by the least absolute shrinkage and selection operator regression model with 10-fold cross-validation (Figure 2).

Model construction and nomogram evaluation

This study evaluated three MRI sequences and four distinct ROIs, comprising the intratumoral region and three peritumoral volumes defined by margins of 3, 5, and 7 mm. Following feature extraction and selection, six machine learning algorithms were employed: logistic regression, support vector machine, random forest, decision tree (DT), bagging DT (BDT), and Gaussian process. Initially, independent radiomics models were constructed for the intratumoral and peritumoral regions. The top-performing peritumoral model for each sequence was identified, and its selected features were integrated with those from the intratumoral region. These composite feature sets were then input into the optimal classifier to establish the final combined (intratumoral + peritumoral) model. Predictive performance was assessed via receiver operating characteristic (ROC) analysis, with the area under the curve (AUC) serving as the primary metric. Furthermore, calibration curves were plotted to assess the agreement between predicted and observed outcomes, and decision curve analysis was performed to determine the model's clinical utility.

Statistical analysis

Statistical analyses were performed using IBM SPSS Statistics for Windows, version 22.0 (IBM Corp., Armonk, NY, USA), and the United Imaging Research Platform. Continuous variables with a normal distribution were expressed as mean ± standard deviation and compared using the independent samples *t*-test. Non-normally distributed variables were reported as the median with interquartile range and analyzed using the Mann–Whitney U test. Categorical variables were presented as frequencies and percentages [n (%)] and compared using the chi-square test or Fisher's exact test, as appropriate. The DeLong test was employed to compare differences in the AUCs between models. A *P* value < 0.05 was considered statistically significant.

Results

Demographic and clinical characteristics

A total of 161 patients with EC were enrolled in this study, comprising 33 in the MSI group and 128 in the MSS group. Patients were assigned to a training cohort (n = 112) and a test cohort (n = 49) at a ratio of 7:3. As shown in Table 2, there were no statistically significant differences between the training and test cohorts regarding baseline clinical characteristics, including age, BMI, menopausal status, comorbidities (hypertension or diabetes), or tumor pathological features (stage, grade, DMI, LVSI, and LNM) (*P* > 0.05).

Table 1. Magnetic resonance imaging scanning parameters

Parameters	TR/TE (ms)	Slice thickness (mm)	Interlayer spacing (mm)	Matrix
T2WI-FRFSE	6,377/92	5	1	352 × 320
DWI	4,700/65	5	1	256 × 192
DCE	4.6/MinFull	3	1	320 × 200

T2WI-FRFSE, T2-weighted imaging-fast recovery fast spin echo; TR, repetition time; TE, echo time; DWI, diffusion-weighted imaging; DCE, dynamic contrast-enhanced magnetic resonance imaging; MinFull, minimum full.

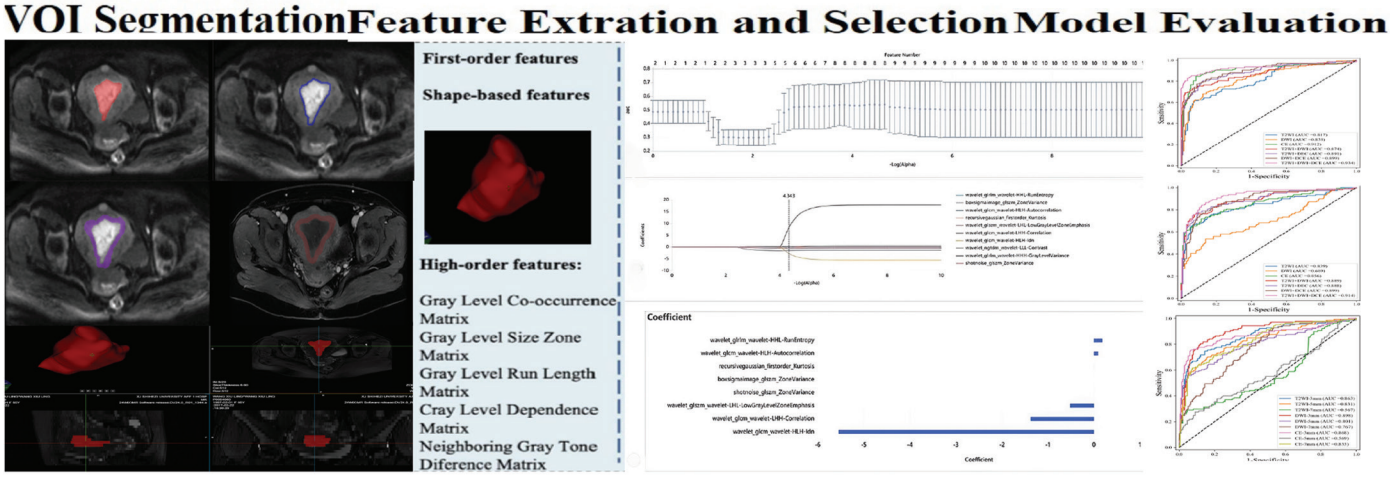


Figure 1. Overview of the study. VOI, volume of interest.

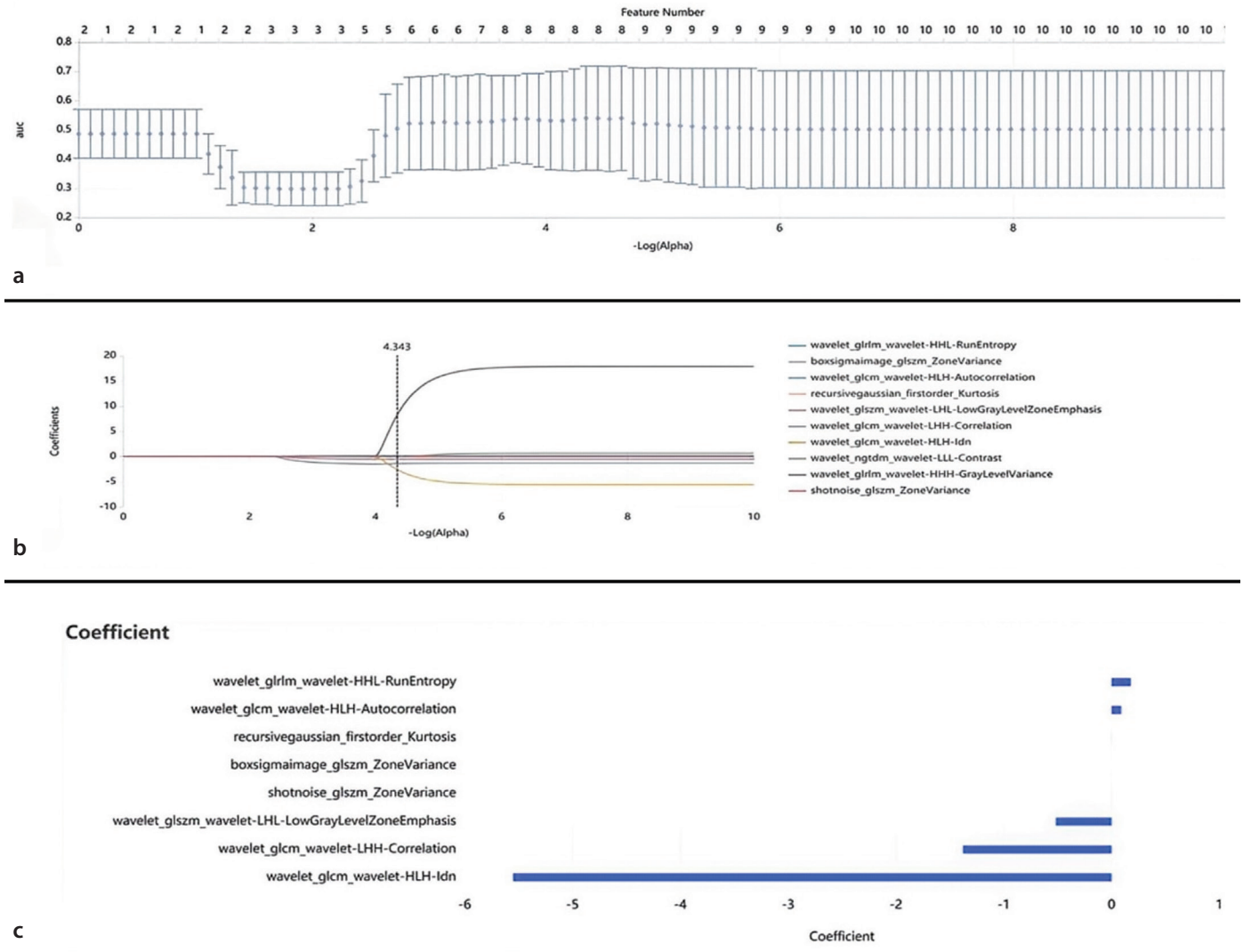


Figure 2. (a–c): LASSO screening of radiomic features related to MSI. **(a)** Optimal hyperparameter values were found through 10-fold cross-validation; **(b)** Relationship diagram of different texture feature coefficients with changes; **(c)** LASSO coefficient values of the selected features. LASSO, Least Absolute Shrinkage and Selection Operator; MSI, microsatellite instability.

Table 2. Comparison of clinical information between the training group and the test group of patients

Parameters	Training group (n = 112)	Test group (n = 49)	t/x²	*P*
Age (years)	49.57 ± 7.28	48.53 ± 8.05	0.821[1]	0.307
BMI (kg/m²)	24.16 ± 2.31	23.32 ± 2.01	0.211[1]	0.402
Hypertension			3.001	0.487
With/without	60/52	25/24		
Diabetes			0.201	0.538
With/without	27/85	12/37		
Tumor stage			0.231	0.135
I+II/III+IV	97/15	43/6		
Tumor grade			1.423	0.332
G1 + G2/G3	82/30	37/12		
DMI			1.673	0.278
(–)/(+)	90/22	45/4		

The values marked with superscript (1) represent statistical results analyzed by the independent samples t-test. BMI, body mass index; DMI, deep myometrial infiltration; G1/G2/G3, tumor differentiation grade.

This indicates a balanced distribution of data between the two sets. Furthermore, univariate and multivariate analyses of clinical variables in the training cohort revealed no independent predictors significantly associated with MSI status (Table 3).

Establishment of radiomics models

A total of 1,904 radiomic features were extracted from the intratumoral region, the peritumoral regions (defined by 3, 5, and 7 mm margins), and the combined intratumoral–peritumoral regions. Comparative analysis using ROC curves across six classifiers demonstrated that the BDT achieved the highest AUC and exhibited superior stability.

Table 3. Univariate and multivariate logistic regression analysis of the training group

Parameters	MSI	MSS	Univariate analysis		Multivariable analysis	
	n = 33	n = 128	OR (95% CI)	*P*	OR (95% CI)	*P*
Age (years)	50.31 ± 1.04	52.07 ± 1.01	0.947 (0.821–1.082)	< 0.05	0.743 (0.617–1.013)	0.512
BMI (kg/m²)	24.18 ± 0.11	23.41 ± 1.34	1.563 (1.340–2.041)	0.301		
Hypertension			1.784 (1.224–2.101)	0.813		
With/without	17/16	65/63				
Diabetes			12.300 (12.120–15.102)	0.013		
With/without	8/25	33/95				
Tumor stage				0.110		
I+II/III+IV	28/5	113/15	4.005 (3.783–4.111)			
Tumor grade				0.223		
G1 + G2/G3	24/9	98/30	4.115 (4.114–6.234)			
DMI				0.112		
(–)/(+)	26/7	118/10	9.894 (8.110–11.211)			

MSI, microsatellite instability; MSS, microsatellite stability; OR, odds ratio; CI, confidence interval; BMI, body mass index; DMI, deep myometrial infiltration; G1/G2/G3, tumor differentiation grade.

Table 4. Area under the receiver operating characteristic curve of 42 intra-tumoral radiomic features in the training group and the test group

	T2WI	DWI	DCE	T2WI +DWI	T2WI +DCE	DWI +DCE	T2WI+DWI +DCE
LR	0.977 (0.909–1)	1 (1–1)	0.646 (0.593–0.876)	1 (1–1)	1 (1–1)	1 (1–1)	1 (1–1)
	0.354 (0.726–0.782)	0.5556 (0.037–1)	0.719 (0.214–0.745)	0.645 (0.426–1)	0.499 (0.037–1)	0.501 (0.040–1)	0.787 (0.073–1)
BDT	0.817 (0.801–0.954)	0.835 (0.794–0.997)	0.912 (0.756–0.967)	0.874 (0.799–1)	0.891 (0.776–1)	0.899 (0.997–1)	0.934 (0.814–0.957)
	0.839 (0.686–0.902)	0.6889 (0.795–1)	0.856 (0.721–1)	0.889 (0.545–1)	0.888 (0.845–1)	0.889 (0.864–1)	0.914 (0.789–0.954)
DT	0.754 (0.632–0.875)	0.804 (0.685–0.923)	0.754 (0.617–0.836)	0.804 (0.598–0.932)	0.804 (0.701-0.903)	0.804 (0.770–0.912)	0.960 (0.685–0.973)
	0.4194 (0.307–0.531)	0.688 (0.140–1)	0.950 (0.435–1)	0.690 (0.351–1)	0.701 (0.298–1)	0.693 (0.303–1)	0.6760 (0.013–1)
GP	0.654 (0.489–0.81)	0.728 (0.580–0.875)	0.654 (0.566–0.831)	0.728 (0.580–0.875)	0.728 (0.580–0.875)	0.728 (0.580–0.875)	0.772 (0.050–0.784)
	0.6774 (0.219–1)	0.777 (0.475–1)	0.702 (0.419–0.721)	0.603 (0.085–1)	0.806 (0.564–1)	0.572 (0.483–1)	0.709 (0.364–1)
RF	0.999 (0.999–1)	1 (1–1)	0.786 (0.200–0.921)	1 (1–1)	1 (1–1)	1 (1–1)	1 (1–1)
	0.209 (0.033–0.385)	0.422 (–0.118 to 0.963)	0.919 (0.200–0.936)	0.422 (–0.107 to 0.892)	0.302 (0.207–0.870)	0.451 (0.200–0.947)	0.433 (0.118–0.899)
SVM	0.999 (0.999–1)	1 (1–1)	0.668 (0.417–0.732)	1 (1–1)	1 (1–1)	1 (1–1)	1 (1–1)
	0.548 (0.092–1)	0.489 (0.108–0.869)	0.725 (0.417–0.735)	0.503 (0.108–0.787)	0.399 (0.080–0.969)	0.601 (0.100–0.799)	0.555 (0.302–0.699)

T2WI, T2-weighted imaging; DWI, diffusion-weighted imaging; DCE, dynamic contrast-enhanced; LR, logistic regression; BDT, bagging decision tree; DT, decision tree; GP, Gaussian process; SVM, support vector machine.

Intratumoral radiomics predicts the value of microsatellite instability

By applying six classifiers to the three MRI sequences and their combinations, a total of 42 intratumoral radiomics models were constructed (Table 4). Among the single-sequence models, the CE sequence demonstrated the most robust predictive performance, yielding an AUC of 0.912 in the training cohort and 0.856 in the test cohort. Furthermore, the combined model incorporating T2WI, DWI, and CE sequences outperformed all single-sequence models, achieving the highest diagnostic efficacy with AUCs of 0.934 and 0.914 in the training and test cohorts, respectively (Table 5).

Peritumoral radiomics predicts microsatellite instability value

A total of 54 peritumoral radiomics models were constructed by applying six classifiers to three peritumoral ROIs (Table 5). The analysis revealed that peritumoral imaging features generally demonstrated favorable predictive value in the test cohort. Specifically, models derived from the 3-mm peritumoral margin of T2WI, DWI, and CE sequences exhibited robust performance. Among these, the DWI 3-mm model yielded the most superior diagnostic efficacy, achieving an AUC of 0.898 in the training cohort and 0.790 in the test cohort.

The value of intratumoral and peritumoral radiomics in predicting microsatellite instability

In this study, we developed combined radiomics models by integrating intratumoral features with the optimal peritumoral features for each MRI sequence and their multiparametric combination (Figure 3). These selected features were input into a BDT classifier. The results demonstrated that the combined intratumoral–peritumoral models consistently yielded higher AUC values than the standalone intratumoral or peritumoral models across all sequences (Table 6). Notably, the multiparametric fusion model (T2WI + DWI + CE + DWI 3 mm) exhibited the most superior predictive performance, achieving an AUC of 0.998 in the test cohort (Figure 3f). Furthermore, the calibration curve indicated excellent concordance between predicted probabilities and observed outcomes in the training cohort (Figure 4). The DeLong test confirmed that the improvement in AUC for the combined model was statistically significant compared with its corresponding single-region models ($P < 0.05$, Table 7).

Table 5. Area Under the Receiver Operating Characteristic Curve of 54 Peri-Tumoral Radiomic features in the Training Group and the Test Group

Model	LR		BDT		DT		GP		SVM	
	Train	Test	Train	Test	Train	Test	Train	Test	Train	Test
T2WI										
3 mm	0.354 (0.726–0.782)	0.438 (0.072–0.697)	0.863 (0.775–0.990)	0.897 (0.789–0.899)	0.4194 (0.3071–0.5316)	0.704 (0.416–0.8501)	0.677 (0.219–1)	0.831 (0.401–1)	0.548 (0.092–1)	0.389 (0.287–1)
5 mm	0.719 (0.214–0.745)	0.719 (0.219–0.745)	0.831 (0.675–0.963)	0.857 (0.789–0.947)	0.950 (0.435–1)	0.409 (0.405–1)	0.713 (0.329–0.810)	0.677 (0.389–0.809)	0.725 (0.4172–0.735)	0.309 (0.044–0.598)
7 mm	0.632 (0.108–0.698)	0.509 (0.108–0.830)	0.567 (0.389–0.745)	0.741 (0.618–0.897)	0.809 (0.509–1)	0.350 (0.339–1)	0.810 (0.709–0.880)	0.590 (0.300–0.745)	0.601 (0.306–0.823)	0.742 (0.010–0.770)
DWI										
3 mm	0.475 (0.463–0.901)	0.554 (0.178–0.801)	0.898 (–0.186–1)	0.790 (0.782–1)	0.794 (0.609–0.821)	0.530 (0.507–0.712)	0.782 (0.238–1)	0.590 (0.409–1)	0.684 (0.292–1)	0.690 (0.163–0.773)
5 mm	0.803 (0.306–0.887)	0.598 (0.023–0.862)	0.801 (0.772–0.987)	0.689 (0.789–0.983)	0.950 (0.435–1)	0.689 (0.2980.891)	0.782 (0.238–1)	0.59 (0.583–0.901)	0.672 (0.538–0.798)	0.725 (0.417–0.735)
7 mm	0.555 (0.207–0.801)	0.919 (0.601–1)	0.767 (0.629–0.899)	0.790 (0.690–0.909)	0.801 (0.643–0.900)	0.550 (0.435–0.670)	0.702 (0.419–0.721)	0.809 (0.509–1)	0.672 (0.507–0.676)	0.599 (0.392–0.821)
DCE										
3 mm	0.589 (0.508–0.794)	0.608 (0.598–0.904)	0.868 (0.798–0.921)	0.798 (0.655–0.900)	0.899 (0.862–1)	0.530 (0.521–0.789)	0.679 (0.539–0.809)	0.481 (0.439–0.801)	0.731 (0.529–0.901)	0.791 (0.700–0.875)
5 mm	0.698 (0.014–0.890)	0.978 (0.649–0.995)	0.569 (0.721–1)	0.743 (0.721–1)	0.809 (0.710–0.830)	0.671 (0.189–0.891)	0.733 (0.029–0.880)	0.567 (0.509–0.590)	0.698 (0.692–0.901)	0.773 (0.691–0.887)
7 mm	0.190 (0.043–0.699)	0.341 (0.240–0.801)	0.833 (0.721–1)	0.734 (0.721–1)	0.753 (0.693–0.917)	0.510 (0.419–0.786)	0.701 (0.328–0.759)	0.509 (0.512–0.798)	0.729 (0.109–0.781)	0.591 (0.478–0.830)

T2WI, T2-weighted imaging; DWI, diffusion-weighted imaging; DCE, dynamic contrast-enhanced; LR, logistic regression; BDT, bagging decision tree; DT, decision tree; GP, Gaussian process; SVM, support vector machine.

Discussion

By aggregating complementary information from three MRI sequences, we effectively captured multidimensional tumor heterogeneity: DWI characterizes cellular density, T2WI discriminates tissue anatomy, and CE reflects tumor vascularity. Although numerous studies have demonstrated the utility of MRI-based models in predicting MSI, most have focused exclusively on the intratumoral volume, often overlooking the critical information provided by the peritumoral region regarding tumor invasiveness and biological behavior.[16-20] The peritumoral region serves as a critical interface for tumor–host interaction. At the microscopic level, this zone encompasses not only tumor cells but also immune cells within the tumor microenvironment, both of which play pivotal roles in tumorigenesis and progression. Recent studies have successfully combined intratumoral and peritumoral radiomics to evaluate HER2 status in breast cancer,[21] predict chemotherapy response in lung adenocarcinoma,[22] grade gliomas,[23] and assess ablation effects in lung malignancies,[24] all yielding promising results. Building on this evidence and considering anatomical constraints, our study defined peritumoral ROIs expanding 3, 5, and 7 mm from the tumor margin, strictly excluding the uterine serosa, cystic changes, and hemorrhage. These margins were selected to effectively capture early pathological changes—such as micro-infiltration, inflammatory responses, and angiogenesis—while minimizing noise from healthy tissue. Our results indicated that among single-sequence intratumoral models, CE demonstrated the most robust predictive performance (training AUC: 0.912; test AUC: 0.856). Furthermore, the multiparametric model (T2WI+DWI+CE) achieved the highest overall diagnostic efficacy (training AUC: 0.934; test AUC: 0.914). These findings corroborate the work of Zhao et al.,[14] who reported similar performance for a combined T2WI, CE, and DWI model in predicting EC-MSI (training AUC: 0.912; test AUC: 0.907). Both studies suggest that integrating multiple sequences provides a comprehensive

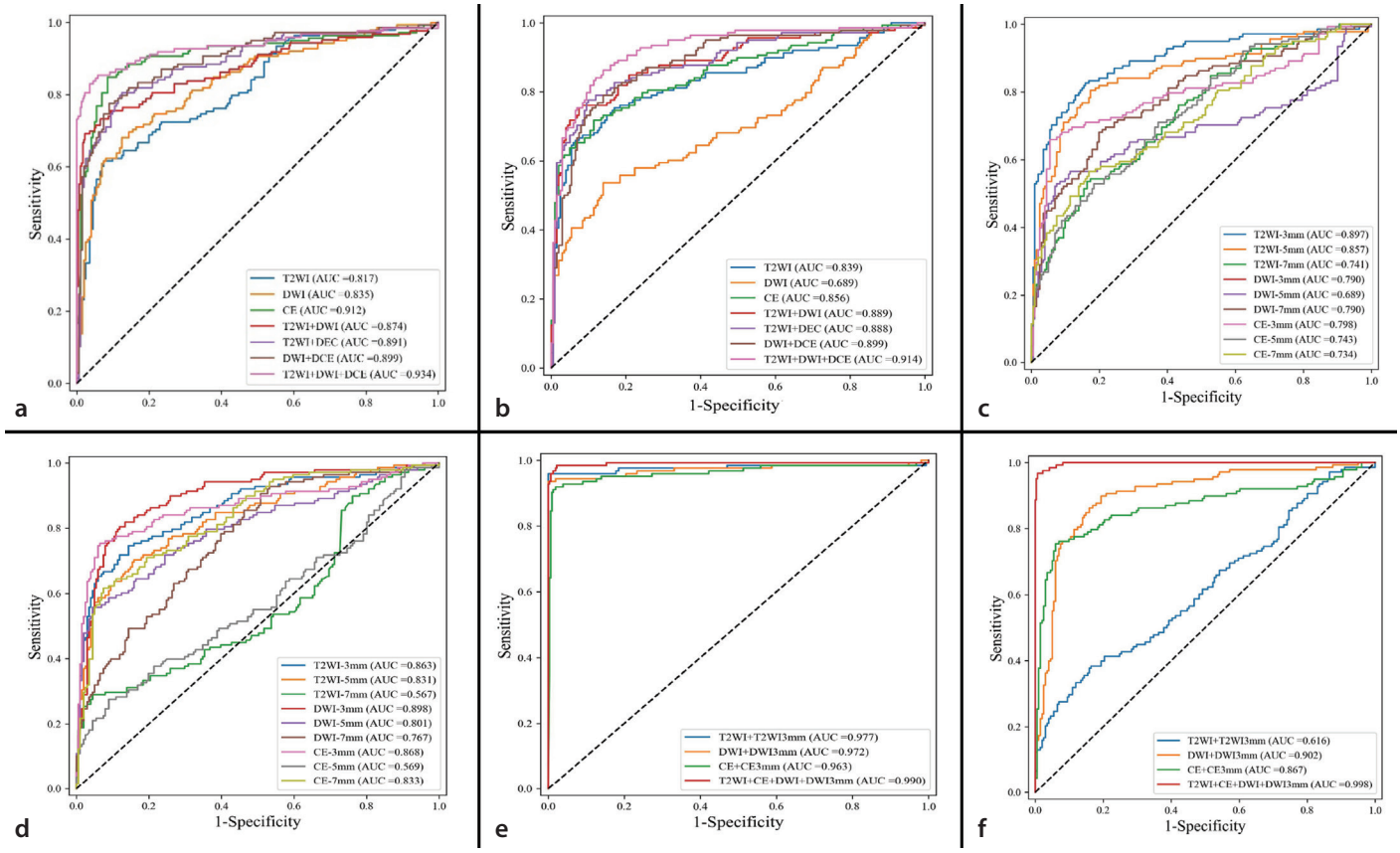


Figure 3. ROC curves of intratumoral, peritumoral, and intratumoral + peritumoral radiomics models in each sequence. **(a)** Training cohort intratumoral; **(b)** test cohort intratumoral; **(c)** training cohort peritumoral; **(d)** test cohort peritumoral; **(e)** training cohort intratumoral + optimal peritumoral and optimal intratumoral + optimal peritumoral; **(f)** test cohort intratumoral + optimal peritumoral and optimal intratumoral + optimal peritumoral. ROC, receiver operating characteristic; T2WI, T2-weighted imaging; DWI, diffusion-weighted imaging; CE, contrast-enhanced; AUC, area under the curve.

Table 6. Prediction efficacy of intratumoral + best peritumoral and best intratumoral + best peritumoral models

Model	Train				Test			
	AUC (95% CI)	SEN	SPE	ACC	AUC (95% CI)	SEN	SPE	ACC
T2WI + T2WI 3 mm	0.977 (0.954–0.999)	0.436	1	0.929	0.616 (0.241–0.991)	0.521	0.931	0.818
DWI + DWI 3 mm	0.972 (0.907–1)	0.801	0.943	0.809	0.902 (0.765–0.943)	0.776	0.854	0.808
CE + CE 7 mm	0.963 (0.932–0.994)	0.2857	1	0.921	0.867 (0.694–1)	0.333	0.965	0.906
T2WI + CE + DWI + DWI 3 mm	0.990 (0.964–1)	0.818	1	0.921	0.998 (0.941–1)	0.670	0.8276	0.727

T2WI, T2-weighted imaging; DWI, diffusion-weighted imaging; CE, contrast-enhanced; AUC, area under the curve; CI, confidence interval; ACC, accuracy; SEN, sensitivity; SPE: specificity.

Table 7. DeLong test

Model	AUC	SEN	SPE	ACC
Intra vs. intra and peri	0.002	0.500	0.625	0.688
Peri vs. intra	0.878	1.000	1.000	0.500
Intra and peri vs. intra	0.031	0.500	0.625	0.688

Intra, intra-tumor; Peri, peri-tumor; AUC, area under the curve; ACC, accuracy; SEN, sensitivity; SPE: specificity.

assessment of tumor malignancy and heterogeneity. We attribute the superior performance of CE-based models to their ability to reflect tumor vascularity and permeability, which aligns with recent findings[25] suggesting that CE imaging holds significant potential for prognostication in EC.

Our analysis of the peritumoral region revealed that radiomic features extracted from the peritumoral margin possess significant predictive value. Specifically, the 3-mm peritumoral regions across T2WI, DWI, and CE sequences all demonstrated favorable efficacy. Among these, the DWI 3 mm model exhibited the most robust performance, achieving AUCs of 0.898 in the training cohort and 0.790 in the test cohort. Notably, this peritumoral performance surpassed that of certain intratumoral models, underscoring the critical role of peritumoral heterogeneity as a supplementary biomarker for MSI status. These findings align with recent observations in hepatocellular carcinoma

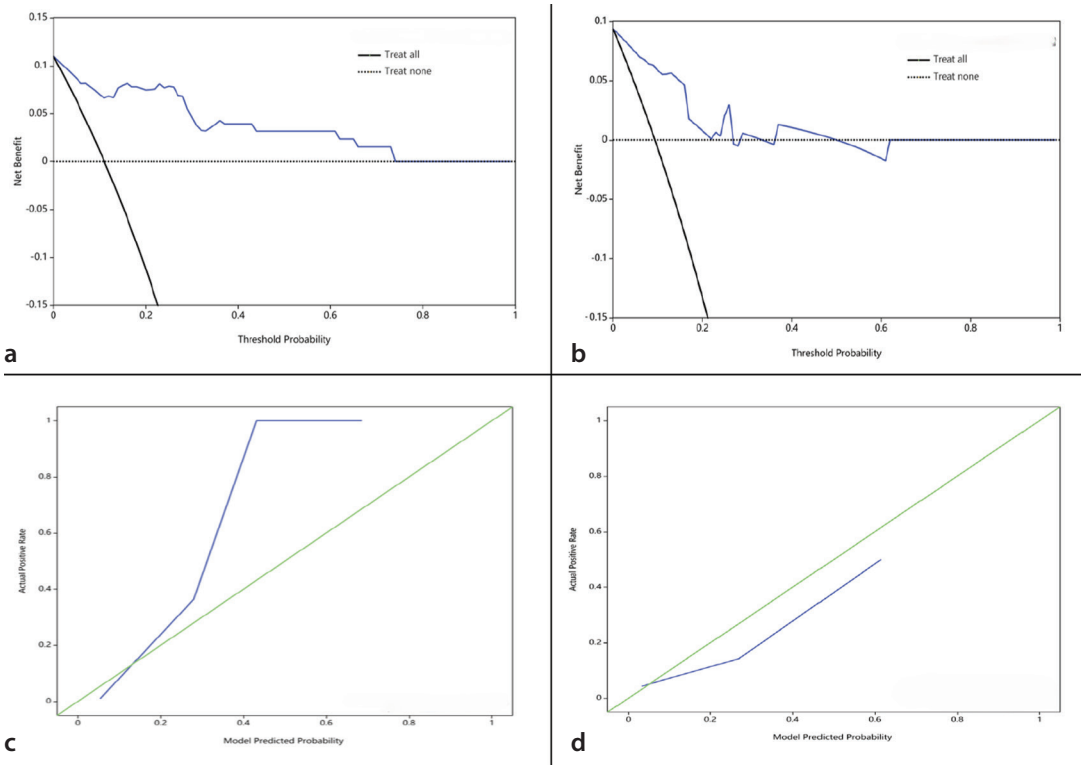


Figure 4. Optimal model DCA curves and calibration curves**. (a)** DCA curve of the training cohort; **(b)** DCA curve of the test cohort; **(c)** calibration curve of the training cohort; **(d)** calibration curve of the test cohort. DCA, decision curve analysis.

research.[26,27] To further enhance diagnostic accuracy, we developed combined models integrating the optimal intratumoral and peritumoral features. Consistent with our hypothesis, the fusion models universally outperformed their corresponding single-region counterparts (intratumoral only or peritumoral only). The most impressive results were obtained from the multiparametric fusion model, which combined intratumoral features from T2WI, DWI, and CE sequences with the optimal peritumoral DWI 3-mm features. This comprehensive model yielded the highest diagnostic efficacy, with AUCs reaching 0.990 and 0.998 in the training and test cohorts, respectively.

Radiomics is a promising high-throughput methodology capable of quantitatively characterizing micro-architectural heterogeneity and structural patterns within medical images, thereby generating novel imaging biomarkers.[28,29] In this study, we extracted radiomic features from the primary tumor and its surrounding 3-, 5-, and 7-mm margins to facilitate a non-invasive virtual biopsy.[30] Our findings revealed a high degree of complementarity between intratumoral and peritumoral features for the preoperative prediction of MSI in EC. This suggests that the peritumoral microenvironment harbors critical biological insights that effectively compensate for the information limitations inherent in analyzing the gross tumor volume alone. Concurrently, advancements in artificial intelligence have enabled the precise screening and efficient integration of high-dimensional radiomics data, expanding the horizon of clinical applications.[31] We employed five distinct machine learning algorithms to identify the optimal predictive model. The BDT emerged as the most robust classifier. Although its performance varied slightly across cohorts, it demonstrated superior stability and generalization capabilities. Mechanistically, BDT enhances classification accuracy by aggregating predictions from multiple DTs. This ensemble approach effectively reduces variance and mitigates the risk of overfitting,[32] thereby providing reliable decision support for the prognostic stratification and clinical management of patients with EC.

This study is subject to certain limitations. First, as a retrospective single-center study, the sample size was relatively modest, which may inherently introduce selection bias. Second, our analysis was restricted to standard clinical MRI sequences. Although effective, the inclusion of advanced functional imaging techniques could potentially offer deeper physiological insights into tumor heterogeneity and further refine predictive accuracy. To address these limitations, future research should adopt a multi-center, large-scale, prospective design. Collaborating across multiple institutions will facilitate the inclusion of a diverse patient population and allow for validation across different MRI scanning platforms and standardized protocols. Such efforts are essential to enhance the generalizability and robustness of the predictive model for broader clinical application.

In conclusion, this study leveraged multiparametric MRI to extract and analyze radiomic features from both intratumoral and peritumoral regions. By employing machine learning algorithms for optimal feature selection, we constructed an integrated intratumoral–peritumoral radiomics model that demonstrated superior diagnostic efficacy in predicting the MSI status of patients with EC. With accuracy comparable to the gold-standard postoperative IHC, this model serves as a reliable, non-invasive imaging tool to guide personalized preoperative treatment planning and prognostic assessment for patients with EC.

Footnotes

Conflict of interest disclosure

The authors declared no conflicts of interest.

Funding

This study was supported in part by grants from the Llinchuang Foundation of First Af-

filiated Hospital of Medical College, Shihezi University (Grant number: LC2025019). References

1. Sung H, Ferlay J, Siegel RL, et al. Global Cancer Statistics 2020: GLOBOCAN estimates of incidence and mortality worldwide for 36 cancers in 185 countries. *CA Cancer J Clin*. 2021;71(3):209-249. [Crossref]
2. Li K, Luo H, Huang L, Luo H, Zhu X. Microsatellite instability: a review of what the oncologist should know. *Cancer Cell Int*. 2020;20:16. [Crossref]
3. Antill Y, Kok PS, Robledo K, et al. Clinical activity of durvalumab for patients with advanced mismatch repair-deficient and repair-proficient endometrial cancer. A nonrandomized phase 2 clinical trial. *J Immunother Cancer*. 2021;9(6):e002255. [Crossref]
4. Song Y, Gu Y, Hu X, Wang M, He Q, Li Y. Endometrial tumors with MSI-H and dMMR share a similar tumor immune microenvironment. *Onco Targets Ther*. 2021;14:4485-4497. [Crossref]
5. Yang YS, Long X, Du XM, Fan WX, Zhang TH. The value of preoperative MR ADC in predicting microsatellite instability status in endometrial carcinoma. *J China Clin Med Imaging*. 2025;36(5):353356. [Crossref]
6. Ren JP, Zhang M, Liu WY. Assessing microsatellite instability of endometrial adenocarcinoma with multimodal intravoxel incoherent motion MRI. *International Journal of Medical Radiology*. 2023;46(4):396-401. [Crossref]
7. Pan MY, Cai WZ, Chen L, Wen J. Establishment of microsatellite instability assessment model for endometrial carcinoma by clinic-imaging omics. *Journal of Molecular Imaging*. 2023;46(1):48-52. [Crossref]
8. Ma CJ, Tian SF, Chen LH, et al. Quantitative assessment of microsatellite instability in endometrial cancer by T2 mapping combined with mDixon-Quant multiparameter imaging. *Chin J Magn Reson Imaging*. 2022;13(8):48-54. [Crossref]
9. Tian SF, Liu AL, Chen LH, et al. Evaluation of microsatellite instability in endometrial carcinoma by amide proton transfer imaging and diffusion kurtosis imaging. *Journal of China Clinic Medical Imaging*. 2022;33(5):345-349. [Crossref]
10. Aerts HJWL, Velazquez ER, Leijenaar RTH, et al. Correction: corrigendum: decoding tumour phenotype by noninvasive imaging using a quantitative radiomics approach. *Nat Commun*. 2014;5:4644. [Crossref]
11. Bera K, Braman N, Gupta A, Velcheti V, Madabhushi A. Predicting cancer outcomes with radiomics and artificial intelligence in radiology. *Nat Rev Clin Oncol*. 2022;19(2):132-146. [Crossref]
12. Liu ZY, Ding YX, Bai GJ. Prediction of endometrial cancer microsatellite expression status via deep transfer learning features based on multi-parameter MRI. *Chin J Med Imaging*. 2025;33(5):546-552,561. [Crossref]
13. Niu YC, Zhou F, Zhao DD, Hou MY, Li JS, Zhang Y. Value of a prediction model based on DWI deep learning features for evaluating microsatellite instability status in endometrial cancer. *Chin J Med Imaging*. 2024;32(9):922-927. [Crossref]
14. Zhao JF, Tian Y, Ma MM, Cao XS. Application research of imaging genomics in preoperative prediction of microsatellite stability of endometrial cancer using mp-MRI. *Chin J Magn Reson Imaging*. 2024;15(11):110-116,122. [Crossref]
15. Jiang M, Jia K, Wang L, et al. Alterations of DNA damage response pathway: Biomarker and therapeutic strategy for cancer immunotherapy. *Acta Pharm Sin B*. 2021;11(10):2983-2994. [Crossref]
16. Wang Z, Hu Y, Cai J, et al. Potential value of novel multiparametric MRI radiomics for preoperative prediction of microsatellite instability and Ki-67 expression in endometrial cancer. *Sci Rep*. 2025;15:3226. [Crossref]
17. Li Z, Su Y, Cui Y, Yin Y, Li Z. Multi-sequence MRI-based clinical-radiomics models for the preoperative prediction of microsatellite instability-high status in endometrial cancer. *Precis Radiat Oncol*. 2025;9(1):43-53. Erratum in: *Precis Radiat Oncol*. 2025;9(3):228. [Crossref]
18. Zhou L, Zheng L, Hong C, et al. A novel model for predicting microsatellite instability in endometrial cancer: integrating deep learning-pathomics and MRI-based radiomics. *Acad Radiol*. 2025;32(10):5940-5950. [Crossref]
19. Wei QY, Li Y, Huang XL, et al. Predicting microsatellite instability in endometrial cancer by multimodal magnetic resonance radiomics combined with clinical factors. *Acad Radiol*. 2025;32(11):6693-6706. [Crossref]
20. Zhang M, Wang X, Li Z, et al. A radiomics model based on diffusion-weighted imaging developed using machine learning enables prediction of microsatellite instability in endometrial cancer. *BMC Med Imaging*. 2025;25:405. [Crossref]
21. Li ZJ, Yang XF, Jiang ZY, et al. Intratumoral and peritumoral radiomics assessment of HER2 status in breast cancer based on DBT. *J Clin Radiol*. 2023;42(9):1436-1441. [Crossref]
22. Khorrami M, Khunger M, Zagouras A, et al. Combination of peri- and intratumoral radiomic features on baseline CT scans predicts response to chemotherapy in lung adenocarcinoma. *Radiol Artif Intell*. 2019;1(2):e180012. [Crossref]
23. Liu SZ, Wang ZB, Lou J, Jiang F, Xia XS. Prediction of glioma pathologic grading based on multisequence peritumor and intratumor radiomics. *Clin Radiol J*. 2024;43(9):14501455. [Crossref]
24. Zhu F, Yang C, Xia Y, et al. Based on peritumoral CT radiomics may assess the early efficacy of microwave ablation in lung malignant tumors. *J Clin Radiol*. 2023;42(8):1317-1321. [Crossref]
25. Zhang Y, Bao X, Wang Y, Li L, Liu L, Wu Q. Machine learning-based radiomics model: prognostic prediction and mechanism exploration in patients with endometrial cancer. *Biomark Res*. 2025;13(1):119. [Crossref]
26. Wang F, Cheng M, Du B, et al. Predicting microvascular invasion in small (≤5 cm) hepatocellular carcinomas using radiomics-based peritumoral analysis. *Insights Imaging*. 2024;15(1):90. [Crossref]
27. Zhao Y, Zhang J, Wang N, et al. Intratumoral and peritumoral radiomics based on contrast-enhanced MRI for preoperatively predicting treatment response of transarterial chemoembolization in hepatocellular carcinoma. *BMC Cancer*. 2023;23(1):1026. [Crossref]
28. Greten TF, Villanueva A, Korangy F, et al. Biomarkers for immunotherapy of hepatocellular carcinoma. *Nat Rev Clin Oncol*. 2023;20(11):780-798. [Crossref]
29. Zhang Z, Wan X, Lei X, et al. Intra- and peri-tumoral MRI radiomics features for preoperative lymph node metastasis prediction in early-stage cervical cancer. *Insights Imaging*. 2023;14(1):65. [Crossref]
30. Roussel E, Capitanio U, Kutikov A, et al. Novel imaging methods for renal mass characterization: a collaborative review. *Eur Urol*. 2022;81(5):476-488. [Crossref]
31. Chen M, Copley SJ, Viola P, Lu H, Aboagye EO. Radiomics and artificial intelligence for precision medicine in lung cancer treatment. *Semin Cancer Biol*. 2023;93:97-113. [Crossref]
32. Shoeibi A, Sadeghi D, Moridian P, et al. Automatic diagnosis of schizophrenia in EEG signals using CNN-LSTM models. *Front Neuroinform*. 2021;15:777977. [Crossref]

Diagn Interv Radiol 2026; DOI: 10.4274/dir.2026.264044

ABDOMINAL IMAGING

LETTER TO THE EDITOR

©Copyright 2026 Author(s) - Available online at dirjournal.org.
Content of this journal is licensed under a Creative Commons Attribution-NonCommercial 4.0 International License.

Letter to the Editor: On the clinical applicability of multiparametric and multimodal approaches in the evaluation of focal liver lesions

Ali Kemal Sivrioglu

Independent Researcher, Radiology, Flanders, Belgium

Dear Editor,

I read with great interest the study by Jabiyev et al.,[1] in which they evaluated the role of multiparametric magnetic resonance imaging (mpMRI), diffusion-weighted imaging (DWI), and magnetic resonance elastography (MRE) in differentiating benign from malignant liver lesions. I congratulate the authors on this valuable technical assessment.

However, although the term "multiparametric" is used in the title and throughout the text, I note that the parameters examined [apparent diffusion coefficient (ADC), stiffness, and T1/T2 mapping] were analyzed primarily as individual variables rather than within an integrated diagnostic model—for example, through logistic regression or a combined scoring system.[1-3] A truly multiparametric approach should demonstrate how the combination of different biophysical parameters guides patient management more reliably than single parameters. The authors implicitly acknowledge this limitation, stating that the contribution of the combined application remains a goal for future studies.[1]

At this point, I believe that the concept of multimodality should not be limited solely to MRI sequences. The fact that MRE still requires specialized equipment in many centers necessitates the integration of more accessible methods.[3] Current literature suggests that multimodal integration of ultrasound (US) and MRI data may provide a more holistic success in revealing both vascular and parenchymal phenotypes of lesions.[2,4] For instance, novel super-resolution US (SR-US) techniques can analyze microvascular architecture—vessel density, fractal dimension, and flow direction entropy—at the 128-micrometer level.[2] Combining such microvascular data with MRI findings such as ADC and stiffness into a single algorithm holds the potential to minimize the need for biopsy, especially in cases with atypical enhancement or overlapping quantitative values.[2,5]

I propose that future research should focus on multimodal algorithms strengthened by artificial intelligence-supported radiomic analyses. Three main approaches stand out.

The first approach involves screening models combining grayscale US and Doppler data with non-contrast MRI findings (DWI/ADC). Such an approach may not completely replace contrast-enhanced imaging for definitive subtype characterization, but it could carry significant clinical value in first-line differential diagnosis and when contrast use is contraindicated.

The second utilizes hybrid approaches simultaneously evaluating microbubble-based vascular mapping—contrast-enhanced US and SR-US—with MRI tissue characterization (stiffness/ADC).[2]

The third approach consists of high-resolution integrated models incorporating all contrast-enhanced and advanced sequences (mapping/elastography) of both US and MRI.[1,4]

In conclusion, the study by Jabiyev et al.[1] successfully demonstrates the effectiveness of mpMRI, DWI, and MRE in evaluating focal liver lesions. However, further prospective, multicenter studies with large patient series, based on the combined use of parameters and modalities, are indispensable for the true integration of these techniques into clinical practice.

Corresponding author: Ali Kemal Sivrioğlu

E-mail: dralikemalkalp@gmail.com

Received 05 April 2026; accepted 06 April 2026.

Epub: 06.05.2026

Publication date: 02.11.2026

DOI: 10.4274/dir.2026.264044

You may cite this article as: Sivrioglu AK. Letter to the editor: on the clinical applicability of multiparametric and multimodal approaches in the evaluation of focal liver lesions. *Diagn Interv Radiol*. 2026;32(6):743-744.

Footnotes

Conflict of interest disclosure

The author declared no conflicts of interest.

References

1. Jabiyev A, Karçaaltıncaba M, Karaosmanoğlu AD, Akata D, Özmen MN, İdilman İS. Multiparametric magnetic resonance imaging, diffusion-weighted magnetic resonance imaging, and magnetic resonance elastography: differentiating benign and malignant liver lesions. *Diagn Interv Radiol*. 2026;32(2):133-138. [Crossref]
2. Couture O, Hingot V, Heiles B, Muleki-Seya P, Tanter M. Ultrasound localization microscopy and super-resolution: a state of the art. *IEEE Trans Ultrason Ferroelectr Freq Control*. 2018;65(8):1304-1320. [Crossref]
3. Idilman IS, Li J, Yin M, Venkatesh SK. MR elastography of liver: current status and future perspectives. *Abdom Radiol (NY)*. 2020;45(11):3444-3462. [Crossref]
4. Banerjee R, Pavlides M, Tunnicliffe EM, et al. Multiparametric magnetic resonance for the non-invasive diagnosis of liver disease. *J Hepatol*. 2014;60(1):69-77. [Crossref]
5. Taouli B, Koh DM. Diffusion-weighted MR imaging of the liver. *Radiology*. 2010;254(1):47-66. [Crossref]

Diagn Interv Radiol 2026; DOI: 10.4274/dir.2026.263844

ABDOMINAL IMAGING

ORIGINAL ARTICLE

©Copyright 2026 Author(s) - Available online at dirjournal.org.
Content of this journal is licensed under a Creative Commons Attribution-NonCommercial 4.0 International License.

Global trends and hotspots of machine learning in the diagnosis of prostate cancer: a bibliometric analysis from 1997 to 2024

Yixiao Shi

Operating Room of Anesthesia Surgery Center, West China Hospital/West China School of Nursing, Sichuan University, Sichuan, China

PURPOSE

Prostate cancer (PCa) diagnosis has advanced with the integration of machine learning (ML). This study analyzes global trends in ML-based PCa diagnosis research using bibliometric methods.

METHODS

A systematic search was conducted in the Web of Science Core Collection database for articles published between 1997 and 2024. Bibliometric analysis was performed using VOSviewer (v1.6.20), CiteSpace (v6.3.R1), and R (v4.3.3).

RESULTS

The analysis included 1,045 articles, involving 6,704 authors from 4,762 institutions across 327 countries or regions. The number of publications increased over time, rising sharply from 2018. China published the highest number of articles (290), whereas the United States demonstrated the greatest research impact, leading in total citations (8,207) and international collaborations. The Berlin Institute of Health published the highest number of articles (120). Within this dataset, European Radiology had the highest H-index. Key authors included Stephan C, Jung K, and Cammann H. Keyword analysis identified "system," "MRI," and "guidelines" as prominent terms, with emerging trends focusing on "convolutional neural network," "data system," and "transfer learning."

CONCLUSION

ML in PCa diagnosis has advanced substantially, transitioning from fundamental biomarker investigations to sophisticated deep learning applications centered on medical imaging. Future directions emphasize the development of accurate, generalizable ML models integrated into clinical workflows with a continued focus on convolutional neural networks and transfer learning.

CLINICAL SIGNIFICANCE

This study delineates the global research evolution of maching learning for prostate cancer diagnosis, offering clear clinical guidance for the translation and routine application of artificial intelligence-assisted diagnostic models.

KEYWORDS

Bibliometrics, research trends, diagnosis, machine learning, prostate cancer

Handling editor: Sonay Aydın

Corresponding author: Yixiao Shi

E-mail: sdian314748761@163.com

Received 31 December 2025; revision requested 13 February 2026; accepted 30 March 2026.

Epub: 30.04.2026

Publication date: 02.11.2026

DOI: 10.4274/dir.2026.263844

Prostate cancer (PCa) is one of the most common malignancies in men and remains a major contributor to cancer-related morbidity worldwide.[1] Recent estimates indicate that PCa is the second most frequently diagnosed cancer among men globally, with approximately 1.4 million new cases annually, and its incidence increases sharply after age 50.[2,3] Because early-stage PCa is often asymptomatic and diagnostic pathways are heterogeneous, improving diagnostic accuracy and efficiency remains clinically important.

Machine learning (ML), a key branch of artificial intelligence (AI), has increasingly been applied to medical diagnostics by identifying patterns in high-dimensional data that may be difficult to detect using conventional approaches.[4] To improve detection, risk stratification, and clinical decision support in PCa diagnosis, ML has been explored across multiple data modali-

You may cite this article as: Shi Y. Global trends and hotspots of machine learning in the diagnosis of prostate cancer: a bibliometric analysis from 1997 to 2024. *Diagn Interv Radiol*. 2026;32(6):745-754.

ties, including multiparametric magnetic resonance imaging (mpMRI), digital pathology, serum and urine biomarkers, and electronic health records.[5] However, translation into practice is constrained by issues such as data heterogeneity, limited external validation, interpretability, and regulatory and ethical requirements.[6] Therefore, a structured overview of how this research area has evolved and which themes are currently emerging may help guide future methodological and clinical work.

Bibliometric analysis quantitatively characterizes scientific literature by identifying influential contributors (authors, institutions, and journals), collaboration patterns, and evolving research topics using citation- and keyword-based mapping.[7,8] Several recent bibliometric studies have examined AI in PCa-related research. For example, Wei et al.[9] reported rapid growth in AI–PCa publications over the last decade, with the United States and China as major contributors and an increasing emphasis on deep learning for imaging tasks. However, existing bibliometric work often focuses on broader AI applications or more recent time windows and may not isolate diagnostic research as a primary theme.[10]

To extend and complement prior studies, we conducted a bibliometric analysis of ML-based PCa diagnosis research. Our objectives were to quantify publication and citation trends over a longer historical period; map global collaboration networks among countries, institutions, and authors; identify influential journals and references; and detect research hotspots and emerging topics through keyword co-occurrence and burst analyses. By explicitly focusing on diagnostic applications and extending the timeline, this study aims to clarify how current themes (e.g., MRI- and deep-learning–driven approaches) align with or diverge from prior bibliometric findings, and to provide context for future research directions and clinical translation.

Main points

- Global research on machine learning (ML) in prostate cancer diagnosis has grown rapidly, with publication output surging from 2018 and a diverse, international research community contributing across 327 regions.
- China leads in publication quantity, whereas the United States drives research impact, visibility, and collaboration, as reflected in citation counts and extensive international partnerships.
- Major institutions and authors shape the field, including the Berlin Institute of Health as a leading contributor and European Radiology as a top publisher by H-index; key researchers include Stephan C, Jung K, and Cammann H.
- Research themes center on imaging-driven ML, particularly magnetic resonance imaging and system-level approaches, with methodological emphasis on convolutional neural networks, data systems, and transfer learning.
- The field has evolved from biomarker-focused studies to advanced deep learning applications, with future work focusing on accurate, generalizable models integrated into clinical workflows.

Search strategies and data source

This study was designed as a descriptive, cross-sectional bibliometric analysis of published literature on ML in PCa diagnosis. The literature search was conducted in the Web of Science Core Collection (WoSCC), which was selected because it provides standardized citation metadata and cited-reference fields that are directly compatible with common bibliometric tools (e.g., VOSviewer, CiteSpace, and bibliometrix).

The search query applied was [WoSCC, topic search (TS)]: TS = ("prostat* cancer*" OR "prostat* carcinoma" OR "prostat* adenocarcinoma" OR "prostat* neoplasm") AND TS = ("machine learning" OR "artificial intelligence" OR "machine intelligence" OR "deep learn*" OR "neural network*" OR "natural language process*" OR "hybrid intelligent system*" OR "CNN" OR "LSTM" OR "RNN") AND TS = (diagnos*).[11] In WoSCC, TS searches the title, abstract, author keywords, and Keywords Plus. The wildcard diagnos* was used to capture multiple diagnostic-related word forms (e.g., diagnosis, diagnostic, diagnosed). As a verification step, we repeated the search using TS = (diagnosis OR diagnostic OR diagnosed) and confirmed that the retrieved record count was identical.

The search covered articles published between January 1, 1997, and October 8, 2024. To minimize bias from database updates, all records were retrieved and exported on a single day (October 8, 2024).

Records were included if they met all of the following criteria: 1. topic relevance: focused on PCa diagnosis and involved ML or AI methods (including deep learning or neural networks); 2. time window: published between 1997 and 2024 (up to October 8, 2024); 3. language: English; and 4. document type: Article (as classified by WoSCC).

Records were excluded if they met any of the following criteria: 1. not related to diagnosis (e.g., ML studies limited to prognosis, treatment planning, basic laboratory mechanisms, or non-diagnostic screening without diagnostic intent); 2. not specific to PCa (e.g., multi-cancer studies without PCa-specific diagnostic analysis); 3. non-article document types (e.g., reviews, editorials, letters, meeting abstracts) if not indexed as "Article" in WoSCC; and 4. duplicates identified during export or processing.

No additional filter was applied to remove "Early Access" items. Therefore, any records indexed by WoSCC as "Article"—including those labeled as Early Access or originating from conference proceedings but categorized as an Article—were eligible for inclusion. We acknowledge that indexing timing for Early Access items may influence publication counts in the most recent year.

The exported records included publication year, title, authors, affiliations, countries or regions, journal information, keywords, citation counts, and cited references, and were saved in plain-text format for subsequent bibliometric analysis. Because this study analyzed publicly available bibliographic metadata and did not involve human participants or identifiable private information, ethical approval and informed consent were not required.

Statistical analysis and visualization

Data preprocessing and cleaning

Before mapping, we performed data cleaning to reduce noise caused by inconsistent WoSCC metadata. During data processing, we encountered typical bibliometric challenges, including author name ambiguity (e.g., authors with similar names or different initials), keyword unification (synonyms and abbreviations), and institutional name variations (e.g., the same organization recorded under multiple spellings).

We therefore applied a combination of automatic normalization and manual checking. Specifically, author names were standardized by merging obvious variants based on consistent co-author patterns, affiliations, and research topics (e.g., abbreviated vs. full forms such as "Stephan C" and "Stephan Carsten" when they referred to the same individual). Keywords were normalized by merging common abbreviations and equivalent terms (e.g., "MRI" and "magnetic resonance imaging"), as well as plural and singular forms and closely related expressions with

the same meaning. Institutional names were harmonized by consolidating clear spelling variants and alternative English names for the same institution.

In addition, we screened for metadata inconsistencies (e.g., missing affiliations or incomplete fields) and performed manual verification when necessary. Duplicate records were removed when identified.

Bibliographic records exported from WoSCC were analyzed using Microsoft Excel for descriptive statistics (e.g., annual publication counts, total citations, and averages). All bibliometric analyses were conducted using the same dataset exported on October 8, 2024. Visualization and network analyses were conducted using VOSviewer (Centre for Science and Technology Studies, Leiden University, Leiden, the Netherlands); CiteSpace (Drexel University, Philadelphia, PA, USA); R version 4.3.3 (R Foundation for Statistical Computing, Vienna, Austria) with the bibliometrix package.

When applicable, a VOSviewer thesaurus file was used to merge equivalent terms and improve the interpretability of keyword maps. VOSviewer was used to construct and visualize co-authorship and collaboration networks (countries, institutions, and authors), as well as keyword co-occurrence networks.[12] The association strength normalization method was used for network construction, and clusters were detected using VOSviewer's built-in clustering algorithm (based on modularity optimization). To improve readability and reduce sparsity, minimum-occurrence thresholds were applied; specifically, keywords were included in the co-occurrence analysis only if they appeared at least eight times. In VOSviewer maps, node size represents occurrence frequency (or publication output), link thickness represents total link strength, and colors indicate clusters or overlay attributes (e.g., average publication year).

CiteSpace was used for temporal analysis of research topics, including timeline and time-zone visualization and keyword burst detection.[13] To highlight major knowledge structures and emergent terms, the following settings were applied: time slicing: 1997–2024 (1 year per slice); node type: keywords; selection criteria: top N per slice; and pruning: Pathfinder (including pruning of merged networks). Burst strength and duration were reported to identify rapidly increasing keywords.

The bibliometrix package was used to compute bibliometric indices, including the H-index, G-index, and M-index, based on citations within the retrieved dataset.[14] The H-index is defined as the maximum value h such that an author or journal has at least h papers, each cited at least h times. The G-index is the largest value g such that the top *g* publications received at least g^2 total citations. The M-index is calculated as the H-index divided by the number of years since the first publication in the dataset, providing a time-normalized measure of impact.[15]

To describe the growth in annual publications, we fitted a simple regression model in Excel and R and reported the coefficient of determination (R^2). This model was used descriptively to summarize the overall growth pattern; no hypothesis testing (e.g., formal trend tests) was performed. Journal influence metrics [e.g., 2023 Journal Impact Factor and Journal Citation Reports quartile (Q1–Q4)] were obtained from the 2023 edition of Journal Citation Reports.

Results

Overview of publications

A total of 1,045 English-language articles on ML in PCa diagnosis published between 1997 and 2024 were analyzed (Figure 1). These studies involved 6,704 authors from 4,762 institutions across 327 countries or regions, were published in 352 journals, and cited 29,554 sources. Each publication had an average of 8.73 co-authors, and 30.81% involved international collaboration. The dataset included 2,052 keywords, and articles received an average of 24.61 citations (Figure 2A).

In the early years (1997–2012), research on ML in PCa diagnosis showed limited output. By 2013, annual publications exceeded 10, followed by a gradual increase from 2013 to 2018. From 2018, research output increased rapidly, peaking at 224 articles in 2023. A fitted curve (R^2: 0.8427) highlights the accelerating growth in publications over the period (Figure 2B).

Distribution and collaborative networks of countries

The 1,045 publications originated from 327 countries or regions. The top contributing countries or regions are summarized in Supplementary Table 1. China led in corresponding-author output with 290 articles (27.8%) and ranked second in total citations (4,762). The USA followed with 199 corresponding-author articles (19.0%), the highest number of multi-country publications (65), and the highest total citations (8,207). Germany ranked third with 66 corresponding-author articles (6.3%) and 1,838 citations (Figure 3A).

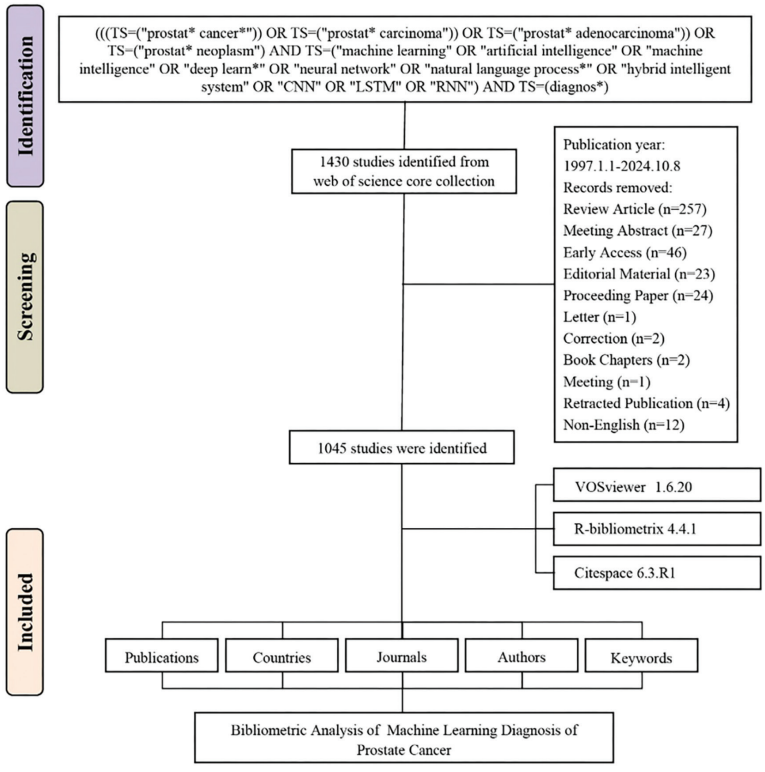


Figure 1. Flow diagram of the bibliographic retrieval process. TS, topic search; CNN, convolutional neural network; LSTM, long short-term memory; RNN, recurrent neural network.

Among the remaining top contributors, the Netherlands had the highest citations per publication (53.8), indicating a comparatively higher citation impact per article. Among the 76 countries that contributed at least one article through international collaboration, the USA led with 357 partnerships, primarily with Germany, Canada, China, and Japan. Germany ranked second with 183 collaborations, mainly involving the United States, the United Kingdom, Austria, the Netherlands, and Switzerland. China ranked third with 163 collaborations, primarily with the United States and Australia (Figure 3B).

Distribution and collaborative networks of institutions

A total of 4,762 institutions contributed to publications on ML in PCa diagnosis. Among the top 10 institutions, the Berlin Institute of Health in Germany led with 120 articles, followed by Stanford University (79 articles) and the University of California system (76 articles), both in the United States (Figure 4A).

In total, 151 institutions participated in international collaborations, each with at least five articles, forming distinct research clusters. Soochow University in China had the highest number of collaborations (54), forming a central dark-blue cluster. Shanghai Jiao Tong University in China was next with 51 collaborations, forming a yellow cluster. The University of Toronto in Canada ranked third with 45 collaborations, represented by a light-blue cluster (Figure 4B).

Contributions and collaborative networks of journals and authors

The articles were published across 352 journals, with the leading outlets and indicators summarized in Supplementary Table 2. By publication volume (TP), Cancers ranked first (TP: 53), followed by Frontiers in Oncology (TP: 35) and Scientific Reports (TP: 30).

In terms of influence metrics, European Radiology had the highest H-index[15] within this dataset, followed by Cancers (H-index: 13) and Medical Image Analysis and Medical Physics (H-index: 12 each). Regarding Journal Citation Reports metrics, Medical Image Analysis and Cancer Research had the highest 2023 impact factors among high-impact journals, and most leading journals were ranked in Q1.

The journal co-occurrence network, which measures joint citations in articles, identified three journals with the highest total link strength: European Radiology (185), Cancers (179), and Lancet Oncology (151) (Figure 5A). A journal coupling network, based on shared references, showed that Cancers (14,447), Frontiers in Oncology (10,387), and European Radiology (8,302) had the strongest link strengths (Figure 5B).

A total of 6,704 authors contributed to the dataset. Stephan C exhibited the highest H-index,[12] G-index,[15] M-index (0.522), and the most total publications,[15] followed by Jung K and Cammann H (Supplementary Table 3). Among 138 authors involved in international collaborations (with at least four articles), Rusu Mirabela led with 75 collaborations, followed by Fan Richard E (72) and Shao Wei (68) (Figure 6).

Keyword co-occurrence network and burst keywords

A total of 133 keywords with at least eight occurrences were identified for co-occurrence network analysis (Figure 7A). In the visualization, purple indicates earlier occurrences and yellow shows more recent ones. Around 2016, frequently occurring keywords included "antigen," "serum," and "identification" (purple). By 2018 (dark blue), terms such as "men," "radical prostatectomy," and "prediction" had emerged. Between 2018 and 2020 (dark green), "diagnosis" had the highest co-occurrence frequency (898), with "biopsy" and "classification" also prominent. Around 2020, newer terms such as "risk," "accuracy," and "features" appeared. Since 2022 (yellow), the most frequent keywords have been "system," "MRI," and "guidelines."

Keyword burst analysis identified terms with sharp increases in frequency, reflecting trends in the field (Figure 7B). The timeline uses gray to indicate periods without major activity, blue for ongoing research, and red for periods of intense activity. These bursts can be divided into two stages.

The first stage (1999–2005) showed prolonged bursts featuring keywords such as "antigen," "artificial neural network," "serum," "digital rectal examination," and "mass spectrometry." The second stage (2013–present) was characterized by shorter bursts and rapid keyword turnover. Between 2013 and 2018, terms such as "classification," "computer-aided diagnosis," and "ISUP Consensus Conference" were prominent. By 2019, new keywords, including "features," "convolutional neural network," "benign," and "data system," had gained prominence.

Since 2022, "transfer learning" has emerged as a key term and remains highly relevant. Many of these keywords persist in the blue phase, indicating ongoing research activity.

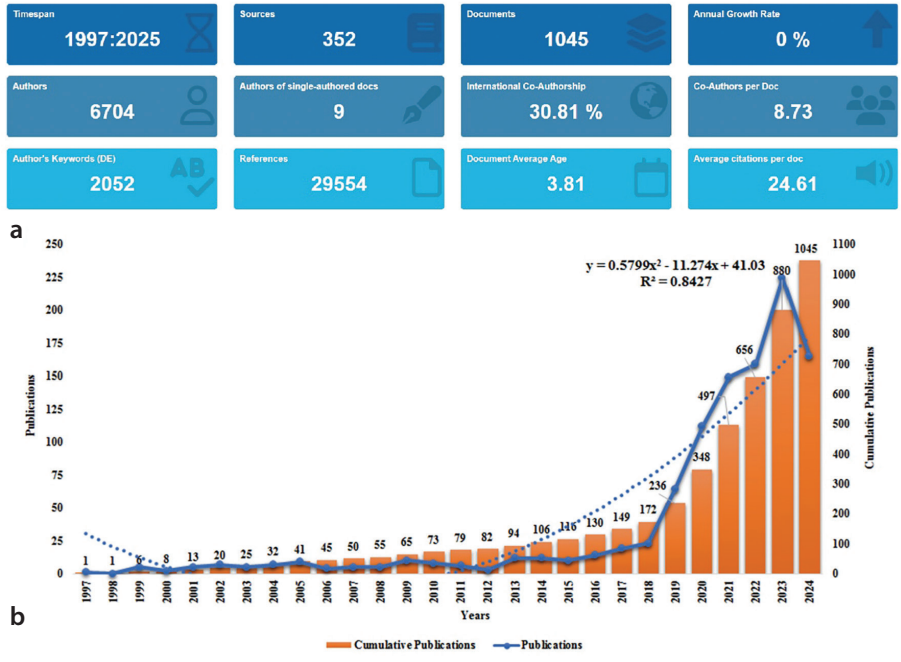


Figure 2. Analysis of general information. **(a)** Summary of the quantitative analysis of publications. **(b)** Annual research output from 1997 to 2024.

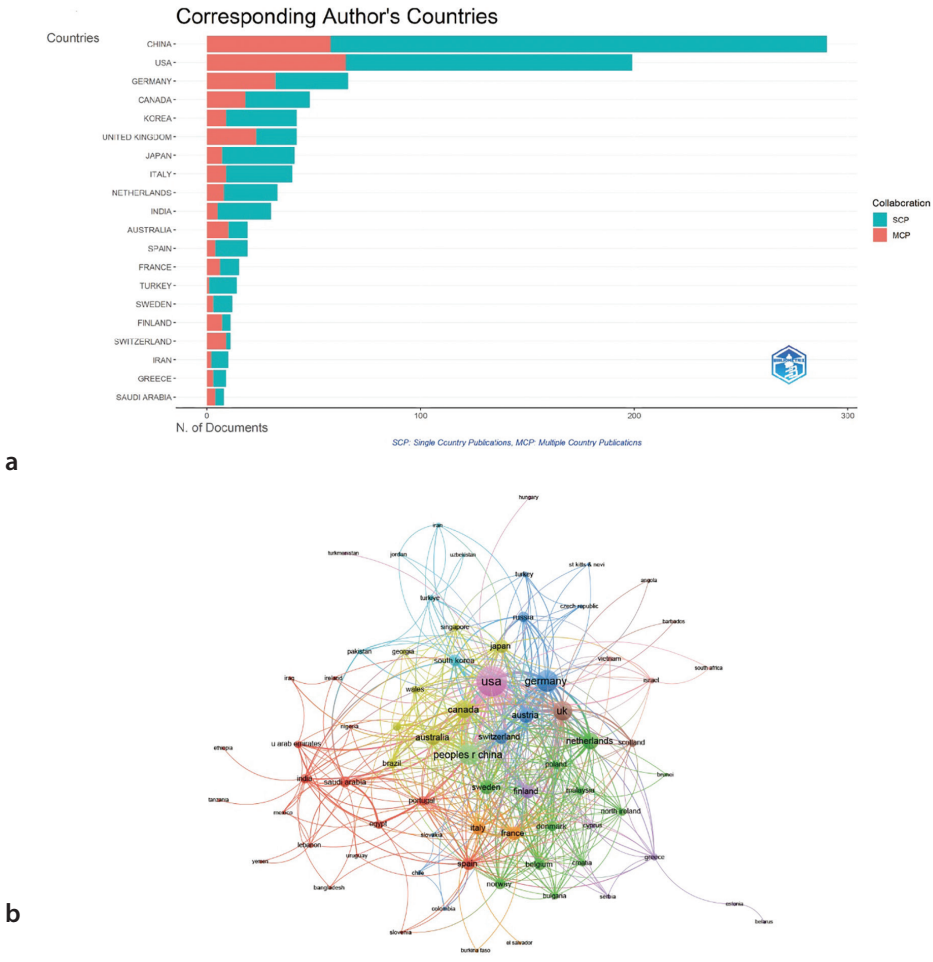


Figure 3. Analysis of countries. **(a)** Distribution of corresponding-author publications by country. **(b)** Visualization map depicting collaboration among countries.

Discussion

This bibliometric study summarizes ML research on PCa diagnosis from 1997 to late 2023. Publications increased rapidly from 2018 and peaked in 2023, suggesting growing interest and faster progress in ML methods and data use. China, the United States, and Germany were the main contributors. The United States and Germany show strong long-term foundations in biomedical and imaging research, and China's high output reflects continued investment in AI and health data science. The collaboration results also show that this field is increasingly driven by international partnerships and shared methods.

High-impact journals such as European Radiology, Cancers, and Medical Image Analysis show that research in this field primarily focuses on imaging, biomarkers, and AI-based diagnostic methods. The most cited study, "clinical-grade computational pathology using weakly supervised deep learning on whole slide images," highlights how deep learning can support digital pathology using slide-level labels without manual annotation.[16] Other influential works, such as the 2002 Cancer Research article on serum protein fingerprinting[17] and the 2019 review in Nature Reviews Clinical Oncology on AI for digital pathology,[18] further emphasize the central role of biomarker and imaging-based ML research in this domain.

In addition, our author-level productivity results indicate a highly skewed contribution pattern consistent with Lotka-type behavior, in which a relatively small group of authors accounts for a disproportionately large share of publications.[19] Within this concentrated expertise structure, key opinion leaders (e.g., Madabhushi and Yang) emerge as high-output, high-impact contributors, suggesting that mentorship and collaboration networks centered around leading groups may play an important role in shaping research directions and accelerating methodological diffusion across institutions.

Research hotspots and technological frontiers

Our keyword and burst analyses reveal a dynamic and evolving research landscape in ML-based PCa diagnosis, with thematic changes that track both clinical priorities and methodological breakthroughs. In the early years (1999–2005), research concentrated on traditional biomarker-oriented terms such as "antigen," "serum," and "identification",[20] reflecting the serum-based diagnostic strategies prevalent at the time. As the field matured, keywords such as "radical prostatectomy" and "prediction" emerged,[21] suggesting a shift toward clinically grounded modeling, including prognosis- and decision-relevant prediction tasks.

Between 2018 and 2020, the surge of "biopsy" and "classification" highlights an increased interest in ML methods that support core diagnostic decision points, particularly tissue confirmation and risk stratification.[22] During this period, frequent terms such as "accuracy" and "features" also indicate sus-

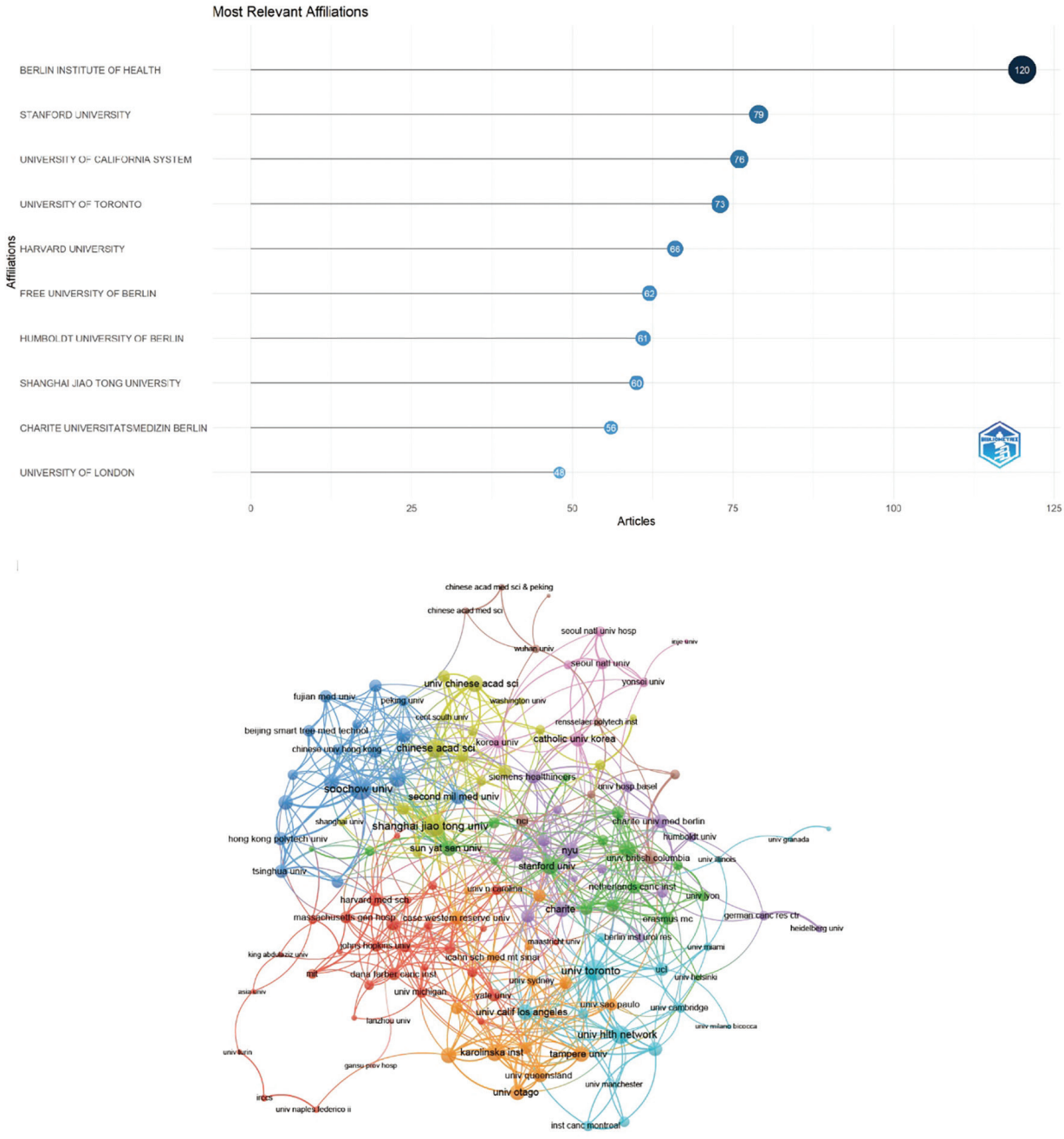


Figure 4. Analysis of institutions. **(a)** Top 10 institutions ranked by article count. **(b)** Visualization map depicting collaboration among institutions.

tained efforts to improve feature representation, model design, and performance evaluation practices.[23]

Why "MRI" has become dominant?

Since 2022, the increasing prominence of "MRI" aligns with the central role of mpMRI in contemporary PCa diagnostic pathways and with the suitability of MRI data for modern deep learning pipelines.[24] Multiparametric MRI provides rich spatial and functional information that supports tasks such as gland and lesion segmentation, lesion detection, and classification—areas in which convolutional neural network (CNN)-based methods have been particularly influential. The prominence of "MRI" in keyword analysis, therefore, likely reflects both its clinical importance in PCa workups and the scalability of imaging datasets for model development and benchmarking.

Contextualizing the "CNN" and "transfer learning" bursts with current technological developments

Burst analysis suggests a transition from earlier artificial neural networks and consensus-related terms (e.g., "ISUP Consensus Conference")[25] to a newer phase dominated by CNNs, data systems, and transfer learning.[26] This pattern is consistent with the broader deep-learning expansion following major CNN breakthroughs in computer vision, which subsequently catalyzed rapid uptake in medical imaging and computational pathology. In PCa diagnosis, CNN-based representation learning reduced reliance on manual feature engineering and enabled end-to-end learning on imaging and whole-slide data.[26]

The sustained "transfer learning" burst between 2022 and 2024[27] can be interpreted as

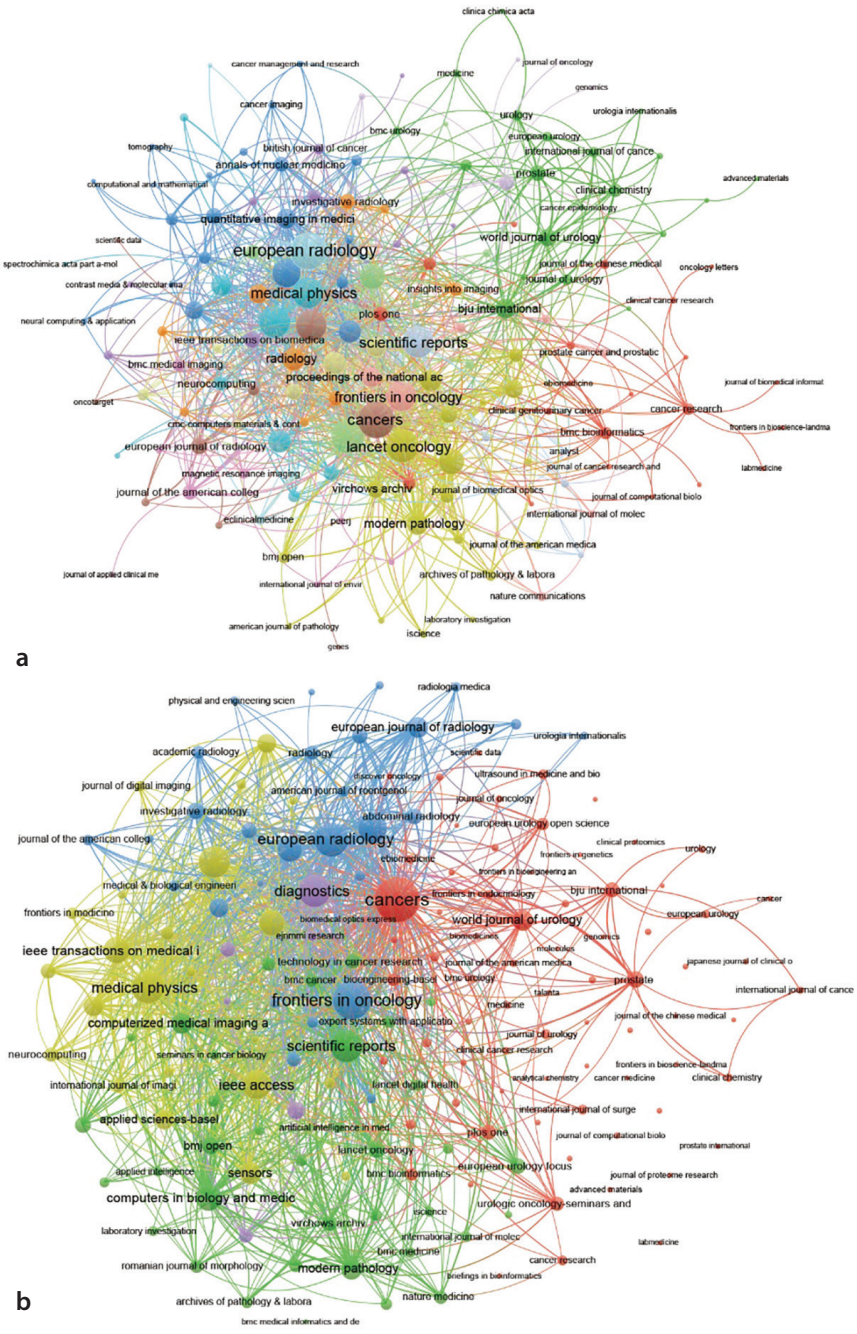


Figure 5. Analysis of journals. **(a)** Co-occurrence network of journals. **(b)** Coupling network of journals.

a response to persistent challenges in clinical AI, including limited annotated datasets, domain shifts across scanners and sites, and the need for robust generalization. Transfer learning enables the reuse of pretrained representations and adaptation to prostate imaging or pathology tasks with fewer labeled examples, supporting faster iteration and potentially improved external validity.[27] In the broader "foundation-model/GPT-era" context, the same underlying principle of leveraging large-scale pretraining to improve downstream performance has become increasingly central to modern AI development. Although the models and modalities differ across domains, this general trend helps explain why transfer learning remains a prominent and sustained hotspot in recent PCa diagnostic ML research.[27]

Although this analysis focuses on diagnosis, the observed keyword and thematic evolution can be interpreted as spanning three practical clusters that commonly co-develop in PCa ML research. First, diagnostic modeling and ML methods, including clinically relevant prediction problems tied to patient risk and outcomes (e.g., prediction-oriented keywords).[21] Second, imaging-driven ML (mpMRI-centric workflows), including detection, segmentation, and classification reflected by "MRI," "biopsy," and "classification".[22,24] Third, downstream clinical applications connected to treatment workflows, which tend to share enabling components such as segmentation, risk modeling, and data systems, and therefore appear adjacent to diagnosis-focused research streams in bibliometric structures.[26] This interpretation is consistent with the observed movement from algorithm keywords toward "system," suggesting increasing emphasis on end-to-end clinical utility rather than isolated model development.[24,26]

International collaboration and policy and infrastructure context

At the country level, China, the United States, and Germany dominate productivity and/or citation impact, and the collaboration network shows dense cross-national linkages. From an implementation perspective, these patterns likely reflect differences in long-term infrastructure (e.g., imaging and pathology digitization capacity, clinical research networks, and data engineering support) and the ability to sustain multidisciplinary teams combining urology, radiology, pathology, and AI. The emergence of highly connected collaboration hubs around established research systems is consistent with the need for large, well-curated datasets and rigorous validation to support clinically credible ML models.[28,29]

Importantly, collaboration results should not be interpreted solely as indicators of current research capacity. International co-authorship may also reflect historical funding structures, shared clinical trial networks, and established data ecosystems. In this context, the concentration of output in certain countries may reflect accumulated advantages in infrastructure and organization that facilitate multicenter studies and reproducibility—factors that are particularly important given ongoing challenges related to heterogeneity, interoperability, and clinical translation.[28,29]

Clinical implications

Bibliometric trends suggest that ML-based PCa diagnosis is moving from proof-of-concept algorithms toward systems designed to support real-world clinical decision-making. However, clinical impact depends on more than performance metrics. Models must be deployable within real workflows (radiology interpretation, biopsy decision-making, pathology review), interoperable with hospital information systems, and supported by

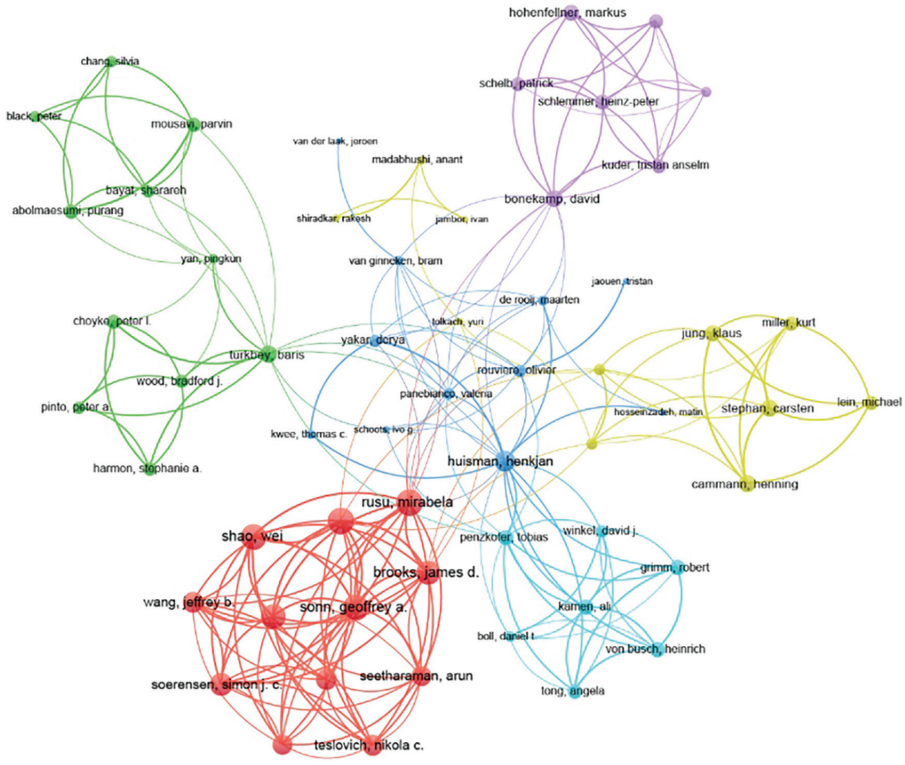


Figure 6. Visualization map depicting collaboration among authors.

user training and clear accountability structures.[28,30]

Although diagnostic accuracy and related metrics have improved over time,[29] further prospective and multicenter validation is needed to establish robustness across sites and populations. The increasing prominence of "system" in keyword trends reflects growing interest in integrated solutions but also highlights the complexity of implementation. Effective clinical integration requires attention to dataset shift, failure modes, and human–AI interaction, rather than focusing solely on retrospective performance.[28,29]

Regulatory, ethical, and clinical integration challenges

Despite rapid progress, regulatory and ethical considerations remain major barriers to clinical translation.[31] The adoption of ML in clinical workflows is constrained by requirements related to data privacy, patient safety, transparency, and governance. Ethical concerns, including algorithmic bias, explainability, reliability, and informed consent, must be proactively addressed to maintain trust and reduce disparities in performance across patient populations.[31]

The findings also suggest a gap between algorithm development and real-world implementation. The "black box" nature of deep learning and limited interpretability can hinder clinician acceptance and complicate error analysis and accountability.[28] As a result, explainable AI is receiving increasing attention. Interpretability methods can support clinical decision-making, facilitate auditing and bias assessment, and improve alignment with regulatory expectations for safety and transparency.

Technical performance and clinical validation

The literature indicates steady improvements in diagnostic accuracy, sensitivity, and specificity, particularly in imaging and pathology applications.[29] However, benchmarking and reporting remain inconsistent across studies, and large-scale prospective validation remains comparatively limited. This is a critical limitation given known challenges in data heterogeneity and domain shift.[28,29]

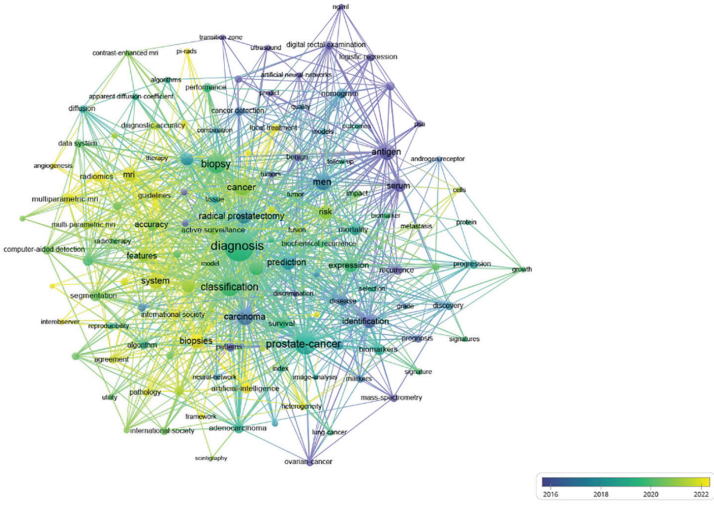
Multimodal ML that integrates imaging, pathology, genomics, and electronic health records offers potential for improved diagnostic precision but introduces additional challenges related to harmonization, missingness, and governance.[31] Approaches such as federated learning can support collaboration without centralizing sensitive patient data, and generative adversarial network–based augmentation may help address limited sample sizes. However, both approaches require careful validation to avoid amplifying bias or creating unrealistic signals.[32,33]

Future directions and recommendations

Based on the observed trends and ongoing barriers to clinical translation, future research should prioritize robust evaluation in clinically challenging settings, including higher-risk and heterogeneous patient subgroups, as limited generalizability across populations and institutions remains a key obstacle to real-world impact.[28,29]

The field should also progress from predominantly single-modality approaches toward multimodal integration where feasible, combining MRI with pathology and routinely collected clinical variables to improve diagnostic confidence and reduce failure modes associated with reliance on a single information source. Achieving this will require standardized data curation, harmonization, and quality-control pipelines.[31]

The increasing prominence of "system" alongside "MRI" in the keyword trends suggests that the next phase of impact will come from workflow-aware decision support tools designed for specific insertion points, such as MRI interpretation assistance and biopsy-related decision steps. These tools



a

View Citation Burst History

Top 20 Keywords with the Strongest Citation Bursts

Keywords	Year	Strength	Begin	End	1997 - 2024
antigen	1999	9.72	1999	2014	
artificial neural network	2000	16.53	2000	2017	
carcinoma	2000	4.82	2000	2008	
serum	2002	10.39	2002	2012	
digital rectal examination	2002	7.57	2002	2011	
mass spectrometry	2003	5.37	2003	2016	
identification	2004	6.38	2004	2021	
logistic regression	2004	5.57	2004	2014	
prostate-specific antigen	2004	3.43	2004	2013	
adenocarcinoma	2005	3.4	2005	2021	
classification	2001	6.11	2013	2019	
computer aided diagnosis	2015	5.69	2015	2018	
diffusion	2016	4.42	2016	2020	
computer aided detection	2016	3.83	2016	2019	
isup consensus conference	2018	3.64	2018	2021	
features	2019	5.71	2019	2020	
convolutional neural network	2017	5.36	2019	2021	
benign	2019	3.73	2019	2020	
data system	2019	3.42	2019	2021	
transfer learning	2022	3.59	2022	2024	

b

Figure 7. Analysis of keywords. **(a)** Visual analysis of the keyword co-occurrence network. **(b)** Top 20 keywords with the strongest citation bursts.

should be evaluated for usability, reliability, and failure modes under realistic clinical conditions rather than only in retrospective experiments.[24,28,29]

In addition, interpretability and governance should be treated as core design requirements. Explainable AI methods and auditing processes should be incorporated early to support transparency, bias assessment, safety monitoring, and trust, thereby aligning development with clinical and regulatory expectations.[31,32]

Finally, more consistent validation and reporting standards are needed, including clear dataset descriptions, external validation, clinically meaningful performance metrics, and transparent reporting of limitations and negative findings. These practices will improve reproducibility and reduce overestimation of model performance.[29,32] Collectively, these directions support a transition from rapid research growth toward more reliable, generalizable, and clinically integrated ML systems for PCa diagnosis.[28,29,,31,32]

This study provides a detailed, data-driven overview of global research trends, technological developments, and emerging hotspots in ML-based PCa diagnosis. By incorporating co-occurrence and burst keyword analyses, it offers a nuanced understanding of the field's evolution and future directions.

However, several limitations should be noted. The use of a simplified regression model may not fully reflect the exponential growth in publications from 2018 onward. Restricting the analysis to English-language articles indexed in WoSCC may introduce language and database biases, potentially excluding relevant studies from other sources. In addition, the rapid pace of AI innovation may result in literature lag, whereby the latest advancements are underrepresented in bibliometric analyses.

Although alternative databases, such as Scopus and PubMed/MEDLINE, were considered, the analysis was limited to the WoSCC to ensure consistency in citation indexing and network analysis. This restriction should be considered a coverage-related limitation.

This bibliometric analysis highlights the evolution of ML applications in PCa diagnosis, showing a transition from early biomarker research to advanced deep learning techniques, particularly in medical imaging. Research output has increased substantially, with major contributions from the United States, China, and Germany. Recent trends emphasize CNNs and transfer learning.

Although diagnostic capabilities have improved, challenges remain in clinical translation, including data heterogeneity, ethical and regulatory considerations, and the need for rigorous clinical validation. Advancing multimodal integration, explainable AI, and standardized evaluation frameworks will be essential to fully realize the potential of ML for early detection and effective management of PCa.

Footnotes

Conflict of interest disclosure

The author declared no conflicts of interest.

Supplementary Tables 1-3: https://d2v96fxpocvxx.cloudfront.net/bda9171a-fae8-4995-8276-2138323f1e16/content-images/1f64efde-a00e-44e8-9cc2-a14a32825a34.pdf

References

1. Rebello RJ, Oing C, Knudsen KE, et al. Prostate cancer. *Nat Rev Dis Primers*. 2021;7(1):8. [Crossref]
2. Sekhoacha M, Riet K, Motloung P, Gumenku L, Adegoke A, Mashele S. Prostate cancer review: genetics, diagnosis, treatment options, and alternative approaches. *Molecules*. 2022;27(17):5730. [Crossref]
3. Schaeffer EM, Srinivas S, Adra N, et al. Prostate cancer, version 4.2023, NCCN Clinical Practice Guidelines in oncology. *J Natl Compr Canc Netw*. 2023;21(10):1067-1096. [Crossref]
4. Suarez-Ibarrola R, Hein S, Reis G, Gratzke C, Miernik A. Current and future applications of machine and deep learning in urology: a review of the literature on urolithiasis, renal cell carcinoma, and bladder and prostate cancer. *World J Urol*. 2020;38(10):2329-2347. [Crossref]
5. Tong Y, Tan Z, Wang P, Gao X. A machine learning method for predicting biomarkers associated with prostate cancer. *Front Biosci (Landmark Ed)*. 2023;28(12):333. [Crossref]
6. Castaldo R, Cavaliere C, Soricelli A, Salvatore M, Pecchia L, Franzese M. Radiomic and genomic machine learning method performance for prostate cancer diagnosis: systematic literature review. *J Med Internet Res*. 2021;23(4):e22394. [Crossref]
7. Choudhri AF, Siddiqui A, Khan NR, Cohen HL. Understanding bibliometric parameters and analysis. *Radiographics*. 2015;35(3):736-746. [Crossref]
8. Wang Y, Zhang J, Zhang Y, Yao J. Bibliometric analysis of global research profile on ketogenic diet therapies in neurological diseases: beneficial diet therapies deserve more attention. *Front Endocrinol (Lausanne)*. 2023;13:1066785. [Crossref]
9. Wei Y, Mei Z, Xie C, Yuan F, Xu D. Mapping the application landscape of artificial intelligence in prostate cancer: a global bibliometric analysis. *Int J Surg*. 2026;112(2):2988-3002. [Crossref]
10. Musa IH, Afolabi LO, Zamit I, et al. Artificial intelligence and machine learning in cancer research: a systematic and thematic analysis of the top 100 cited articles indexed in Scopus database. *Cancer Control*. 2022;29:10732748221095946. [Crossref]
11. Zeng N, Sun JX, Liu CQ, et al. Knowledge mapping of application of image-guided surgery in prostate cancer: a bibliometric analysis (2013-2023). *Int J Surg*. 2024;110(5):2992-3007. [Crossref]
12. van Eck NJ, Waltman L. Software survey: VOSviewer, a computer program for bibliometric mapping. *Scientometrics*. 2010;84(2):523-538. [Crossref]
13. Zhang C, Zhang M, Cao X, et al. Navigating the landscape of MANF research: a scientometric journey with CiteSpace analysis. *Cell Mol Neurobiol*. 2023;43(8):3897-3913. [Crossref]
14. Arruda H, Silva ER, Lessa M, Proença D Jr, Bartholo R. VOSviewer and Bibliometrix. *J Med Libr Assoc*. 2022;110(3):392-395. [Crossref]
15. Garg K, Ranjan M, Krishna V, Singh M, Rezai A. A scientometric analysis of the 100 most cited articles on magnetic resonance guided focused ultrasound. *Front Hum Neurosci*. 2022;16:981571. [Crossref]
16. Campanella G, Hanna MG, Geneslaw L, et al. Clinical-grade computational pathology using weakly supervised deep learning on whole slide images. *Nat Med*. 2019;25(8):1301-1309. [Crossref]
17. Adam BL, Qu Y, Davis JW, et al. Serum protein fingerprinting coupled with a pattern-matching algorithm distinguishes prostate cancer from benign prostate hyperplasia and healthy men. *Cancer Res*. 2002;62(13):3609-3614. [Crossref]
18. Bera K, Schalper KA, Rimm DL, Velcheti V, Madabhushi A. Artificial intelligence in digital pathology - new tools for diagnosis and precision oncology. *Nat Rev Clin Oncol*. 2019;16(11):703-715. [Crossref]
19. Qiu J, Zhao R, Yang S, Dong K. Informetrics: theory, methods and applications. Singapore: Springer; 2017. [Crossref]
20. Wei C, Tian L, Jia B, et al. Association between serum triglycerides and prostate specific antigen (PSA) among U.S. males: National Health and Nutrition Examination Survey (NHANES), 2003-2010. *Nutrients*. 2022;14(7):1325. [Crossref]
21. Jović S, Miljković M, Ivanović M, Šaranović M, Arsić M. Prostate cancer probability prediction by machine learning technique. *Cancer Invest*. 2017;35(10):647-651. [Crossref]
22. Omer A, Lamb AD. Optimizing prostate biopsy techniques. *Curr Opin Urol*. 2019;29(6):578-586. [Crossref]
23. Rammal A, Assaf R, Goupil A, Kacim M, Vrabie V. Machine learning techniques on homological persistence features for prostate cancer diagnosis. *BMC Bioinformatics*. 2022;23(1):476. [Crossref]
24. van Leenders GJLH, van der Kwast TH, Grignon DJ, et al. The 2019 International Society of Urological Pathology (ISUP) Consensus Conference on grading of prostatic carcinoma. *Am J Surg Pathol*. 2020;44(8):e87-e99. [Crossref]
25. Hamm CA, Baumgärtner GL, Biessmann F, et al. Interactive explainable deep learning model informs prostate cancer diagnosis at MRI. *Radiology*. 2023;307(4):e222276. [Crossref]
26. Islam R, Imran A, Rabbi MF. Prostate cancer detection from MRI using efficient feature extraction with transfer learning. *Prostate Cancer*. 2024;2024:1588891. [Crossref]
27. Poddar M, Marwaha JS, Yuan W, Romero-Brufau S, Brat GA. An operational guide to translational clinical machine learning in academic medical centers. *NPJ Digit Med*. 2024;7(1):129. [Crossref]
28. Khalifa M, Albadawy M. AI in diagnostic imaging: revolutionising accuracy and efficiency. *Comput Methods Programs Biomed Update*. 2024;5:100146. [Crossref]
29. Ye Y, Liu Z, Zhu J, et al. Development trends and knowledge framework in the application of magnetic resonance imaging in prostate cancer: a bibliometric analysis from 1984 to 2022. *Quant Imaging Med Surg*. 2023;13(10):6761-6777. [Crossref]
30. Tan X, Su AT, Hajiabadi H, Tran M, Nguyen Q. Applying machine learning for integration of multi-modal genomics data and imaging data to quantify heterogeneity in tumour tissues. *Methods Mol Biol*. 2021;2190:209-228. [Crossref]
31. Gangwal A, Ansari A, Ahmad I, Azad AK, Wan Sulaiman WMA. Current strategies to address data scarcity in artificial intelligence-based drug discovery: a comprehensive review. *Comput Biol Med*. 2024;179:108734. [Crossref]
32. Mennella C, Maniscalco U, De Pietro G, Esposito M. Ethical and regulatory challenges of AI technologies in healthcare: a narrative review. *Heliyon*. 2024;10(4):e26297. [Crossref]

Diagn Interv Radiol 2026; DOI: 10.4274/dir.2026.264093

ABDOMINAL IMAGING

LETTER TO THE EDITOR

©Copyright 2026 Author(s) - Available online at dirjournal.org.
Content of this journal is licensed under a Creative Commons Attribution-NonCommercial 4.0 International License.

Reply: Regarding "multiparametric magnetic resonance imaging, diffusion-weighted magnetic resonance imaging, and magnetic resonance elastography: differentiating benign and malignant liver lesions"

İlkay S. İdilman

Hacettepe University Faculty of Medicine, Department of Radiology, Ankara, Türkiye

Dear Editor,

We would like to thank the author of the letter for their insightful comments and interest in our study, which evaluated the diagnostic performance of multiparametric magnetic resonance imaging (mpMRI), diffusion-weighted imaging, and magnetic resonance elastography (MRE) in characterizing focal liver lesions.[1] We appreciate the opportunity to clarify our methodology and discuss the future of multimodal liver imaging. Regarding the definition of "multiparametric," the author rightly points out that although we used several quantitative parameters, we analyzed them primarily as individual variables. In our study, the term "multiparametric" refers to the acquisition and evaluation of multiple independent quantitative biomarkers—T1/T2 mapping, apparent diffusion coefficient (ADC), and stiffness—within a single MRI session. Our primary goal was to establish the baseline diagnostic accuracy and optimal cut-off values for these emerging techniques. We agree that utilizing a logistic regression model to assess the additive value of these findings is a crucial step for future research. However, due to the retrospective nature of our study and the limited number of lesions, we focused on the individual efficacy of these quantitative measures rather than complex modeling.

Novel ultrasound (US) imaging techniques, which may aid in the characterization of focal liver lesions, have been introduced in the literature, as the author discussed.[2] Although MRI remains a reference standard for lesion characterization, we acknowledge that some advanced techniques, such as mpMRI and MRE, are not yet available in every center. Similarly, many novel US techniques, as well as contrast-enhanced US techniques, are currently restricted to specialized institutions. Consequently, optimizing the use of existing, locally available imaging modalities is a pragmatic and necessary approach. Furthermore, the suggestion to integrate MRI with US-based techniques is highly valuable; combining microvascular data from US with the tissue stiffness and diffusivity data from MRI would be an innovative approach.

We agree with the author that future research should focus on artificial intelligence-supported radiomic analyses and multimodal algorithms.[3] As we noted in our conclusion, prospective studies with larger, more homogeneous cohorts are necessary to demonstrate the impact of combining these modalities on clinical diagnostic accuracy. In summary, our findings indicate that ADC and lesion stiffness are currently the strongest individual performers among the studied parameters. We believe that moving from "analyzing parameters" to "integrated multimodal algorithms" will be the key to minimizing biopsies for focal liver lesions in the near future.

Corresponding author: İlkay S. İdilman

E-mail: ipolater@yahoo.com

Received 28 April 2026; accepted 29 April 2026.

Epub: 06.05.2026

Publication date: 02.11.2026

DOI: 10.4274/dir.2026.264093

You may cite this article as: İdilman İS. Reply: regarding "multiparametric magnetic resonance imaging, diffusion-weighted magnetic resonance imaging, and magnetic resonance elastography: differentiating benign and malignant liver lesions". *Diagn Interv Radiol*. 2026;32(6):755-756.

Footnotes

Conflict of interest disclosure

İkay S. İdilman, MD, serves as Section Editor of Diagnostic and Interventional Radiology. He had no involvement in the peer review of this article and had no access to information regarding its peer review..

References

1. Jabiyev A, Karçaaltıncaba M, Karaosmanoğlu AD, Akata D, Özmen MN, İdilman İS. Multiparametric magnetic resonance imaging, diffusion-weighted magnetic resonance imaging, and magnetic resonance elastography: differentiating benign and malignant liver lesions. *Diagn Interv Radiol*. 2026;32(2):133-138. [Crossref]
2. Couture O, Hingot V, Heiles B, Muleki-Seya P, Tanter M. Ultrasound localization microscopy and super-resolution: a state of the art. *IEEE Trans Ultrason Ferroelectr Freq Control*. 2018;65(8):1304-1320. [Crossref]
3. Park HJ, Park B, Lee SS. Radiomics and deep learning: hepatic applications. *Korean J Radiol*. 2020;21(4):387-401. [Crossref]

Diagn Interv Radiol 2026; DOI: 10.4274/dir.2026.263954

ARTIFICIAL INTELLIGENCE AND INFORMATICS

ORIGINAL ARTICLE

©Copyright 2026 Author(s) - Available online at dirjournal.org.
Content of this journal is licensed under a Creative Commons Attribution-NonCommercial 4.0 International License.

Predicting drainage success of peritonsillar abscesses: a radiomics-based machine learning approach using contrast-enhanced computed tomography

İzzet Selçuk Parlak[1]
Bökebatur Ahmet Raşit Mendi[2]
Alperen Özkan[1]

[1]Bilkent City Hospital, Clinic of Radiology, Ankara, Türkiye

[2]Yıldırım Beyazıt University Medical School, Department of Radiology, Ankara, Türkiye

PURPOSE

To develop and validate radiomics-based machine learning models combined with clinical parameters derived from venous phase contrast-enhanced computed tomography (CECT) for predicting drainage success in patients with peritonsillar abscess (PTA), aiming to reduce unnecessary invasive procedures.

METHODS

This retrospective study included 94 adult patients with PTA who underwent venous phase CECT followed by incision and drainage within 24 hours. Patients were categorized into drainage (n = 52) and non-drainage (n = 42) groups based on procedural outcomes. Clinical parameters (age, sex, trismus, and uvula deviation) were integrated with 107 extracted radiomics features. Three-dimensional manual segmentation was performed using 3D Slicer. Feature selection was conducted using the least absolute shrinkage and selection operator (LASSO) regression with 10-fold cross-validation. Four machine learning algorithms—support vector machine (SVM), random forest classifier (RFC), decision tree, and extreme gradient boosting (XGBoost)—were developed, and a combined clinical–radiomics model was constructed. Model performance was evaluated using sensitivity, specificity, and area under the receiver operating characteristic curve (AUC).

RESULTS

The LASSO selected 10 discriminative features (optimal λ: 0.043). Inter- and intraobserver reproducibility demonstrated good agreement (intraclass correlation coefficient ≥ 0.75; Spearman's $\rho > 0.8$). Among the radiomics-only models, XGBoost achieved the highest diagnostic performance (AUC: 0.919). The combined clinical–radiomics model further improved diagnostic performance, reaching an AUC of 0.934, with a sensitivity of 90.2% and a specificity of 94.1%. The SVM yielded an AUC of 0.899, whereas the decision tree and RFC demonstrated AUCs of 0.887 and 0.850, respectively. Notably, the high specificity of the combined model suggests strong potential for identifying non-drainable collections.

CONCLUSION

Integrating clinical parameters with radiomics-based machine learning, particularly the combined clinical–radiomics model, can accurately predict drainage success in PTA using pre-procedural CECT images. This quantitative approach may improve patient selection for invasive interventions.

CLINICAL SIGNIFICANCE

Pre-procedural identification of non-drainable collections may help avoid unnecessary drainage attempts, reduce procedure-related morbidity, and support more informed clinical decision-making in the management of PTA.

KEYWORDS

Peritonsillar abscess, radiomics, machine learning, contrast-enhanced computed tomography, drainage

Handling editor: Barbaros Çil

Corresponding author: İzzet Selçuk Parlak

E-mail: selcukparlakdr@gmail.com

Received 25 February 2026; revision requested 30 March 2026; accepted 04 May 2026.

Epub: 11.05.2026

Publication date: 02.11.2026

DOI: 10.4274/dir.2026.263954

You may cite this article as: Parlak İS, Mendi BAR, Özkan A. Predicting drainage success of peritonsillar abscesses: a radiomics-based machine learning approach using contrast-enhanced computed tomography. *Diagn Interv Radiol*. 2026;32(6):757-764.

Peritonsillar abscess (PTA) is defined as a collection of pus within the peritonsillar space, representing the most common deep neck infection in the adult population. Its clinical presentation includes severe unilateral sore throat, fever, dysphagia, and odynophagia, often accompanied by trismus.[1] The established management for PTA is the evacuation of purulent material through an invasive procedure—either needle aspiration or incision and drainage (I&D)—supported by systemic antibiotic therapy.[2,3]

Although clinical assessment is the first step, contrast-enhanced computed tomography (CECT) is frequently employed to confirm the diagnosis, especially in ambiguous cases, and to differentiate a suspected abscess from non-suppurative peritonsillar cellulitis (phlegmon).[4] The typical radiological finding suggestive of an abscess is a peripherally rim-enhancing fluid collection. This finding is crucial because it directly informs the decision to proceed with an invasive drainage attempt.[5]

However, a critical clinical challenge arises from the fact that a decision to intervene based on current diagnostic standards does not guarantee a successful outcome. A non-negligible proportion of drainage procedures, performed on lesions that appear as well-defined abscesses on CECT, result in a "dry tap" or failure to evacuate purulent material despite surgical incision.[6,7] This outcome means that the patient underwent an invasive procedure without the intended therapeutic benefit; furthermore, these attempts are not without their own potential for morbidity. These procedural risks include considerable pain, iatrogenic bleeding from local vasculature, and potential injury to critical nearby structures.[1,8]

Main points

- Conventional contrast-enhanced computed tomography findings alone may not reliably predict whether a peritonsillar abscess (PTA) is amenable to successful drainage.
- Computed tomography-based radiomics can quantitatively analyze internal lesion heterogeneity and provide additional information beyond visual assessment.
- Among the tested models, the radiomics-based extreme gradient boosting model demonstrated high diagnostic performance [area under the receiver operating characteristic curve (AUC): 0.919], which was further improved by integrating clinical parameters in the combined model (AUC: 0.934).
- Pre-procedural prediction of drainage success may help reduce unnecessary invasive interventions and improve clinical decision-making in patients with PTA.

The mechanisms underlying failed drainage remain incompletely understood. It is conceivable that some collections, although radiologically consistent with an abscess, may represent partially organized or inspissated material with increased viscosity rather than freely drainable fluid.[9] However, conventional imaging assessment primarily focuses on the presence of a rim-enhancing collection and does not directly evaluate internal fluid characteristics, such as viscosity or organization, which may influence drainability.[10] This limitation highlights an unmet clinical need for quantitative, non-invasive imaging biomarkers capable of predicting drainability before intervention.

To address this challenge and minimize unnecessary invasive interventions, we propose a novel approach using radiomics and machine learning. Radiomics enables quantitative characterization of lesion heterogeneity, texture, and spatial complexity, which may reflect underlying differences in fluid composition, viscosity, and organization.[11,12] We hypothesize that radiomics-derived features may enable quantitative differentiation between liquefied, drainable collections and organized, non-drainable collections.

This study utilizes I&D as the reference standard for drainage success, as it provides a more definitive evaluation of the abscess cavity than needle aspiration, thereby minimizing potential technical failures. Therefore, the primary aim of this study is to develop and validate machine learning models—specifically random forest classifier (RFC), support vector machine (SVM), extreme gradient boosting (XGBoost), and decision tree—based on radiomics features extracted from venous phase CECT scans integrated with key clinical parameters (age, sex, trismus, and uvula deviation) to predict drainage success in patients with suspected PTA. By identifying non-drainable collections pre-procedurally, this approach may help avoid unnecessary invasive interventions, reduce morbidity, and optimize clinical decision-making.

Methods

The study was conducted at Ankara Bilkent City Hospital, a tertiary care center. Ethical approval was granted by the Bilkent City Hospital Medical Research Scientific and Ethical Review Board (TABED) (decision number: 2/1912/2026, date: 04.02.2026). Given the retrospective nature of the study, the use of anonymized data, and the lack of potential risk to participants, the requirement for informed consent was waived by the Ethical Review Board. All procedures were conducted in accordance with the principles outlined in the Declaration of Helsinki.

Study population

The institutional database was screened for patients who underwent CECT with a preliminary diagnosis of PTA. The exclusion criteria comprised age younger than 18 years, evaluation with imaging modalities other than CECT, prior drainage attempts or surgical interventions before imaging, prolonged antibiotic therapy (> 72 hours) before CT acquisition, presence of coexisting head and neck malignancy, and significant motion or beam-hardening artifacts impairing image quality.

The inclusion criteria consisted of adult patients diagnosed with PTA who underwent neck CECT acquired in the venous phase and subsequently received I&D with a clearly documented clinical outcome. Only patients whose CT examinations were performed within 24 hours before the intervention were included to ensure temporal consistency between imaging and treatment.

A retrospective analysis was performed on 94 eligible patients between January 2022 and December 2025. Of these, 42 patients were classified as the non-drainage group and 52 as the drainage group. Given the balanced distribution of the two groups (52 drainage vs. 42 non-drainage), specific oversampling or undersampling techniques were not required.

In the non-drainage group, there were 23 men and 19 women aged 21–74 years (mean age: 45.8 years). The drainage group consisted of 28 men and 24 women aged 19–76 years (mean age: 47.2 years).

Patient demographics (age and sex) and physical examination findings at admission (trismus and uvula deviation) were retrospectively retrieved from the institutional database. Due to the retrospective nature of the study, clinical findings were analyzed based on available documentation; data for trismus and uvula deviation were available for 79/94 (84%) and 82/94 (87%) patients, respectively.

The imaging data of the included patients were independently reviewed by two radiologists (İSP, with 26 years of experience, and BARM, with 8 years of experience).

The flowchart of the study is depicted in Figure 1.

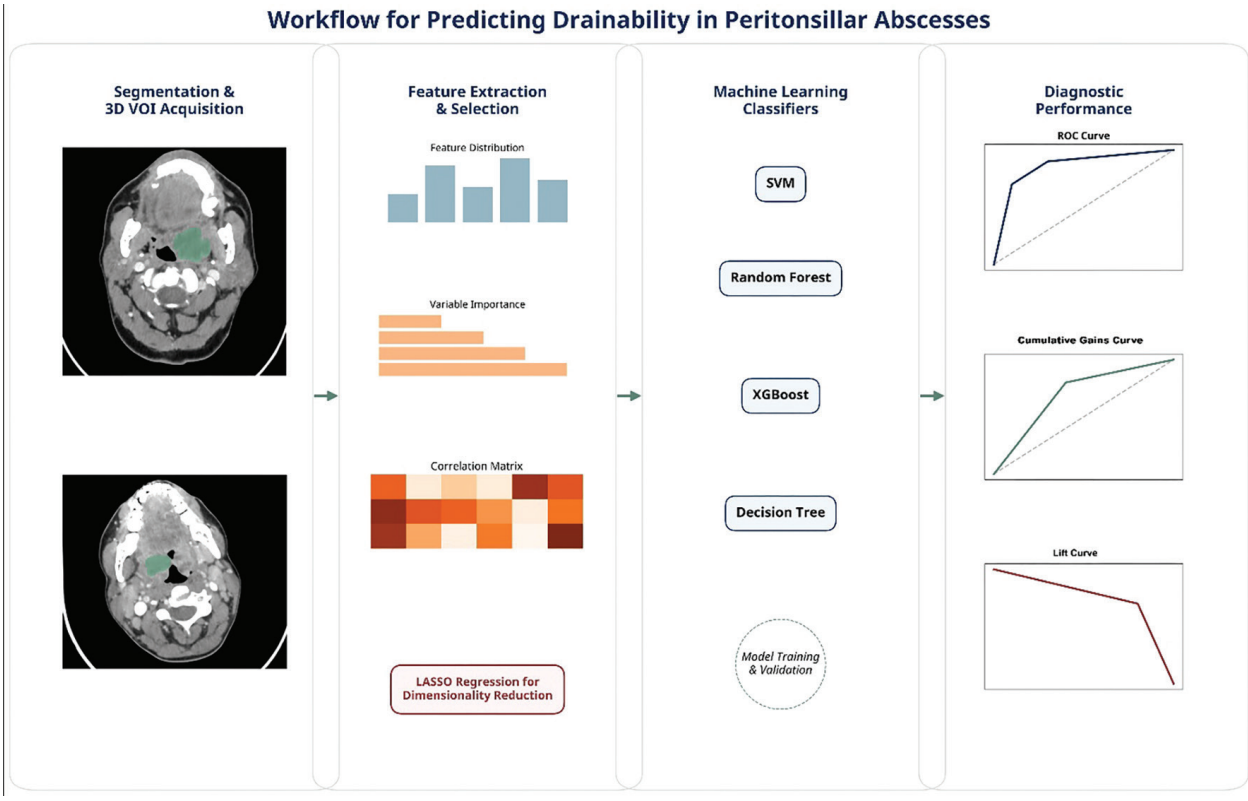


Figure 1. Flowchart of the study. 3D, three-dimensional; VOI, volume of interest; LASSO, least absolute shrinkage and selection operator; SVM, support vector machine; XGBoost, extreme gradient boosting; ROC, receiver operating characteristic.

Computed tomography acquisition and preprocessing

The examinations were performed using a 128-detector CT scanner (GE Revolution, General Electric, Milwaukee, WI, USA). Acquisition parameters consisted of a tube voltage of 100–120 kVp, a tube current of 250–270 mAs, a 512 × 512 reconstruction matrix, a 1.25-mm slice thickness, a body filter, and a pitch of 1.375. Intravenous iodinated contrast material (300 mgI/mL; 80–100 mL per patient) was administered at a rate of 3 mL/s. Contrast-enhanced images were acquired during the venous phase, approximately 60–90 seconds after contrast injection.

The selected CT datasets were imported into 3D Slicer software (version 5.6.2)[13] for three-dimensional manual segmentation of the PTA. Segmentations were carefully reviewed by the same radiologists to identify and correct potential inaccuracies, including the inadvertent inclusion of adjacent fat, air, or bone structures, as well as the unintended partial exclusion of the abscesses. Example images illustrating PTA segmentation are presented in Figure 2.

To assess intra- and interobserver reproducibility, 20 randomly chosen cases were re-segmented following the same standardized protocol.

Texture analysis

Radiomics features were extracted using the SlicerRadiomics extension based on the PyRadiomics library after completion of segmentations.[14] Feature extraction was performed on original, non-filtered images. All images were resampled to an isotropic voxel size of 1 × 1 × 1 mm^3 using linear interpolation. Intensity discretization was applied using a fixed bin width of 64 Hounsfield units, which was selected to balance noise reduction and the preservation of meaningful intensity heterogeneity, thereby improving the stability and reproducibility of radiomics features. No additional image filters (e.g., wavelet or Laplacian of Gaussian) were applied.

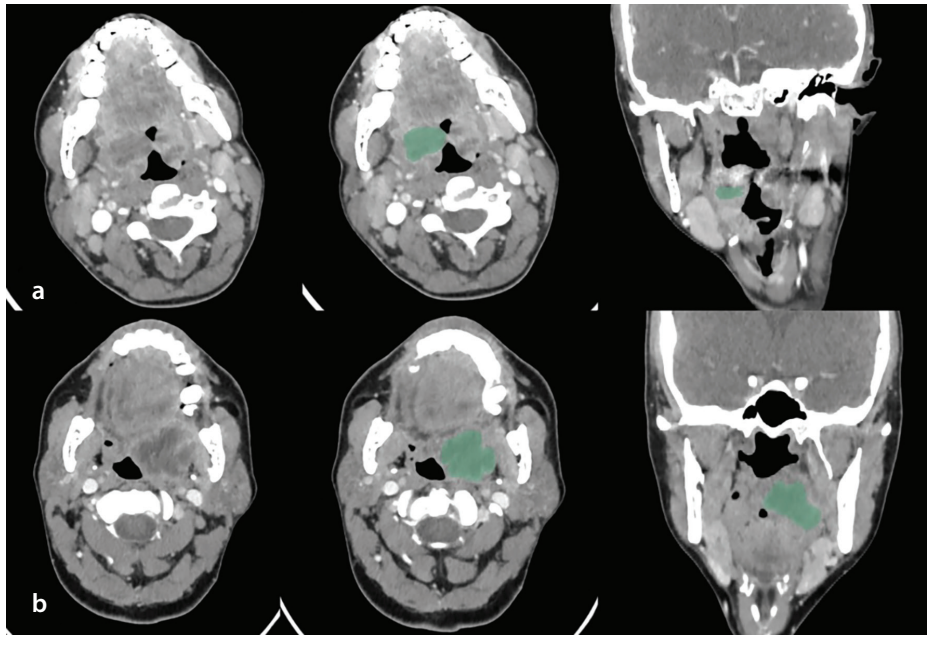


Figure 2. (**a, b**) Examples illustrating peritonsillar abscess segmentation.

Following the preset configuration, a total of 107 radiomics features were extracted. These features were categorized as shape-based features, first-order statistics, gray level co-occurrence matrix (GLCM), gray level run length matrix, neighboring gray tone difference matrix, gray level size zone matrix (GLSZM), and gray level dependence matrix.

Statistical analysis

The normality of data distribution was evaluated using the Kolmogorov–Smirnov test. Variables with a normal distribution were expressed as mean ± standard deviation, whereas non-normally distributed variables were reported as median and interquartile range.

Intraobserver agreement was assessed using the intraclass correlation coefficient (ICC), with values ≥ 0.75 considered indicative of good reproducibility.[15] Interobserver agreement of the selected features was assessed using Spearman's rank correlation coefficient (ρ), with values greater than 0.8 considered indicative of good reproducibility for each parameter.

Before feature selection and model training, feature standardization (Z-score normalization) was applied. Normalization parameters (mean and standard deviation) were calculated using the training set and subsequently applied to the validation set to prevent data leakage.

The least absolute shrinkage and selection operator (LASSO) regression was applied for dimensionality reduction and feature selection. The optimal regularization parameter (λ) was determined using 10-fold cross-validation on the training set. The relationship between the mean squared error (MSE) and λ values was examined to identify the most appropriate model. Feature importance was quantified based on the magnitude of the regression coefficients.

Missing clinical data were managed using complete-case analysis for the respective sub-cohorts.

The predictive performance of the combined clinical–radiomics model was compared against the radiomics-only and clinical-only models using the area under the receiver operating characteristic curve (AUC), sensitivity, and specificity to determine if the integration of clinical variables provided a significant improvement in predicting drainage success. DeLong's test was applied to compare the AUCs between different models.

Decision curve analysis was performed according to the method described by Vickers and Elkin[16] using Python (version 3.11), with custom-written code implementing standard net benefit calculations. The decision curve was visualized using the Matplotlib library to assess the clinical utility of the models across a range of threshold probabilities.

All statistical analyses were performed using XLSTAT statistical and data analysis software (version 2024.2.2; Addinsoft, NY, USA). A two-tailed *P* value of < 0.05 was considered statistically significant.

Machine learning

SVM,[17] RFC,[18] decision tree,[19] and XGBoost[20] algorithms were implemented for model development. The dataset was randomly partitioned into training and validation cohorts using a 70:30 split. Model performance was evaluated by calculating sensitivity, specificity, and the AUC.

The SVM model was configured using a linear kernel with a regularization parameter (C) set to 1.0 and a tolerance value of 0.001. Given the substantial variability in radiomics feature values, feature standardization was applied as a preprocessing step before model training. To reduce the potential influence of variability and selection bias on performance estimates, 10-fold bootstrapping was performed in accordance with the approach described by Vrigazova and Ivanov.[21]

The RFC model was constructed using a bagging approach with bootstrap sampling (random sampling with replacement). A total of 200 decision trees were generated, with the maximum tree depth limited to 20. Model evaluation additionally included calculation of the misclassification rate, analysis of the out-of-bag (OOB) error progression, and assessment of feature importance based on the mean decrease in accuracy.

Decision tree analysis was performed using a classification tree based on the chi-square Automatic Interaction Detection algorithm. The significance level was set at 0.05, with a maximum tree depth of 3 and a merge threshold of 0.05. Model validation was conducted using a two-fold cross-validation. In addition, model performance was evaluated using gain and lift curves.

The XGBoost model was configured with a maximum of 100 boosting iterations, a learning rate of 0.3, and a maximum tree depth of 6. The objective function was specified as quadratic, with the minimum loss reduction (gamma) set to 0. In addition to the primary performance metrics, gain and lift curves were generated for further evaluation of model performance.

To evaluate the added value of clinical integration, three distinct modeling approaches were developed: (1) a clinical-only model, (2) radiomics-only models using four machine learning algorithms (SVM, RFC, decision tree, and XGBoost), and (3) a combined clinical–radiomics model. The clinical parameters were integrated with the selected radiomics features using logistic regression to develop a combined clinical–radiomics nomogram.

Results

Study population

A total of 94 patients with PTA were included in this retrospective study, comprising 42 patients in the non-drainage group and 52 in the drainage group. The mean age was 45.8 ± 12.4 years (range: 21–74 years) in the non-drainage group and 47.2 ± 13.1 years (range: 19–76 years) in the drainage group, with no significant difference between the groups (independent-samples t-test, $P = 0.621$).

The non-drainage group included 23 men (54.8%) and 19 women (45.2%), whereas the drainage group consisted of 28 men (53.8%) and 24 women (46.2%). Sex distribution did not differ significantly between the groups (χ^2 test, $P = 0.929$).

Regarding physical examination findings, trismus was documented in 79 patients, with a prevalence of 73.1% (32/44) in the drainage group compared with 61.9% (22/35) in the non-drainage group ($P = 0.349$). Uvula deviation was observed in 82 patients, with a prevalence of 80.8% (36/45) in the drainage group and 71.4% (26/37) in the non-drainage group ($P = 0.307$).

Inter- and intraobserver reproducibility

Twenty cases were randomly selected during the segmentation process. Interobserver reproducibility was assessed using the first-order radiomics features "mean" and "range." Both features showed strong agreement between the two observers, as reflected by Spearman's rank correlation coefficients (mean: $\rho = 0.837$, $P = 0.016$; range: $\rho = 0.822$, $P = 0.023$).

The same randomly selected cases were used to evaluate intraobserver reproducibility. Each observer repeated the

segmentation procedure twice, and the first-order "mean" and "range" features were analyzed. Intraobserver agreement was good for both observers: the mean ICC was 0.852 (range: 0.773–0.946) for Observer 1 (İSP) and 0.844 (range: 0.762–0.927) for Observer 2 (BARM).

Dimensionality reduction of the parameters

The LASSO regression selected 10 features that exhibited low intercorrelation and strong discriminatory power. The optimal λ value was determined to be 0.043. The correlation matrix is provided in Supplementary Figure 1, whereas the most relevant features and their standardized coefficients are summarized in Table 1. Supplementary Figure 2 shows the association between the λ parameter and the MSE.

Diagnostic efficacy of machine learning algorithms

The diagnostic performance of the SVM model was as follows: sensitivity of 87.1% [95% confidence interval (CI): 84.1–90.3], specificity of 87.25% (95% CI: 83.9–90.25), and an AUC of 0.899 (95% CI: 0.869–0.928).

The diagnostic accuracy metrics of the RFC model consisted of a misclassification rate of 0.15, sensitivity of 88.3% (95% CI: 85.25–91.35), specificity of 82.2% (95% CI: 78.63–85.74), and an AUC of 0.85 (95% CI: 0.811–0.892). Figure 3 displays the progression of the OOB error over iterations.

For the XGBoost model, sensitivity was 88.65% (95% CI: 85.05–92.19), specificity was 92.55% (95% CI: 89.4–95.6), and the AUC reached 0.919 (95% CI: 0.887–0.951). Figure 4 illustrates the gain and lift curves associated with the model.

Table 1. The most significant radiomics parameters based on LASSO regression

Parameter	Standardized coefficient
Small dependence emphasis	0.207
Coarseness	0.180
Run percentage	0.166
Mean absolute deviation	–0.140
Short run high gray level emphasis	–0.120
90th percentile	–0.088
Interquartile range	–0.083
Least axis length	0.074
Cluster shade	–0.062
Run length non-uniformity	0.059

LASSO, least absolute shrinkage and selection operator.

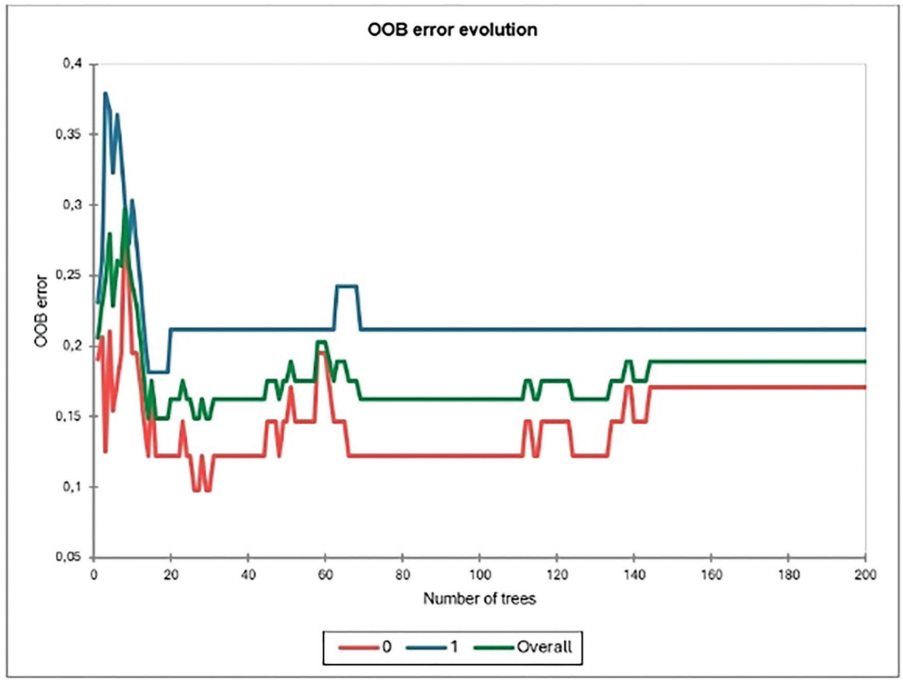


Figure 3. Evolution of the out-of-bag (OOB) error in the random forest classifier. The x-axis represents the number of constructed trees, and the y-axis indicates the error rate. The red curve corresponds to the error rate for the drainage group, the blue curve represents the error rate for the non-drainage group, and the green curve shows the overall OOB observations.

Decision tree analysis demonstrated a sensitivity of 90.24% (95% CI: 86.41–93.85), a specificity of 88.75% (95% CI: 85.05–92.55), and an AUC of 0.887 (95% CI: 0.861–0.914). Figure 5 presents the corresponding gain and lift curves.

Performance of the combined clinical–radiomics model

Although the clinical-only model demonstrated limited predictive performance, with an AUC of 0.642 (95% CI: 0.581–0.703), integrating clinical parameters into the radiomics-based XGBoost model resulted in a significant improvement. The combined clinical–radiomics model achieved the highest diagnostic performance, yielding an AUC of 0.934 (95% CI: 0.902–0.966), a sensitivity of 90.2%, and a specificity of 94.1%. This combined approach outperformed the radiomics-only XGBoost model (AUC: 0.919), highlighting the synergistic value of clinical variables in predicting drainage success. DeLong's test demonstrated that the combined clinical–radiomics model achieved a statistically significantly higher AUC than all other models (Table 2).

Decision curve analysis

Decision curve analysis showed that the combined model provided the highest net benefit across most threshold probabilities (Figure 6). The radiomics-only model also performed well but remained below the combined model. In contrast, the clinical-only model showed a lower net benefit and more limited clinical usefulness than the other models. Both the combined and radiomics-only models outperformed the "treat all" and "treat none" strategies over a wide range of threshold probabilities.

Discussion

This study explores the potential of radiomics-based machine learning models, derived from venous phase CECT, to predict the drainage success of PTA. Among the evaluated algorithms, the XGBoost model exhibited the highest diagnostic performance with an AUC of 0.919, followed by SVM (0.899) and the decision tree (0.887). These results suggest that quantitative radiomics analysis may capture subtle internal characteristics of peritonsillar collections that are not readily apparent to the human eye, potentially offering a non-invasive tool to inform clinical decision-making and reduce unnecessary invasive procedures.

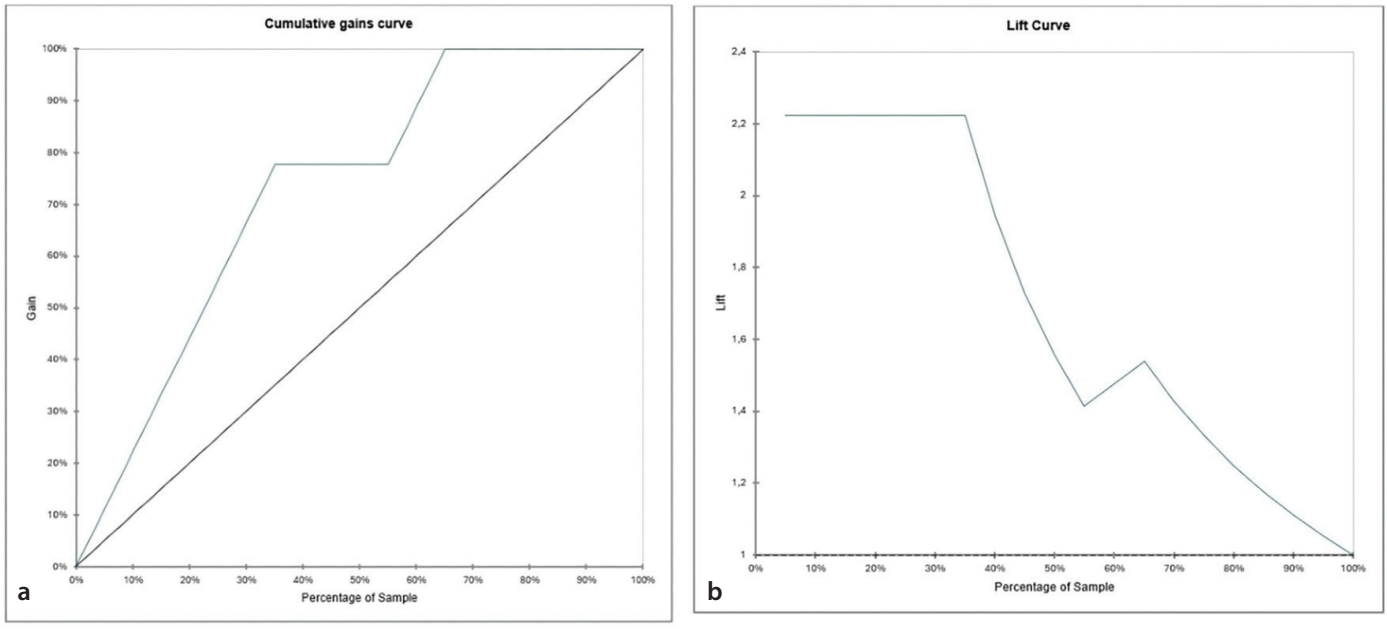


Figure 4. The diagnostic efficacy of XGBoost depicted with **(a)** gain and **(b)** lift curves. The gain curve illustrates the true positive rate in percent versus the percent of total observations. The lift curve reflects the ratio of the model's gain to the percentage of the dataset utilized. XGBoost, extreme gradient boosting.

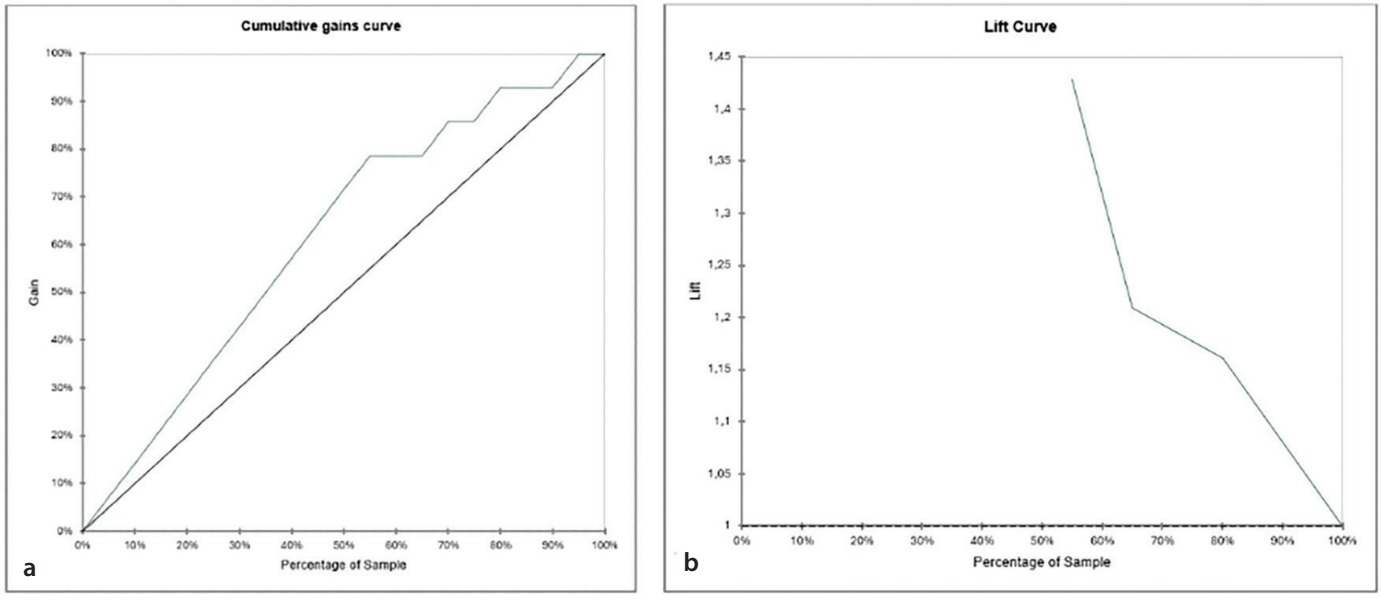


Figure 5. The diagnostic performance of the decision tree demonstrated with **(a)** gain and **(b)** lift curves. The gain curve depicts the true-positive rate in percent versus the percentage of total observations, and the lift curve represents the ratio of the model's gain to the percentage of the dataset used.

Table 2. Diagnostic performance comparison of the models and DeLong's test results

Model type	AUC (95% CI)	Sensitivity (recall) (%)	Specificity (%)	Precision (%)	F1 score	DeLong's *P* value*
Clinical only	0.642 (0.581–0.703)	62.4%	58.1%	64.8	0.636	<0.001
SVM	0.899 (0.869–0.928)	87.1%	87.2%	89.4	0.882	0.038
Decision tree	0.887 (0.861–0.914)	90.2%	88.7%	90.8	0.905	0.029
RFC	0.850 (0.811–0.892)	88.3%	82.2%	86.0	0.871	0.012
XGBoost	0.919 (0.887–0.951)	88.6%	92.5%	93.6	0.910	0.046
XGBoost + clinical	0.934 (0.902–0.966)	90.2%	94.1%	95.0	0.925	Reference

P values represent the statistical comparison of each model's AUC against the combined model (reference) using DeLong's test. A *P* value <0.05 indicates a statistically significant difference in diagnostic performance. AUC, area under the curve; CI, confidence interval; SVM, support vector machine; RFC, random forest classifier; XGBoost, extreme gradient boosting.

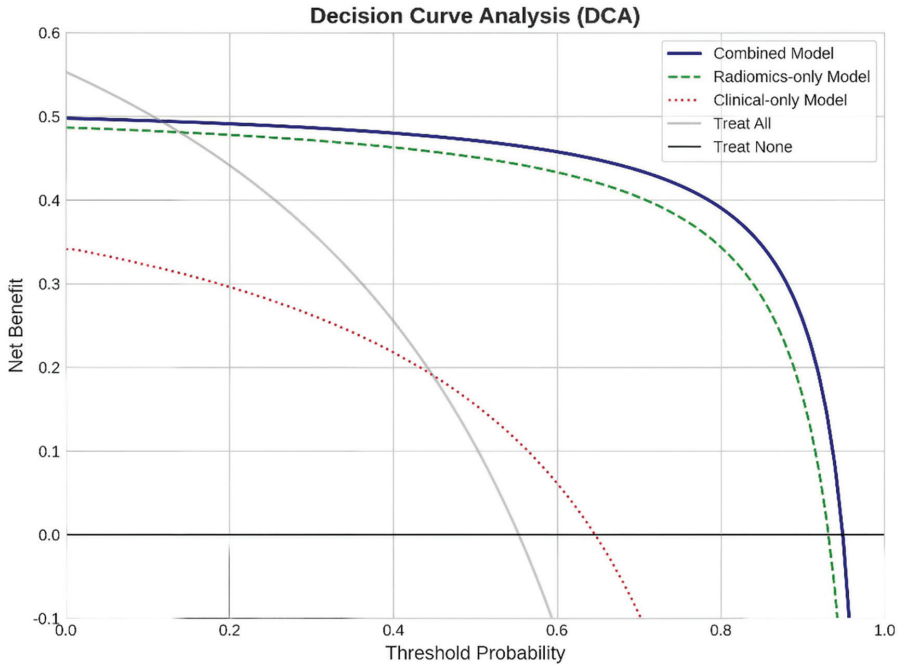


Figure 6. Decision curve analysis showing the net benefit of the clinical model, radiomics model, and combined clinical–radiomics model across a range of threshold probabilities, along with the "treat all" and "treat none" strategies. The combined model demonstrates superior clinical utility across most threshold probabilities.

In this study, CT-based radiomics features were analyzed in conjunction with clinical parameters—including age, sex, trismus, and uvula deviation—to evaluate their collective contribution to predicting drainage success in PTA. The combined clinical–radiomics model demonstrated an AUC of 0.934, compared with 0.919 for the radiomics-only model. This observation suggests that while radiomics captures internal lesion heterogeneity, clinical variables provide additional context that contributes to the model's overall predictive performance and clinical applicability. The inclusion of clinical signs such as trismus and uvula deviation is relevant, as these findings are traditional indicators of PTA severity. Although these clinical parameters alone showed limited predictive value in our cohort (AUC: 0.642), their integration with radiomics data suggests a multi-dimensional approach to evaluating peritonsillar collections.

We utilized I&D as the reference standard to potentially reduce the technical uncertainties associated with needle aspiration, such as needle malposition, the limitations of small-gauge needles in aspirating viscous material, or the presence of multiloculated septations. This approach was intended to provide a more consistent ground truth for our models by focusing on the intrinsic characteristics of the collection rather than procedural variables.

The management of PTA traditionally relies on the identification of a rim-enhancing collection on CECT to justify needle aspiration or I&D.[4,5] However, the diagnostic accuracy of CECT in identifying truly drainable collections remains a subject of debate. Previous studies have reported that while CECT is highly sensitive (approaching 100%), its specificity and positive predictive value (PPV) in identifying successful drainage outcomes can be as low as 75%.[4,10] Hagelberg et al.,[10] in a recent meta-analysis, highlighted the substantial variability in the PPV of CECT for neck abscesses, suggesting that the classic rim enhancement sign is not always synonymous with the presence of freely drainable pus.

This diagnostic uncertainty often leads to a "dry tap," where no purulent material is obtained despite radiological evidence of an abscess. This challenge is echoed in previous literature, where reported false-positive rates for identifying drainable collections range from approximately 20% to 25%, reflecting the inherent limitations of conventional diagnostic standards.[6,7] In our cohort, 44.7% (42/94) of the cases resulted in a non-drainable outcome—a rate higher than these reported averages. This discrepancy likely reflects the complex nature of cases managed at our tertiary center, where collections may represent more organized or viscous material that is resistant to successful drainage.[9]

Our findings align with and extend recent research into predictive markers for PTA drainage. Although previous studies have explored machine learning for PTA diagnosis or surgical intervention prediction using clinical and conventional imaging features,[9,22] to our knowledge, this is the first study to utilize CT radiomics-based machine learning to predict the success of PTA drainage. For instance, Wilson et al.[22] developed a machine learning model incorporating clinical symptoms and findings—such as trismus, neck pain, and otalgia—to predict PTA, demonstrating moderate predictive performance with an accuracy of up to 0.72. However, clinical signs are often subjective and may not always clearly differentiate collections requiring drainage from those that do not. In contrast, our approach leverages high-dimensional quantitative data directly from the lesion. Li et al.[9] recently identified that specific CT findings, such as soft palate effacement, continuous ring enhancement, and larger abscess size, are significantly associated with successful drainage. Although conventional imaging features are clinically valuable, they are inherently subject to interobserver variability and may not adequately capture the internal structural complexity of an abscess.

The role of imaging in predicting drainability has also been explored through other modalities, most notably ultrasound (US). Kim et al.[23] and Costantino et al.[24] have shown that intraoral US has high sensitivity but moderate specificity in identifying PTA, with the advantages of being radiation-free, cost-effective, and capable of real-time visualization of fluid dynamics to assess the presence of drainable pus. However, the application of US can be technically challenging in patients with severe trismus and is inherently operator-dependent. Although US remains a preferred initial tool for many clinicians due to its accessibility, CT is frequently performed in clinical practice to evaluate the extent of the infection into deeper neck spaces or when the diagnosis remains ambiguous. Our radiomics-based approach aims to enhance the utility of these already-acquired CT scans by providing a level of content characterization that traditional visual inspection might lack. Feature groups such as the GLCM and GLSZM, which contributed to our selected model features, quantify the spatial relationships and distribution patterns of voxel attenuation values. These parameters likely reflect the internal heterogeneity of the abscess cavity, enabling differentiation between freely drainable purulent collections and more organized, highly viscous, or septated components.[11,12]

The XGBoost model achieved the best performance among the evaluated algorithms, consistent with its success in other radiomics applications. Its ability to handle non-linear relationships and its robust regularization parameters make it particularly well-suited for high-dimensional radiomics datasets.[20] The high specificity achieved by our models (up to 92.5% for XGBoost) is relevant from a clinical perspective. In the context of PTA, high specificity results in a low rate of false positives for drainage, effectively identifying patients who are unlikely to benefit from an invasive procedure. By opting for conservative medical management in these cases, clinicians can avoid the risks of iatrogenic bleeding, pain, and injury to the internal carotid artery.[8]

Despite the promising results, this study has several limitations. First, its retrospective, single-center design and relatively small sample size may limit the generalizability of the findings. Although we employed bootstrapping and cross-validation to ensure model robustness, external validation in larger, multi-center prospective cohorts is essential to confirm broader applicability. Second, the manual segmentation process, though reviewed by experienced radiologists, is time-intensive and inherently prone to interobserver variability. The integration of automated or semi-automated segmentation tools in future iterations could improve efficiency, minimize observer dependency, and facilitate clinical adoption. Third, the retrospective nature of the study led to incomplete clinical data. Although trismus and uvula deviation were included in the analysis, they were documented for only 84% and 87% of the cohort, respectively. Furthermore, other relevant parameters—such as symptom duration and specific laboratory markers—could not be analyzed due to missing records. Future prospective studies utilizing standardized clinical reporting protocols may further refine and improve model performance.

In conclusion, radiomics-based machine learning models offer a highly accurate, quantitative approach to predicting drainage success in PTA. By identifying non-drainable collections before intervention, this method has the potential to optimize treatment strategies, reduce patient morbidity, and enhance the efficiency of emergency care delivery. Future research should prioritize prospective validation and the development of intuitive software interfaces to support real-time clinical decision-making.

Footnotes

Conflict of interest disclosure

The authors declared no conflicts of interest.

Supplementary Figures 1-2: https://d2v96fxpocvxx.cloudfront.net/beb8919b-f013-4ea1-b1c8-40332e840fe1/content-images/85c3ced9-ef05-4c99-93d2-9ae-fa69b526c.pdf

References

1. Galioto NJ. Peritonsillar abscess. *Am Fam Physician*. 2017;95(8):501-506. [Crossref]
2. Johnson RF, Stewart MG. The contemporary approach to diagnosis and management of peritonsillar abscess. *Curr Opin Otolaryngol Head Neck Surg*. 2005;13(3):157-160. [Crossref]
3. Herzon FS, Martin AD. Medical and surgical treatment of peritonsillar, retropharyngeal, and parapharyngeal abscesses. *Curr Infect Dis Rep*. 2006;8(3):196-202. [Crossref]
4. Scott PM, Loftus WK, Kew J, Ahuja A, Yue V, van Hasselt CA. Diagnosis of peritonsillar infections: a prospective study of ultrasound, computerized tomography and clinical diagnosis. *J Laryngol Otol*. 1999;113(3):229-232. [Crossref]
5. Steyer TE. Peritonsillar abscess: diagnosis and treatment. *Am Fam Physician*. 2002;65(1):93-96. Erratum in: *Am Fam Physician* 2002;66(1):30. [Crossref]
6. Powell J, Wilson JA. An evidence-based review of peritonsillar abscess. *Clin Otolaryngol*. 2012;37(2):136-145. [Crossref]
7. Ban MJ, Jung JY, Kim JW, et al. A clinical prediction score to determine surgical drainage of deep neck infection: a retrospective case-control study. *Int J Surg*. 2018;52:131-135. [Crossref]
8. Thomas JA, Ware TM, Counselman FL. Internal carotid artery pseudoaneurysm masquerading as a peritonsillar abscess. *J Emerg Med*. 2002;22(3):257-261. [Crossref]
9. Li AC, Wadley A, Aciu S, Zhao H, Jain N, Soliman AMS. Computed tomographic and clinical findings predictive of successful peritonsillar abscess drainage. *Laryngoscope*. 2026;136(1):151-157. [Crossref]
10. Hagelberg J, Pape B, Heikkinen J, Nurminen J, Mattila K, Hirvonen J. Diagnostic accuracy of contrast-enhanced CT for neck abscesses: a systematic review and meta-analysis of positive predictive value. *PLoS One*. 2022;17(10):e0276544. [Crossref]
11. Lambin P, Rios-Velazquez E, Leijenaar R, et al. Radiomics: extracting more information from medical images using advanced feature analysis. *Eur J Cancer*. 2012;48(4):441-446. [Crossref]
12. Gillies RJ, Kinahan PE, Hricak H. Radiomics: images are more than pictures, they are data. *Radiology*. 2016;278(2):563-577. [Crossref]
13. Fedorov A, Beichel R, Kalpathy-Cramer J, et al. 3D Slicer as an image computing platform for the Quantitative Imaging Network. *Magn Reson Imaging*. 2012;30(9):1323-1341. [Crossref]
14. van Griethuysen JJM, Fedorov A, Parmar C, et al. Computational radiomics system to decode the radiographic phenotype. *Cancer Res*. 2017;77(21):e104-e107. [Crossref]
15. Koo TK, Li MY. A guideline of selecting and reporting intraclass correlation coefficients for reliability research. *J Chiropr Med*. 2016;15(2):155-163. Erratum in: *J Chiropr Med*. 2017;16(4):346. [Crossref]
16. Vickers AJ, Elkin EB. Decision curve analysis: a novel method for evaluating prediction models. *Med Decis Making*. 2006;26(6):565-574. [Crossref]
17. Borstelmann SM. Machine learning principles for radiology investigators. *Acad Radiol*. 2020;27(1):13-25. [Crossref]
18. Breiman L. Random forests. *Mach Learn*. 2001;45:5-32. [Crossref]
19. Navada A, Ansari AN, Patil S, Sonkamble BA. Overview of use of decision tree algorithms in machine learning. In: 2011 IEEE Control and System Graduate Research Colloquium; 2011; Shah Alam, Malaysia. p. 37-42. [Crossref]
20. Chen T, Guestrin C. XGBoost: a scalable tree boosting system. In: Proceedings of the 22nd ACM SIGKDD International Conference on Knowledge Discovery and Data Mining; 2016. p. 785-794. [Crossref]
21. Vrigazova B, Ivanov I. Tenfold bootstrap procedure for support vector machines. *Comput Sci*. 2020;21(2):241-257. [Crossref]
22. Wilson MB, Ali SA, Kovatch KJ, Smith JD, Hoff PT. Machine learning diagnosis of peritonsillar abscess. *Otolaryngol Head Neck Surg*. 2019;161(5):796-799. [Crossref]
23. Kim DJ, Burton JE, Hammad A, et al. Test characteristics of ultrasound for the diagnosis of peritonsillar abscess: a systematic review and meta-analysis. *Acad Emerg Med*. 2023;30(8):859-869. [Crossref]
24. Costantino TG, Satz WA, Dehnkamp W, Goett H. Randomized trial comparing intraoral ultrasound to landmark-based needle aspiration in patients with suspected peritonsillar abscess. *Acad Emerg Med*. 2012;19(6):626-631. [Crossref]

Diagn Interv Radiol 2025; DOI: 10.4274/dir.2025.253619

ARTIFICIAL INTELLIGENCE AND INFORMATICS

LETTER TO THE EDITOR

©Copyright 2026 Author(s) - Available online at dirjournal.org.
Content of this journal is licensed under a Creative Commons Attribution-NonCommercial 4.0 International License.

Letter to the Editor: Challenges of applying large language models to image-based interpretation in abdominal radiology

Eren Çamur[1]
Turay Cesur[2]
Yasin Celal Güneş[3]

[1]Ministry of Health Ankara 29 Mayıs State Hospital, Clinic of Radiology, Ankara, Türkiye

[2]Ankara Mamak State Hospital, Clinic of Radiology, Ankara, Türkiye

[3]Kırıkkale High Specialization Hospital, Clinic of Radiology, Kırıkkale, Türkiye

Corresponding author: Eren Çamur

E-mail: eren.camur@outlook.com

Received 24 August 2025; accepted 31 August 2025.

Epub: 04.11.2025

Publication date: 02.11.2026

DOI: 10.4274/dir.2025.253619

Dear Editor,

We read with great interest the study by Elek et al.[1] This pioneering study deserves recognition for moving beyond natural language applications to directly evaluate image-based interpretation, thereby opening an important avenue for translational research in abdominal radiology.

The authors demonstrated that Bing ChatGPT-4 performed well in basic categorization, correctly identifying modality, anatomical region, and imaging plane. However, performance declined significantly when greater domain-specific expertise was required, such as differentiating magnetic resonance imaging pulse sequences, characterizing contrast enhancement, or recognizing pathology. These findings underscore the gap between surface-level pattern recognition and the deeper integrative reasoning central to radiologic diagnosis. Unlike convolutional neural networks or vision transformers trained on pixel-level radiology data, large language models (LLMs) are fundamentally language-based systems. Their image analysis relies on multimodal encoders that generate coarse visual embeddings, which are inadequate for detecting subtle grayscale variations, texture details, or multiparametric signal patterns. Diagnostic interpretation also requires the dynamic assessment of multiphase acquisitions, volumetric navigation across planes, and the integration of clinical metadata—all beyond the scope of single-image input models.

Considering that the authors did not employ radiology-specific pretraining, the favorable results demonstrated by relatively older models may reflect selection bias or stereotypical features (e.g., modality-specific appearances, anatomical landmarks) rather than genuine interpretive capacity. Prior exposure to similar images during training could also explain the model's apparent accuracy. Moreover, due to the black box nature of these systems, performance in image interpretation may vary across contexts. Comparing outcomes with the interpretations of radiologists with differing levels of experience would further clarify the true clinical relevance of such models.

The model's restriction to single-image inputs represents a major limitation, since radiologists rarely interpret isolated slices. Accurate diagnosis typically requires the analysis of image series across multiple planes and sequences. Future model development should therefore focus on sequential or volumetric image ingestion, approximating human workflow more closely.

Another important point is the absence of structured prompts. While this absence provided a fair "out-of-the-box, browser-based" evaluation, it may have underestimated the model's performance. Prior studies show that carefully designed prompts and stepwise reasoning frameworks can markedly enhance accuracy.[2-4] Collaborative efforts between artifical intelligence (AI) scientists and radiologists to develop structured, validated prompt libraries for specific diagnostic tasks may represent a key step forward.

Similarly, while the exclusion of patient history was methodologically justified to isolate image interpretation, it created a synthetic setting that diverges from clinical reality. Radiologists nearly always integrate clinical data into diagnostic reasoning. Excluding such information

You may cite this article as: Çamur E, Cesur T, Güneş YC. Letter to the editor: challenges of applying large language models to image-based interpretation in abdominal radiology. *Diagn Interv Radiol*. 2026;32(6):765-766.

may underestimate the potential of LLMs, which are fundamentally language-processing systems. Ultimately, an effective AI assistant must synthesize both imaging and clinical data.

In conclusion, Elek et al.[1] provide valuable early evidence on the opportunities and limitations of LLMs in abdominal radiology. Their study initiates a critical discussion and highlights important directions for future studies in this emerging field.

Conflict of interest disclosure

The authors declared no conflicts of interest.

References

1. Elek A, Ekizalioğlu DD, Güler E. Evaluating Microsoft Bing with ChatGPT-4 for the assessment of abdominal computed tomography and magnetic resonance images. *Diagn Interv Radiol.* 2025;31(3):196-205. [Crossref]
2. Kaba E, Solak M, Çeliker FB. The role of prompt engineering in radiology applications of generative AI. *Acad Radiol*. 2024;31(6):2641. [Crossref]
3. Nguyen D, MacKenzie A, Kim YH. Encouragement vs. liability: how prompt engineering influences ChatGPT-4's radiology exam performance. *Clin Imaging*. 2024;115:110276. [Crossref]
4. Alam S, Rahman A, Sohail SS. Optimizing ChatGPT-4's radiology performance with scale-invariant feature transform and advanced prompt engineering. *Clin Imaging*. 2025;118:110368. [Crossref]

Diagn Interv Radiol 2025; DOI: 10.4274/dir.2025.253680

ARTIFICIAL INTELLIGENCE AND INFORMATICS

LETTER TO THE EDITOR

©Copyright 2026 Author(s) - Available online at dirjournal.org.
Content of this journal is licensed under a Creative Commons Attribution-NonCommercial 4.0 International License.

Reply: challenges of applying large language models to image-based interpretation in abdominal radiology

Alperen Elek[1]
Duygu Doğa Ekizalioğlu[2]
Ezgi Güler[2]

[1]Ege University Faculty of Medicine, İzmir, Türkiye

[2]Ege University Faculty of Medicine, Department of Radiology, İzmir, Türkiye

Dear Editor,

We thank our colleagues for their valuable comments[1] on our study.[2] Below, we address the points raised in the context of our study's aim and design choices, and we outline potential improvements for future research.

The primary aim of our work was to provide an objective baseline assessment of a general-purpose large language model (LLM) in the most straightforward and realistic "out-of-the-box," browser-based scenario. This approach was intentionally chosen to highlight the current limitations of model architectures and training data, particularly the absence of radiology-specific pretraining. Recent reviews[3-5] have highlighted that LLMs continue to face challenges in data scarcity, coarse visual embeddings, and limited explainability, all of which contribute to difficulties in capturing subtle signal or texture patterns.

We agree that radiologists base their decisions on volumetric, multiplanar, and multiphase image series. Our study, however, was designed as a standardized and ethically safe browser-based scenario to establish a "minimum requirement" baseline. Future studies will incorporate sequential and volumetric inputs, as well as multiphase evaluation. Of course, this will require LLMs to become technically capable of ingesting larger and more complex inputs.

To isolate image-based signal interpretation, patient history was excluded, allowing us to measure the model's pure image-based performance. In clinical reality, the integration of imaging and history is essential. Yet, as Bulut et al.[6] recently demonstrated, even when clinical findings were provided, overall accuracy remained low. Although their work focused on pneumothorax detection, these results still indicate that the performance of current models remains questionable, even in a clinical context.

Moving forward, we believe improvements should include: (i) the ingestion of sequential/volumetric and multiphase data; (ii) radiology-specific pretraining and/or adapter fine-tuning; (iii) structured prompt libraries and chain-of-thought reasoning; (iv) the integration of clinical metadata; and (v) blinded multicenter studies comparing different levels of radiologist expertise. Industry collaboration will be crucial to achieving these goals.

In conclusion, although many of the limitations highlighted by our colleagues were already acknowledged in our original manuscript, we view these comments as an opportunity to expand the scope of our subsequent studies and to establish a concrete roadmap for future research.

Handling editor: Mehmet Ruhi Onur

Corresponding author: Ezgi Güler

E-mail: gulerezgi@yahoo.com

Received 02 October 2025; accepted 13 October 2025.

Epub: 04.11.2025

Publication date: 02.11.2026

DOI: 10.4274/dir.2025.253680

You may cite this article as: Elek A, Ekizalioğlu DD, Güler E. Reply: challenges of applying large language models to image-based interpretation in abdominal radiology. *Diagn Interv Radiol*. 2026;32(6):767-768.

Conflict of interest disclosure

The authors declared no conflicts of interest.

References

1. Letter to the editor: challenges of applying large language models to image-based interpretation in abdominal radiology. Diagn Interv Radiol. Ahead of Print. [Crossref]
2. Elek A, Ekizalioğlu DD, Güler E. Evaluating Microsoft Bing with ChatGPT-4 for the assessment of abdominal computed tomography and magnetic resonance images. *Diagn Interv Radiol*. 2025;31(3):196-205. [Crossref]
3. Nam Y, Kim DY, Kyung S, et al. Multimodal large language models in medical imaging: current state and future directions. *Korean J Radiol*. 2025;26(10):900-923. [Crossref]
4. Zhang A, Zhao E, Wang R, Zhang X, Wang J, Chen E. Multimodal large language models for medical image diagnosis: challenges and opportunities. *J Biomed Inform*. 2025;169:104895. [Crossref]
5. Lanzafame LRM, Gulli C, Mazziotti S, et al. Chatbots in radiology: current applications, limitations and future directions of ChatGPT in medical imaging. *Diagnostics (Basel)*. 2025;15(13):1635. [Crossref]
6. Bulut B, Öz M, Genç M, et al. New frontiers in radiologic interpretation: evaluating the effectiveness of large language models in pneumothorax diagnosis. *PLoS One*. 2025;20(9):e0331962. [Crossref]

Diagn Interv Radiol 2026; DOI: 10.4274/dir.2026.263742

BREAST IMAGING

ORIGINAL ARTICLE

©Copyright 2026 Author(s) - Available online at dirjournal.org.
Content of this journal is licensed under a Creative Commons Attribution-NonCommercial 4.0 International License.

Peritumoral-to-tumoral apparent diffusion coefficient ratio as a marker of tumor microenvironment activity across breast cancer molecular subtypes

Seçil Gündoğdu[1]
Eda Elverici[1]
Arzu Özsoy[2]
Leman Günbey Karabekmez[3]
Muhammed Said Beşler[4]
Emre Gündoğdu[5]

[1]Ankara Bilkent City Hospital, Clinic of Radiology, Ankara, Türkiye

[2]Ankara Medipol University Faculty of Medicine, Department of Radiology, Ankara, Türkiye

[3]Ankara Bilkent City Hospital, Yıldırım Beyazıt University Faculty of Medicine, Department of Radiology, Ankara, Türkiye

[4]İstanbul Medeniyet University Faculty of Medicine, Department of Radiology, İstanbul, Türkiye

[5]Yüksek İhtisas University Faculty of Medicine, Department of Surgery, Ankara, Türkiye

PURPOSE

This study aimed to evaluate the prognostic significance of tumoral apparent diffusion coefficient (tADC), peritumoral ADC (pADC), and the peritumoral-to-tumoral ADC (p/tADC) ratio in invasive breast cancers using high-resolution diffusion-weighted imaging.

METHODS

A retrospective cohort of 149 patients with invasive breast cancer was analyzed. pADC, tADC, and p/tADC values were independently measured by two experienced radiologists. The associations between these parameters and histological grade, receptor status, Ki-67 index, and molecular subtypes were assessed. Interobserver agreement was evaluated using the intraclass correlation coefficient (ICC), and multivariate logistic regression was performed to identify independent predictors.

RESULTS

Although tADC was significantly associated only with tumor size ($P < 0.050$), both pADC and p/tADC were significantly associated with high histological grade, estrogen receptor/progesterone receptor negativity, human epidermal growth factor receptor 2 positivity, and high Ki-67 index ($P < 0.01$). The p/tADC ratio emerged as an independent predictor of high-grade tumors and Ki-67 ≥ 20%. Excellent interobserver agreement was observed for all ADC measurements (ICC > 0.90).

CONCLUSION

The p/tADC ratio reflects stromal and microenvironmental alterations associated with tumor aggressiveness and demonstrates stronger prognostic relevance than tADC alone. Incorporating the p/tADC ratio into routine magnetic resonance imaging (MRI) interpretation may improve preoperative risk stratification and support personalized treatment planning in invasive breast cancer.

CLINICAL SIGNIFICANCE

The p/tADC ratio reflects stromal and microenvironmental changes associated with tumor aggressiveness and may serve as a non-invasive imaging biomarker. Its integration into preoperative MRI protocols may facilitate risk stratification and personalized treatment planning.

KEYWORDS

Breast cancer, diffusion-weighted magnetic resonance imaging, apparent diffusion coefficient, tumor microenvironment, molecular subtype, Ki-67, human epidermal growth factor receptor 2, peritumoral region, prognostic imaging biomarker

Handling editor: Serap Gültekin

Corresponding author: Seçil Gündoğdu

E-mail: drsecilgundogdu@gmail.com

Received 11 November 2025; revision requested 26 December 2025; accepted 11 February 2026.

Epub: 26.02.2026

Publication date: 02.11.2026

DOI: 10.4274/dir.2026.263742

Breast cancer is among the most frequently encountered malignancies worldwide, with an annual incidence of approximately 2.3 million cases and over 666,000 deaths, ranking as the fourth leading cause of cancer-related mortality.[1] To address this burden, global efforts have intensified through early detection strategies, including national screening programs and awareness campaigns.

You may cite this article as: Gündoğdu S, Elverici E, Özsoy A, Günbey Karabekmez L, Beşler MS, Gündoğdu E. Peritumoral-to-tumoral apparent diffusion coefficient ratio as a marker of tumor microenvironment activity across breast cancer molecular subtypes. *Diagn Interv Radiol*. 2026;32(6):769-776.

Tumor microenvironment

Breast cancers exhibit remarkable heterogeneity in both genetic and cellular behavior, influencing disease progression and treatment response.[2,3] The tumor microenvironment (TME)—comprising immune cells, fibroblasts, and the extracellular matrix—plays a pivotal role in tumor development.[4-9] In invasive breast cancers, phenomena such as lymphatic obstruction and matrix remodeling around tumors contribute to peritumoral edema, a known feature of malignancy.[5] This edema, linked to increased vascular permeability via proteolytic enzymes and angiogenesis, has been associated with more aggressive tumor behavior and poorer prognosis.[10-13] Notably, the peritumoral stroma harbors genetic distinctions from intratumoral regions, suggesting it provides biologically distinct and prognostically relevant information.[14-16]

Magnetic resonance imaging and diffusion-weighted imaging

Magnetic resonance imaging (MRI) offers superior sensitivity for breast cancer detection, enabling detailed anatomical and functional assessments.[17] However, its specificity remains limited.[18] Diffusion-weighted imaging (DWI), which measures water-molecule movement, enhances diagnostic accuracy by providing apparent diffusion coefficient (ADC) values, which are typically lower in malignant tissues due to higher cellularity.[19-22]

Several studies have explored correlations between ADC values and histopathologic features, including tumor size, grade, lymphovascular invasion, nodal status, and molecular subtype; however, results have been inconsistent due to methodological variability.[23-25] Peritumoral edema has emerged as a promising imaging marker, but limited data exist on its association with histopathologic aggressiveness or DWI parameters.[26,27]

Main points

- The peritumoral-to-tumoral apparent diffusion coefficient (p/tADC) ratio is significantly elevated in tumors with aggressive biological features.
- Unlike tumoral apparent diffusion coefficient (ADC), peritumoral ADC and p/tADC show robust correlations with multiple prognostic markers.
- ADC measurements demonstrated excellent interobserver reproducibility, supporting their clinical reliability.

In this study, the term peritumoral region specifically refers to the stromal tissue surrounding the tumor rather than to peritumoral edema alone. Although peritumoral edema seen on T2-weighted imaging may be a visual manifestation of stromal changes, our diffusion-weighted analysis focused on quantitative ADC measurements from the biologically active peritumoral stroma, excluding cystic, necrotic, or purely edematous regions.

Aim

This study investigates the relationship between MRI features and histopathological characteristics of breast cancer, with a specific focus on the prognostic significance of the peritumoral-to-tumoral ADC (p/tADC) ratio.

Methods

Study group

This retrospective study was conducted with the approval of the Ethics Committee of Ankara Bilkent City Hospital (decision number: E1-23-3199, date: 11.01.2023). The requirement for written informed consent was waived by the institutional ethics committee due to the retrospective nature of the study. Between April 2020 and July 2023, 367 patients who underwent high-resolution DWI with a narrow-field-of-view protocol on a 3-Tesla (T) MRI scanner were reviewed. Among these, 149 women (mean age: 53 ± 10.5 years; range 33–86 years) who had preoperative breast MRI- and biopsy-confirmed invasive breast cancer were included in the study. Patients with pure *in situ* carcinoma, a prior history of neoadjuvant chemotherapy, or the absence of surgery following breast MRI were excluded from the study.

Demographic data and the pathology reports of the patients were retrieved from the hospital information management system.

The patient selection process is summarized in Figure 1.

Magnetic resonance imaging protocol

All breast MRI examinations were performed on a 3.0-T scanner (Signa Pioneer, General Electric Medical Systems, Milwaukee, WI, USA) in the prone position using a dedicated 16-channel phased-array bilateral breast coil (NeoCoil 3.0 T, General Electric Medical Systems, Milwaukee, WI, USA).

The imaging protocol included the following sequences:

- Axial T1-weighted fast spin-echo [repetition time (TR)/echo time (TE): 484/8.5 ms; slice thickness: 5 mm]
- Axial and sagittal T2-weighted fat-suppressed fast spin-echo (TR/TE: 4,786/82.5 ms and 5,116/83.5 ms, respectively; slice thickness: 5 mm)
- Dynamic contrast-enhanced (DCE) axial T1-weighted fat-suppressed sequence (TR/TE: 6.1/1.7 ms; slice thickness: 2.2 mm), acquired before and after intravenous administration of a gadolinium-based contrast agent (0.1 mmol/kg), followed by a 20-mL saline flush
- DWI using single-shot echo-planar imaging with b values of 50 and 800 s/mm^2. ADC maps were automatically generated on the workstation.

Histopathological evaluation

Histopathological specimens obtained from surgical samples were evaluated by the Pathology Department of Ankara Bilkent City Hospital. Pathological data included information on estrogen receptor (ER) status, progesterone receptor (PR) status, human epidermal growth factor receptor 2 (HER2) status, Ki-67 index, and tumor size.

Apparent diffusion coefficient measurements

ADC measurements and T1-weighted, T2-weighted, and DCE images were used for anatomical reference. On the ADC map, the slice with the largest lesion cross-sectional diameter was selected. For tADC measurement, a circular region of interest (ROI) with a fixed diameter of 10 pixels (approximately 10 mm^2) was manually placed within the most restricted (visually darkest) solid portion of the tumor, avoiding necrotic, cystic, hemorrhagic, and fatty areas. The lowest ADC value obtained from three measurements was recorded as the representative tADC. For peritumoral ADC (pADC) assessment, three ROIs of identical size and shape (10 pixels in diameter) were placed in the adjacent breast parenchyma within a 5–10 mm distance from the tumor border, excluding fibroglandular tissue, large vessels, ducts, and artifacts. These ROIs were placed in areas with the highest signal intensity on the ADC map, consistent with increased diffusivity. Among these, the highest ADC value was recorded as the pADC, in line with previously published methods.[28] The p/tADC ratio was calculated by dividing the pADC by the tADC. Sample images of tumors with high and low pADC values were

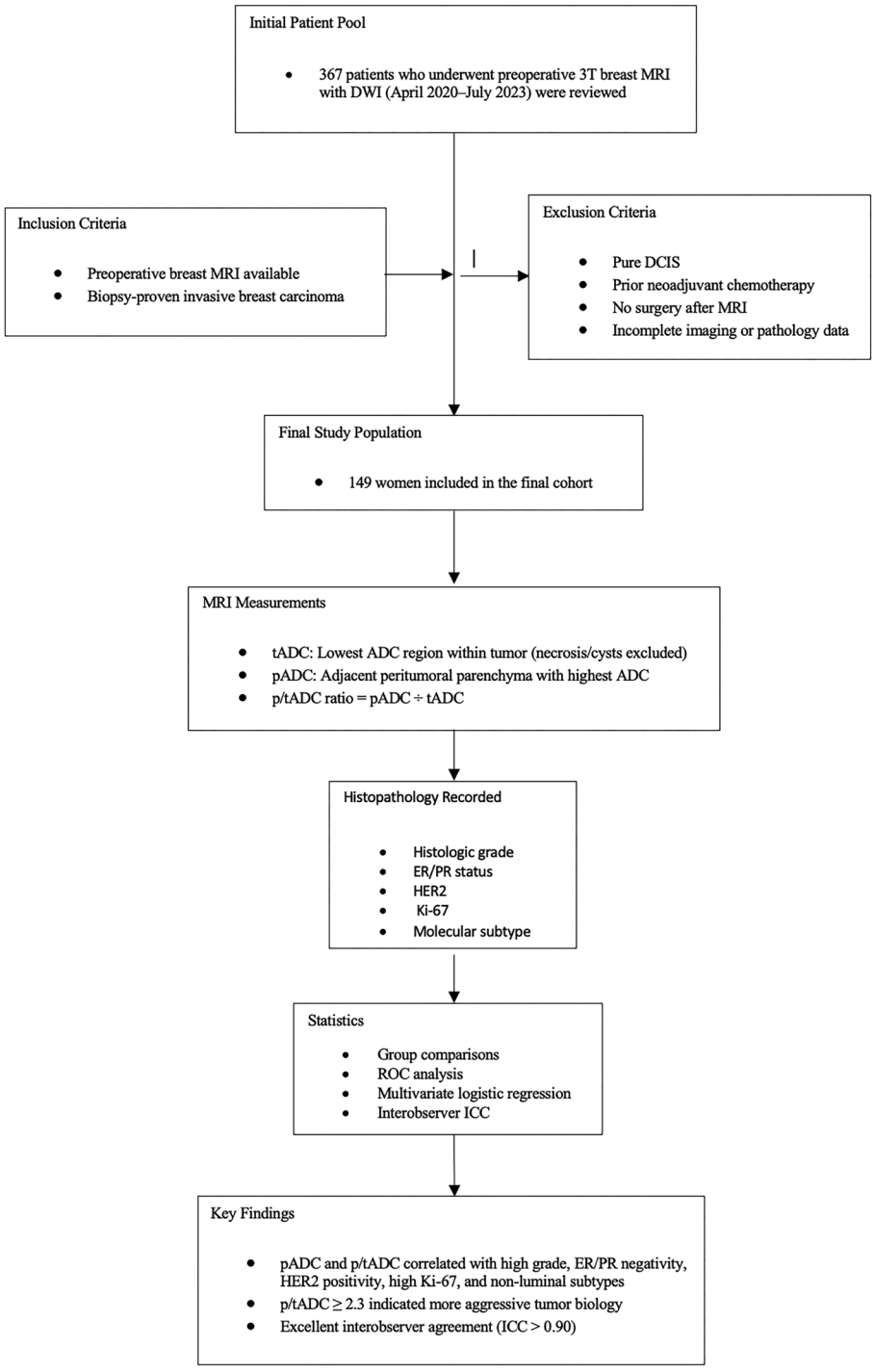


Figure 1. Flow diagram of the patient selection process. MRI, magnetic resonance imaging; DWI, ffusion-weighted imaging; DCIS, ductal carcinoma *in situ*; ADC, apparent diffusion coefficient; p/tADC, peritumoral-to-tumoral apparent diffusion coefficient; pADC, peritumoral apparent diffusion coefficient value; tADC, tumoral apparent diffusion coefficient value; ER, estrogen receptor; PR, progesterone receptor; HER2, human epidermal growth factor 2; ROC, receiver operating characteristic; ICC, intraclass correlation coefficient.

shown in Figures 2 and 3, respectively. All measurements were performed by two radiologists with over 5 years of experience in breast imaging. Each measurement was performed independently, and the mean value was used for analysis. The interobserver agreement was assessed using the intraclass correlation coefficient (ICC).

Pathological assessment

All patients underwent pathological evaluation of surgical specimens. Parameters such as histological grade, ER status, PR status, HER2 status, Ki-67 index, and axillary lymph node status were analyzed as binary variables as follows:

• ER/PR status was evaluated using the Allred scoring system, and a total score > 2 was considered positive.

• The HER2 score was evaluated immunohistochemically on a scale of 0–3; scores of 0–1 were considered negative, and a score of 3 was considered positive. Cases with a score of 2 underwent further evaluation with fluorescent *in situ* hybridization testing.

• Ki-67 values < 20% were classified as negative and values ≥ 20% as positive.

Statistical analysis

All statistical analyses were performed using SPSS version 30.0 (IBM, Chicago, IL, USA). ADC values were considered continuous dependent variables. Histopathological parameters were treated as binary independent variables, including the following:

• Histological grade: Grade 1–2 vs. Grade 3

• ER and PR status: Negative vs. positive

• HER2 status: Negative vs. positive

• Ki-67: < 20% vs. ≥ 20%

• Axillary lymph node metastasis: Negative vs. positive

• Tumor type: Ductal vs. lobular

• Molecular subtype: Luminal (luminal A, luminal B and luminal B-HER2+) vs. non-luminal (HER2-enriched, basal-like)

The normality of data distribution was assessed using the Shapiro–Wilk test. For normally distributed variables, comparisons between two groups were conducted using the independent samples Student's t-test, and results were expressed as mean ± standard deviation (SD).

For comparisons among luminal molecular subtypes (luminal A, luminal B, luminal B-HER2+, HER2-enriched, and basal-like), one-way analysis of variance was performed. When overall significance was observed, post-hoc pairwise comparisons were conducted using the Tukey test to identify intergroup differences.

Two-tailed tests were used for all analyses, and a P value < 0.05 was considered statistically significant.

Receiver operating characteristic (ROC) curve analysis was performed to determine optimal cut-off values for the p/tADC ratio to predict aggressive tumor characteristics. For each cut-off, sensitivity, specificity, and positive likelihood ratios (LR+)

were calculated to assess discriminative performance.

Variables with $P < 0.05$ in univariate analysis were entered into a multivariate binary logistic regression model to identify independent predictors of a high p/tADC ratio. The p/tADC ratio was dichotomized at 2.3 based on ROC analysis; ROC curves were generated to evaluate the ability of the p/tADC ratio to distinguish high-grade tumors (grade 3) and a high Ki-67 index (≥ 20%) from lower-risk tumors. The cut-off value was selected by maximizing the Youden index across these prognostic measures. Model calibration and performance were assessed using the Hosmer–Lemeshow goodness-of-fit test and Nagelkerke R^2.

Interobserver agreement

To assess measurement reproducibility between the two radiologists, interobserver agreement was evaluated for tADC, pADC, and p/tADC values in a randomly selected subset of 40 lesions (approximately 25% of the sample). The ICC (two-way random-effects model, absolute agreement) was calculated. Agreement was interpreted as follows: poor (< 0.50), moderate (0.50–0.75), good (0.75–0.90), and excellent (> 0.90).

Additionally, Bland–Altman plots were generated to visualize systematic bias and 95% limits of agreement between the two observers for each parameter.

Results

Between April 2020 and July 2023, a total of 149 women (mean age: 53 ± 10.5 years; range: 33–86 years) with invasive breast cancer were included in the study.

Interobserver agreement

Excellent interobserver agreement was observed for all ADC-based measurements. The ICC values for tADC, pADC, and the p/tADC ratio were 0.94 [95% confidence interval (CI): 0.90–0.97], 0.91 (95% CI: 0.86–0.95), and 0.93 (95% CI: 0.88–0.96), respectively (all $P < 0.001$).

Bland–Altman analysis demonstrated a mean difference of 0.02×10^{-3} mm²/s for tADC and 0.05×10^{-3} mm²/s for pADC, with no significant proportional bias. All differences lay within ± 1.96 SD, confirming acceptable agreement between readers (Table 1).

Demographic data and tumor characteristics are summarized in Table 2.

tADC values were significantly associated with tumor size ($P = 0.005$). However, no significant associations were found with histological grade ($P = 0.252$), Ki-67 index ($P = 0.635$), ER ($P = 0.562$), PR ($P = 0.652$), HER2 ($P = 0.556$), axillary lymph node status ($P = 0.957$), or molecular subtype ($P = 0.703$).

pADC was significantly associated with tumor size ($P = 0.009$), axillary lymph node positivity ($P = 0.02$), molecular subtype ($P < 0.001$), HER2 ($P = 0.002$), ER ($P = 0.001$), PR ($P = 0.002$), Ki-67 ($P < 0.001$), and histological grade ($P = 0.010$).

The p/tADC ratio showed significant associations with tumor size ($P < 0.001$), histological grade ($P = 0.004$), Ki-67 index ($P < 0.001$),

Table 1. Bland–Altman plots illustrating interobserver agreement for tADC, pADC, and p/tADC measurements

Parameter	ICC (95% CI)	*P* value	Interpretation
tADC	0.94 (0.90–0.97)	< 0.001	Excellent
pADC	0.91 (0.86–0.95)	< 0.001	Excellent
p/tADC	0.93 (0.88–0.96)	< 0.001	Excellent

tADC, tumoral apparent diffusion coefficient; pADC, peritumoral apparent diffusion coefficient; p/tADC, peritumoral-to-tumoral apparent diffusion coefficient; ICC, intraclass correlation coefficient; CI, confidence interval.

Table 2. Patients' demographic data and tumor characteristics

Number of patients	149
Age (years) (mean ± SD)	53 ± 10.5
Tumor size (mean ± SD)	3.01 ± 1.77
Lymph node	
Positive	67 (45%)
Negative	82 (55%)
Grade	
G1	28 (18.8%)
G2	92 (61.7%)
G3	29 (19.5%)
Estrogen receptor	
Positive	117 (78.5%)
Negative	32 (21.5%)
Progesterone receptor	
Positive	115 (77.2%)
Negative	34 (22.8%)
HER2 receptor	
Positive	106 (71.1%)
Negative	43 (28.9%)
Ki-67 expression	
< 20%	59 (39.6%)
≥ 20%	90 (60.4%)
Tumor type	
Ductal	132 (88.6%)
Lobular	14 (9.4%)
Others	3 (2%)
Luminal subtype	
Luminal A	52 (34.9%)
Luminal B	37 (24.8%)
Luminal B/HER2 +	30 (20.1%)
HER2 overexpression	12 (8.1%)
Basal-Like	18 (12.1%)

SD, standard deviation; HER2, human epidermal growth factor 2.

ER ($P = 0.006$), PR ($P = 0.015$), and HER2 ($P = 0.010$) but not with lymph node positivity ($P = 0.08$).

Associations between pADC and tADC values, p/tADC ratios, histopathological parameters, and lymph nodes status are shown in Table 3.

Comparison by molecular subtype

No statistically significant difference in tADC values was observed between luminal and non-luminal subgroups ($P = 0.703$). By contrast, both pADC and p/tADC values demonstrated a statistically significant difference among the luminal subtypes ($P < 0.001$ and $P = 0.002$, respectively).

No statistically significant differences in pADC ($P = 0.085$) or p/tADC ratios ($P = 0.327$) were observed between luminal A and luminal B groups. However, the luminal A group demonstrated significantly lower pADC and p/tADC ratios than the luminal B-HER2+ ($P = 0.003$, $P = 0.007$, respectively), HER2-enriched ($P < 0.001$, $P = 0.035$, respectively), and basal-like tumor groups ($P = 0.001$, $P = 0.003$, respectively).

By contrast, no significant differences were found among the luminal B, luminal B-HER2+, HER2-enriched, and basal-like groups in terms of pADC and p/tADC ratios. Additionally, tADC values did not differ significantly across molecular subtypes.

Prognostic performance of peritumoral-to-tumoral apparent diffusion coefficient ratios

Analysis of the prognostic predictive power of the p/tADC ratio revealed the highest discriminative performance for tumor size (LR+: 1.99), whereas the lowest was observed for HER2 status (LR+: 1.56). Cut-off values, sensitivity, specificity, and LR+ are summarized in Table 4.

Multivariate logistic regression

In the multivariate logistic regression analysis, the model demonstrated acceptable fit (Hosmer–Lemeshow χ^2: 11.55, df: 8, $P = 0.17$) and accounted for approximately 24% of the variance in the high p/tADC ratio (Nagelkerke R^2: 0.24). High histological grade and a Ki-67 index ≥ 20% were identified as independent predictors of a high p/tADC ratio (≥ 2.3), whereas ER, PR, and HER2 status did not remain significant in the multivariate model (Table 5). The ROC analysis confirmed that a p/tADC threshold of 2.3 provided the optimal balance of sensitivity and specificity for differentiating high-grade tumors and elevated Ki-67 expression.

Discussion

This study underscores the prognostic potential of the p/tADC ratio as a non-invasive imaging biomarker in invasive breast cancer. We demonstrated that although tADC was significantly associated only with tumor size, the p/tADC ratio showed independent associations with high histological grade and elevated Ki-67 index and was significantly different across molecular subtypes. These findings suggest that alterations in diffusion within the peritumoral microenvironment provide clinically relevant biological information beyond what tADC alone can reveal.

The inverse association between ADC values and cellularity is well established, as lower tADC values often indicate high cellular density and reduced extracellular space.[23,29] However, prior studies have reported inconsistent correlations between ADC and key pathological markers such as receptor status, Ki-67, and tumor grade.[20,30] Our findings are consistent with this inconsistency, as tADC did not correlate significantly with ER, PR, HER2, or Ki-67 in our cohort.

Interobserver agreement for all diffusion metrics was excellent (ICC > 0.90), confirming the reproducibility of our measurement protocol.

In contrast to tADC, both pADC and the p/tADC ratio showed significant associations with histological grade, hormone receptor status, HER2 expression, and Ki-67 index. This supports the notion that the peritumoral stroma is an active component of the TME and may mirror stromal remodeling, angiogenesis, immune suppression, and extracellular matrix changes.[6,16,31,32]

Several histopathological and imaging-based studies have identified edema, inflammation, and stromal activation in peritumoral tissues of high-grade tumors.[11,33] Zhang et al.[33] showed that peritumoral edema is more pronounced in HER2+ and triple-negative tumors, reflecting elevated vascular permeability and cytokine-mediated stromal stress.[34] These findings are fur-

Table 3. Associations between tumor and peritumor ADC values, p/tADC ratios, histopathological parameters, and lymph node status

	Tumor size	LN	Histologic subtype	HER2	ER	PR	Ki67	Grade
p/tADC	< 0.001	0.08	0.002	0.010	0.006	0.015	< 0.001	0.004
pADC	0.009	0.02	0.001	0.002	0.001	0.002	< 0.001	0.010
tADC	0.005	0.957	0.703	0.556	0.562	0.652	0.635	0.252

ADC, apparent diffusion coefficient; p/tADC, peritumoral-to-tumoral apparent diffusion coefficient; pADC, peritumoral apparent diffusion coefficient value; tADC, tumoral apparent diffusion coefficient value; LN, lymph node metastasis; HER2, human epidermal growth factor 2; ER, estrogen receptor, PR, progesterone receptor.

Table 4. Cut-off values, sensitivity, specificity, and positive likelihood ratios of p/tADC ratios

ADC ratio	Cut-off value	Sensitivity (%)	Specificity (%)	LR+	*P* value
Tumor size > 2 cm	2.3	66.3	66.7	1.99	0.00
Grade	2.6313	65.5	65.8	1.92	0.002
Molecular subtype	2.5496	63.3	62.2	1.67	0.00
ER negativity	2.5496	62.5	62.4	1.66	0.002
PR negativity	2.537	61.8	60.9	1.58	0.005
HER2	2.5162	60.5	61.3	1.56	0.006
Ki-67	2.3581	61.1	61	1.57	0.00

ADC, apparent diffusion coefficient; p/tADC, peritumoral-to-tumoral apparent diffusion coefficient; ER, estrogen receptor; PR, progesterone receptor; HER2, human epidermal growth factor 2; LR+, positive likelihood ratio.

Table 5. Multivariate logistic regression analysis identifying independent predictors of high p/tADC ratio

Variable	Univariate *p*	Multivariate OR (95% CI)	***P* value**
ER negative	0.006	1.8 (0.9–3.6)	0.09
PR negative	0.015	1.5 (0.7–3.0)	0.18
HER2 positive	0.010	1.7 (0.8–3.2)	0.11
Ki-67 ≥ 20%	< 0.001	2.9 (1.5–5.8)	0.002
Grade 3	0.004	2.3 (1.1–4.7)	0.021

OR, odds ratio; CI, confidence interval; ER, estrogen receptor; PR, progesterone receptor; HER2, human epidermal growth factor 2; p/tADC, peritumoral-to-tumoral apparent diffusion coefficient.

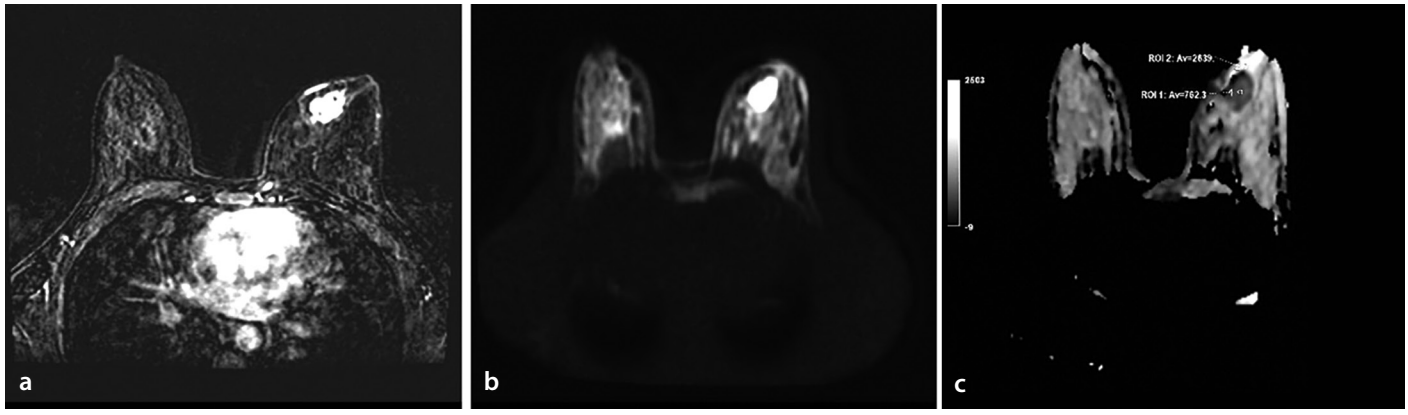


Figure 2. Breast lesion in a 52-year-old female patient with a high peritumor/tumor apparent diffusion coefficient (ADC) ratio. **(a)** Axial T1-weighted fat-suppressed dynamic sequence shows a mass with heterogeneous enhancement in the left breast; **(b)** high peritumoral signal intensity is shown in Axial T2-weighted fat-suppressed sequence; **(c)** the ADC map shows restricted diffusion in the mass. The lowest mean tumor ADC value (shown as ROItumor) was 0.7×10^{-3} mm^2/s, and the highest mean peritumor ADC value (shown as ROI peritumor) was 2.6×10^{-3} mm^2/s. The peritumor/tumor ADC ratio was 3.71. The clinical and histopathological features of the lesion were grade 3, human epidermal growth factor receptor 2 positive, estrogen receptor and progesterone receptor negative, Ki-67 high (> 20%).

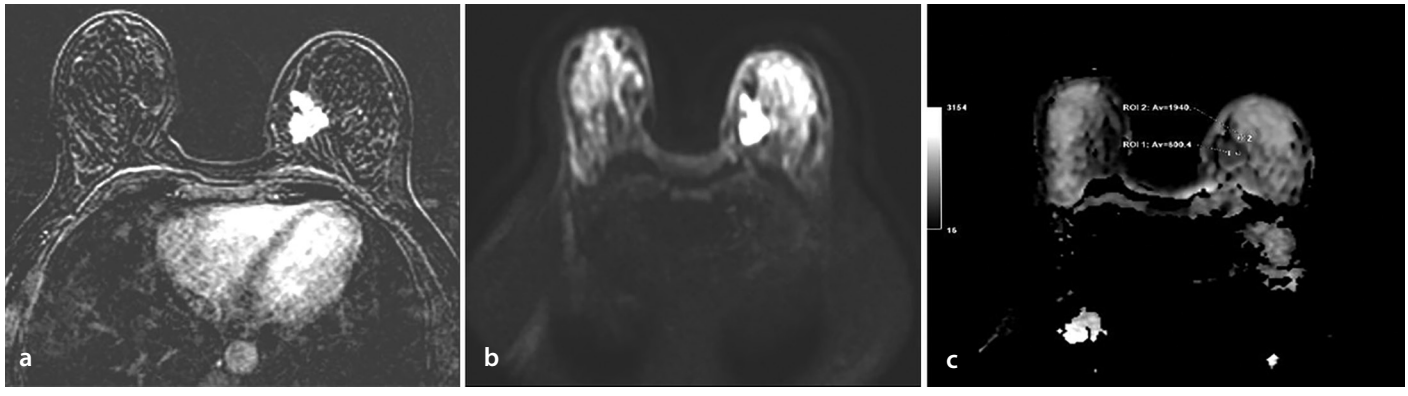


Figure 3. Breast lesion in a 63-year-old female patient with a low peritumor/tumor apparent diffusion coefficient (ADC) ratio. **(a)** Axial T1-weighted fat-suppressed dynamic sequence shows a mass with irregular margin and heterogeneous enhancement in the left breast; **(b)** normal peritumoral signal intensity is shown in axial T2-weighted fat-suppressed sequence; **(c)** the ADC map shows restricted diffusion in the mass. The lowest mean tumor ADC value (shown as ROI tumor) was 0.8×10^{-3} mm^2/s, and the highest mean peritumor ADC value (shown as ROIperitumor) was 1.9×10^{-3} mm^2/s. The peritumor/tumor ADC ratio was 2.3. The clinical and histopathological features of the lesion were: grade 1, estrogen receptor and progesterone receptor negative, Ki-67 low (< 20%).

ther supported by DWI-based studies linking high pADC values to HER2 overexpression and high Ki-67,[12,35] which align with our observation that aggressive tumors exhibit higher pADC and p/tADC ratios.

From a molecular perspective, our analysis revealed that HER2-enriched, basal-like, and triple-negative tumors had significantly higher pADC and p/tADC values than luminal A subtypes. These subtypes are known to exhibit more intense stromal remodeling and angiogenesis.[36-39]

Notably, tADC did not differentiate tumor grade, whereas the p/tADC ratio did ($P = 0.004$ vs. $P = 0.252$). This supports the findings of Doğan et al.,[40] who argued that peritumoral diffusion metrics better reflect biological aggressiveness, and those of Choi et al.,[41] who suggested that the p/tADC ratio mitigates variability introduced by tumor heterogeneity and imaging artifacts.

We also calculated cut-off values for predicting high-grade features. The optimal p/tADC threshold of 2.3, determined via ROC analysis, yielded the best balance between sensitivity and specificity. The p/tADC ratio was moderately predictive across different features, with the highest LR+ for tumor size (LR+: 1.99) and the lowest for HER2 status (LR+: 1.56). Although not highly diagnostic on their own, these values offer quantifiable markers that can assist in clinical risk stratification.

In multivariate analysis, only high histological grade and Ki-67 ≥ 20% retained statistical significance, emphasizing the p/tADC ratio's closer relationship with proliferative activity and stromal remodeling rather than receptor expression per se.

Our findings are consistent with those of Okuma et al.,[28] who also identified associations between p/tADC and tumor size and grade, Ki-67, and lymph node status. Similarly, El-Metwally et al.[42] supported a link between ADC metrics and Ki-67, whereas associations with hormone receptors were weaker.

Incorporating peritumoral diffusion metrics into breast MRI has been supported by a recent meta-analysis published in 2024 (PMID: 38334760).[43] However, many prior studies lacked interobserver reproducibility assessments or multivariate control. Our study addresses these gaps by demonstrating that the p/tADC ratio is not only reproducible (ICC > 0.90) but also an independent predictor of histopathological aggressiveness.

We also contributed to the literature by offering molecular subtype-specific analysis and defined p/tADC cut-offs for biologically aggressive features. Together, these findings position the p/tADC ratio as a promising adjunct to conventional MRI parameters for risk stratification in invasive breast cancer.

Our findings highlight the clinical value of the p/tADC ratio as a non-invasive imaging biomarker of tumor aggressiveness. The p/tADC ratio was independently associated with high histological grade and Ki-67 index and showed distinct patterns across molecular subtypes. By using a standardized ROI placement and defining specific cut-off values, this metric may aid in preoperative risk stratification. Integrating the p/tADC ratio into routine MRI protocols could support more personalized treatment planning. Future studies should also explore advanced diffusion techniques, such as diffusion tensor imaging, to better characterize peritumoral tissue heterogeneity.

Footnotes

Conflict of interest disclosure

The authors declared no conflicts of interest.

References

1. International Agency for Research on Cancer. Global Cancer Observatory: Cancer Today. Lyon, France: IARC; 2022. Accessed June 23, 2025. [Crossref]
2. Remšík J, Fedr R, Navrátil J, et al. Plasticity and intratumoural heterogeneity of cell surface antigen expression in breast cancer. *Br J Cancer*. 2018;118(6):813-819. [Crossref]
3. Zardavas D, Irrthum A, Swanton C, Piccart M. Clinical management of breast cancer heterogeneity. *Nat Rev Clin Oncol*. 2015;12(7):381-394. [Crossref]
4. Nelson DA, Tan TT, Rabson AB, Anderson D, Degenhardt K, White E. Hypoxia and defective apoptosis drive genomic instability and tumorigenesis. *Genes Dev*. 2004;18(17):2095-2107. [Crossref]
5. Polyak K, Kalluri R. The role of the microenvironment in mammary gland development and cancer. *Cold Spring Harb Perspect Biol*. 2010;2(11):a003244. [Crossref]
6. Hanahan D, Coussens LM. Accessories to the crime: functions of cells recruited to the tumor microenvironment. *Cancer Cell*. 2012;21(3):309-322. [Crossref]
7. Petitprez F, Meylan M, de Reyniès A, Sautès-Fridman C, Fridman WH. The Tumor microenvironment in the response to immune checkpoint blockade therapies. *Front Immunol*. 2020;11:784. [Crossref]
8. Hirata E, Sahai E. Tumor microenvironment and differential responses to therapy. *Cold Spring Harb Perspect Med*. 2017;7(7):a026781. [Crossref]
9. Beck AH, Sangoi AR, Leung S, et al. Systematic analysis of breast cancer morphology uncovers stromal features associated with survival. *Sci Transl Med*. 2011;3(108):108ra113. [Crossref]
10. Baltzer PA, Yang F, Dietzel M, et al. Sensitivity and specificity of unilateral edema on T2w-TSE sequences in MR-Mammography considering 974 histologically verified lesions. *Breast J*. 2010;16(3):233-239. [Crossref]
11. Cheon H, Kim HJ, Kim TH, et al. Invasive breast cancer: prognostic value of peritumoral edema identified at preoperative MR imaging. *Radiology*. 2018;287(1):68-75. [Crossref]
12. Kettunen T, Okuma H, Auvinen P, et al. Peritumoral ADC values in breast cancer: region of interest selection, associations with hyaluronan intensity, and prognostic significance. *Eur Radiol*. 2020;30(1):38-46. [Crossref]
13. Panzironi G, Moffa G, Galati F, Marzocca F, Rizzo V, Pediconi F. Peritumoral edema as a biomarker of the aggressiveness of breast cancer: results of a retrospective study on a 3 T scanner. *Breast Cancer Res Treat*. 2020;181(1):53-60. [Crossref]
14. Cvetković D, Cvetkovic A, Ninković S, Milutinovic M, Mitrović S, Marković S. The role of molecular markers of angiogenesis in disease prediction in breast cancer patients. *Biologia Serbica*. 2020;41(2):63-69. [Crossref]
15. Franchi M, Masola V, Bellin G, Onisto M, Karamanos KA, Piperigkou Z. Collagen fiber array of peritumoral stroma influences epithelial-to-mesenchymal transition and invasive potential of mammary cancer cells. *J Clin Med*. 2019;8(2):213. [Crossref]
16. Artacho-Cordón A, Artacho-Cordón F, Ríos-Arrabal S, Calvente I, Núñez MI. Tumor microenvironment and breast cancer progression: a complex scenario. *Cancer Biol Ther*. 2012;13(1):14-24. [Crossref]
17. Choyke PL, Dwyer AJ, Knopp MV. Functional tumor imaging with dynamic contrast-enhanced magnetic resonance imaging. *J Magn Reson Imaging*. 2003;17(5):509-520. [Crossref]
18. Bluemke DA, Gatsonis CA, Chen MH, et al. Magnetic resonance imaging of the breast prior to biopsy. *JAMA*. 2004;292(22):2735-2742. [Crossref]
19. Kul S, Cansu A, Alhan E, Dinc H, Gunes G, Reis A. Contribution of diffusion-weighted imaging to dynamic contrast-enhanced MRI in the characterization of breast tumors. *AJR Am J Roentgenol*. 2011;196(1):210-217. [Crossref]
20. Ginat DT, Mangla R, Yeaney G, Johnson M, Ekholm S. Diffusion-weighted imaging for differentiating benign from malignant skull lesions and correlation with cell density. *AJR Am J Roentgenol*. 2012;198(6):W597-W601. [Crossref]
21. Anderson AW, Xie J, Pizzonia J, Bronen RA, Spencer DD, Gore JC. Effects of cell volume fraction changes on apparent diffusion in human cells. *Magn Reson Imaging*. 2000;18(6):689-695. [Crossref]
22. Hirano M, Satake H, Ishigaki S, Ikeda M, Kawai H, Naganawa S. Diffusion-weighted imaging of breast masses: comparison of diagnostic performance using various apparent diffusion coefficient parameters. *AJR Am J Roentgenol*. 2012;198(3):717-722. [Crossref]
23. Partridge SC, McDonald ES. Diffusion weighted magnetic resonance imaging of the breast: protocol optimization, interpretation, and clinical applications. *Magn Reson Imaging Clin N Am*. 2013;21(3):601-624. [Crossref]
24. Kim SH, Cha ES, Kim HS, et al. Diffusion-weighted imaging of breast cancer: correlation of the apparent diffusion coefficient value with prognostic factors. J Magn Reson Imaging. 2009;30(3):615-620. [Crossref]
25. Horvat JV, Bernard-Davila B, Helbich TH, et al. Diffusion-weighted imaging (DWI) with apparent diffusion coefficient (ADC) mapping as a quantitative imaging biomarker for prediction of immunohistochemical receptor status, proliferation rate, and molecular subtypes of breast cancer. *J Magn Reson Imaging*. 2019;50(3):836-846. [Crossref]
26. Uematsu T. Focal breast edema associated with malignancy on T2-weighted images of breast MRI: peritumoral edema, prepectoral edema, and subcutaneous edema. *Breast*

Cancer. 2015;22(1):66-70. [Crossref]

27. Gemici AA, Ozal ST, Hocaoğlu E, et al. Relation of peritumoral, prepectoral and diffuse edema with histopathologic findings of breast cancer in preoperative 3T magnetic resonance imaging. *J Surg Med*. 2019;3(1):49-53. [Crossref]
28. Okuma H, Sudah M, Kettunen T, et al. Peritumor to tumor apparent diffusion coefficient ratio is associated with biologically more aggressive breast cancer features and correlates with the prognostication tools. *PLoS One*. 2020;15(6):e0235278. [Crossref]
29. Woodhams R, Matsunaga K, Iwabuchi K, et al. Diffusion-weighted imaging of malignant breast tumors: the usefulness of apparent diffusion coefficient (ADC) value and ADC map for the detection of malignant breast tumors and evaluation of cancer extension. *J Comput Assist Tomogr*. 2005;29(5):644-649. [Crossref]
30. Hatakenaka M, Soeda H, Yabuuchi H, et al. Apparent diffusion coefficients of breast tumors: clinical application. *Magn Reson Med Sci*. 2008;7(1):23-29. [Crossref]
31. Quail DF, Joyce JA. Microenvironmental regulation of tumor progression and metastasis. *Nat Med*. 2013;19(11):1423-1437. [Crossref]
32. Junttila MR, de Sauvage FJ. Influence of tumour micro-environment heterogeneity on therapeutic response. *Nature*. 2013;501(7467):346-354. [Crossref]
33. Zhang H, Miao Q, Fu Y, et al. Intratumoral and peritumoral radiomics based on automated breast volume scanner for predicting human epidermal growth factor receptor 2 status. *Front Oncol*. 2025;15:1556317. [Crossref]
34. Harney AS, Arwert EN, Entenberg D, et al. Real-time imaging reveals local, transient vascular permeability, and tumor cell intravasation stimulated by TIE2hi macrophage-derived VEGFA. *Cancer Discov*. 2015;5(9):932-943. [Crossref]
35. Han Y, Huang M, Xie L, Cao Y, Dong Y. The value of intratumoral and peritumoral radiomics features based on multiparametric MRI for predicting molecular staging of breast cancer. *Front Oncol*. 2025;15:1379048. [Crossref]
36. Li X, Fang J, Wang F, Zhang L, Jiang X, Mao X. Prediction of HER2 expression in breast cancer patients based on multi-parametric MRI intratumoral and peritumoral radiomics features combined with clinical and imaging indicators. *Front Oncol*. 2025;15:1531553. [Crossref]
37. Fan M, He T, Zhang P, et al. Diffusion-weighted imaging features of breast tumours and the surrounding stroma reflect intrinsic heterogeneous characteristics of molecular subtypes in breast cancer. *NMR Biomed*. 2018;31(2). [Crossref]
38. Amini B, Ghasemi M, Rashidi F, et al. A comprehensive evaluation of quantitative diffusion parameters for differentiating histopathological features and subtypes of breast cancers: diffusion kurtosis imaging (DKI), intravoxel incoherent motion (IVIM) and histogram analysis of ADC. Preprint. Published January 3, 2023. [Crossref]
39. Zhao M, Fu K, Zhang L, et al. Intravoxel incoherent motion magnetic resonance imaging for breast cancer: a comparison with benign lesions and evaluation of heterogeneity in different tumor regions with prognostic factors and molecular classification. *Oncol Lett*. 2018;16(4):5100-5112. [Crossref]
40. Doğan GM, Sığırcı A, Taşolar S, et al. Do intratumoral and peritumoral apparent diffusion coefficient (ADC) values have a role in the diagnosis of pediatric brain tumors? *Childs Nerv Syst*. 2020;36(3):251-259. [Crossref]
41. Choi EJ, Youk JH, Choi H, Song JS. Dynamic contrast-enhanced and diffusion-weighted MRI of invasive breast cancer for the prediction of sentinel lymph node status. *J Magn Reson Imaging*. 2020;51(2):615-626. [Crossref]
42. El-Metwally D, Monier D, Hassan A, Helal AM. Preoperative prediction of Ki-67 status in invasive breast carcinoma using dynamic contrast-enhanced MRI, diffusion-weighted imaging and diffusion tensor imaging. *Egypt J Radiol Nucl Med*. 2023;54(1):62. [Crossref]
43. Zhao S, Li Y, Ning N, et al. Association of peritumoral region features assessed on breast MRI and prognosis of breast cancer: systematic review and meta-analysis. *Eur Radiol*. 2024;34(9):6108-6120. [Crossref]

Diagn Interv Radiol 2026; DOI: 10.4274/dir.2026.263750

CARDIOVASCULAR IMAGING

ORIGINAL ARTICLE

©Copyright 2026 Author(s) - Available online at dirjournal.org.
Content of this journal is licensed under a Creative Commons Attribution-NonCommercial 4.0 International License.

Magnetic resonance imaging evaluation of myocardial and hepatic tissue remodeling and cardiac function in sickle cell anemia

Serhat Başaran
Kaan Esen
Aydan Akdeniz
Hasan H. Yüksek
Yüksel Balcı

Mersin University, Department of Radiology, Mersin, Türkiye

PURPOSE

To assess myocardial and hepatic tissue remodeling in patients with sickle cell anemia (SCA) using T1 mapping and extracellular volume (ECV) measurements, and to evaluate diastolic dysfunction (DD) using magnetic resonance imaging (MRI).

METHODS

This prospective study enrolled 32 patients with SCA (19 women; mean age: 37 years) and 12 healthy controls (8 men; mean age: 31 years). Myocardial T1, T2, and T2* values and hepatic T1 and T2* values were measured in both groups. Myocardial and hepatic ECV measurements were performed in the patient group. DD was evaluated using transmitral flow (TMF) curves and left atrial volume index (LAVI).

RESULTS

In patients with SCA, the mean myocardial T1 value was 1,030.91 ms, significantly higher than in controls, and the mean ECV was 31.7% ± 3.1%, higher than published reference ranges. Moreover, LAVI was significantly higher in patients than in controls (46.48 ± 15.35 vs. 30.58 ± 5.0 mL/m^2; $P < 0.001$). Diastolic function assessment revealed findings suggestive of a restrictive filling pattern in 10 individuals, who had an average age of 33 years. Within the SCA cohort, patients with TMF-derived early/late ratio >2 (n = 10) had significantly higher LAVI than the remaining patients (54.05 ± 10.12 vs. 43.0 ± 16.26 mL/m^2; $P = 0.027$). Myocardial ECV was significantly higher in patients with findings suggestive of a restrictive filling pattern than in the remaining patients (34.14% ± 2.39% vs. 30.62% ± 2.67%; $P = 0.001$). The mean myocardial T2* value was 39.25 ± 5.9 ms, and no cardiac iron accumulation was detected. The mean hepatic T2* value was 12.20 ms, with iron accumulation observed in 16 patients. Iron accumulation can have an impact on T1 values, and measurements in patients without iron accumulation revealed a mean liver T1 value (626.5 ms) that was significantly higher than that in controls ($P < 0.001$). These patients also had an ECV (40.4%) that was higher than published reference ranges ($P < 0.001$).

CONCLUSION

Increased myocardial and hepatic T1 and ECV values were observed in patients with SCA, suggesting expansion of the extracellular space, largely consistent with diffuse interstitial fibrosis in this clinical context. Diastolic function assessment revealed a restrictive filling pattern in a substantial proportion of patients, supporting a possible association between SCA and this pattern. Myocardial ECV was significantly higher in patients with findings suggestive of a restrictive filling pattern than in the remaining patients, suggesting an association between diffuse interstitial fibrosis and advanced DD patterns. MRI may be a valuable modality for evaluating myocardial and hepatic fibrosis and assessing cardiac function.

CLINICAL SIGNIFICANCE

MRI with mapping and ECV quantification may contribute to a non-invasive, quantitative assessment of myocardial and hepatic fibrosis-related tissue remodeling in patients with SCA. Moreover, TMF analysis may provide valuable insights into diastolic function. Together, these methods could contribute to the clinical evaluation and management of SCA and other diseases characterized by fibrosis-related remodeling.

KEYWORDS

Myocardial fibrosis, hepatic fibrosis, T1 mapping, extracellular volume, sickle cell anemia, cardiac function, diastolic dysfunction, T2* mapping

Handling editor: Furkan Ufuk

Corresponding author: Serhat Başaran

E-mail: serhat_4432@hotmail.com

Received 17 November 2025; revision requested 15 December 2025; last revision requested 10 February 2026; accepted 24 February 2026.

Epub: 18.03.2026

Publication date: 02.11.2026

DOI: 10.4274/dir.2026.263750

You may cite this article as: Başaran S, Esen K, Akdeniz A, Yüksek HH, Balcı Y. Magnetic resonance imaging evaluation of myocardial and hepatic tissue remodeling and cardiac function in sickle cell anemia. *Diagn Interv Radiol*. 2026;32(6):777-786.

Sickle cell anemia (SCA) is an autosomal recessive genetic disorder characterized by erythrocytes containing abnormal hemoglobin that become spherical and rigid under the influence of various stressors in the vascular microenvironment. Chronic hemolysis and recurrent ischemia-reperfusion injury in multiple organs constitute the fundamental mechanisms underlying the disease.[1] SCA-associated cardiac disease is one of the leading causes of mortality and morbidity in young adults.[2] Repeated microvascular occlusions result in ischemia and myocardial fibrosis. Additionally, chronic inflammation contributes to these processes, thereby impairing diastolic function. Diastolic dysfunction (DD), classified as impaired relaxation, pseudonormal, or restrictive filling patterns, is an independent risk factor for mortality.[3] Similarly, hepatic complications are frequently encountered and represent a significant cause of morbidity, negatively affecting prognosis. Processes such as ischemia and sequestration caused by vaso-occlusion, as well as iron accumulation from chronic hemolysis or treatment, can result in hepatic fibrosis.[4]

Cardiovascular magnetic resonance (CMR) imaging provides a comprehensive, non-invasive assessment of cardiac morphology and function, is highly reproducible, and plays a central role in myocardial tissue characterization using multiparametric techniques. Cine CMR provides high-temporal-resolution assessment of left ventricle and right ventricle function and enables accurate, highly reproducible three-dimensional quantification of ventricular volumes and ejection fraction (EF) without geometric assumptions. Phase-contrast (PC)-CMR can quantify blood-flow velocity and flow across vessels and heart valves, including transmitral flow (TMF) and pulmonary venous flow.[5] Late gadolinium enhancement (LGE) is widely used for detecting focal replacement fibrosis/scarring.[6] However, LGE may be limited in diffuse interstitial processes, making parametric mapping techniques increasingly important. Native T1 mapping and post-contrast extracellular volume (ECV) quantification enable detection and quantification of diffuse myocardial fibrosis, whereas T2 mapping can provide complementary information related to edema/inflammation.[7] In addition, T2* mapping is an established quantitative approach for assessing myocardial iron deposition in transfusion-related iron overload and other iron storage conditions.[8] For the liver, magnetic resonance imaging (MRI) relaxometry-based approaches (including R2/R2* and T2*) are increasingly used for non-invasive quantification of liver iron concentration and longitudinal follow-up, enabling assessment of transfusional iron burden alongside fibrotic remodeling.[9] Moreover, liver T1 mapping and ECV measurements have been explored as non-invasive markers of hepatic fibrosis and have been shown to correlate with fibrosis severity in chronic liver disease.[10]

The primary aim of this study was to evaluate myocardial fibrosis in patients with SCA using MRI-based T1 mapping and ECV measurements. DD, which may be related to fibrotic remodeling, was assessed using TMF analysis and left atrial (LA) volume index (LAVI) measurements. Hepatic tissue characterization was performed in parallel with myocardial assessment; T2* mapping was also performed to assess myocardial and hepatic iron deposition that could confound fibrosis-related metrics.

Main points

- Magnetic resonance imaging can contribute to the non-invasive assessment of fibrosis-related tissue remodeling through mapping techniques and provide insight into diastolic function using transmitral flow (TMF) analysis.
- In patients with sickle cell anemia (SCA), increased myocardial and hepatic native T1 and extracellular volume values may indicate the presence of fibrosis.
- Diastolic function evaluation using TMF curves and left atrial volume analysis revealed that findings suggestive of restrictive filling patterns were relatively common among patients with SCA, suggesting a potential association.

Methods

Study design and participants

In this prospective study, cardiac and hepatic MRI examinations were performed on 32 patients with SCA (19 women, 13 men; mean age: 37 years) and 12 healthy controls (4 women, 8 men; mean age: 31 years) between September 2022 and March 2023. This study was approved by the Mersin University Clinical Research Ethics Committee (approval date: June 22, 2022; decision number: 2022/430). Written informed consent was obtained from all participants prior to inclusion in the study. Exclusion criteria included valvular heart disease, implanted cardiac devices, myocardial infarction, contrast allergies, diabetes, hypertension, cardiotoxic drug use, renal failure, pregnancy, age under 18 years, or refusal to provide informed consent. Blood samples were collected to assess hematocrit levels for ECV measurements. The flow of participant recruitment and exclusion is shown in Figure 1.

Magnetic resonance imaging technique

The MRI protocol included myocardial T1, T2, and T2* mapping and hepatic T1 and T2* mapping, in both the patient group and the control group. Myocardial and hepatic ECV measurements were performed, and LAVI and TMF curves were obtained to assess diastolic function in both groups. All examinations were performed using a 1.5-Tesla (T) MRI scanner (MAGNETOM Aera, Siemens Healthineers, Erlangen, Germany).

Native T1 mapping images of the heart and liver were acquired before contrast administration using the MOLLI sequence [parameters for cardiac imaging: repetition time

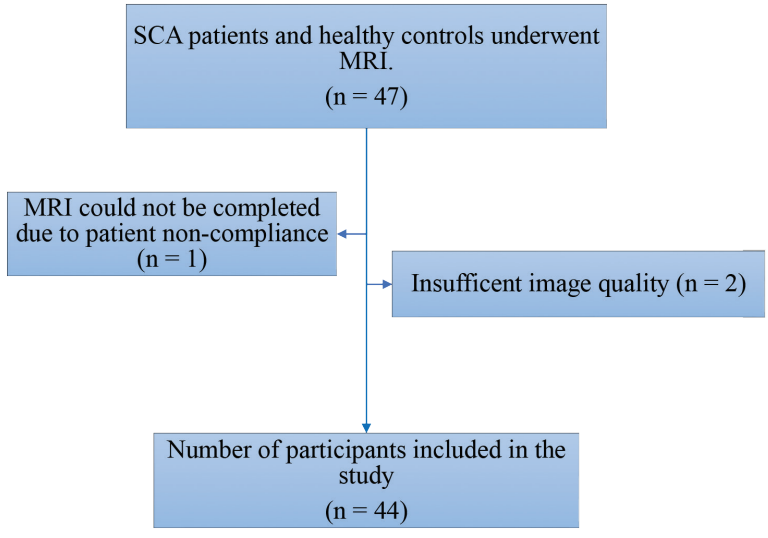


Figure 1. Flow diagram of the study. SCA, sickle cell anemia; MRI, magnetic resonance imaging.

(TR): 280.5 ms; time to echo (TE): 1.12 ms; flip angle: 35°; voxel size: 1.4 × 1.4 × 8.0 mm^3; for liver imaging: TR: 362.16 ms; TE: 1.12 ms; flip angle: 35°; voxel size: 1.4 × 1.4 × 8.0 mm^3]. After acquiring the native T1 maps, a contrast agent was administered intravenously at a dose of approximately 0.10 mmol/kg (gadobutrol, Gadovist®, Bayer AG, Berlin, Germany). Contrast-enhanced T1 mapping images were obtained 10–15 minutes later.

To evaluate hepatic and cardiac iron deposition, T2* maps were obtained before contrast administration using a multi-echo gradient-echo sequence with eight echo times (TE: 1.2, 3, 5, 7, 9, 11, 13, and 15 ms). TMF assessment was performed using PC-MRI. The imaging plane was planned on four-chamber cine images and was prescribed to be parallel to the mitral annulus at the level of the mitral valve leaflet tips at end-diastole. The resulting PC acquisition corresponds anatomically to a short-axis orientation at the level of the mitral valve. A through-plane velocity encoding value of 150 cm/s was used, and it was adjusted as needed to avoid velocity aliasing.

Magnetic resonance imaging analysis

Image analysis was conducted with the vendor-provided syngo.via post-processing software.

Myocardial native T1 times were calculated on pre-contrast T1 mapping images by drawing regions of interest (ROIs) on the left ventricular myocardium at the mid-ventricular level. A global myocardial approach was used, with ROIs encompassing most of the left ventricular wall while excluding the blood pool, papillary muscles, and trabeculations to minimize partial-volume effects.

Hepatic native T1 times were measured on pre-contrast T1 mapping images by placing a single, conservatively sized, circular-to-oval ROI in a homogeneous area of the right hepatic lobe. Measurements were performed once per patient using a representative slice. The ROI was positioned at least 1 cm away from the liver capsule, and areas affected by vascular structures, bile ducts, focal lesions, or susceptibility-related artifacts were visually identified and excluded to minimize partial-volume effects, using the same ROI template across patients. Considering the T1-shortening effect of iron deposition,[11,12] hepatic T1 values were calculated and analyzed both in the entire patient cohort and separately in patients without hepatic iron overload.

Myocardial and hepatic ECV values were calculated using post-contrast T1 values obtained by drawing corresponding ROIs on post-contrast T1 mapping images for both the myocardium and liver. Blood-pool T1 values were acquired from the left ventricular cavity and abdominal aorta on both pre- and post-contrast images (Figure 2). On the same day, the patient's blood hematocrit level was measured, and ECV values were calculated using the following formula:

$$ECV = (1\text{-}hematocrit) \times \left(\frac{1/T1(myo/liver\ postcontrast) - 1/T1(myo/liver\ precontrast)}{1/T1(blood\ postcontrast) - 1/T1(blood\ precontrast)}\right).$$

Myocardial T2* measurement was performed by manually drawing an ROI in the interventricular septum at the mid-ventricular level (Figure 3). A conservative, oval-to-circular ROI of standardized size was used to minimize partial-volume effects. The ROI was

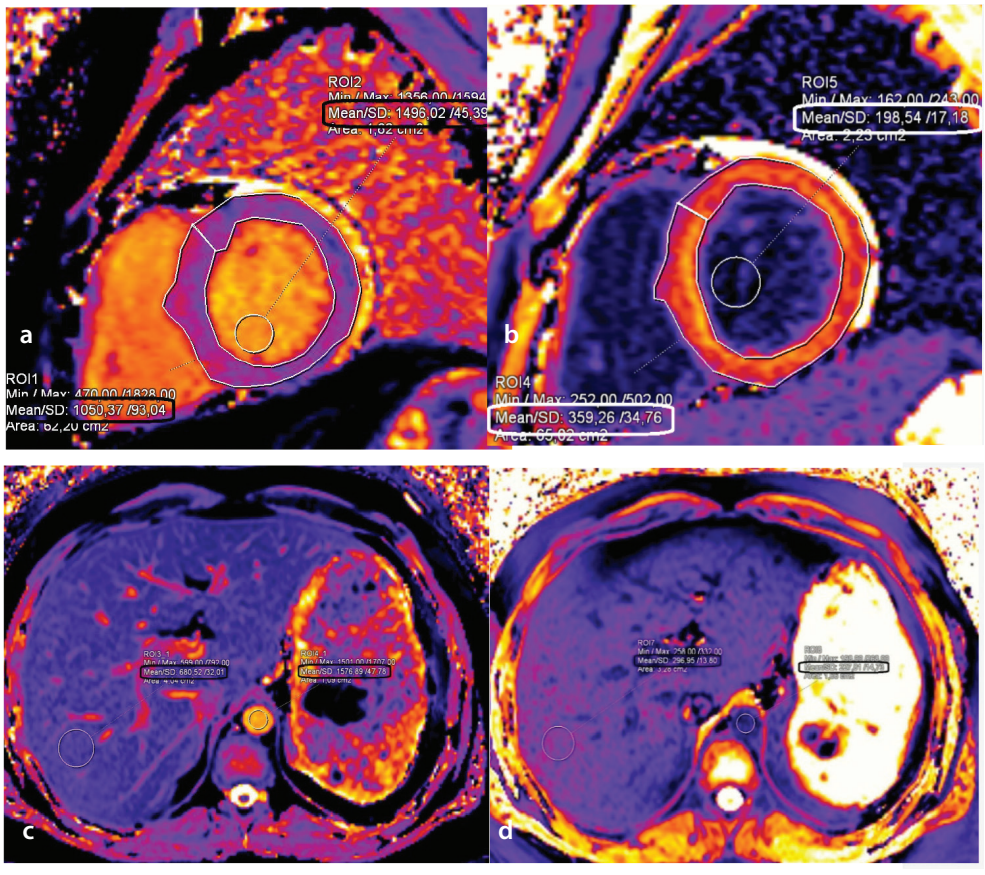


Figure 2. Measurement of native and post-contrast T1 values in myocardial and hepatic tissue for ECV assessment in a 25-year-old woman with SCA. (**a, b**) T1 relaxation times were measured from the myocardium and blood pool on **(a)** native and **(b)** post-contrast T1 map images obtained from short-axis views at the midventricular level. (**c, d**) T1 relaxation times were measured from the liver parenchyma and blood pool in the abdominal aorta on **(c)** native and **(d)** post-contrast T1 map images. ECV, extracellular volume; SCA, sickle cell anemia; SD, standard deviation; ROI, region of interest.

positioned to exclude the blood pool, endocardial border, trabeculations, and papillary muscles. In a 1.5-T magnetic field, myocardial T2* values are considered normal if they are greater than 20 ms.[8,13,14]

Hepatic T2* times were measured on hepatic T2* mapping images by placing a single, conservatively sized, circular-to-oval ROI in a homogeneous area of the right hepatic lobe on a representative slice, at least 1 cm from the liver capsule; regions containing large vessels or bile ducts, focal lesions, or susceptibility-related artifacts were visually excluded to minimize partial-volume effects (Figure 3). Based on hepatic T2* imaging values, hepatic iron overload is classified into four categories: normal (T2* > 6.3 ms), mild (T2*: 2.8–6.3 ms), moderate (T2*: 1.4–2.8 ms), and severe (T2* < 1.4 ms).[15,16]

Myocardial T2 times were calculated on T2 mapping images by drawing conservatively sized ROIs on the left ventricular myocardium at the mid-ventricular level. A global myocardial approach was used, with ROIs encompassing most of the left ventricular wall while excluding the blood pool, papillary muscles, and trabeculations to minimize partial-volume effects. Areas affected by susceptibility-related artifacts were visually identified and avoided during ROI placement.

TMF velocity–time curves were generated by placing an ROI at the center of the mitral valve orifice on phase images (Figure 4). Early (E) and late (A) diastolic filling waves were derived from these velocity–time curves. The E wave was defined as the peak early diastolic TMF velocity, and the A wave as the peak velocity during atrial contraction.

LA volumes were measured using the biplane area–length method. At the end of systole, the LA area and anteroposterior length were traced in four-chamber (A1–L1) and two-chamber (A2–L2) views. LA volume was calculated using the formula $0.85 \times A1 \times A2 / L$, where L represents the shorter of the

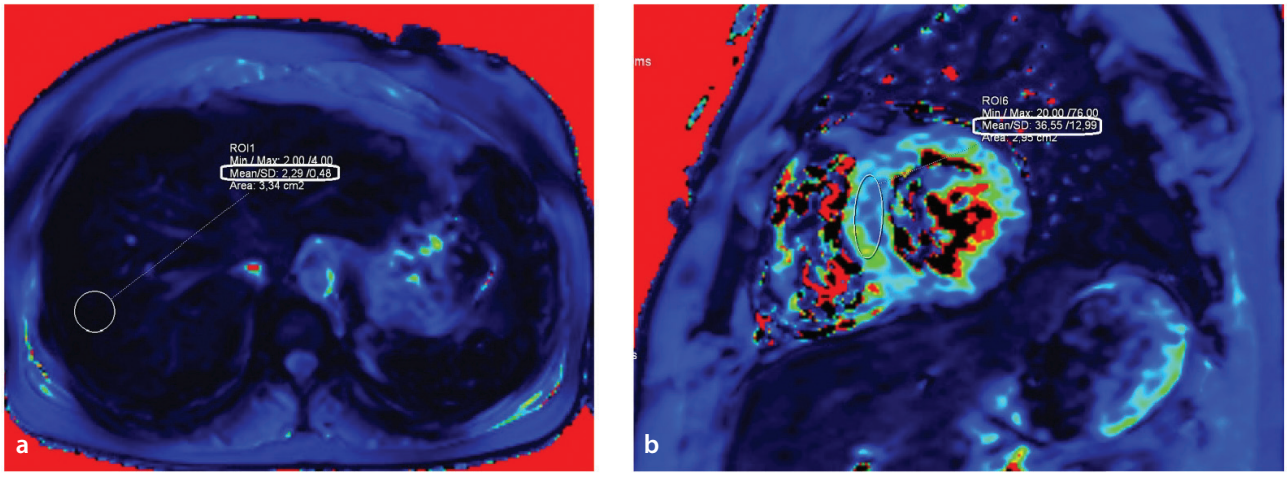


Figure 3. Measurement of hepatic and myocardial iron deposition in a 51-year-old man with SCA. **(a)** Hepatic T2* map image showing moderate iron deposition. **(b)** Cardiac T2* map image showing no iron deposition. SCA, sickle cell anemia; SD, standard deviation; ROI, region of interest.

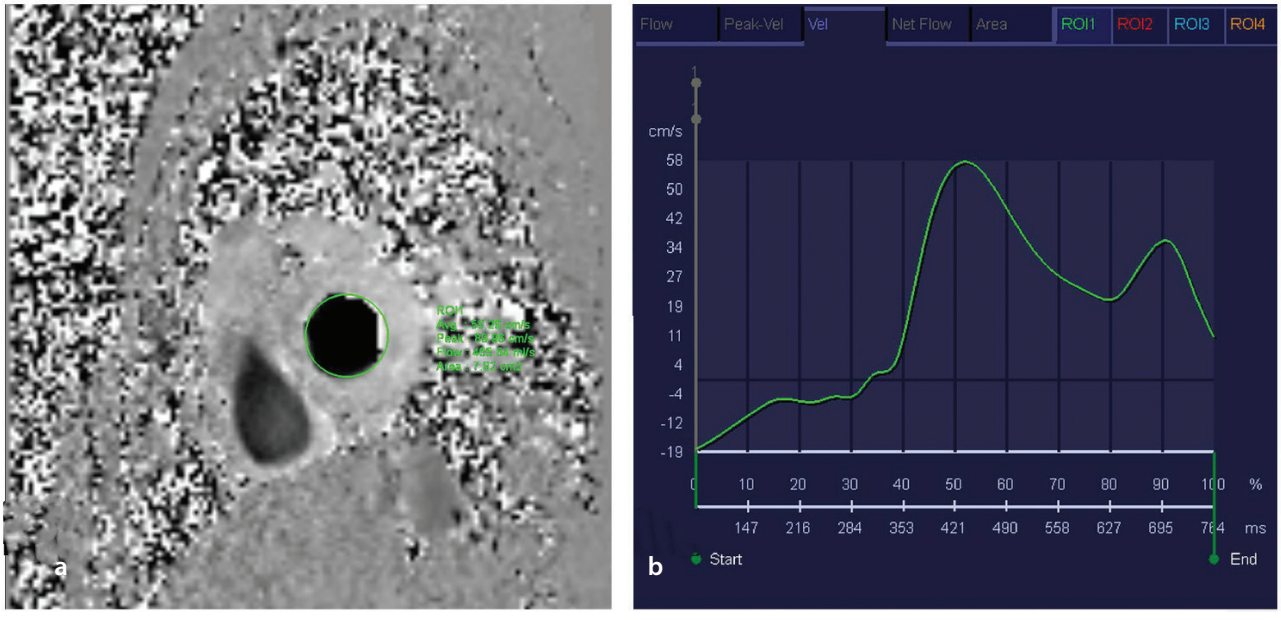


Figure 4. Obtaining the TMF curve in a healthy 30-year-old woman. Although the imaging plane was planned on the four-chamber cine view, the resulting through-plane PC-MRI acquisition corresponds anatomically to a short-axis orientation at the mitral valve level. **(a)** Through-plane PC-MRI phase image acquired with a VENC of 120 cm/s; a region of interest is placed within the mitral orifice to generate the TMF curve. **(b)** The resulting curve shows an E/A ratio of 1–2, consistent with normal filling. TMF, transmitral flow; PC-MRI, phase-contrast magnetic resonance imaging; VENC, velocity encoding.

two measured lengths (L1 or L2).[17] The LAVI was then calculated by indexing LA volume to body surface area and expressed as mL/m^2. Patients with an E/A ratio < 1 with normal or mildly increased LAVI were classified as having findings suggestive of an impaired relaxation filling pattern. Patients with an E/A ratio of 1–2 and increased LAVI were classified as having findings suggestive of a pseudonormal filling pattern. Patients with an E/A ratio > 2 with markedly increased LAVI were classified as having findings suggestive of a restrictive filling pattern (Figure 5).

Statistical analysis

Interobserver agreement was assessed using the intraclass correlation coefficient (ICC). Descriptive statistics for categorical variables were presented as frequencies and percentages, whereas continuous variables were expressed as mean ± standard deviation. The relationship between categorical variables was evaluated using the chi-square test. Variance equality between the patient and control groups was assessed using Levene's test, and, based on the results, the appropriate t-test (Student's or Welch's) was used to examine differences in mean measurements. In addition, one-sample t-tests were performed to compare the mean myocardial and hepatic ECV values of our patient cohort with previously published reference values. Pearson's correlation coefficient was used to assess the linear relationship between measurements. Statistical significance was defined as $P < 0.05$.

Results

Demographic and clinical characteristics

A total of 32 patients with SCA and 12 healthy individuals were included in the study. Demographic characteristics of the participants are presented in Table 1. There was no significant difference in mean age between the patient and control groups ($P = 0.083$). No participants in either group had a history of hypertension, diabetes mellitus, valvular heart disease, or known coronary artery disease. Among the patients, 27 were receiving hydroxyurea therapy, whereas 5 were not. Transfusion exposure was heterogeneous: 8 patients had no transfusion history. Of the 24 patients with a transfusion history, 13 received transfusions in the last year (range, 4–12 per year), whereas the remaining 11 had only sporadic transfusions in the past (typically 1–3 episodes) without a regular transfusion schedule. Among patients with a transfusion history, the interval between the most recent transfusion and MRI was at least 4 months in all cases. All MRI examinations were scheduled as outpatient scans and were performed during the steady-state period; none of the patients were imaged during an acute vaso-occlusive crisis.

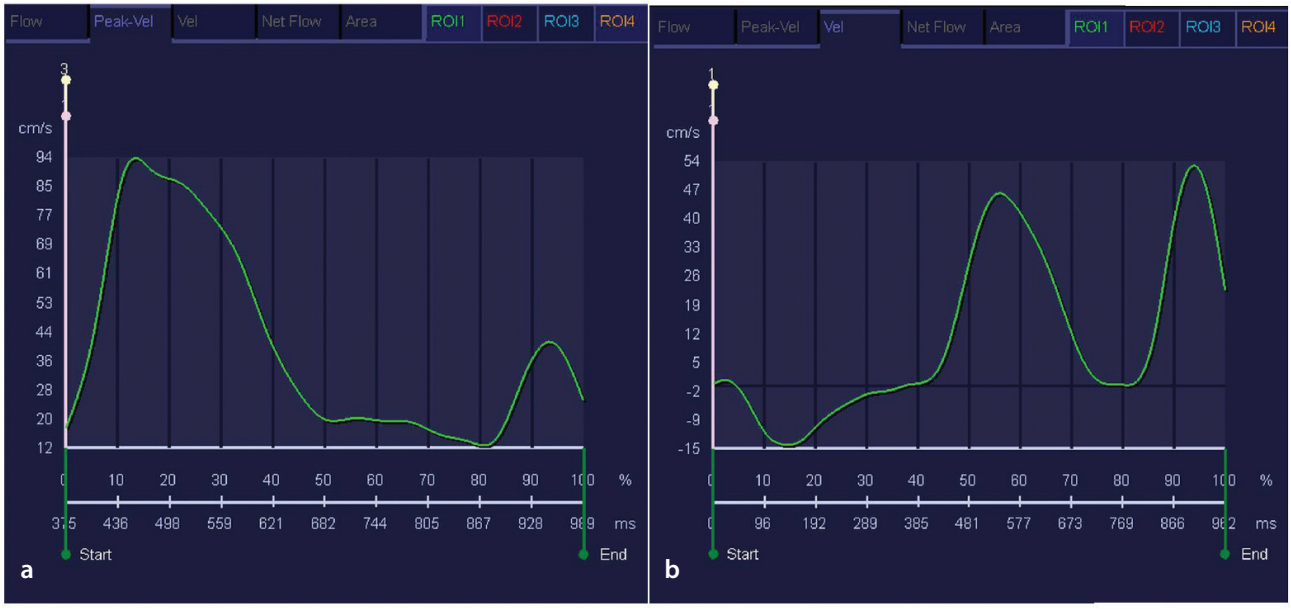


Figure 5. Transmitral flow curves showing impaired relaxation and restrictive filling patterns. **(a)** Transmitral flow pattern consistent with a restrictive filling pattern, showing an E/A ratio > 2 (E: 94, A: 39, E/A: 2.41) in a 27-year-old woman with SCA. **(b)** Transmitral flow pattern consistent with an impaired relaxation pattern, showing an E/A ratio < 1 (E: 47, A: 54, E/A: 0.8) in a 51-year-old man with SCA. SCA, sickle cell anemia; ROI, region of interest.

Table 1. Demographic characteristics of study participants

Characteristic	Control (n = 12)	Patients (n = 32)	*P* value
Age (years)	31.4 ± 6.8	37.5 ± 11.09	0.083
Male sex, n (%)	8 (66.7)	13 (40.6)	0.124
Hydroxyurea therapy, n (%)	NA	27 (84.4)	–
Transfusion (ever), n (%)	NA	24 (75)	–
Transfusions in the last year	NA	13 (40.6)	–
Hemoglobin (g/dL)	–	8.0 ± 1.3	–
Hematocrit (%)	–	24.8 ± 4.0	–

Values are presented as mean ± standard deviation. n, number; NA, not applicable.

Cardiac magnetic resonance imaging parameters

Cardiac MRI parameters are summarized in Table 2. Myocardial native T1 was significantly higher in patients with SCA than in controls (1,030.9 ± 28.4 ms in the SCA group vs. 1,000.3 ± 23.8 ms in controls; $P = 0.002$). In contrast, myocardial T2 values did not differ significantly between groups. Myocardial T2* values remained within the normal range in the SCA group, and no patient demonstrated myocardial iron accumulation. Cine-derived left ventricular end-diastolic volume index (LVEDVi), left ventricular end-systolic volume index (LVESVi), and left ventricular mass index were significantly higher in patients with SCA than in controls (all $P < 0.001$); LAVI was significantly higher in the SCA group than in controls (46.48 ± 15.35 vs. 30.58 ± 5.0 mL/m^2; $P < 0.001$); EF did not differ significantly between the two groups.

Myocardial extracellular volume findings

Myocardial ECV measurements are presented in Table 3. The mean myocardial ECV in the SCA group was 31.7%, which was higher than previously reported reference ranges.[18]

Within the SCA cohort, myocardial ECV was significantly higher in patients with findings suggestive of a restrictive filling pattern (n = 10) than in the remaining patients (n = 22) (34.14 ± 2.39% vs. 30.62 ± 2.67%; $P = 0.001$) (Table 4).

Distribution of diastolic dysfunction

DD was evaluated based on TMF-derived E/A ratios, assessed in conjunction with LAVI. In the SCA group, findings suggestive of DD were identified in 15 of 32 patients (46.9%), whereas none were observed in the control group (Table 2). The findings showed that 10 patients (31%) exhibited findings suggestive of a restrictive filling pattern, 2 (6%) showed findings suggestive of an impaired relaxation filling pattern, and 3 (9%) exhibited findings suggestive of a pseudonormal filling pattern; 17 patients (53%) had no findings suggestive of DD. The distribution of DD is shown in Figure 6. In a subgroup analysis, patients with TMF-derived E/A > 2 (n = 10) had significantly higher LAVI than the remaining patients (n = 22) (54.05 ± 10.12 vs. 43.0 ± 16.26 mL/m^2; $P = 0.027$) (Table 4).

Hepatic magnetic resonance imaging findings

Hepatic MRI parameters are summarized in Table 2. Hepatic iron accumulation was detected in 16 of 32 patients, and the mean hepatic T2* value was significantly lower in the SCA group than in controls ($P = 0.006$). Although the mean hepatic native T1 value was higher in the SCA group, the difference was not significant. In the SCA subgroup without hepatic iron deposition, the mean hepatic T1 value was significantly higher than in controls ($P < 0.001$).

The mean hepatic ECV was 46.1% in the entire SCA group and 40.4% in the subgroup without hepatic iron deposition, both higher than previously reported reference ranges.[19,20] Hepatic ECV measurements are presented in Table 3.

Interobserver agreement

Myocardial T1 relaxation times and ECV values were independently measured by two radiologists with 5 and 15 years of experience, respectively, whereas other parameters were assessed together. There was a high interobserver agreement for native T1 [ICC: 0.85, 95% confidence interval (CI): 0.80, 0.93] and ECV [ICC: 0.96 (95% CI: 0.93, 0.98)].

Table 2. Magnetic resonance imaging characteristics of study participants

Characteristic	Control (n = 12)	Patients (n = 32)	*P* value
Cardiac function parameters			
EF (%)	60 ± 4.1	60.7 ± 4.6	0.233
LAVI (mL/m^2)	30.58 ± 5	**46.48 ± 15.35**	**< 0.001**
LVEDVi (mL/m^2)	75.67 ± 12.95	**101.95 ± 16.75**	**< 0.001**
LVESVi (mL/m^2)	30.09 ± 6.50	**40.28 ± 9.28**	**< 0.001**
Left ventricular mass index (g/m^2)	54.49 ± 6.27	**76.95 ± 13.23**	**< 0.001**
Myocardial parameters			
Myocardial T1 (ms)	1,000.33 ± 23.76	**1,030.91 ± 28.40**	**0.002**
Myocardial T2 (ms)	47.92 ± 3.67	47.94 ± 3.16	0.985
Myocardial T2* (ms)	36.41 ± 5.24	39.25 ± 5.92	0.151
Hepatic parameters			
Hepatic T1 (ms)	537.83 ± 29.07	564.03 ± 108.88	0.402
Hepatic T1† (ms)	537.83 ± 29.07	**626.56 ± 61.45**	**< 0.001**
Hepatic T2* (ms)	19.15 ± 4.26	**12.20 ± 7.77**	**0.006**
Diastolic dysfunction			
DD present	0 (0%)	**15 (46.9%)**	–
DD absent	12 (100%)	**17 (53.1%)**	–

†: SCA subgroup without hepatic iron deposition (n = 16). Values are presented as mean ± standard deviation or n (%). Statistically significant measurements are shown in bold. EF, ejection fraction; LAVI, left atrial volume index; LVEDVi, left ventricular end-diastolic volume index; LVESVi, left ventricular end-systolic volume index; n, number; DD, diastolic dysfunction.

Table 3. Comparison of ECV values in the patient group and those in the literature

	Group	n	Mean	Standard deviation	*P* value
Myocardial ECV	Patient	32	**31.7%**	3.1	**< 0.001**
	Control*	81	25.3%	3.5	
Hepatic ECV†	Patient	16	**40.4%**	7.2	**< 0.001**
	Control**	22	25.9%	4.5	

*The control group in reference 18; **The control group in reference 19. †: SCA subgroup without hepatic iron deposition (n = 16). The *P* values were calculated using one-sample t-tests comparing the patient group's mean ECV values with published reference means. Statistically significant measurements are shown in bold. ECV, extracellular volume; n, number.

Table 4. Comparative evaluation of myocardial ECV and LAVI in patients with SCA with findings suggestive of a restrictive filling pattern versus the remaining SCA cohort

Parameter	Restrictive filling pattern group (n = 10)	Remaining SCA cohort (n = 22)	*P* value
Myocardial ECV (%)	34.14 ± 2.39	30.62 ± 2.67	0.001
LAVI (mL/m^2)	54.05 ± 10.12	43.03 ± 16.26	0.027

Values are presented as mean ± standard deviation. ECV, extracellular volume; LAVI, left atrial volume index; SCA, sickle cell anemia; n, number.

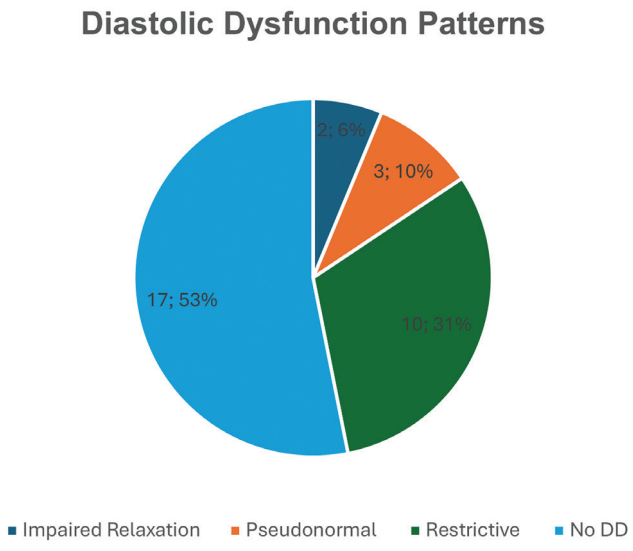


Figure 6. Distribution of diastolic filling patterns in the patient group (n = 32) based on TMF-derived E/A ratio in conjunction with LAVI. Values are shown as n (%). TMF, transmitral flow; LAVI, left atrial volume index; DD, diastolic dysfunction.

Discussion

The present study was designed to evaluate myocardial fibrosis in patients with SCA using advanced MRI tissue mapping techniques and ECV quantification, and to assess associated DD through TMF analysis and LA volume measurements. Hepatic fibrosis-related MRI metrics were also evaluated. The principal findings of this study demonstrated that patients with SCA exhibited significantly increased myocardial native T1 and ECV values, suggesting expansion of the myocardial extracellular space, largely consistent with diffuse interstitial fibrosis in this cohort, in the absence of myocardial iron overload as indicated by normal myocardial T2* values. Importantly, diastolic function assessment revealed a high prevalence of findings suggestive of advanced DD, including restrictive filling patterns, in relatively young patients. Notably, myocardial ECV was significantly higher in patients with findings suggestive of a restrictive filling pattern than in the remaining SCA cohort, supporting an association between diffuse myocardial fibrosis and advanced diastolic filling abnormalities in SCA. In a secondary, exploratory analysis, hepatic tissue characterization demonstrated elevated native T1 and ECV values, particularly in patients without hepatic iron deposition, supporting fibrosis-related tissue remodeling beyond iron-related effects.

The increase in native T1 values, reflecting tissue differences, particularly in conditions involving fibrosis and edema, along with the increase in ECV values, which correlate strongly with tissue collagen content, suggests myocardial fibrosis in patients with SCA. Cardiomyopathy, the leading cause of mortality in SCA, is associated with cardiac chamber enlargement, perfusion abnormalities, myocardial fibrosis, DD, and, occasionally, iron deposition.[21] In a study by Bakeer et al.[22] using cardiac imaging–histopathology correlation in mice with SCA, it was determined that, in addition to anemia-induced hyperdynamic physiology, a restrictive condition was also present, which was associated with myocardial fibrosis. In another study, Alsaied et al.[23] identified the relationship between LA dysfunction and myocardial fibrosis in patients with SCA. Furthermore, Niss et al.[24] found that sickle cell-related cardiomyopathy was associated with hyperdynamic processes and DD, with DD being linked to myocardial fibrosis. In that study, significantly elevated T1 relaxation times and ECV values were observed in the patient group, consistent with our results. When acquisition and post-processing are standardized, ECV measurements show good reproducibility; moreover, the dependence of ECV on field strength and sequence choice appears lower than for native T1.[7,25] Moreover, there is a strong correlation between ECV and histopathologically measured collagen levels in fibrosis.[26] This makes ECV a useful tool for identifying myocardial fibrosis and a promising, non-invasive alternative to labor-intensive procedures. However, ECV reflects expansion of the myocardial extracellular space and is not entirely specific for fibrosis; it may also be elevated in the presence of myocardial edema/inflammation or infiltrative cardiomyopathies. In our cohort, infiltrative disease was considered unlikely given the young age and clinical context, and myocardial T2 values were not increased compared with

controls, arguing against clinically relevant myocardial edema at the time of imaging. Taken together, elevated native T1/ECV in the presence of normal T2 supports diffuse interstitial fibrosis as the likely predominant explanation, although subtle edema cannot be completely excluded.

Studies have shown a significant link between collagen content, ventricular relaxation, and diastolic function. In experimental models, reducing myocardial collagen with bacterial collagenase[27] or plasmin[28] increased sarcomere length and ventricular volume, whereas fibrotic conditions with higher collagen levels impaired elasticity and diastolic function. These findings suggest that myocardial fibrosis, characterized by increased collagen content, could be biochemically linked to DD in patients with SCA. Both Niss et al.[24] and Alsaied et al.[23] evaluated cardiac functions using transthoracic echocardiography (TTE). Alsaied et al.[23] identified an association between myocardial fibrosis and LA dysfunction. Similarly, Niss et al.[24] proposed a connection between myocardial fibrosis and DD. In our study, we assessed diastolic function using TMF indices derived from PC-CMR. Comparative studies have shown that these PC-CMR–derived indices correlate well with Doppler TTE, with good agreement particularly for the E/A ratio and deceleration time when standardized acquisition and analysis are applied.[29-31] Nevertheless, invasive hemodynamic assessment (e.g., right heart catheterization with pulmonary capillary wedge pressure) remains the reference standard for confirming elevated filling pressures;[32] therefore, PC-CMR–derived diastolic indices warrant further validation against invasive metrics in larger cohorts.

A substantial prevalence of findings suggestive of a restrictive filling pattern was observed in relatively young patients with SCA, representing another key finding of this study. To the best of our knowledge, this is the first study to evaluate diastolic function in patients with SCA using MRI based on LA volume measurements and TMF curves. Among the 32 patients, 15 had findings suggestive of DD: 2 with findings suggestive of impaired relaxation filling pattern (E/A ratio < 1, aged 51 and 53 years), 3 with findings suggestive of pseudonormal filling pattern (E/A ratio 1–2, significantly increased LAVI, aged 60, 51, and 51 years), and 10 with findings suggestive of a restrictive filling pattern (E/A ratio > 2, mean age: 33.3 years). This raises the possibility that aging may also play a role in the etiology of impaired relaxation and pseudonormal filling patterns, suggesting that age-related changes may influence these measurements. Indeed, the DD that emerged in these 5 patients with SCA, who had no comorbidities such as diabetes or hypertension and no known history of cardiac disease, may be related to myocardial fibrosis associated with SCA. However, it would not be accurate to ignore age-related changes. A particularly striking finding was that 10 relatively young patients (mean age: 33.3 years), all without comorbidities other than SCA, showed TMF and LAVI findings suggestive of a restrictive filling pattern. In these patients, the E/A ratio was >2, along with a markedly increased LAVI (54.05 ± 10.12 mL/m^2), and all had elevated ECV values (minimum 28.7%, maximum 36.8%). The underlying pathology in a restrictive filling pattern is myocardial stiffening and decreased elasticity. We believe that the diffuse myocardial fibrosis observed in SCA is associated with this pathology. Consistent with this interpretation, myocardial ECV was significantly higher in patients with findings suggestive of a restrictive filling pattern than in the remaining SCA cohort ($P = 0.001$) (Table 4), suggesting an association between diffuse interstitial fibrosis and advanced DD patterns. Due to the cross-sectional design, temporal or causal relationships between fibrosis-related MRI findings and diastolic abnormalities cannot be established; therefore, these observations should be interpreted as hypothesis-generating. From a methodological perspective, our diastolic evaluation relied on PC-CMR–derived TMF (E/A) and LAVI and did not incorporate additional diastolic parameters, such as tissue Doppler e' and E/e', pulmonary venous flow, tricuspid regurgitation velocity, or invasive filling pressures. In SCA, chronic anemia and a high-output state may influence TMF and contribute to a restrictive-like pattern; therefore, this pattern should be interpreted in the clinical context and not equated with a clinical diagnosis of heart failure with preserved EF or restrictive cardiomyopathy. Consistent with a chronic volume-loaded, high-output physiology, LVEDVi, LVESVi, and left ventricular mass index were higher in patients with SCA ($P < 0.001$), supporting volume load-related structural remodeling, whereas EF remained similar between groups, indicating preserved systolic function.

Using T2* mapping, we observed no cardiac iron accumulation in patients with SCA, consistent with the literature. Previous studies have likewise shown that cardiac iron is uncommon in SCA despite frequent hepatic iron overload. For example, Junqueira et al.[33] reported hepatic iron accumulation in 26/30 patients with only one case of cardiac iron, and Inati et al.[34] found no cardiac iron in 20 patients with SCA. In line with prior reports, hepatic iron accumulation was present in a substantial proportion of our cohort. Hepatic fibrosis may develop due to both iron accumulation and the disease's pathophysiology. ECV measurements, which are valuable in evaluating myocardial fibrosis, may also be useful in assessing hepatic fibrosis. Mesropyan et al.[19] conducted a study involving 68 patients with cirrhosis and 22 healthy individuals, measuring hepatic ECV and finding that ECV was higher in the patients with cirrhosis than in the control group. Following this approach, we, to the best of our knowledge, measured hepatic parenchymal ECV values in patients with SCA for the first time. However, hepatic iron deposition can shorten native T1, thereby masking underlying fibrosis. Iron-corrected T1 (cT1) accounts for this effect by incorporating an iron-sensitive measure, such as T2* or R2*, thereby improving the interpretation of T1 in the presence of iron. Accordingly, cT1 may provide a more reliable assessment of fibro-inflammatory changes in iron-loaded livers than native T1 alone. Because cT1 was not available in our study due to software limitations, we analyzed hepatic T1/ECV measurements separately in patients with and without hepatic iron accumulation.

In patients without hepatic iron deposition, hepatic native T1 and ECV values were significantly higher than in controls, consistent with fibrotic remodeling related to recurrent vaso-occlusions and resultant ischemia in SCA, even in the absence of significant iron accumulation. Additionally, iron deposition clearly contributes to fibrosis at the biochemical level.[35] When including patients with hepatic iron accumulation in the analysis of the entire patient group, hepatic native T1 values were higher than those of the control group but did not reach statistical significance, likely because iron deposition lowers T1 values. Similarly, hepatic ECV values for the entire patient group were markedly higher than the ranges reported in the literature and the values observed in patients without iron accumulation. However, it remains unclear whether this increase is solely due to the contribution of iron deposition to fibrosis. This issue requires further investigation using a larger patient cohort and studies that employ cT1 values to provide clarity. Nonetheless, hepatic native T1/ECV are useful surrogates but are not specific for fibrosis. Liver MOLLI/shMOLLI T1 measurements can

be influenced by hepatic fat (via fat–water/off-resonance effects, which may cause an apparent T1 overestimation in steatosis) and by diffuse inflammatory/congestive changes, whereas iron has a more pronounced T1-shortening confounding effect.[36,37] Accordingly, although we addressed iron via subgroup analyses, residual confounding from unmeasured steatosis or other diffuse hepatic processes cannot be completely excluded. Future studies incorporating quantitative fat assessment [proton density fat fraction (PDFF)] may further reduce confounding and strengthen the interpretation of hepatic fibrosis-related MRI metrics.

Our study has several limitations. First, this was a relatively small observational study, which limits the generalizability of our findings. Additionally, this was a single-center, adult-predominant cohort with high hydroxyurea use and specific transfusion patterns; therefore, our findings may not be generalizable to pediatric populations with SCA, patients managed with different treatment strategies, or regions with differing disease severity. Subgroup analyses were small—particularly DD subgroups and hepatic ECV subgroups based on iron status—limiting the robustness of subgroup comparisons and increasing the risk of sampling variability in subgroup classification. Moreover, no formal correction for multiple comparisons was applied despite multiple subgroup analyses, t-tests against literature reference values, and correlation analyses; therefore, the findings should be interpreted with caution. Although we observed clear differences in key MRI metrics, conclusions regarding associations between tissue characterization findings and DD should be interpreted as hypothesis-generating. Second, although major comorbidities were absent by study design, we could not comprehensively account for potential confounders, including age-related effects, disease severity, and treatment exposure (e.g., transfusion history and hydroxyurea therapy). Although treatment histories were available, the sample size and study design did not allow a reliable assessment of their impact on diastolic indices or MRI-based tissue metrics; therefore, residual confounding cannot be ruled out. Additionally, detailed clinical data and comprehensive laboratory parameters—including liver function tests and cardiac biomarkers—were not available, which could have provided valuable correlations with imaging findings. Third, we could not administer contrast to controls for ethical reasons; as such, control ECV values were not available, and patient ECV measurements were compared with literature reference ranges. This comparison is subject to methodological variability across T1-mapping/ECV techniques and platforms, meaning our ECV findings should be interpreted cautiously. Published reference ranges were used primarily for context, and these comparisons should not be interpreted as definitive abnormality thresholds. Fourth, hepatic tissue characterization was limited by the inability to use cT1 due to a lack of appropriate software, and hepatic steatosis was not quantitatively assessed (e.g., by PDFF), which may affect the specificity of hepatic native T1/ECV for fibrosis. In addition, hepatic fibrosis was not confirmed by liver biopsy, meaning hepatic findings should be considered exploratory and are not equivalent to histologic fibrosis staging. Fifth, echocardiographic parameters (e.g., E/e' and echo-derived E/A) were not available for most participants, precluding a systematic echo–CMR correlation analysis. As such, the CMR-based DD classification should be interpreted as suggestive, and future studies using standardized echocardiography and/or invasive hemodynamic reference measurements would be valuable. Finally, the absence of findings suggestive of DD in the control group should be interpreted cautiously, given the small control sample size (n = 12) and the lack of universally established normal reference ranges and diagnostic thresholds for PC-CMR–derived diastolic indices such as the E/A ratio. Future studies with larger sample sizes, more balanced DD subgroups, multivariable adjustment for confounders, the use of cT1 values, and ethically feasible inclusion of control ECV measurements are needed to confirm and extend these findings.

In conclusion, in patients with SCA, myocardial T1 and ECV values were significantly higher, suggesting expansion of the myocardial extracellular space, largely consistent with diffuse interstitial fibrosis in the studied clinical context. Moreover, T2* mapping revealed no cardiac iron deposition, indicating that cardiac findings were unlikely to be related to myocardial iron accumulation. Furthermore, TMF curves and LA volume measurements revealed findings suggestive of a restrictive filling pattern in a considerable number of young patients without any comorbidities other than SCA, and myocardial ECV was significantly higher in these patients, supporting an association between diffuse interstitial fibrosis and advanced filling patterns. These data suggest that CMR, which allows non-invasive and comprehensive evaluation of myocardial tissue characteristics and cardiac function in patients with SCA, may have clinical value for early diagnosis and follow-up. In liver evaluations using T2* mapping, iron accumulation was detected in some patients, whereas in the group without iron deposition, significantly increased hepatic T1 and ECV values were observed. These secondary hepatic findings should be interpreted as exploratory and hypothesis-generating, and suggest that combined liver T2* and T1/ECV mapping may provide complementary information on iron burden and tissue remodeling in SCA, pending validation in larger studies. Further studies with dedicated liver endpoints are needed to clarify the clinical implications of these observations.

Footnotes

Conflict of interest disclosure

The authors declared no conflicts of interest.

Funding

This study was supported by the Scientific Research Projects Unit of Mersin University (Project No: 2022-2-TP3-4766).

References

1. Rees DC, Williams TN, Gladwin MT. Sickle-cell disease. *Lancet*. 2010;376(9757):2018-2031. [Crossref]
2. Fitzhugh CD, Lauder N, Jonassaint JC, et al. Cardiopulmonary complications leading to premature deaths in adult patients with sickle cell disease. *Am J Hematol*. 2010;85(1):36-40. [Crossref]
3. Sachdev V, Machado RF, Shizukuda Y, et al. Diastolic dysfunction is an independent risk factor for death in patients with sickle cell disease. *J Am Coll Cardiol*. 2007;49:472-479. [Crossref]
4. Manganas K, Delicou S, Xydaki A, et al. Predisposing factors for advanced liver fibrosis in patients with sickle cell disease. *Br J Haematol*. 2023;202(6):1192-1198. [Crossref]
5. American College of Cardiology Foundation Task Force on Expert Consensus Documents; Hundley WG, Bluemke DA, et al. ACCF/ACR/AHA/NASCI/SCMR 2010 expert consensus document on cardiovascular magnetic resonance: a report of the American College of Cardiology Foundation Task Force on Expert Consensus Documents. *J Am Coll Cardiol*. 2010;55(23):2614-2662. [Crossref]
6. Prasad SK, Akbari T, Bishop MJ, Halliday BP, Leyva-Leon F, Marchlinski F. Late gadolinium enhancement imaging and sudden cardiac death. *Eur Heart J*. 2025;46(36):3555-3568. [Crossref]

7. Messroghli DR, Moon JC, Ferreira VM, et al. Clinical recommendations for cardiovascular magnetic resonance mapping of T1, T2, T2* and extracellular volume: a consensus statement by the Society for Cardiovascular Magnetic Resonance (SCMR) endorsed by the European Association for Cardiovascular Imaging (EACVI). *J Cardiovasc Magn Reson*. 2017;19(1):75. Erratum in: *J Cardiovasc Magn Reson*. 2018;20(1):9. [Crossref]
8. Triadyaksa P, Oudkerk M, Sijens PE. Cardiac T2* mapping: techniques and clinical applications. *J Magn Reson Imaging*. 2020;52(5):1340-1351. [Crossref]
9. Tipirneni-Sajja A, Shrestha U, Esparza J, et al. State-of-the-art quantification of liver iron with MRI-vendor implementation and available tools. *J Magn Reson Imaging*. 2025;61(3):1110-1132. [Crossref]
10. Obmann VC, Ardoino M, Klaus J, et al. MRI extracellular volume fraction in liver fibrosis: a comparison of different time points and blood pool measurements. *J Magn Reson Imaging*. 2024;60(4):1678-1688. [Crossref]
11. Torlasco C, Cassinerio E, Roghi A, et al. Role of T1 mapping as a complementary tool to T2* for non-invasive cardiac iron overload assessment. *PLoS One*. 2018;13(2):e0192890. [Crossref]
12. Alam MH, Auger D, Smith GC, et al. T1 at 1.5T and 3T compared with conventional T2* at 1.5T for cardiac siderosis. *J Cardiovasc Magn Reson*. 2015;17:102. [Crossref]
13. Koohi F, Kazemi T, Miri-Moghaddam E. Cardiac complications and iron overload in beta thalassemia major patients-a systematic review and meta-analysis. *Ann Hematol*. 2019;98(6):1323-1331. [Crossref]
14. Kawel-Boehm N, Maceira A, Valsangiacomo-Buechel ER, et al. Normal values for cardiovascular magnetic resonance in adults and children. *J Cardiovasc Magn Reson*. 2015;17(1):29. [Crossref]
15. Labranche R, Gilbert G, Cerny M, et al. Liver iron quantification with MR imaging: a primer for Radiologists. *Radiographics*. 2018;38(2):392-412. [Crossref]
16. Khadivi Heris H, Nejati B, Rezazadeh K, et al. Evaluation of iron overload by cardiac and liver T2* in β-thalassemia: correlation with serum ferritin, heart function and liver enzymes. *J Cardiovasc Thorac Res*. 2021;13(1):54-60. [Crossref]
17. Caudron J, Fares J, Bauer F, Dacher JN. Evaluation of left ventricular diastolic function with cardiac MR imaging. *Radiographics*. 2011;31:239-259. [Crossref]
18. Sado DM, Flett AS, Banypersad SM, et al. Cardiovascular magnetic resonance measurement of myocardial extracellular volume in health and disease. *Heart*. 2012;98(19):1436-1441. [Crossref]
19. Mesropyan N, Kupczyk PA, Dold L, et al. Assessment of liver cirrhosis severity with extracellular volume fraction MRI. *Sci Rep*. 2022;12(1):9422. [Crossref]
20. Dolan RS, Stillman AE, Davarpanah AH. Feasibility of hepatic T1-mapping and extracellular volume quantification on routine cardiac magnetic resonance imaging in patients with infiltrative and systemic disorders. *Acad Radiol*. 2022;29(Suppl 4):S100-S109. [Crossref]
21. Desai AA, Patel AR, Ahmad H, et al. Mechanistic insights and characterization of sickle cell disease-associated cardiomyopathy. *Circ Cardiovasc Imaging*. 2014;7(3):430-437. [Crossref]
22. Bakeer N, James J, Roy S, et al. Sickle cell anemia mice develop a unique cardiomyopathy with restrictive physiology. *Proc Natl Acad Sci U S A*. 2016;113(35):E5182-E5191. [Crossref]
23. Alsaied T, Niss O, Tretter JT, et al. Left atrial dysfunction in sickle cell anemia is associated with diffuse myocardial fibrosis, increased right ventricular pressure and reduced exercise capacity. *Sci Rep*. 2020;10:1767. Erratum in: *Sci Rep*. 2020;10(1):4880. [Crossref]
24. Niss O, Fleck R, Makue F, et al. Association between diffuse myocardial fibrosis and diastolic dysfunction in sickle cell anemia. *Blood*. 2017;130(2):205-213. [Crossref]
25. Moon JC, Messroghli DR, Kellman P, et al. Myocardial T1 mapping and extracellular volume quantification: a Society for Cardiovascular Magnetic Resonance (SCMR) and CMR Working Group of the European Society of Cardiology consensus statement. *J Cardiovasc Magn Reson*. 2013;15:92. [Crossref]
26. Sibley CT, Noureldin RA, Gai N, et al. T1 mapping in cardiomyopathy at cardiac MR: comparison with endomyocardial biopsy. *Radiology*. 2012;265:724-732. [Crossref]
27. MacKenna DA, Omens JH, McCulloch AD, Covell JW. Contribution of collagen matrix to passive left ventricular mechanics in isolated rat hearts. *Am J Physiol*. 1994;266:H1007-H1018. [Crossref]
28. Stroud JD, Baicu CF, Barnes MA, Spinale FG, Zile MR. Viscoelastic properties of pressure overload hypertrophied myocardium: effect of serine protease treatment. *Am J Physiol Heart Circ Physiol*. 2002;282:H2324-H2335. [Crossref]
29. Rathi VK, Doyle M, Yamrozik J, et al. Routine evaluation of left ventricular diastolic function by cardiovascular magnetic resonance: a practical approach. *J Cardiovasc Magn Reson*. 2008;10(1):36. [Crossref]
30. Bollache E, Redheuil A, Defrance C, et al. The clinical value of phase-contrast CMR mitral inflow diastolic parameters: comparison with echocardiography. *J Cardiovasc Magn Reson*. 2011;13(Suppl 1):P32. [Crossref]
31. Fujikura K, Sathya B, Acharya T, et al. CMR provides comparable measurements of diastolic function as echocardiography. *Sci Rep*. 2024;14(1):11658. [Crossref]
32. Nagueh SF, Sanborn DY, Oh JK, et al. Recommendations for the evaluation of left ventricular diastolic function by echocardiography and for heart failure with preserved ejection fraction diagnosis: an update from the American Society of Echocardiography. *J Am Soc Echocardiogr*. 2025;38(7):537-569. [Crossref]
33. Junqueira FP, Fernandes JL, Cunha GM, et al. Right and left ventricular function and myocardial scarring in adult patients with sickle cell disease: a comprehensive magnetic resonance assessment of hepatic and myocardial iron overload. *J Cardiovasc Magn Reson*. 2013;15(1):83. [Crossref]
34. Inati A, Musallam KM, Wood JC, Sheikh-Taha M, Daou L, Taher AT. Absence of cardiac siderosis by MRI T2* despite transfusion burden, hepatic and serum iron overload in Lebanese patients with sickle cell disease. *Eur J Haematol*. 2009;83:565-571. [Crossref]
35. Mehta KJ, Farnaud SJ, Sharp PA. Iron and liver fibrosis: mechanistic and clinical aspects. *World J Gastroenterol*. 2019;25:521-538. [Crossref]
36. Mozes FE, Tunnicliffe EM, Moolla A, et al. Mapping tissue water T1 in the liver using the MOLLI T1 method in the presence of fat, iron and B0 inhomogeneity. *NMR Biomed*. 2019;32:e4030. [Crossref]
37. Thomaides-Brears HB, Lepe R, Banerjee R, Duncker C. Multiparametric MR mapping in clinical decision-making for diffuse liver disease. *Abdom Radiol (NY)*. 2020;45:3508-3522. [Crossref]

Diagn Interv Radiol 2025; DOI: 10.4274/dir.2025.253677

EMERGENCY RADIOLOGY

ORIGINAL ARTICLE

©Copyright 2026 Author(s) - Available online at dirjournal.org.
Content of this journal is licensed under a Creative Commons Attribution-NonCommercial 4.0 International License.

The relationship between hypostasis and gas detected in postmortem computed tomography and the postmortem interval

Vefa Çakmak[1]
Abdülkadir İzci[2]
Tuğçe Dönmez[1]
Zeynab Zülfügarlı[1]
Ayşe Kurtuluş Dereli[3]
Kemalettin Acar[3]

[1]Pamukkale University Faculty of Medicine, Department of Radiology, Denizli, Türkiye

[2]Afyonkarahisar Health Sciences University Faculty of Medicine, Department of Forensic Medicine, Afyonkarahisar, Türkiye

[3]Pamukkale University Faculty of Medicine, Department of Forensic Medicine, Denizli, Türkiye

PURPOSE

To evaluate the relationship between gas detected in solid organs, such as the aorta and heart, and hypostasis in the lung parenchyma on postmortem computed tomography (PMCT) in relation to the postmortem interval (PMI).

METHODS

Between January 2021 and January 2025, 74 individuals (60 men, 14 women; 18–84 years; mean age, 41.8 ± 17.6 years) who underwent autopsy due to various forensic causes were retrospectively evaluated using PMCT images obtained prior to autopsy. The presence of gas in the heart, liver, kidneys, and aorta on postmortem thoracic and abdominal CT images was graded as follows: grade 0, absent; grade 1, ≤ 25%; grade 2, > 25% but < 50%; and grade 3, ≥ 50%. These findings were compared with the PMI. In addition, the presence of hypostasis and clotting in the lungs on thoracic PMCT was compared with the PMI.

RESULTS

Intravascular gas was observed within the cardiac chambers in all but seven cases, and the amount of intracardiac gas increased in direct proportion to the PMI. The presence of clotting in the pulmonary arteries showed a statistically significant association with the PMI (P = 0.015). A strong positive correlation (r: 0.720) was identified between intravascular gas in the liver and that in the cardiac chambers. Furthermore, a statistically significant and strong positive correlation was found between pulmonary hypostasis and clotting in the pulmonary arteries (r: 0.892, P = 0.001). A strong correlation was also observed between pulmonary arterial clotting and the density differences between hypostatic and non-hypostatic regions of the lung parenchyma (r: 0.918).

CONCLUSION

On PMCT, decomposition-related gas can be detected in solid organs, particularly in the liver and heart, as early as within 48 hours postmortem, and its presence is associated with the PMI. A strong correlation exists between pulmonary arterial clotting or sedimentation and hypostasis in the lung parenchyma.

CLINICAL SIGNIFICANCE

PMCT can help determine the PMI, in addition to identifying forensic causes of death, and may contribute to routine forensic assessment.

KEYWORDS

Hypostasis, postmortem computed tomography, forensic imaging, autopsy, postmortem interval

Handling editor: Sonay Aydın

Corresponding author: Vefa Çakmak

E-mail: vefacakm1408@gmail.com

Received 30 September 2025; revision requested 21 October 2025; accepted 01 November 2025.

Epub: 24.11.2025

Publication date: 02.11.2026

DOI: 10.4274/dir.2025.253677

You may cite this article as: Çakmak V, İzci A, Dönmez T, Zülfügarlı Z, Kurtuluş Dereli A, Acar K. The relationship between hypostasis and gas detected in postmortem computed tomography and the postmortem interval. *Diagn Interv Radiol.* 2026;32(6):787-793.

Postmortem computed tomography (PMCT) is performed to identify abnormalities that may be overlooked during forensic autopsy and to complement autopsy findings.[1,2] In addition to typical postmortem changes, PMCT can provide ballistic information in firearm injuries, such as bullet localization, type, and trajectory, thereby contributing to the determination of the cause of death. Moreover, PMCT can demonstrate findings related to other forensic cases, such as assault, stab wounds, or penetrating injuries.[3] In countries with a large elderly population, postmortem thoracic CT is particularly useful for detecting lung and cardiovascular pathologies.

Evaluation of the lungs and pleural cavities with PMCT prior to autopsy facilitates the differentiation of certain structural and acquired cardiopulmonary conditions from traumatic pathologies such as contusion or laceration. Pulmonary congestion, which often develops due to cardiac events, appears on CT as ground-glass opacities with peribronchial thickening, whereas pulmonary contusions manifest as ground-glass opacities not conforming to specific segments or distributions. Hypostasis (dependent density), commonly observed in PMCT, may mimic or overlap with these findings. It is characterized by gravity-dependent ground-glass opacities in the lower regions of the lung parenchyma, resulting from higher water content than in other lobes.[4] The presence of hypostasis, a phenomenon that can also be observed in otherwise healthy individuals, varies according to the postmortem interval (PMI).[5]

Main points

- Postmortem computed tomography (PMCT) helps determine the forensic causes of death by providing ballistic information about bullet localization and the type and direction of bullets in firearm injuries, along with radiological findings of assaults, stabbings, and other penetrating injuries.
- In PMCT, the presence of gas in organs caused by putrefaction is moderately correlated with the postmortem interval. Gas is consistently observed in the heart within 0–7 hours after death and in the liver and aorta within 8–16 hours or more.
- In PMCT, hypostasis is demonstrated by the presence of clotting or sediment in the pulmonary arteries, with distribution dependent on the position of the corpse. After approximately 48–72 hours postmortem, pulmonary hypostasis regresses in parallel with the resolution of clotting or sediment in the pulmonary arteries.

During the postmortem period, it has been reported that decomposition-related gas begins to form within 24–48 hours after death, mainly produced by the intestinal flora. Environmental factors, such as body preservation status, ambient temperature, and humidity, also influence gas formation due to putrefaction.[6,7] Even small amounts of intraparenchymal or intravascular gas, which may be difficult to detect at autopsy, can be easily identified on PMCT. It is crucial, however, to distinguish decomposition-related gas from air embolism. Although the distribution of postmortem gas varies depending on the PMI, it is most frequently detected in the liver and heart. In forensic investigations, both the extent of intravascular and parenchymal gas on CT and the presence or absence of pulmonary hypostasis appear to be important indicators for estimating the PMI. Accordingly, we hypothesize that gas formation and pulmonary hypostasis observed on PMCT correlate positively with the PMI.

The aim of this study was to evaluate the relationship between gas and hypostasis detected in organs on PMCT and the PMI.

Methods

Ethical statement

This study was initiated after approval by the Pamukkale University Non-Invasive Clinical Research Ethics Committee (protocol number: E-60116787-020-556684, date: 07/23/2024).

Study group

Between January 2021 and January 2025, PMCT images [number of cases (n) = 84] obtained prior to autopsy from individuals with preserved cranial, thoracic, and abdominal organ integrity in the Radiology Archive of Pamukkale University Faculty of Medicine Hospital were retrospectively reviewed. Cases were excluded if organ integrity was compromised, the body was not found in a supine position, there was evidence of death due to burns or blast injuries, or if the CT images exhibited missing data or extensive artifacts.

For all cases, the PMI was calculated as the time elapsed between the reported time of death (documented by the police or judicial authorities) and the CT scan. The final study group consisted of 74 individuals (60 men, 14 women; age range 18–84 years; mean age, 41.8 ± 17.6 years) who underwent forensic autopsy. The CT images included in the study were selected to ensure artifact-free quality, a supine body position, preserved organ integrity, and appropriate postmortem preservation conditions (Figure 1).

PMCT images were independently evaluated by two radiologists for interobserver assessment.

Computed tomography

CT examinations were performed using a 64-detector array multislice CT scanner (LightSpeed VCT 64; GE Healthcare, Milwaukee, WI, USA). The imaging parameters for the brain and neck CT were as follows: tube voltage, 100 kV; tube current, 150–320 mAs; slice thickness, 2.5 mm; collimation, 64 × 0.625 mm; matrix, 512 × 512; rotation time, 0.5 seconds; and field of view (FOV), 250 mm. The imaging parameters for the thorax and abdomen CT were as follows: tube voltage, 140 kV; tube current, 150–320 mAs; slice thickness, 1.25 mm; collimation, 64 × 0.625 mm; matrix,

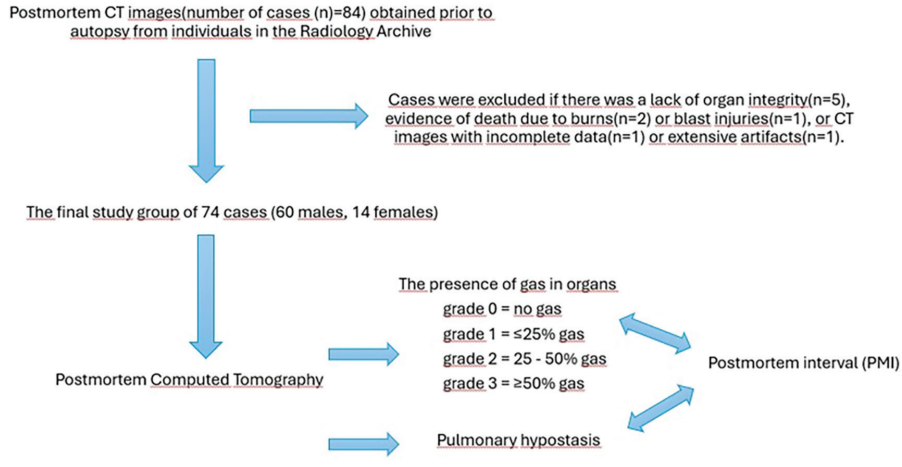


Figure 1. Flowchart of the relationship between hypostasis and gas detected in postmortem computed tomography and the postmortem interval. CT, computed tomography.

512 × 512; rotation time, 0.5 seconds; and FOV, 500 mm. All PMCT images were evaluated at the workstation in axial, sagittal, and coronal planes.

Image analysis

On postmortem brain CT, the presence of gas in intracranial vascular structures was assessed (Figure 2). On thoracic and abdominal PMCT, the presence of gas in the heart, liver, kidneys, and aorta was graded as follows: grade 0, no gas; grade 1, ≤ 25% gas; grade 2, > 25% but < 50% gas; and grade 3, ≥ 50% gas. These findings were compared with the PMI (Figures 3 and 4). On thoracic CT, the presence or absence of pulmonary hypostasis was assessed in the lung window. Density measurements were obtained using a region of interest of 500–600 mm^2 from lung parenchyma with and without hypostasis (Figure 5). In the mediastinal window, the presence of clotting in the pulmonary trunk or lobar pulmonary arteries was evaluated (Figure 6). The density of clots was also measured, and findings of hypostasis and clotting were compared with the PMI.

Statistical analysis

Data analysis was performed using SPSS software (version 27.0 for Windows; IBM Corp., Armonk, NY, USA). Descriptive statistics were presented as mean ± standard deviation for continuous variables and as frequencies and percentages for categorical variables. Chi-squared and Fisher's exact tests were used for categorical variables. Pearson correlation analyses were conducted to assess the relationships between hypostasis, clotting in the pulmonary arteries, and intravascular gas in organs. Independent samples t-tests were used to compare continuous variables. A P value <0.05 was considered statistically significant. An inter-observer reliability analysis with the Kappa statistic was performed to determine consistency among radiologists. Inter-observer agreement was categorized as follows: 0–0.20, slight; 0.21–0.40, moderate; 0.41–0.60, fair; 0.61–0.80, substantial; and 0.81–1.00, almost perfect.

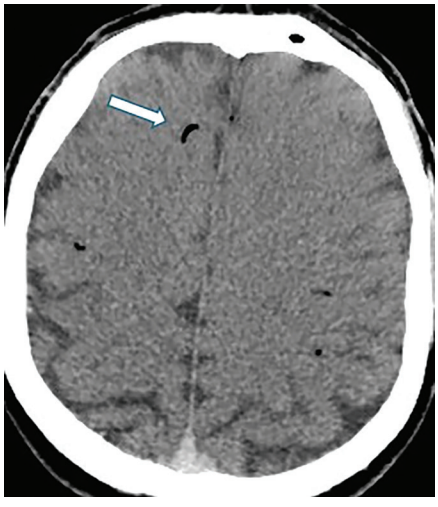


Figure 2. Intravascular gas (arrow) on non-contrast axial postmortem brain computed tomography.

Results

In the study group, 50 individuals (67.6%) died due to penetrating injuries caused by firearms or sharp objects, 14 (18.9%) due to blunt trauma or battery, 2 (2.7%) due to hanging or strangulation, and 8 (10.8%) from natural or medical causes. The PMIs of the cases in the study group were obtained through postmortem examination and autopsy findings, crime scene reports, and incident histories, and it was revealed that 35.1% died 0–7 hours prior to autopsy and 33.8% died 8–16 hours prior to autopsy.

Gas density was observed in the intracranial vascular structures in 66.2% of cases and in the cervical spinal canal in 44.6% of cases, with increasing frequency correlating with longer PMIs. Intravascular gas in the cardiac chambers was present in all cases except for seven individuals who died within 0–7 hours, and its frequency increased with time after death. The presence of clotting in the pulmonary arteries showed a statistically significant association with the PMI (P = 0.015). By contrast, there was no statistically significant relationship between the PMI and the presence of hypostasis in the lung parenchyma (P = 0.119) (Table 1).

A strong positive correlation (r: 0.720) was observed between intravascular gas in the liver and in the cardiac chambers. Furthermore, a moderate positive and statistically significant correlation was found between the PMI and the presence of intracranial intravascular gas, intravascular gas in the liver, gas in the cardiac chambers, and intravascular gas in the kidneys and aorta (Table 2).

Clots were identified in the pulmonary trunk and its branches in 35 cases. Clotting density ranged between 20 and 108 Hounsfield unit (HU). A statistically significant (P = 0.001) and strong positive correlation (r: 0.892) was found between pulmonary hypostasis and the presence of clots in the pulmonary arteries. The shared variance between these variables was calculated as 79.6%, indicating that approximately 79.6% of hypostasis could be explained by the presence of pulmonary arterial clotting (Table 3).

In density measurements, lung regions with hypostasis showed values ranging from -165 to -513 HU, whereas regions without hypostasis showed values ranging from -507 to -896 HU. A statistically significant and strong correlation was observed between pulmonary arterial clotting and the density differences between hypostatic and non-hypostatic lung parenchyma (r: 0.918) (Table 4). Interobserver reliability for detecting intraparenchymal and intravascular gas and pulmonary hypostasis on PMCT was found to be high (κ: 0.952–0.992).

Discussion

Determining the PMI is a critical component of criminal investigations.[7,8] In the present study, autopsy examinations together with law enforcement and judicial authority reports were used to establish the PMI. In our cohort, gas was observed in the heart in 73.1% and in the liver in 61.5% of corpses (n = 26) within 0–7 hours of death (r: 0.720). The amount of gas detected in the heart was greater than that in the liver. Previous studies have reported early intrahepatic and cardiac gas accumulation within the first postmortem hours;[9,10] our results support these findings, with higher levels of gas in the heart than in the liver. This might be explained by the greater elasticity of the right cardiac chambers than of the liver.

In this study, hepatic gas was detected in 81.1% of cases, except in those with very short PMIs. Jackowski et al.[11] reported hepatic gas in 59.5% of cases, whereas Takahashi et al.[12] reported a rate of 31.7%. Takahashi et al.[12] also found no correlation between intrahepatic gas and the PMI. By contrast, our results demonstrate a significant correlation between intravascular gas in the liver, heart, kidneys, and aorta with the PMI. Furthermore, cardiac gas was present in all corpses with a PMI of 0–7 hours, whereas hepatic and aortic gas were consistently detected in corpses with PMIs of 8–16 hours or longer. Ishida et al.[7] similarly reported that gas could be detected simultaneously in the liver, kidneys, spleen, and pancreas; in this study, gases in these organs also appeared approximately simultaneously.

Egger et al.[13] reported venous collapse in 61.9% and arterial collapse in 33.1% of the 118 PMCT images with PMIs of 3 hours to 12 days and also found a negative correlation between venous collapse and age. In this study, gas was absent in the aorta in 52.7% of cases; however, it was present in the aorta of all corpses with PMIs longer than 48 hours.

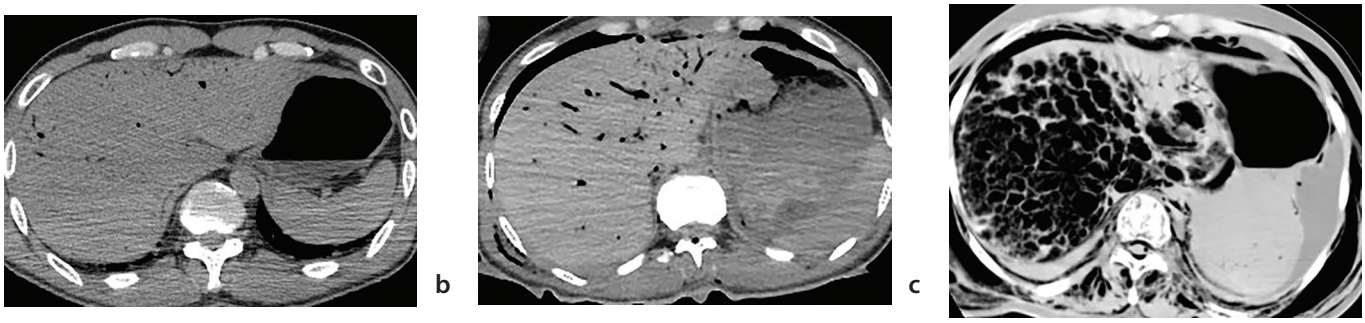


Figure 3. Intraparenchymal gas in the liver on non-contrast axial postmortem abdominal computed tomography, shown as **(a)** grade 1, **(b)** grade 2, and **(c)** grade 3.

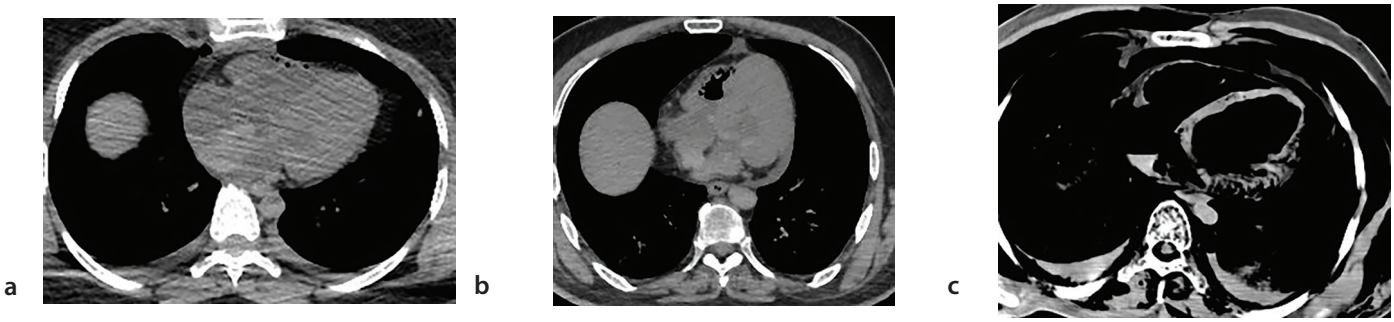


Figure 4. Gas in the cardiac chambers on non-contrast axial postmortem thoracic computed tomography, shown as **(a)** grade 1, **(b)** grade 2, and **(c)** grade 3.

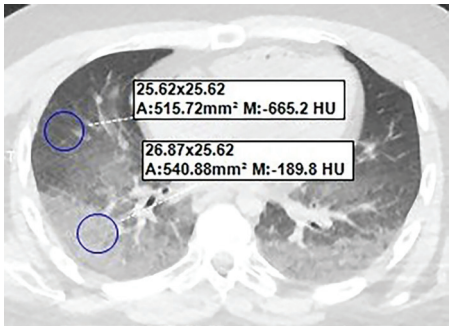


Figure 5. Increased attenutation in the dependent portions of both lungs on non-contrast axial postmortem thoracic computed tomography, consistent with hypostasis. Density measurements were obtained using a region of interest of 500–600 mm^2 from lung parenchyma with and without hypostasis. HU, Hounsfield unit.

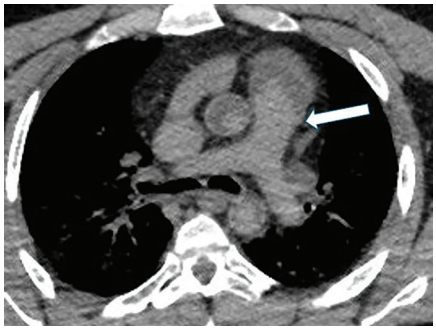


Figure 6. Hyperdense clotting in the pulmonary trunk and lobar pulmonary arteries on non-contrast axial postmortem thoracic computed tomography (arrow).

Cartocci et al.[14] evaluated 41 corpses with PMIs ranging from 4 to 930 days, correlating external decomposition with the radiological alteration index (RAI) on PMCT. They found that gas above grade 2 in the heart, liver, and major vessels was associated with an RAI score > 61, which corresponded to moderate-to-severe putrefaction. Additionally, 54% of cases demonstrated more than 50% intracranial gas.[14] In another study of 159 PMCTs, intracranial gas was identified in 62 corpses, and 40.2% of these cases were reported as having intravascular gas.[15] In this study, we did not grade the extent of intracranial intravascular gas. However, we observed gas in intracranial vessels in 34.6% of corpses with a PMI of 0–7 hours and in all corpses with PMIs greater than 48 hours.

The most common pulmonary finding on PMCT is hypostasis, which develops as a result of the loss of tone in the respiratory muscles and diaphragm after death. The expiratory position of the diaphragm in the postmortem period further contributes to attenuation differences in the basal lung regions.[16] In this study, we evaluated the relationship between hypostasis detected on PMCT and the PMI. Hypostasis was observed in 47.3% of our study group but was absent in corpses with a PMI exceeding 72 hours.

Jackowski et al.[11] reported hypostasis in 79.5% of cases on PMCT and magnetic resonance imaging (MRI). In a study by Tumanova et al.,[4] MRI examinations of 62 newborns and infants with PMIs of 0–72 hours were assessed. The PMIs were stratified, and hypostasis was compared with the PMI according to MR signal gradient differences. Hypostasis-related MR signal changes were detected in 57.1% of cases at 0–6 hours and 33% at 6–12 hours, with the strongest signal gradient consistent with hypostasis detected in 75% of cases at 18–24 hours.[4] Similarly, Kinoshita et al.[5] evaluated four pigs at hourly intervals for 24 hours postmortem. Based on density measurements from the dorsal and ventral lung regions, attenuation differences began to appear in the dorsal regions at hour 8 and continued to increase until 24 hours. Although significant differences were noted between baseline and later measurements, no significant changes were observed between 8 and 24 hours.[5] In this study, hypostasis was observed with increasing frequency up to 48 hours and in corpses with a PMI of 48–72 hours.

Matsuyama et al.[17] evaluated antemortem and postmortem lung CT images in nine rats scanned in the prone position. They reported a transient decrease in lung volume with a temporary increase in tracheal and bronchial volumes. Pulmonary congestion and consolidations were identified at 48 hours postmortem, although interstitial parenchymal

Table 1. Relationship between the postmortem interval and gas detected in organs, lung hypostasis, and pulmonary artery clotting on postmortem computed tomography

Postmortem computed tomography		Postmortem interval							
		0–7 hours	8–16 hours	17–48 hours	48–72 hours	73–120 hours	> 120 hours		*P*
Intravascular gas in the cranium	Negative	17 (23%)	5 (6.8%)	3 (4.1%)	0	0	0	25 (33.8%)	0.002
	Positive	9 (12.2%)	20 (27%)	12 (16.2%)	4 (5.4%)	1 (1.4%)	3 (4.1%)	49 (66.2%)	
Intracardiac gas	Absent	7 (9.5%)	0	0	0	0	0	7 (9.5%)	0.000
	Grade 1	13 (17.6%)	5 (6.8%)	3 (4.1%)	0 (0%)	0 (0%)	0	21 (28.4%)	
	Grade 2	6 (8.1%)	13 (17.6%)	6 (8.1%)	0	0	0	25 (33.8%)	
	Grade 3	0	7 (9.5%)	6 (8.1%)	4 (5.4%)	1 (1.4%)	3 (4.1%)	21 (28.4%)	
Intravascular gas in the liver	Absent	10 (13.5%)	4 (5.4%)	0	0	0	0	14 (18.9%)	0.000
	Grade 1	10 (13.5%)	5 (6.8%)	3 (4.1%)	0	0	0	18 (24.3%)	
	Grade 2	5 (6.8%)	15 (20.3%)	11 (14.9%)	1 (1.4%)	0	0	32 (43.2%)	
	Grade 3	1 (1.4%)	1 (1.4%)	1 (1.4%)	3 (4.1%)	1 (1.4%)	3 (4.1%)	10 (13.5%)	
Intravascular gas in the aorta	Absent	21 (28.4%)	12 (16.2%)	6 (8.1%)	0	0	0	39 (52.7%)	0.000
	Grade 1	4 (5.4%)	4 (5.4%)	4 (5.4%)	0	0	0	12 (16.2%)	
	Grade 2	0	3 (4.1%)	1 (1.4%)	0	0	0	4 (5.4%)	
	Grade 3	1 (1.4%)	6 (8.1%)	4 (5.4%)	4 (5.4%)	1 (1.4%)	3 (4.1%)	19 (25.7%)	
Intravascular gas in the kidney	Absent	24 (32.4%)	18 (24.3%)	8 (10.8%)	2 (2.7%)	0	0	52 (70.3%)	0.000
	Grade 1	1 (1.4%)	5 (6.8%)	4 (5.4%)	0	0	0	10 (13.5%)	
	Grade 2	1 (1.4%)	2 (2.7%)	2 (2.7%)	0	0	0	5 (6.8%)	
	Grade 3	0	0	1 (1.4%)	2 (2.7%)	1 (1.4%)	3 (4.1%)	7 (9.5%)	
Clotting in the pulmonary artery	Negative	8 (10.8%)	18 (24.3%)	6 (8.1%)	3 (4.1%)	1 (1.4%)	3 (4.1%)	39 (52.7%)	0.015
	Positive	18 (24.3%)	7 (9.5%)	9 (12.2%)	1 (1.4%)	0	0	35 (47.3%)	
Hypostasis	Negative	10 (13.5%)	16 (21.6%)	6 (8.1%)	3 (4.1%)	1 (1.4%)	3 (4.1%)	39 (52.7%)	0.119
	Positive	16 (21.6%)	9 (12.2%)	9 (12.2%)	1 (1.4%)	0	0	35 (47.3%)	
Total		26 (35.1%)	25 (33.8%)	15 (20.3%)	4 (5.4%)	1 (1.4%)	3 (4.1%)	74 (100%)	

Table 2. Correlation analysis between gas detected in organs and the postmortem interval on postmortem computed tomography

		Postmortem interval	Intravascular gas in the cranium	Intravascular gas in the liver	Intravascular gas in the kidney	Intracardiac gas	Intravascular gas in the aorta
Postmortem interval	Pearson r	1	0.419	0.624	0.658	0.636	0.585
	P		0.000	0.000	0.000	0.000	0.000
Intravascular gas in the cranium	Pearson r		1	0.477	0.318	0.607	0.429
	P			0.000	0.006	0.000	0.000
Intravascular gas in the liver	Pearson r			1	0.599	0.720	0.568
	P				0.000	0.000	0.000
Intravascular gas in the kidney	Pearson r				1	0.505	0.638
	P					0.000	0.000
Intracardiac gas	Pearson r					1	0.621
	P						0.000

Table 3. Relationship between the presence of pulmonary arterial clotting and lung hypostasis on postmortem computed tomography

		Clotting in the pulmonary artery	
		Positive	Negative
Hypostasis	Positive	37 (50%)	2 (2.7%)
	Negative	2 (2.7%)	33 (44.6%)
Total		39 (52.7%)	35 (47.3%)
P		*P* = 0.001	
			Hypostasis
Clotting in the pulmonary artery		Pearson r	0.892
		P	0.001
		n	74

Table 4. Correlation analysis between pulmonary hypostasis and pulmonary arterial clotting on postmortem computed tomography

		Density of hypostatic parenchyma	Density of non-hypostatic parenchyma	Pulmonary artery clotting	Pulmonary artery clotting density
Density of hypostatic parenchyma	Pearson r	1	0.918	0.831	0.697
	P		0.000	0.000	0.000
Density of non-hypostatic parenchyma	Pearson r		1	0.889	0.748
	P			0.000	0.000
Pulmonary artery clotting	Pearson r			1	0.880
	P				0.000

changes could not be assessed due to the small lung volume.[17] Although we did not assess the trachea and bronchi morphologically in this study, we observed that hypostasis increased particularly in corpses with PMIs of 0–72 hours.

Pulmonary clotting is seen on CT as hyperdense intraluminal clots without fluid–fluid levels.[18,19] In our cohort, clots were detected in 35 cases within the pulmonary trunk or its branches. A statistically significant ($P = 0.001$) and strong positive correlation (r: 0.892) was found between hypostasis and the presence of pulmonary arterial clotting. No signs of hypostasis were observed in corpses with collapsed pulmonary arteries or intravascular gas in the pulmonary arteries. Accordingly, we suggest that pulmonary hypostasis may develop as a consequence of clotting or sedimentation within the pulmonary arteries.

This study has several limitations. First, the number of cases included was relatively small. Accordingly, no significant relationship was found between hypostasis and the PMI in this study. We believe that a larger sample size might reveal a statistically significant difference regarding hypostasis. Second, the PMI was estimated based on autopsy findings and law enforcement reports, which may introduce bias. Third, external factors such as environmental conditions (e.g., hot and humid weather during summer) and the time taken for corpses to be transported from the field to CT and autopsy may have affected the PMI. High ambient temperatures during the summer accelerate the decomposition process, and in this study, the PMI values of bodies found in this period were relatively short. The forensic cause of death and positional changes occurring during the postmortem period may also influence the development of hypostasis. Therefore, in this study, particular attention was paid to ensuring complete body integrity and that all bodies were found in the supine position. Finally, information regarding chronic diseases, sepsis, or infections in the study group was unavailable.

In conclusion, on PMCT, decomposition-related gas can be detected in solid organs, particularly in the liver and heart, as early as within 48 hours postmortem. A moderate correlation exists between gas detected on PMCT and the PMI. Additionally, a strong correlation was observed between clotting or sedimentation in the pulmonary arteries and pulmonary hypostasis on PMCT.

Footnotes

Conflict of interest disclosure

The authors declared no conflicts of interest.

References

1. Decker SJ, Braileanu M, Dey C, et al. Forensic radiology: a primer. *Acad Radiol*. 2019;26(6):820-830. [Crossref]
2. Klein WM, Bosboom DG, Koopmanschap DH, Nievelstein RA, Nikkels PG, van Rijn RR. Normal pediatric postmortem CT appearances. *Pediatr Radiol*. 2015;45(4):517-526. [Crossref]
3. Del Fante Z, De Matteis A, Fazio V, et al. The importance of post mortem computed tomography (PMCT) in the reconstruction of the bullet trajectory. *Clin Ter*. 2019;170(2):129-133. [Crossref]
4. Tumanova UN, Bychenko VG, Serova NS, Shchegolev AI. Postmortem MRI characterization of cadaveric hypostases in deceased newborns. *Bull Exp Biol Med*. 2021;170(3):371-377. [Crossref]
5. Kinoshita K, Sakai T, Inai K, et al. Postmortem temporal chest CT and its pathological correlation in piglets. *J Med Invest*. 2024;71(3-4):232-236. [Crossref]
6. Shenton A, Kralt P, Suvarna SK. Death, post mortem changes and decomposition on post mortem computed tomography. In: Shenton A, Kralt P, Suvarna SK, eds. Post mortem CT for non-suspicious adult death. Cham: Springer; 2021:50-56. [Crossref]
7. Ishida M, Gonoi W, Hagiwara K, et al. Intravascular gas distribution in the upper abdomen of non-traumatic in-hospital death cases on postmortem computed tomography. *Leg Med (Tokyo)*. 2011;13(4):174-179. [Crossref]
8. Romanelli MC, Marrone M, Veneziani A, et al. Hypostasis and time since death: state of the art in Italy and a novel approach for an operative instrumental protocol. *Am J Forensic Med Pathol*. 2015;36(2):99-103. [Crossref]
9. Fischer F, Grimm J, Kirchhoff C, Reiser MF, Graw M, Kirchhoff S. Postmortem 24-h interval computed tomography findings on intrahepatic gas development and changes of liver parenchyma radiopacity. *Forensic Sci Int*. 2012;214(1-3):118-123. [Crossref]
10. Egger C, Bize P, Vaucher P, et al. Distribution of artifactual gas on post-mortem multidetector computed tomography (MDCT). *Int J Legal Med*. 2012;126(1):3-12. [Crossref]
11. Jackowski C, Sonnenschein M, Thali MJ, et al. Intrahepatic gas at postmortem computed tomography: forensic experience as a potential guide for in vivo trauma imaging. *J Trauma*. 2007;62(4):979-988. [Crossref]
12. Takahashi N, Higuchi T, Shiotani M, Maeda H, Hirose Y. Intrahepatic gas at postmortem multislice computed tomography in cases of nontraumatic death. *Jpn J Radiol*. 2009;27(7):264-268. [Crossref]
13. Egger C, Wiskott K, Vaucher P, et al. Postmortem changes of the vascular system: a thanatological study using multidetector computed tomography. *Int J Legal Med*. 2023;137(4):1109-1115. [Crossref]
14. Cartocci G, Santurro A, Neri M, et al. Postmortem computed tomography (PMCT) radiological findings and assessment in advanced decomposed bodies. *Radiol Med*. 2019;124(11):1018-1027. [Crossref]
15. Borowska-Solonynko A, Koczyk K, Blacha K, Prokopowicz V. Significance of intracranial gas on post-mortem computed tomography in traumatic cases in the context of medico-legal opinions. *Forensic Sci Med Pathol*. 2020;16(1):3-11. [Crossref]
16. Filograna L, Thali MJ. Post-mortem CT imaging of the lungs: pathological versus

non-pathological findings. *Radiol Med*. 2017;122(12):902-908. [Crossref]

17. Matsuyama T, Ota S, Inui Y, et al. Examination of postmortem changes in the lungs, trachea, and bronchi in a rat model imaged with small-animal computed tomography. *Fujita Med J*. 2023;9(2):101-104. [Crossref]
18. Ishida M, Gonoi W, Okuma H, et al. Common Postmortem computed tomography findings following atraumatic death: differentiation between normal postmortem changes and pathologic lesions. *Korean J Radiol*. 2015;16(4):798-809. [Crossref]
19. Offiah CE, Dean J. Post-mortem CT and MRI: appropriate post-mortem imaging appearances and changes related to cardiopulmonary resuscitation. *Br J Radiol*. 2016;89(1058):2015085. [Crossref]

Diagn Interv Radiol 2026; DOI: 10.4274/dir.2026.263838

GENERAL RADIOLOGY

LETTER TO THE EDITOR

Copyright @ 2026 Author(s) - Available online at dirjournal.org.
Content of this journal is licensed under a Creative Commons Attribution-NonCommercial 4.0 International License.

Letter to the Editor: On the role of mentorship, ethics, and quality in publication success

Atilla Hikmet Çilengir

İzmir Democracy University Faculty of Medicine, Department of Radiology, İzmir, Türkiye

Dear Editor,

I read with great interest the article entitled "Bibliometric analysis of radiology residency theses in Türkiye: publication metrics and trends" by Salbas and Koc[1], published in Diagnostic and Interventional Radiology. This comprehensive bibliometric analysis makes a valuable contribution to the field by elucidating the potential of radiology residency theses in Türkiye to be transformed into academic publications and by identifying factors that influence this process.

Among the study's findings, one observation that particularly drew my attention and merits deeper academic discussion is that publications in which the first author was not a resident were more frequently published in Science Citation Index – Expanded indexed journals (50.8% vs. 74.7%), received a higher number of citations (2 vs. 17), and had a shorter time to publication (1,430 vs. 916 days). As the authors also imply, this finding may initially be attributed to the greater experience of mentors in academic writing, journal selection, and navigation of the publication process.

Consistent with these findings, the literature has reported strong associations between experienced mentorship and successful scholarly output. For example, in postgraduate year one research projects, the presence of mentors with at least one first-author publication was associated with a significantly higher rate of full-text publication than with projects lacking such mentorship (50.0% vs. 8.6%, $P < 0.001$).[2] This finding underscores the importance of conceptualizing mentorship not merely as a product-oriented endeavor but as an educational process. Furthermore, the involvement of mentors or senior research collaborators has been shown to increase the likelihood that resident research projects progress to publication.[3] Conversely, insufficient mentorship during the research process has been associated with inadequate academic skill development and the emergence of substantial barriers throughout the publication process.[4]

However, interpreting this result solely through the lens of experience may risk overlooking an important opportunity with respect to one of the core objectives of residency training: the cultivation of independent researchers. An ideal mentorship relationship should not merely involve the supervisor using their experience to expedite publication but should also encompass the transfer of this experience to the resident, thereby fostering their development as a competent researcher. The residency thesis represents the most critical practical training through which a resident experiences the entire scientific research process from conception to completion. Assuming first authorship of the resulting manuscript constitutes one of the most essential components of this educational process.

This finding invites a broader discussion regarding the ethical and educational dimensions of mentorship in residency training. In this context, it is important to distinguish between productivity-oriented mentorship, which prioritizes rapid publication and journal impact, and educational or guided mentorship, which emphasizes resident-led authorship, skill acquisition in scientific writing, data interpretation, and independent scholarly development.[5,6] Although the former may optimize short-term bibliometric outcomes, the latter aligns more closely with the core educational mission of residency training. Similarly, a study examining

Handling editor: Furkan Ufuk

Corresponding author: Atilla Hikmet Çilengir

E-mail: acilengir@gmail.com

Received 28 December 2025; accepted 18 January 2026.

Epub: 10.02.2026

Publication date: 02.11.2026

DOI: 10.4274/dir.2026.263838

You may cite this article as: Çilengir AH. Letter to the editor: on the role of mentorship, ethics, and quality in publication success. *Diagn Interv Radiol*. 2026;32(6):794-795.

the publication profiles of dermatology residency graduates demonstrated that the total number of publications, the number of first-author publications during residency, and h-index values were positively associated with graduates' propensity to pursue academic medicine and with indicators of long-term scholarly productivity.[7] In particular, graduates who chose academic career paths had significantly higher numbers of both total publications and first-author publications during residency, suggesting that first authorship may serve as a marker of sustained scientific productivity throughout an academic career.

The residency thesis represents the most comprehensive opportunity for trainees to experience the full scientific process, from research design to manuscript submission and revision. First authorship of the resulting publication is a critical educational milestone within this process. Therefore, the systematically lower performance of resident-first-authored publications observed in the study may reflect not only differences in experience but also a potential gap in structured mentorship and academic training. If supervisors assume primary responsibility for manuscript writing to accelerate acceptance or improve journal ranking, residents may be inadvertently deprived of essential opportunities to develop writing proficiency, journal selection skills, and confidence in responding to peer review.

From this perspective, the findings reported by Salbas and Koc[1] extend beyond bibliometric description and prompt reflection on how mentorship practices are structured within training institutions. To address this issue, several practical strategies may be considered: (i) implementation of structured writing mentorship programs in which supervisors provide feedback on resident-drafted manuscripts; (ii) allocation of writing time during the final year of residency; and (iii) explicit institutional expectations favoring resident-led first authorship, when appropriate. Such measures may help balance publication quality with the educational objectives of residency training. Ultimately, the goal should not be limited to maximizing publication metrics but should also include the cultivation of independent physicians equipped with strong scientific reasoning and academic writing skills. Future bibliometric studies incorporating qualitative assessments of mentorship practices may further clarify the distinction between productive supervision and genuine educational mentorship.

I would like to express once again my appreciation to the authors for their work addressing an important issue in radiology residency training.

Conflict of interest disclosure

The author declared no conflicts of interest.

References

1. Salbas A, Koc AM. Bibliometric analysis of radiology residency theses in Türkiye: publication metrics and trends. *Diagn Interv Radiol*. 2026;32(1):71-80. [Crossref]
2. Datt M, Sikora A, Henry K. Association between experienced mentorship and successful publication of PGY1 resident research at an academic medical center. *Hosp Pharm*. 2025:00185787251326237. [Crossref]
3. Stranges PM, Vouri SM. Impact of co-investigators on pharmacy resident research publication. *Pharm Pract (Granada)*. 2017;15(2):928. [Crossref]
4. Kamya D, Macharia B, Siika WW, Mbuba CK. A qualitative study exploring graduated medical residents' research experiences, barriers to publication and strategies to improve publication rates from medical residents. *BMC Med Educ*. 2024;24(1):1091. [Crossref]
5. van Schalkwyk GI, Katz RB, Resignato J, van Schalkwyk SC, Rohrbaugh RM. Effective research mentorship for residents: meeting the needs of early career physicians. *Acad Psychiatry*. 2017;41(3):326-332. [Crossref]
6. Straus SE, Chatur F, Taylor M. Issues in the mentor-mentee relationship in academic medicine: a qualitative study. *Acad Med*. 2009;84(1):135-139. [Crossref]
7. Anderson JM, Wenger D, Johnson AL, et al. Publication trends and their relationship with academic success among dermatology residents: cross-sectional analysis. *JMIR Dermatol*. 2021;4(2):e30015. [Crossref]

Diagn Interv Radiol 2026; DOI: 10.4274/dir.2026.263892

GENERAL RADIOLOGY

LETTER TO THE EDITOR

Copyright @ 2026 Author(s) - Available online at dirjournal.org.
Content of this journal is licensed under a Creative Commons Attribution-NonCommercial 4.0 International License.

Reply: On the role of mentorship, ethics, and quality in publication success

Ali Salbas
Ali Murat Koc

İzmir Katip Çelebi University, Atatürk Training and Research Hospital, Department of Radiology, İzmir, Türkiye

Dear Editor,

We would like to thank the author for the thoughtful and constructive letter regarding our article and for highlighting the important educational and ethical dimensions of mentorship in residency training.[1,2] We agree that mentorship should be viewed not only as a means to improve publication outcomes but also as a central component of scientific training and professional development for residents.

The author appropriately emphasizes the educational value of resident-led authorship and the role of structured mentorship in fostering independent researchers. We fully acknowledge that first authorship represents an important learning milestone and that effective mentorship should aim to transfer academic skills rather than merely accelerate publication.

At the same time, we believe that our findings should be interpreted with caution, particularly with respect to the underlying reasons for first-authorship patterns. Our bibliometric design allowed us to identify the first author and publication outcomes, but it did not permit us to determine why the first author was not the resident in certain cases. Several factors may contribute to this observation, including loss of interest after graduation, time constraints, relocation to other institutions, or expansion of the original thesis into a broader collaborative project. Therefore, these differences are likely multifactorial and should be interpreted cautiously.

An additional aspect that deserves consideration is the substantial proportion of theses that were never converted into publications. In our cohort, 62.9% of radiology residency theses remained unpublished.[2] This finding indicates that a large amount of scientific data generated during residency training does not reach the academic literature. In this context, the active involvement of supervisors may sometimes reflect an effort to ensure that valuable clinical and research data are incorporated into the scientific literature.

The goal of training independent researchers, as emphasized by the author, represents a cornerstone of residency education. The process of converting a residency thesis into a publication provides an important opportunity for acquiring these skills. However, the successful completion of this process is inherently bidirectional and requires both effective mentorship and sufficient academic motivation on the part of the resident. In this regard, institutional strategies that encourage resident engagement, provide dedicated time for research and manuscript preparation, and support structured mentorship may be particularly beneficial. Moreover, the recent increase in radiology residency positions in Türkiye may place additional demands on existing faculty resources, which could further challenge individualized mentorship.[3] Strengthening institutional support and mentoring frameworks may therefore help sustain both educational quality and academic productivity.

Finally, we share the author's view that future studies incorporating qualitative assessments of mentorship practices would provide valuable insight into how different supervisory models influence both publication outcomes and long-term academic development.

We sincerely thank the author for contributing to this meaningful discussion and for extending the impact of our work beyond bibliometric description alone.

Handling editor: Evrim Özmen

Corresponding author: Ali Salbas

E-mail: dralisalbas@gmail.com

Received 20 January 2026; accepted 28 January 2026.

Epub: 10.02.2026

Publication date: 02.11.2026

DOI: 10.4274/dir.2026.263892

You may cite this article as: Salbas A, Koc AM. Reply: on the role of mentorship, ethics, and quality in publication success. *Diagn Interv Radiol*. 2026;32(6):796-797.

Conflict of interest disclosure

The authors declared no conflicts of interest.

References

1. Çilengir H. On the role of mentorship, ethics, and quality in publication success. *Diagn Interv Radiol.* Epub ahead of print. [Crossref]
2. Salbas A, Koc AM. Bibliometric analysis of radiology residency theses in Türkiye: publication metrics and trends. *Diagn Interv Radiol.* 2026;32(1):71-80. [Crossref]
3. ÖSYM. Student Selection and Placement Center (ÖSYM) – Official Website [Internet]. Ankara: Student Selection and Placement Center of Turkey; c2022. [Crossref]

Diagn Interv Radiol 2026; DOI: 10.4274/dir.2026.263942

GENERAL RADIOLOGY

LETTER TO THE EDITOR

Copyright @ 2026 Author(s) - Available online at dirjournal.org.
Content of this journal is licensed under a Creative Commons Attribution-NonCommercial 4.0 International License.

Methodological considerations regarding control preference interpretation: a comment on management of contrast media-related risk factors by Öztürk and Karabıyık

Franklin de Jesus Santiago Villegas
Juan Manuel Calero Canaval

Universidad de los Andes, School of Medicine, Bogotá D.C., Colombia

Dear Editor,

We read with great interest the article by Öztürk and Karabıyık[1] on radiologists' preferences in managing risk factors associated with contrast media. The study addresses a relevant question for the safety of radiological practice and provides valuable initial data.[1] It also contributes to a very essential question of interprofessional and inter-specialty dynamics, with insights that the reader can apply to any institution. However, we believe that certain interpretations, given the descriptive nature of the study, should be considered cautiously.

First, a modified version of the Control Preferences Scale (CPS), an excellent tool used for decades across the world, was used, yet the reader is left wondering if the adaptation was tested or, alternatively, if the validity of the translation (if it was translated) was assessed. Without evidence that the modified scale measures the same construct as the original, comparative interpretation and generalizability remain limited.

Second, 6 of the 50 interviews (12%) were excluded due to "invalid permutations"[1] without describing the characteristics of the excluded participants. Although some permutations may appear to be, to a certain extent, incoherent, the reader is left curious as to why a given specialist may have chosen such a combination, even if the end result remains their prudent exclusion. Furthermore, face-to-face administration by a single interviewer increases the risk of social desirability bias and interviewer influence.

An important aspect that is not mentioned in the article is the cultural dimension. There are negative stereotypes about all specialties, repeated since one's days as a medical student by both peers and instructors, that help create dynamics of incivility between specialties or even between individual physicians.[2,3] We are left wondering if there is a social dimension behind the lack of a desire for an active role that the paper illustrates, such as whether radiologists perceive themselves as having outside decision-making roles generally, or if more personal dynamics could not be generalized.

We suggest that future revisions consider tempering causal interpretations, reporting the psychometric properties of the adapted CPS version, elaborating on the excluded participants, and considering the cultural aspects possibly involved. These nuances would strengthen the study's usefulness for healthcare managers and planners.

Conflict of interest disclosure

The authors declared no conflicts of interest.

Corresponding author: Franklin de Jesus Santiago Villegas

E-mail: f.santiago@uniandes.edu.co

Received 16 February 2026; accepted 18 February 2026.

Epub: 11.03.2026

Publication date: 02.11.2026

DOI: 10.4274/dir.2026.263942

You may cite this article as: Santiago Villegas FdJ, Calero Canaval JM. Methodological considerations regarding control preference interpretation: a comment on Öztürk and Karabıyık. *Diagn Interv Radiol*. 2026;32(6):798-799.

References

1. Öztürk B, Karabıyık Ö. Radiologists, tendency to collaborate with referring physicians in managing contrast media-related risk factors. *Diagn Interv Radiol*. 2026;32(1):65-70. **[Crossref]**
2. Lewis C. The impact of interprofessional incivility on medical performance, service and patient care: a systematic review. *Future Healthc J*. 2023;10(1):69-77. **[Crossref]**.
3. Brawley R, Kumar S, Kibble J. Understanding factors motivating trainees to pursue a career in radiology: an interview study. *Cureus*. 2026;18(1):e102745. **[Crossref]**

Diagn Interv Radiol 2026; DOI: 10.4274/dir.2026.263733

HEAD AND NECK IMAGING

ORIGINAL ARTICLE

Copyright© Author(s) - Available online at dirjournal.org.
Content of this journal is licensed under a Creative Commons Attribution-NonCommercial 4.0 International License.

Semicircular canal aplasia: radiologic spectrum and clinical correlations on computed tomography and magnetic resonance imaging

Nisa Başpınar[1]
Mehmet Atalar[1]
Serdar Aktı[1]
Adem Bora[2]

[1]Sivas Cumhuriyet University Faculty of Medicine, Department of Radiology, Sivas, Türkiye

[2]Sivas Cumhuriyet University Faculty of Medicine, Department of Otorhinolaryngology, Sivas, Türkiye

PURPOSE

This study aimed to characterize the imaging patterns of semicircular canal (SCC) aplasia on high-resolution computed tomography (CT) and magnetic resonance imaging (MRI) to identify associated cochleovestibular and internal auditory canal (IAC) abnormalities and to explore potential syndromic correlations.

METHODS

We retrospectively evaluated 12 patients (24 ears) diagnosed with SCC aplasia between January 2021 and January 2025. Imaging findings were reviewed for canal type, cochlear and vestibular abnormalities, vestibular aqueduct morphology, and IAC configuration. Syndromic associations and clinical outcomes were also assessed.

RESULTS

Lateral SCC aplasia was most common (41.7%), followed by budding remnants (12.5%) and total aplasia (12.5%). Total aplasia consistently coexisted with vestibular hypoplasia ($P = 0.020$) and was frequently accompanied by narrowing of the IAC ($P = 0.04$). Cochlear hypoplasia was found in one patient with bilateral total aplasia. Sensorineural hearing loss was present in 75% of patients, and caloric testing revealed subclinical vestibular dysfunction in two clinically asymptomatic adults. Syndromic associations included two cases of DiGeorge syndrome and a newly identified coexistence with Gitelman syndrome.

CONCLUSION

SCC aplasia encompasses a spectrum of rare anomalies, most commonly affecting the lateral canal and closely related to vestibular dysplasia. Recognition of IAC narrowing is important, as it can complicate cochlear implantation. The identification of Gitelman syndrome as a new association expands the spectrum of systemic diseases associated with SCC abnormalities. Comprehensive imaging with both CT and MRI is essential not only for diagnosis but also for surgical planning and syndromic screening.

CLINICAL SIGNIFICANCE

Systematic assessment of the IAC and vestibular structures on CT and MRI is essential in patients with congenital hearing loss. Recognizing IAC narrowing and vestibular dysplasia aids in preoperative cochlear implant planning and supports targeted syndromic or genetic evaluation.

KEYWORDS

Aplasia, cochlear implantation, computed tomography, internal auditory canal, magnetic resonance imaging, semicircular canal

Handling editor: Erkan Gökçe

Corresponding author: Mehmet Atalar

E-mail: mhatalar@gmail.com

Received 20 November 2025; revision requested 15 December 2025; accepted 25 January 2026.

Epub: 12.02.2026

Publication date: 02.11.2026

DOI: 10.4274/dir.2026.263733

Semicircular canal (SCC) anomalies are rare congenital inner ear malformations that may present as part of syndromic entities such as CHARGE, DiGeorge, or Goldenhar syndromes, and they can occur in isolation. Although some patients may exhibit sensorineural hearing loss and vestibular dysfunction, others remain asymptomatic. Among SCC malformations, including aplasia and hypoplasia, lateral SCC (LSCC) aplasia is the most commonly reported type.[1-7]

You may cite this article as: Başpınar N, Atalar M, Aktı S, Bora A. Semicircular canal aplasia: radiologic spectrum and clinical correlations on computed tomography and magnetic resonance imaging. *Diagn Interv Radiol*. 2026;32(6):800-807.

Inner ear development begins in the 6th week of gestation. The pars superior, comprising the utricle and SCCs, forms earlier than the cochlea and saccule of the pars inferior. Therefore, developmental disturbances affecting the pars superior may also influence the cochlea and vestibule. Embryologically, the superior SCC (SSCC) is the first to form, followed by the posterior SCC (PSCC), whereas the LSCC is the last to develop, making it more susceptible to isolated aplasia. Although SCC dysplasia is often accompanied by cochlear malformations, several reports have documented normal cochlear morphology in isolated LSCC aplasia.[7-9]

Imaging with computed tomography (CT) and magnetic resonance imaging (MRI) is critical for the evaluation of these anomalies. Although CT provides superior detail of osseous structures, MRI offers high-resolution visualization of the membranous labyrinth and associated neural structures.[6,8]

This study aimed to evaluate CT and MRI findings in patients with SCC aplasia, assess associated cochlear and vestibular abnormalities, and investigate possible syndromic relationships. Previous studies have often focused on isolated LSCC aplasia or syndromic malformations but have lacked combined CT–MRI correlation. This study addresses existing gaps in the literature by integrating high-resolution CT and MRI findings, systematically evaluating narrowing of the internal auditory canal (IAC) as a radiologic marker, and reporting a newly identified syndromic association with Gitelman syndrome.

Main points

- Lateral semicircular canal (SCC) aplasia is the most common anomaly, often presenting with vestibular dysplasia.
- Total SCC aplasia always coexists with vestibular hypoplasia, highlighting embryologic timing.
- Narrowing of the internal auditory canal is a key radiologic marker with surgical implications.
- The newly identified association with Gitelman syndrome expands the known syndromic spectrum.
- Computed tomography and magnetic resonance imaging offer complementary insights essential for diagnosis and preoperative mapping.

Methods

Study design and population

This retrospective study was conducted between January 2021 and January 2025 at a tertiary care university hospital. Patients who presented with hearing loss, dizziness, or balance disorders and were radiologically diagnosed with SCC aplasia by either CT or MRI were included. Of the 13 patients initially identified, 1 was excluded because motion artifacts significantly affected image quality, leaving 12 patients for final analysis. All patients with SCC aplasia diagnosed during the study period were included, regardless of referral indication, to minimize selection bias. However, some patients were assessed in the context of possible cochlear implantation, which may have influenced referral patterns. Vestibular testing was not performed uniformly in all patients because of differences in clinical presentation and patient cooperation, particularly among children. In adult patients who were able to cooperate, caloric testing was performed as part of the routine otoneurological evaluation. This limitation was mainly due to age- and cooperation-related constraints in pediatric patients. The patient flowchart of the study is shown in Figure 1.

Imaging protocols

High-resolution CT scans were performed using a 128-slice multidetector scanner (GE Revolution EVO, Milwaukee, WI, USA). The imaging parameters were standardized as follows: 0.625-mm collimation, 0.375 pitch, 0.625-mm section thickness, 140 kVp (80 kVp for pediatric patients), 400 mAs (150 mAs for pediatric patients), and a 199-mm field of view.

MRI examinations were acquired using a 1.5-Tesla scanner (Magnetom Aera, Siemens Healthineers, Erlangen, Germany) with 20- and 64-channel head coils. The imaging protocol included axial T2-weighted fast spin–echo sequences [repetition time (TR): 5,136 ms, echo time (TE): 96 ms, slice thickness: 5 mm], T1-weighted volumetric interpolated breath-hold examination with fat saturation (TR: 18 ms, TE: 3.69 ms, slice thickness: 1 mm), three-dimensional T2-weighted sampling perfection with application-optimized contrasts using different flip-angle evolution sequences (TR: 1,200 ms, TE: 183 ms, slice thickness: 0.58 mm), and diffusion-weighted imaging (TR: 5,800 ms, TE: 98 ms, slice thickness: 5 mm, b values of 0 and 1,000 s/mm^2).

Image evaluation

All imaging studies were retrospectively reviewed by two experienced neuroradiologists, one with 14 years and the other with 9 years of experience. In cases of discrepancy, consensus was reached through consultation with a senior neuroradiologist with more than 15 years of experience. High-resolution temporal bone CT scans were assessed in axial and coronal planes. The following structures were systematically evaluated in both ears of all patients: presence or absence of the LSCC, PSCC, and SSCC; cochlear morphology, categorized as normal or hypoplastic; vestibule morphology, defined as normal, hypoplastic, or enlarged/dysmorphic; integrity of the round and oval windows; presence or absence of the vestibular aqueduct; and IAC diameter, measured in the axial

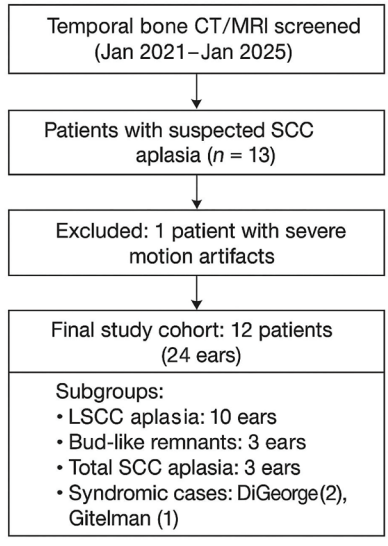


Figure 1. Study flow diagram. CT, computed tomography; MRI, magnetic resonance imaging; SCC, semicircular canal; LSCC, lateral semicircular canal.

plane and classified as narrow if ≤ 2.0 mm. The measurement was performed at the mid-porus level of the IAC on axial images, perpendicular to the canal axis, using standardized bone window settings to ensure reproducibility. SCC aplasia was defined as the complete absence of the canal, with or without a rudimentary bud. Bud-like remnants were also categorized as aplasia, consistent with the literature. This approach aligns with embryology-based classifications of inner ear malformations, in which rudimentary or bud-like IAC structures are considered aplastic variants rather than true hypoplasia.[1,5,8]

Statistical analysis

All statistical analyses were performed using SPSS version 26.0 (IBM Corp., Armonk, NY, USA). Descriptive data are presented as mean ± standard deviation for continuous variables and as counts and percentages for categorical variables. Group comparisons were conducted using chi-square or Fisher's exact tests for categorical variables and independent-samples t-tests for continuous variables. Due to the limited sample size, nonparametric comparisons were preferred. A *P* value of <0.05 was considered statistically significant.

Ethics

This study was conducted in accordance with the ethical standards of the Declaration of Helsinki. The Ethics Committee of Sivas Cumhuriyet University approved the study (approval number: 2025-04/127, date: April 24, 2025).

Results

Twelve patients, seven men and five women, with a mean age of 23.3 ± 23.0 years (range: 2–66 years), were included in the analysis. A total of 24 ears were examined. Isolated aplasia of the LSCC was the most common anomaly, affecting 10 ears (41.7%) (Figure 2). Bilateral LSCC aplasia was identified in two patients, whereas bud-like LSCC remnants were present in three ears, two of which were in the same individual (Figure 3). Complete aplasia of all three IACs was observed in three ears, including one patient with bilateral involvement.

All cases of total SCC aplasia were associated with vestibular hypoplasia, and this association was statistically significant (*P* = 0.02). In most patients with LSCC aplasia, the vestibule was enlarged or dysmorphic, and the absence of the LSCC bony island was a consistent imaging feature (Figure 4). Multistructural involvement was more common in cases of total SCC aplasia, where vestibular and cochlear anomalies often coexisted (Figure 5). Representative CT and MRI images of different SCC aplasia patterns are illustrated in Figures 6 and 7.

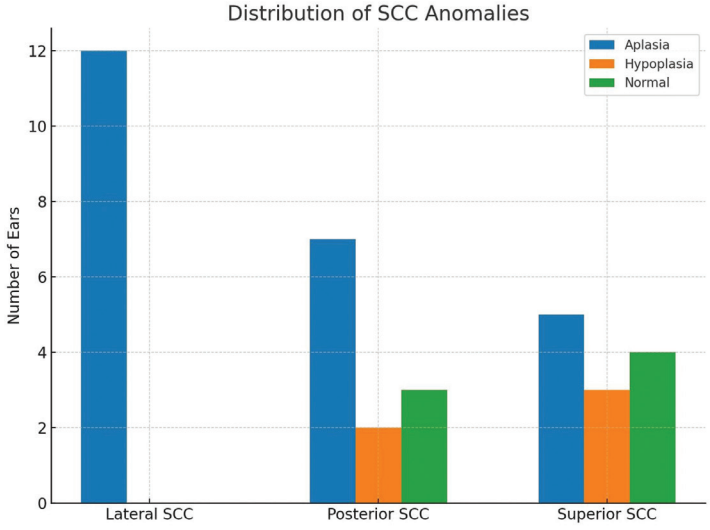


Figure 2. Distribution of semicircular canal anomalies. SCC, semicircular canal.

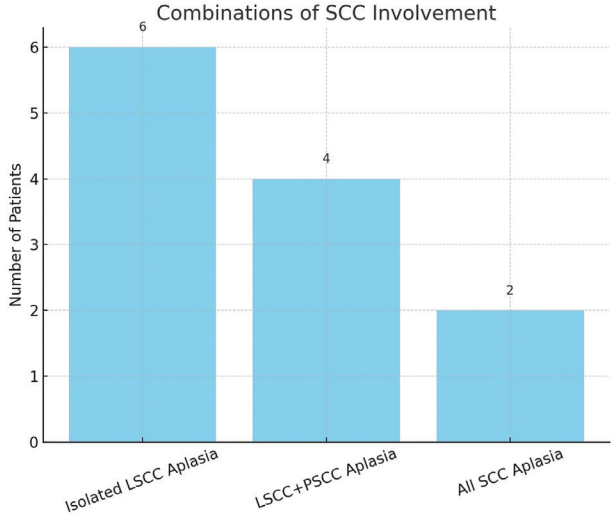


Figure 3. Combinations of semicircular canal anomalies. SCC, semicircular canal; LSCC, lateral semicircular canal; PSCC, posterior semicircular canal.

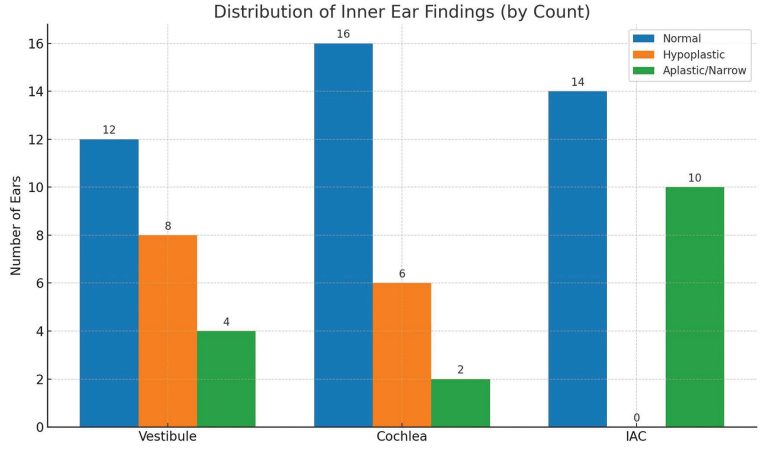


Figure 4. Distribution of inner ear findings. IAC, internal auditory canal.

Narrowing of the IAC, defined as a diameter of ≤ 2.0 mm, was detected in patients with bilateral total SCC aplasia and in some with bud-like remnants. Statistical analysis demonstrated a significant relationship between SCC aplasia and IAC narrowing (P = 0.04). This finding underscores the relevance of IAC caliber assessment during preoperative evaluation. The vestibular aqueduct was identified in 6 of the 10 ears with LSCC aplasia, without evidence of enlargement. A summarized overview of radiologic patterns, associated inner ear anomalies, IAC findings, and clinical characteristics is provided in Table 1. The distribution of anomalies involving the SCCs, cochlea, vestibule, oval and round windows, and IAC measurements is summarized in Table 2. Overall, radiologic findings demonstrated a continuum from isolated LSCC aplasia to total labyrinthine dysplasia, reflecting embryologic severity. Given the limited sample size and small subgroup distributions, categorical variables were compared using Fisher's exact test.

Syndromic associations were documented in three patients. One patient with bilateral SCC aplasia had Gitelman syndrome, representing the first reported case of this coexistence in the literature. Two additional patients with LSCC aplasia were diagnosed with DiGeorge syndrome. Sensorineural hearing loss was observed in 9 of 12 patients (75%). Caloric testing, available in two adult patients, revealed unilateral canal paresis despite the absence of overt vestibular symptoms. Vertigo was less frequently reported in adults, although caloric testing revealed canal paresis in two cases, suggesting that vestibular dysfunction may remain clinically silent in some individuals.

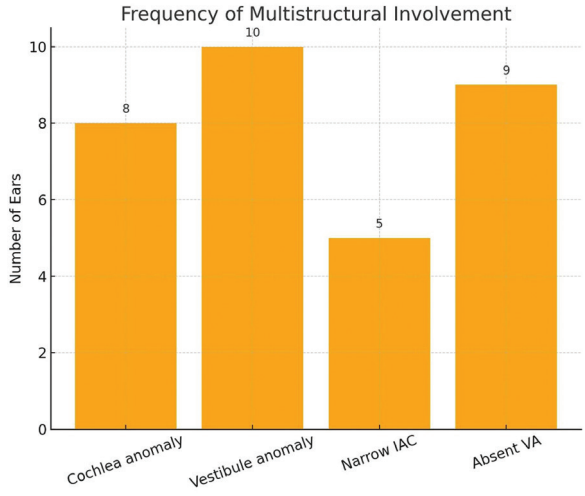


Figure 5. Frequency of multistructural involvement. IAC, internal auditory canal; VA, vestibular aqueduct.

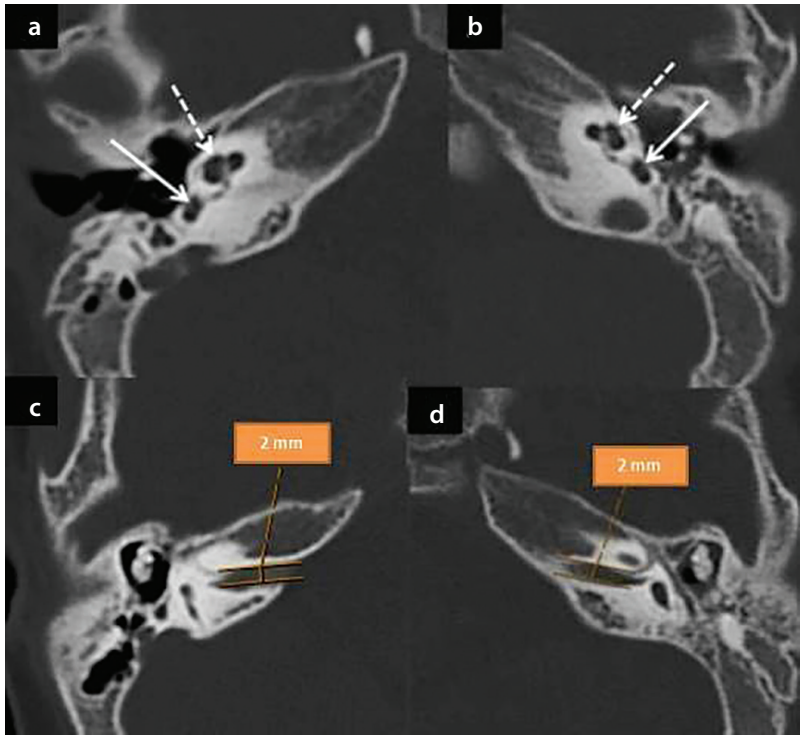


Figure 6. A 2-year-old girl with complete aplasia of the bilateral semicircular canals. **(a, b)** Non-contrast-enhanced axial temporal high-resolution computed tomography images show bilateral cochlear hypoplasia (dotted arrows) and hypoplastic vestibules (arrows). **(c, d)** The bilateral internal auditory canals are 2 mm below the lower threshold.

Discussion

SCC aplasia and hypoplasia represent a broad spectrum of congenital inner ear malformations. In our series, LSCC aplasia was the most common anomaly, reflecting embryologic susceptibility due to its later development.[1,5] Interruption of development at earlier stages resulted in more extensive anomalies affecting the cochlea and vestibule, consistent with embryologic principles.[6,7]

In our cohort, LSCC aplasia was predominant, consistent with its later embryologic development and increased vulnerability to isolated developmental arrest. Earlier disruption of the pars superior resulted in more extensive malformations, explaining the consistent association between total SCC aplasia and vestibular hypoplasia. This developmental continuum was previously described by Sennaroğlu and Bajin[8] who emphasized that the timing of embryonic disruption determines the extent of associated anomalies. In our cohort, one patient with bilateral total SCC aplasia also demonstrated cochlear hypoplasia, providing further evidence that early developmental arrest produces more severe and combined anomalies.

Radiologically, the most reliable markers of SCC aplasia in our study were an enlarged or dysmorphic vestibule, absence of the LSCC bony island, and narrowing of the IAC. Previous reports have suggested that IAC narrowing may coexist with labyrinthine malformations and may even predict cochlear nerve deficiency.[9] In our series, IAC narrowing was significantly more common in patients with total SCC aplasia or bud-like remnants, indicating that evaluation of IAC caliber should be an integral part of imaging

assessment in suspected SCC malformations. From a surgical perspective, these structural variations have direct relevance to cochlear implantation outcomes. This finding has important implications for preoperative planning in candidates for cochlear implantation, where cochlear nerve integrity must be established before surgery.[10]

Previous studies have reported associations between SCC aplasia and Kallmann syndrome, CHARGE syndrome, and chromosomal abnormalities.[11] A notable feature of our cohort was the presence of syndromic associations in a quarter of the patients. Beyond classical syndromes such as CHARGE and DiGeorge, our study identified a previously unreported association. The coexistence of bilateral SCC aplasia with Gitelman syndrome is, to our knowledge, the first report of its kind in the literature. Although Gitelman syndrome is primarily a disorder of the renal tubules caused by mutations in the *SLC12A3* gene, experimental studies have demonstrated the expression of sodium–chloride cotransporters in the endolymphatic sac, suggesting a possible mechanism linking electrolyte imbalance to vestibular morphogenesis.[12] This observation broadens the spectrum of syndromes associated with SCC abnormalities. In addition, two patients with LSCC aplasia were diagnosed with DiGeorge syndrome (22q11.2 deletion), which is consistent with previous studies reporting frequent ear abnormalities in this syndrome due to abnormal development of the pharyngeal arch.[13,14] This finding warrants further investigation, as SLC12A3 mutations in Gitelman syndrome may disrupt inner ear fluid homeostasis.

Clinically, SCC aplasia presents with diverse manifestations. Most patients in our series had sensorineural hearing loss, but vestibular dysfunction was not always clinically evident. Notably, caloric testing revealed canal paresis in two adults who denied vertigo, suggesting the possibility of central compensation for chronic congenital vestibular dysfunction. Although vestibular dysfunction may remain clinically silent due to central compensation, vestibular tests such as caloric testing or video head impulse testing can reveal subclinical deficits and should be considered, particularly in adult patients and in cases of bilateral or total SCC aplasia. This highlights the importance of systematic vestibular testing, as subtle but clinically relevant deficits may otherwise be missed. Previous studies have also shown that congenital

Table 1. Summary of radiologic and clinical findings in patients with semicircular canal aplasia

Parameter	Number (%)
Patients (n)	12
Ears evaluated (n)	24
Type of SCC aplasia (ears)	
• Isolated LSCC aplasia	10 (41.7%)
• Bud-like LSCC remnants	3 (12.5%)
• Total SCC aplasia	3 (12.5%)
Laterality	
• Unilateral involvement	9 patients
• Bilateral involvement	3 patients
Associated inner ear findings	
• Vestibular hypoplasia (total SCC aplasia)	3/3 (100%)
• Enlarged/dysmorphic vestibule (LSCC aplasia)	Majority
• Cochlear hypoplasia	1 patient
Internal auditory canal	
• Narrow IAC (≤ 2.0 mm)	3 patients
Clinical findings	
• Sensorineural hearing loss	9/12 (75%)
• Vertigo symptoms	Rare
• Abnormal caloric test (tested patients)	2 patients
Syndromic associations	
• DiGeorge syndrome	2 patients
• Gitelman syndrome	1 patient

SCC, semicircular canal; LSCC, lateral semicircular canal; IAC, internal auditory canal.

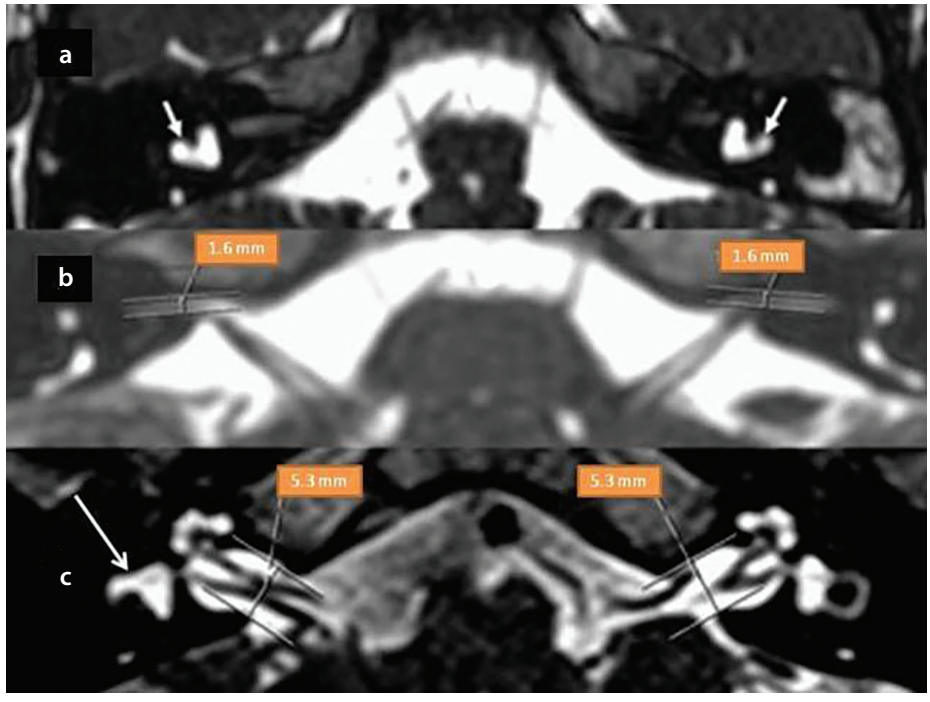


Figure 7. Three-dimensional T2-weighted SPACE magnetic resonance images in the axial plane. A 3-year-old boy with bilateral lateral semicircular canal (LSCC) aplasia shows bud-like structures (**a**, arrows) and bilateral narrow internal auditory canals (IACs) **(b)**. **(c)** A 2-year-old girl shows a bud-like formation of the right LSCC (arrow) with dysplastic and hypoplastic canal structures; the IAC diameters are normal.

Table 2. Distribution of findings of semicircular canal, cochlea, vestibular, oval and round window, and internal auditory canal

Case number	Age (year)	Gender	Side	Lateral SCC	Posterior SCC	Superior SCC	Vestibular aquaduct	Oval window	Cochlea	Round window	Vestibule	IAC diameter (mm)
1	23	M	R	Absent	Absent	Absent	Absent	Absent	Normal	Normal	Hypoplastic	4.1
			L	Present	Present	Present	Present	Absent	Normal	Normal	Normal	5.3
2	2	M	R	Present	Present	Present	Absent	Absent	Normal	Normal	Normal	3.2
			L	Absent	Present	Present	Present	Absent	Normal	Normal	Enlarged/ dysmorphic	2.6
3	22	M	R	Absent	Present	Present	Present	Absent	Normal	Normal	Enlarged/ dysmorphic	4.3
			L	Absent	Present	Present	Present	Absent	Normal	Normal	Enlarged/ dysmorphic	4.3
4	9	M	R	Present	Present	Present	Present	Absent	Normal	Normal	Normal	3.6
			L	Absent	Present	Present	Present	Absent	Normal	Normal	Enlarged/ dysmorphic	3.4
5	17	F	R	Present	Present	Present	Absent	Absent	Normal	Normal	Normal	3.8
			L	Absent	Present	Present	Absent	Absent	Normal	Normal	Enlarged/ dysmorphic	3.4
6	43	M	R	Absent	Present	Present	Present	Absent	Normal	Normal	Enlarged/ dysmorphic	4.7
			L	Absent	Present	Present	Absent	Absent	Normal	Normal	Enlarged/ dysmorphic	4.7
7	63	F	R	Absent	Present	Present	Absent	Absent	Normal	Normal	Enlarged/ dysmorphic	3.8
			L	Present	Present	Present	Absent	Absent	Normal	Normal	Normal	4.3
8	2	F	R	Bud (rudimentary)	Present	Present	Not assessed	Not assessed	Not assessed	Not assessed	Enlarged/ dysmorphic	5.3
			L	Present	Present	Present	Not assessed	Not assessed	Normal	Not assessed	Normal	5.3
9	3	M	R	Bud (rudimentary)	Present	Present	Present	Absent	Aplasia	Aplasia	Enlarged/ dysmorphic	1.6
			L	Bud (rudimentary)	Present	Present	Absent	Absent	Normal	Normal	Enlarged/ dysmorphic	1.6
10	2	F	R	Absent	Absent	Absent	Absent	Hypoplastic	Normal	Normal	Hypoplastic	2.0
			L	Absent	Absent	Absent	Absent	Hypoplastic	Aplasia	Normal	Hypoplastic	2.0
11	66	M	R	Present	Present	Present	Present	Absent	Normal	Normal	Normal	4.0
			L	Absent	Present	Present	Present	Absent	Aplasia	Normal	Enlarged/ dysmorphic	3.6
12	28	F	R	Hypoplastic	Present	Present	Present	Absent	Normal	Normal	Normal	5.0
			L	Present	Present	Present	Present	Absent	Normal	Normal	Normal	4.7

Note: Narrow IAC is defined as ≤ 2 mm. F, female; M, male; L, left; R, right; IAC, internal auditory canal; SCC, semicircular canal.

vestibular deficits, even when asymptomatic, may contribute to delayed motor milestones and impaired balance in children.[15]

Positioning our findings within the literature (Table 3), early tomography-era work by Phelps[13] first highlighted frequent LSCC dysmorphology but lacked the neural and membranous detail provided by modern cross-sectional imaging. Subsequent cochlear implant center series broadened the anatomic spectrum: Satar et al.[12] reported high rates of oval window anomalies and variable cochlear dysplasia with syndromic enrichment (predominantly CHARGE), whereas the CHARGE-focused cohort of Morimoto et al.[10] quantified cochlear aperture atresia and frequent posterior displacement of the facial nerve canal. Radiologic cohorts have also emphasized middle ear associations and aberrant courses of the facial nerve canal, which are crucial for surgical planning.[16] More recent vestibular function-oriented LSCC cohorts linked the absence of a central bony island with more severe caloric paresis and showed that bilateral LSCC dysplasia or aplasia often presents with bilateral vestibular loss.[14,15] Across these studies, LSCC anomalies consistently predominate, consistent with the embryologic vulnerability described by Jackler et al.[1] and by Sennaroglu and Saatci.[2] Our series aligns with this pattern but adds two practice-informing elements: first, a combined CT–MRI characterization that highlights IAC narrowing as an ancillary marker accompanying severe SCC malformations, and second, a novel syndromic association with Gitelman syndrome, expanding the syndromic spectrum beyond CHARGE and 22q11.2 deletion. Taken together, the comparative evidence supports routine scrutiny of the IAC and meticulous mapping of the facial and cochlear nerves before cochlear

Table 3. Comparison of reported cases of semicircular canal aplasia in the literature

Author/year	Number of patients/ears	SCC type	Associated malformations	Syndromic associations	Key findings
Phelps,[13] 1974	34	Mostly LSCC aplasia/dysplasia	Limited cochlear anomalies	Not specified	First systematic description using tomography
Satar et al.,[12] 2003	12	LSCC aplasia, total SCC aplasia	Cochlear dysplasia, oval window anomalies	CHARGE	Emphasized surgical challenges and FN anomalies
Morimoto et al.,[10] 2006	15 (CHARGE)	Absent or hypoplastic SCC	Cochlear aperture atresia, aberrant FN canal	CHARGE	Highlighted absent SCC as radiologic marker in CHARGE
Shin et al.,[16] 2009	10	LSCC aplasia, total SCC aplasia	Middle ear anomalies, FN canal anomalies	Mixed	CT/MR study; surgical mapping importance
Costa et al.,[11] 2020	8	Bilateral SCC malformations	Variable cochlear and vestibular findings	Mixed/ chromosomal	Reported hearing loss profiles and rehabilitation approaches
Azzahiri et al.,[2] 2023	1 case	Bilateral LSCC aplasia	Vestibular enlargement/ none	Non-syndromic	Rare bilateral aplasia; in some reports without hearing loss
Michel et al.,[3] 2016	1 case	Isolated LSCC aplasia	Vestibular and cochlear dysfunction	Non-syndromic	VEMP and VNG showed vestibular impairment
Parnes and Chernoff,[4] 1990	2	Bilateral SCC aplasia	Near-normal cochlea	Non-syndromic	Bilateral SCC aplasia with preserved cochlea
Kwak et al.,[14] 2020	22	LSCC aplasia/ dysplasia	Cochlea usually normal	Non-syndromic	Strong correlation between LSCC aplasia and caloric paresis
Yun et al.,[15] 2024	18	LSCC aplasia/ dysplasia	Absence of central bony island	Non-syndromic	Bilateral LSCC aplasia associated with bilateral vestibular loss
Present study	12	LSCC (41.7%), bud-like remnants, total SCC aplasia	Vestibular hypoplasia, IAC narrowing, cochlear hypoplasia (rare)	DiGeorge, Gitelman (novel)	First Gitelman association; IAC narrowing highlighted

CT, computed tomography; LSCC, lateral semicircular canal; MRI, magnetic resonance imaging; SCC, semicircular canal; IAC, internal auditory canal; PSCC, posterior semicircular canal; FN, facial nerve.

implantation, as well as systematic syndromic screening, particularly in pediatric patients and those with bilateral or total SCC aplasia.

From a surgical perspective, accurate identification of SCC aplasia and its associated anomalies is essential for safe and effective cochlear implantation. Abnormal vestibular morphology, IAC narrowing, or cochlear nerve hypoplasia may complicate electrode insertion and affect postoperative outcomes. Therefore, both CT and MRI are indispensable in the preoperative evaluation of these patients, providing complementary information about osseous, membranous, and neural structures.

This study offers one of the few systematic evaluations of SCC aplasia using high-resolution CT and MRI, highlighting radiologic markers that have not been consistently emphasized in previous reports. Its main contribution is the identification of a novel syndromic association between bilateral SCC aplasia and Gitelman syndrome, expanding the spectrum of systemic diseases linked to these malformations. By correlating embryologic timing with imaging findings, the study clarifies the developmental mechanisms underlying cochleovestibular anomalies. The findings are clinically relevant, emphasizing IAC narrowing and vestibular hypoplasia as key imaging markers for surgical planning. The reproducibility of the results is supported by standardized imaging protocols and independent review by experienced neuroradiologists.

Nonetheless, certain limitations must be acknowledged. The study's retrospective, single-center design and limited sample size restrict generalizability and preclude multivariate or receiver operating characteristic analyses. Additionally, vestibular testing and genetic evaluations were not consistently performed, especially in pediatric patients, which may have resulted in underestimation of functional deficits and syndromic associations. Despite these constraints, the study offers valuable insights by integrating radiologic and embryologic perspectives and introducing a previously unreported syndromic association.

SCC aplasia is not a single entity but a spectrum of malformations with varying embryologic timing, radiologic features, and clinical effects. Recognition of characteristic imaging findings, such as vestibular dysplasia, absence of the bony LSCC island, and narrowing of the IAC, should alert radiologists to the possibility of SCC aplasia. Additionally, identifying syndromic associations highlights the importance of comprehensive systemic and genetic testing. Future multicenter studies with larger patient cohorts, systematic vestibular testing, and genetic profiling will be essential to refine classification, clarify pathogenesis, and improve clinical management strategies for these rare but clinically significant abnormalities.

In conclusion, SCC aplasia represents a heterogeneous spectrum of congenital inner ear malformations with clinically significant anatomic variability. More severe forms of SCC aplasia are consistently associated with vestibular hypoplasia and narrowing of the IAC, reflecting their shared embryologic origin and direct relevance to surgical planning. Systematic evaluation of the IAC and vestibular structures using both CT and MRI is therefore essential, particularly in candidates for cochlear implantation. Finally, the identification of a novel association with Gitelman syndrome underscores the importance of comprehensive syndromic assessment in patients with SCC anomalies.

Footnotes

Conflict of interest disclosure

The authors declared no conflicts of interest.

References

1. Jackler RK, Luxford WM, House WF. Congenital malformations of the inner ear: a classification based on embryogenesis. *Laryngoscope*. 1987;97:2-14. [Crossref]
2. Azzahiri I, Kirami S, Benzalim M, Alj S. Isolated aplasia of the lateral semicircular canal without hearing loss: a case report. *Sch J Med Case Rep*. 2023;11(6):1234-1237. [Crossref]
3. Michel G, Espitalier F, Delemazure AS, Bordure P. Isolated lateral semicircular canal aplasia: functional consequences. *Eur Ann Otorhinolaryngol Head Neck Dis*. 2016;133(3):199-201. [Crossref]
4. Parnes LS, Chernoff WG. Bilateral semicircular canal aplasia with near-normal cochlear development. Two case reports. *Ann Otol Rhinol Laryngol*. 1990;99(12):957-959. [Crossref]
5. Sennaroglu L, Saatci I. A new classification for cochleovestibular malformations. *Laryngoscope*. 2002;112(12):2230-2241. [Crossref]
6. Papsin BC. Cochlear implantation in children with anomalous cochleovestibular anatomy. *Laryngoscope*. 2005;115:1-26. [Crossref]
7. Huang BY, Roche JP, Buchman CA, Castillo M. Brain stem and inner ear abnormalities in children with auditory neuropathy spectrum disorder and cochlear nerve deficiency. *AJNR Am J Neuroradiol*. 2010;31(10):1972-1979. [Crossref]
8. Sennaroğlu L, Bajin MD. Classification and current management of inner ear malformations. *Balkan Med J*. 2017;34(5):397-411. [Crossref]
9. Joshi VM, Navlekar SK, Kishore GR, Reddy KJ, Kumar EC. CT and MR imaging of the inner ear and brain in children with congenital sensorineural hearing loss. *Radiographics*. 2012;32(3):683-698. [Crossref]
10. Morimoto AK, Wiggins RH 3rd, Hudgins PA, et al. Absent semicircular canals in CHARGE syndrome: radiologic spectrum of findings. *AJNR Am J Neuroradiol*. 2006;27(8):1663-1671. [Crossref]
11. Costa JR, Coutinho M, Soares T, Almeida e Sousa C. Bilateral congenital semicircular canal malformation and hearing loss – case report. *Nascer Crescer Birth Growth Med J*. 2020;29(1):36-42. [Crossref]
12. Satar B, Mukherji SK, Telian SA. Congenital aplasia of the semicircular canals. *Otol Neurotol*. 2003;24(3):437-446. [Crossref]
13. Phelps PD. Congenital lesions of the inner ear, demonstrated by tomography: a retrospective study of 34 cases with special reference to the lateral semicircular canal. *Arch Otolaryngol*. 1974;100(1):11-18. [Crossref]
14. Kwak SH, Kim MK, Kim SH, Jung J. Audiological and vestibular functions in patients with lateral semicircular canal dysplasia and aplasia. *Clin Exp Otorhinolaryngol*. 2020;13(3):255-260. [Crossref]
15. Yun JM, Kim SH, Bae SH. Vestibular dysfunction in lateral semicircular canal dysplasia. *Front Neurol*. 2024;15:1341812. [Crossref]
16. Shin CH, Hong HS, Yi BH, et al. CT and MR imagings of semicircular canal aplasia. *J Korean Soc Radiol*. 2009;61(1):9-15. [Crossref]

Diagn Interv Radiol 2025; DOI: 10.4274/dir.2025.253518

HEAD AND NECK IMAGING

LETTER TO THE EDITOR

Copyright© Author(s) - Available online at dirjournal.org.
Content of this journal is licensed under a Creative Commons Attribution-NonCommercial 4.0 International License.

Reply: Letter to Editor: Dual-energy computed tomography-based volumetric thyroid iodine quantification: correlation with thyroid hormonal status, pathologic diagnosis, and phantom validation

Younghen Lee

Korea University College of Medicine, Ansan Hospital, Departments of Radiology, Ansan-si, Korea

Dear Editor,

I would like to express my sincere appreciation for your thoughtful consideration of my recent publication, "Dual-Energy Computed Tomography-Based Volumetric Thyroid Iodine Quantification: Correlation with Thyroid Hormonal Status, Pathologic Diagnosis, and Phantom Validation," in Diagnostic and Interventional Radiology.[1] I am particularly grateful for your suggestion regarding the potential utility of our dual-energy computed tomography (DECT)-based iodine quantification method for monitoring iodine organification before and after radioactive iodine (RAI) therapy. This insightful perspective highlights an important clinical application that we had not previously explored in depth.

Since the 1940s, RAI therapy using the oral administration of ^{131}I has been widely employed for the ablation of residual or recurrent differentiated thyroid carcinoma and normal thyroid tissue after total thyroidectomy, as well as for the normalization of hormonal function and volume reduction in benign thyroid diseases such as Graves' disease, toxic nodules, and non-toxic nodular goiter.[2] To optimize radioiodine uptake, patients are required to undergo a prolonged washout period of up to 6–8 weeks for iodine-containing agents. In some instances, treatment is initiated only after confirmation of 24-hour urinary iodine concentration (IC). Despite its widespread use, RAI therapy is associated with certain limitations, including radiation-induced thyroiditis, which may transiently exacerbate hyperthyroidism and, in rare instances, precipitate thyroid storm. Furthermore, larger thyroid glands or more severe hyperthyroidism may exhibit greater radioresistance, necessitating higher doses of ^{131}I. However, current RAI treatment protocols are typically based on 24-hour radioiodine uptake measurements or the clinician's experience, rather than the actual thyroid radiation dose, and there are reports of thyroid stunning caused by diagnostic use of ^{123}I or ^{131}I.[3]

In light of the foregoing considerations, we believe that DECT iodine quantification may offer unique advantages in the management of benign thyroid disorders–such as Graves' disease–in which the thyroid gland remains intact, as opposed to the post-thyroidectomy state. Notably, this technique eliminates the need for administration of ^{123}I or ^{131}I, thereby avoiding the risk of thyroid stunning and enabling simultaneous assessment of thyroid parenchymal IC and glandular volume without requiring additional patient visits. Furthermore, this approach could serve as a valuable adjunct for monitoring dynamic changes in thyroid hormonal status during and after therapeutic interventions.

In our study, non-contrast dual-energy neck computed tomography was utilized for the preoperative evaluation of lymph node metastasis in patients undergoing thyroid surgery. Nonetheless, the accuracy of iodine quantification was validated using phantom studies, and the associated radiation dose (volume computed tomography dose index: 3.4 ± 0.6 mGy; dose-length product: 61.1 ± 14.5 mGy·cm; effective dose: 0.36 ± 0.09 mSv) was found to be lower than that of conventional 24-hour radioiodine uptake measurements using ^{123}I (0.74 mSv) or ^{131}I (1.5 mSv).[4,5] However, as you have pointed out, further optimization of the ra-

Handling editor: Mehmet Ruhi Onur

Corresponding author: Younghen Lee

E-mail: younghen@korea.ac.kr

Received 14 June 2025; accepted 25 July 2025.

Epub: 18.08.2025

Publication date: 02.11.2026

DOI: 10.4274/dir.2025.253518

You may cite this article as: Lee Y. Reply: letter to editor: dual-energy computed tomography-based volumetric thyroid iodine quantification: correlation with thyroid hormonal status, pathologic diagnosis, and phantom validation. *Diagn Interv Radiol*. 2026;32(6):808-809.

diation dose and timing for thyroid parenchymal IC measurement using non-contrast DECT images remains necessary. We fully agree that additional validation studies, ideally in conjunction with nuclear medicine tracer uptake assessments, are required before this technique can be reliably incorporated into clinical decision-making.

Once again, I thank you for your constructive comments, which have substantially enhanced the clinical relevance and potential impact of our findings.

Footnotes

Conflict of interest disclosure

The author declared no conflicts of interest.

References

1. Lee Y. Dual-energy computed tomography-based volumetric thyroid iodine quantification: correlation with thyroid hormonal status, pathologic diagnosis, and phantom validation. *Diagn Interv Radiol.* 2025;31(3):226-233. [CrossRef]
2. Silberstein EB, Alavi A, Balon HR, et al. The SNMMI practice guideline for therapy of thyroid disease with ^{131}I 3.0. *J Nucl Med.* 2012;53(10):1633-1651. [CrossRef]
3. Park H-M, Gerard SK. Stunning: Untoward Effect of 131I Thyroid Imaging Prior to Radioablation Therapy. In: Wartofsky L, Van Nostrand D, eds. *Thyroid Cancer: A Comprehensive Guide to Clinical Management.* Totowa, NJ: Humana Press; 2006:337-345. [CrossRef]
4. Christner JA, Kofler JM, McCollough CH. Estimating effective dose for CT using dose-length product compared with using organ doses: consequences of adopting International Commission on Radiological Protection publication 103 or dual-energy scanning. *AJR Am J Roentgenol.* 2010;194(4):881-889. Erratum in: *AJR Am J Roentgenol.* 2010;194(5):1404. [CrossRef]
5. Giovanella L, Avram AM, Iakovou I, et al. EANM practice guideline/SNMMI procedure standard for RAIU and thyroid scintigraphy. *Eur J Nucl Med Mol Imaging.* 2019;46(12):2514-2525. [CrossRef]

Diagn Interv Radiol 2026; DOI: 10.4274/dir.2026.263679

INTERVENTIONAL RADIOLOGY

ORIGINAL ARTICLE

©Copyright 2026 Author(s) - Available online at dirjournal.org.
Content of this journal is licensed under a Creative Commons Attribution-NonCommercial 4.0 International License.

Tract embolization using absorbable gelatin sponge torpedoes following transsplenic or transhepatic access in pediatric patients

Mert Bayramoğlu
Yunus Emre Şentürk
Enes Muhammed Cantürk
Vügar Samadli
Levent Oğuzkurt

Koç University Hospital, Clinic of Radiology, İstanbul, Türkiye

PURPOSE

To evaluate the feasibility and early postprocedural hemorrhage outcomes of absorbable gelatin sponge (AGS) torpedo tract closure and to briefly describe the tract-closure method used following portal vein recanalization in pediatric native-liver extrahepatic portal vein obstruction.

METHODS

We retrospectively reviewed the cases of 18 consecutive children [11 boys, 7 girls; median age, 7 years (range, 5–12)] treated between 2020 and 2025 who underwent transsplenic and/or trans-hepatic portal vein recanalization with planned tract embolization using AGS torpedoes. The access sheath sizes were 5F and 6F, and unfractionated heparin was administered intraprocedurally in all cases. Procedures with inadvertent sheath dislodgment before embolization or intraprocedural wire perforation were excluded. The primary outcome was clinically significant access-tract hemorrhage within 24 hours, defined as a hemoglobin decrease > 2 g/dL together with an interval increase in intraperitoneal free fluid on ultrasound. Descriptive statistics were used; technical outcomes were summarized per tract and safety outcomes per patient.

RESULTS

Eighteen patients underwent embolization of 28 access tracts (13 transsplenic and 15 trans-hepatic). The median number of torpedoes used per tract was three (range, 2–4). All access tracts were successfully embolized with AGS torpedoes (28/28, 100%). No clinically significant access-tract hemorrhage occurred at either the patient (0/18) or tract level (0/28) within 24 hours after AGS embolization. Small perisplenic or perihepatic fluid collections were observed in 16 (88.9%) patients immediately after the procedure without an interval increase on follow-up ultrasound within 24 hours following the intervention.

CONCLUSION

AGS torpedo tract closure appears feasible and effective in preventing clinically significant access-tract hemorrhage after pediatric portal vein recanalization, including cases requiring dual access with introducer sheaths of up to 6F and intraprocedural anticoagulation. Prospective, large, multicenter studies using standardized hemostasis endpoints are needed to validate these preliminary findings.

CLINICAL SIGNIFICANCE

A readily available, absorbable material deployed as torpedoes can achieve controlled, layered parenchymal sealing in pediatric portal venous interventions.

KEYWORDS

Child, embolization, therapeutic, gelatin sponge, portal hypertension, portal vein

Handling editor: Bahri Üstünsöz

Corresponding author: Mert Bayramoğlu

E-mail: mbayramoglu@kuh.ku.edu.tr

Received 16 October 2025; revision requested 01 November 2025; last revision requested 14 December 2025; accepted 18 January 2026.

Epub: 04.02.2026

Publication date: 02.11.2026

DOI: 10.4274/dir.2026.263679

You may cite this article as: Bayramoğlu M, Şentürk YE, Cantürk EM, Samadli V, Oğuzkurt L. Tract embolization using absorbable gelatin sponge torpedoes following transsplenic or transhepatic access in pediatric patients. *Diagn Interv Radiol*. 2026;32(6):810-817.

Meso-Rex bypass surgery is a commonly used technique in pediatric patients with chronic extrahepatic portal vein obstruction (EHPVO) and its related complications. Recently, percutaneous portal vein recanalization has emerged as an alternative approach and has been included as a new recommendation in the Baveno VII consensus, providing a guideline-based rationale for clinical use in appropriate candidates.[1] Both strategies aim to redirect splanchnic blood flow to the liver, thereby restoring physiological hepatopetal portal flow, which, in turn, alleviates portal hypertension.[2]

Historically, safety concerns have surrounded percutaneous transsplenic and transhepatic portal venous interventions.[3-5] In contrast to diagnostic splenoportography, percutaneous portal vein recanalization procedures are technically more complex yet have become indispensable for managing portal venous complications in pediatric recipients of liver transplant.[6] However, studies specifically addressing native liver with chronic EHPVO in pediatric patients remain limited. In this cohort, hypersplenism-associated thrombocytopenia, intraprocedural anticoagulation, and the need for dual splenic/hepatic access with sheaths of up to 6F may increase the risk of access-tract hemorrhage, defined as bleeding from the percutaneous access tract through the hepatic or splenic parenchyma.[7-9] In children, even small-volume blood loss may be hemodynamically significant, underscoring the need for tract embolization.[10,11]

A variety of embolic agents have been described to minimize access-tract hemorrhage, albeit with limitations such as cost and the risk of non-target embolization or imaging artifacts. Nevertheless, there is no universally accepted optimal technique for tract embolization.[12-14] Absorbable gelatin sponge (AGS) has traditionally been used in slurry form, but its torpedo configuration may offer more controlled delivery and effective parenchymal sealing.

Given the limited evidence regarding AGS torpedoes for access-tract embolization in pediatric native-liver EHPVO, we describe our method for AGS torpedo tract closure and retrospectively evaluate its feasibility and early postprocedural hemorrhage outcomes following transsplenic and/or transhepatic recanalization.

Main points

- Following pediatric portal vein recanalization, absorbable gelatin sponge (AGS) torpedo tract embolization closed all 28 access tracts, with no cases meeting the 24-hour primary hemorrhage endpoint.
- The technique remained effective in cases requiring dual access, the use of sheaths of up to 6F, and intraprocedural anticoagulation. The technique described in this study enabled controlled, layered AGS torpedo delivery and helped avoid bleeding during sheath exchange.
- AGS torpedo embolization is a safe, cost-effective technique that minimizes imaging artifacts and preserves options for future percutaneous reinterventions.

Methods

Ethical approval

The study was conducted in accordance with the principles of the Declaration of Helsinki and was approved by the institutional ethics committee of the Koç University Committee on Human Research (approval number: 2025.440.IRB2.197, date: 08.10.2025). Due to the retrospective design, the requirement for informed consent for study participation was waived.

Study design and patient population

This retrospective, single-center cohort study included pediatric patients who underwent endovascular recanalization for chronic EHPVO between 2020 and 2025. A total of 24 patients were screened. Demographic data, clinical presentation, and the underlying etiologies of portal vein thrombosis were retrospectively extracted from medical records. The inclusion criteria were pediatric native-liver chronic EHPVO with relevant clinical manifestations. The exclusion criteria were procedures in which tract closure could not be attempted because the access sheath was inadvertently dislodged prior to embolization and procedures complicated by intraprocedural hemorrhage due to guidewire perforation during the recanalization attempt. These exclusion criteria were selected to focus the safety analysis on cases in which tract embolization was technically feasible, thereby avoiding the misclassification of hemorrhage events that were not preventable by tract closure. The study group selection process is summarized in Figure 1. Five patients were excluded because tract embolization could not be completed after sheath dislocation, and one patient was excluded due to vascular perforation during recanalization. The final cohort comprised 18 patients [11 boys, 7 girls; median age, 7 years (range, 5–12)].

Interventional procedure

Transsplenic or transhepatic access was obtained under ultrasound guidance using a 21-gauge introducer needle (AccuStick II, Cook Medical, Bloomington, IN, USA). A V-18 control wire (Boston Scientific, Natick, MA, USA) was advanced into the punctured parenchymal portal or splenic vein branch, followed by introducer placement and diagnostic portography. Following placement of a stiff guidewire (Amplatz Super Stiff, Boston Scientific, Marlborough, MA, USA), the introducer was withdrawn and a 5F or 6F 11-cm sheath (Avanti+ Sheath Introducer, Cordis,

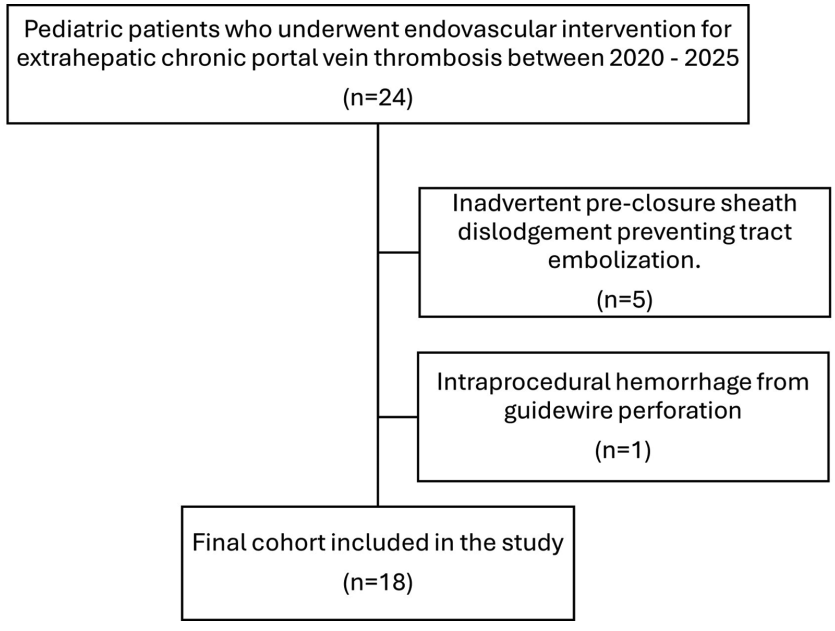


Figure 1. Flow diagram summarizing the study group selection process.

Santa Clara, CA, USA) inserted; for transsplenic access with tortuous splenic veins, a 6F 23-cm-long sheath (Brite Tip Sheath Introducer) was preferred to provide additional support.

In five procedures, sheath placement could not be maintained after the initial tract assessment; the procedure was therefore completed via alternative access, and these cases were excluded from the primary analysis. One additional procedure was excluded because guidewire perforation might have confounded access-tract hemorrhage assessment. All access tracts, including those from alternative access and the original tract in the perforation case, were successfully embolized.

Systemic anticoagulation was administered with an initial unfractionated heparin bolus (75 U/kg), followed by a continuous infusion of 20 U/kg per hour. Periprocedural activated clotting time monitoring was not performed. Recanalization, defined as the restoration of hepatopetal flow in the previously occluded main portal vein through balloon angioplasty (PTA), was achieved using standard wire and catheter techniques. No stents were used in this cohort, reflecting our institutional preference of avoiding permanent fixed-diameter implants in children that may not accommodate somatic growth and may complicate future reinterventions. At the end of the procedure, the sheath was withdrawn under ultrasound and fluoroscopic guidance until the tip was positioned just outside the vessel wall and clamped at the skin. The sheath was then cut approximately 3 cm proximal to the clamp. This approach was particularly useful with long sheaths, enabling non-deformed AGS delivery and more uniform tract packing, potentially achieving sealing with less material and a lower foreign-material burden. Sterile AGS blocks (Cutanplast, 50 × 70 × 10 mm; Mascia Brunelli S.p.A., Milan, Italy) were cut into rectangular strips along the short and horizontal axes with a scalpel. Each piece was manually rolled to form a tight cylindrical torpedo, sized to match the sheath lumen, and then shortened, yielding final torpedo lengths of approximately 15–25 mm. After instillation of a small volume of undiluted contrast medium into the sheath lumen, the torpedoes were introduced manually or using forceps. Under fluoroscopic guidance, the torpedoes were advanced through a manually stabilized sheath using a shortened manipulation catheter. The catheter and contrast-impregnated torpedoes were both visible under fluoroscopy, allowing precise placement. After deployment of the first torpedo, additional torpedoes were delivered as required, with intermittent contrast instillation and gradual unsheathing to ensure layered embolization until the whole tract was embolized (Figure 2). Embolization was completed using 2–4 torpedoes per tract. The procedure was concluded if either contrast was observed beyond the splenic or hepatic capsule during torpedo advancement or the sheath was freely mobile outside the parenchyma on fluoroscopy after unsheathing (Figure 3).

Follow-up

Ultrasound assessments were performed immediately after the procedure, on the evening of the procedure, and again prior to discharge at approximately 24 hours. During hospitalization, patients were clinically monitored for their general condition, abdominal pain, and signs of leakage or infection at the puncture site. Laboratory follow-up for hemorrhage included serial complete blood count measurements at approximately 4, 8, and 24 hours after the procedure, and analyses were based on the 24-hour values to align with the prespecified endpoint and to reduce variability from early post-procedural hemodilution and fluid shifts. Unfractionated heparin was discontinued at the end of the procedure and not resumed that day. In the absence of hemorrhage, all patients were started on low-molecular-weight heparin the following morning, which was continued for 1 month. After discharge, all patients returned at approximately 1 month for clinical evaluation and targeted Doppler ultrasound.

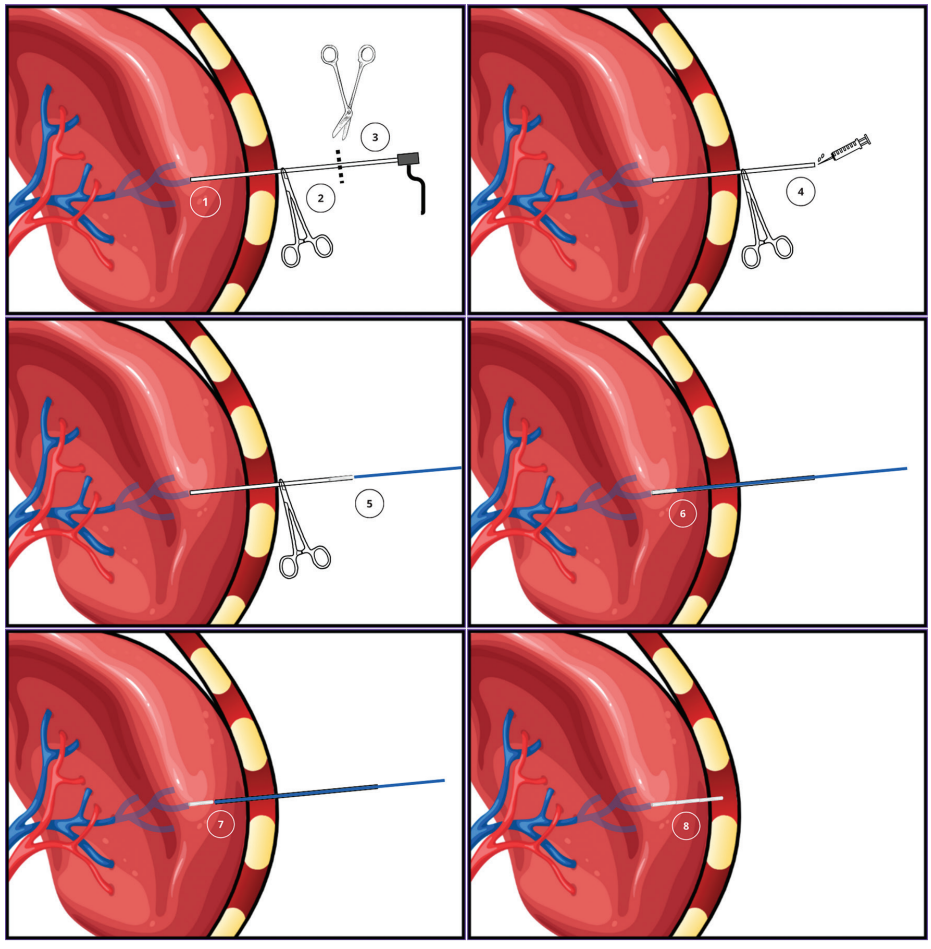


Figure 2. Schematic of the stepwise technique for absorbable gelatin sponge (AGS) torpedo tract embolization following transsplenic portal vein recanalization. Although the illustration relates to transsplenic access, the same technique is applicable to transhepatic embolization. (1) The sheath was withdrawn under ultrasound guidance until the tip lay just outside the vessel wall. (2) The sheath was clamped at the skin. (3) The sheath was cut approximately 3 cm proximal to the clamp. (4) A few drops of contrast were instilled into the sheath lumen. (5) An AGS torpedo was introduced into the lumen. (6) The torpedo was advanced to the sheath tip under fluoroscopic guidance using a manipulation catheter. (7) The sheath was gradually retracted using the unsheathing technique. (8) Additional torpedoes were delivered as required, with intermittent contrast instillation and gradual unsheathing to achieve complete tract embolization.

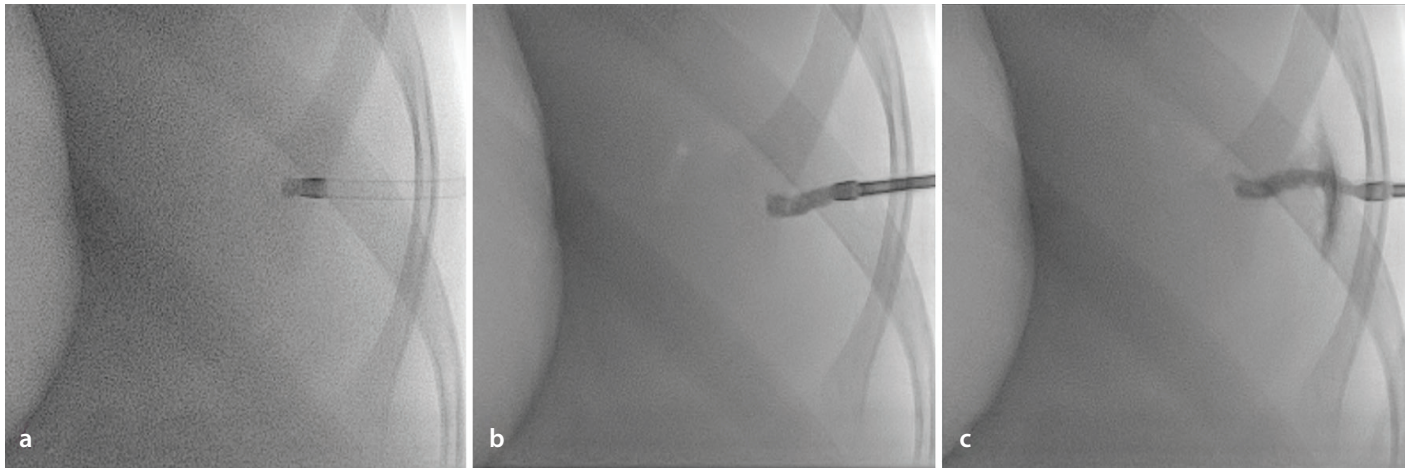


Figure 3. Fluoroscopic images demonstrate the stepwise process of absorbable gelatin sponge (AGS) torpedo tract embolization. **(a)** Contrast instilled into the sheath allows clear visualization of the first AGS torpedo after positioning. **(b)** Additional AGS torpedoes are sequentially deployed while the sheath is gradually retracted using the unsheathing technique. **(c)** A small amount of contrast leaking beyond the parenchymal surface can be used as an indicator of complete tract embolization.

Study endpoints

The primary outcome was the presence of postprocedural hemorrhage within 24 hours, ascertained by a retrospective review of laboratory and procedural records and defined as a hemoglobin decrease > 2 g/dL together with an interval increase in intraperitoneal free fluid on follow-up ultrasonography.[15]

Statistical analysis

Continuous variables were summarized as the median (range) and categorical variables as counts (%). Technical outcomes were summarized per tract and safety outcomes per patient. No hypothesis testing or imputation was performed. Given the exploratory design and zero primary-outcome events, no further inferential analyses were undertaken. Proportions are reported with 95% confidence intervals (CIs) using the Clopper–Pearson exact method; zero-event outcomes are presented with exact upper bounds.

Results

Study population

A total of 24 patients were screened between 2020 and 2025. Of these, 6 were excluded according to the predefined criteria, leaving 18 patients [11 boys, 7 girls; median age, 7 years (range, 5–12)] for analysis. The underlying etiologies of portal vein thrombosis were umbilical vein catheterization in 14 (77.8%) patients, umbilical infection in 1 (5.6%) patient, elevated von Willebrand factor in 1 (5.6%) patient, and *PAI-1* 4G/5G mutation in 1 (5.6%) patient; the etiology remained unknown in 1 (5.6%) patient (Table 1). The most common presenting features were hypersplenism, growth impairment, and hematochezia, which frequently co-occurred in the same patients.

Procedural details

All vascular entries were performed under ultrasound guidance, with successful cannulation in every patient. Of the 18 patients, percutaneous access was achieved using a transsplenic approach in 3 (16.7%) patients, a transhepatic approach in 5 (27.8%) patients, and a combined transsplenic–transhepatic approach in 10 (55.6%) patients. EHPVO recanalization was technically successful in 14 (77.8%) patients, with the portal vein restored with PTA (Figures 4 and 5). In four (22.2%) patients, recanalization could not be achieved. Across 18 patients, 28 access tracts were embolized with AGS torpedoes (13 transsplenic and 15 transhepatic), and embolization succeeded in all tracts (28/28, 100%). No patient met the prespecified primary outcome of clinically significant access-tract hemorrhage within 24 hours (0/18, 0.0%; 95% CI: 0.0%–15.3%). On a per tract basis, no clinically significant hemorrhage occurred after AGS embolization (0/28, 0.0%; 95% CI: 0.0%–10.1%). Among the transsplenic interventions, five (38.5%) were performed with a 6F sheath and eight (61.5%) with a 5F sheath. Among the transhepatic interventions, six (40.0%) were performed with a 6F sheath and nine (60.0%) with a 5F sheath. The median number of torpedoes used per tract was three (range, 2–4).

The median preprocedural hemoglobin level was 10.4 g/dL (range, 7.1–12.5), and the median postprocedural hemoglobin level was 10.3 g/dL (range, 6.1–12.6). The median

Table 1. Demographic and etiological characteristics of the study population

Characteristic	Value
Total patients	18
Gender	
Boys	11 (61.1%)
Girls	7 (38.9%)
Age	
Median (range)	7 (5–12) years
Etiology	
Umbilical vein catheterization	14 (77.8%)
Umbilical infection	1 (5.6%)
Elevated vWF	1 (5.6%)
PAI-1 gene mutations	1 (5.6%)
No known etiology	1 (5.6%)

vWF, von Willebrand factor.

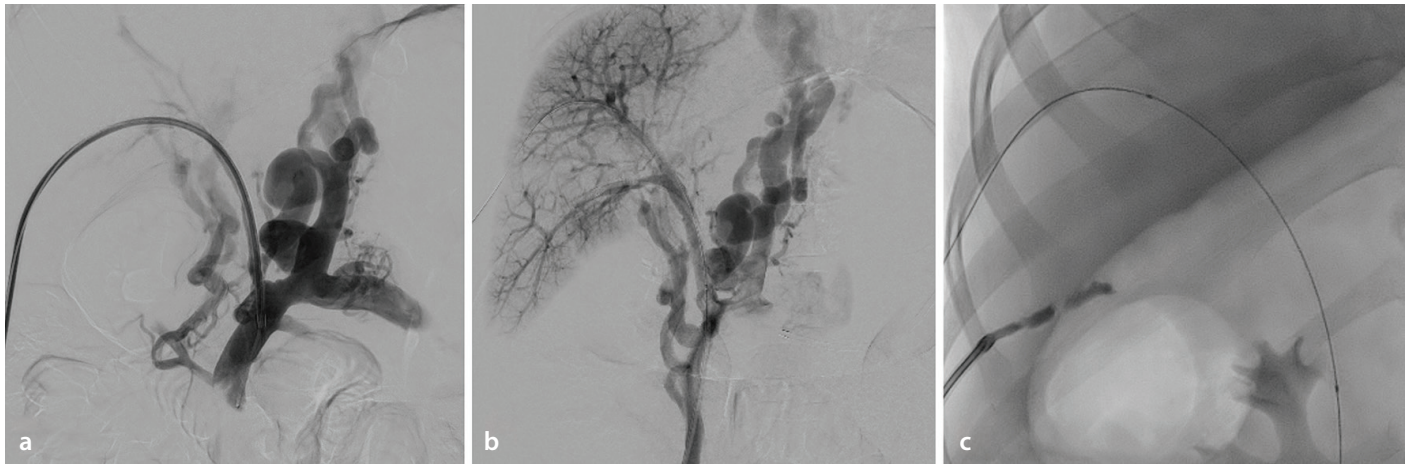


Figure 4. Combined transsplenic and transhepatic approach in a pediatric patient with chronic extrahepatic portal vein obstruction likely related to an umbilical vein catheter placed immediately after birth. **(a)** Transhepatic access was used to traverse the portal vein obstruction, and the portogram obtained before balloon dilatation demonstrates complete obstruction of the main portal vein with opacification of periportal collaterals. At this stage, no filling of the intrahepatic portal veins is observed. **(b)** Following angioplasty, simultaneous opacification of the segmental intrahepatic portal vein branches confirms restoration of hepatopetal flow through the recanalized main portal vein and its right portal branches. Although catheterization of the left portal branches was technically feasible through the transsplenic approach, further manipulation was avoided to prevent potential injury to the recanalized main portal vein. **(c)** Fluoroscopic image shows transhepatic tract embolization with absorbable gelatin sponge torpedoes. Small gaps left between torpedoes were acceptable, as the material expands after deployment to achieve complete sealing.

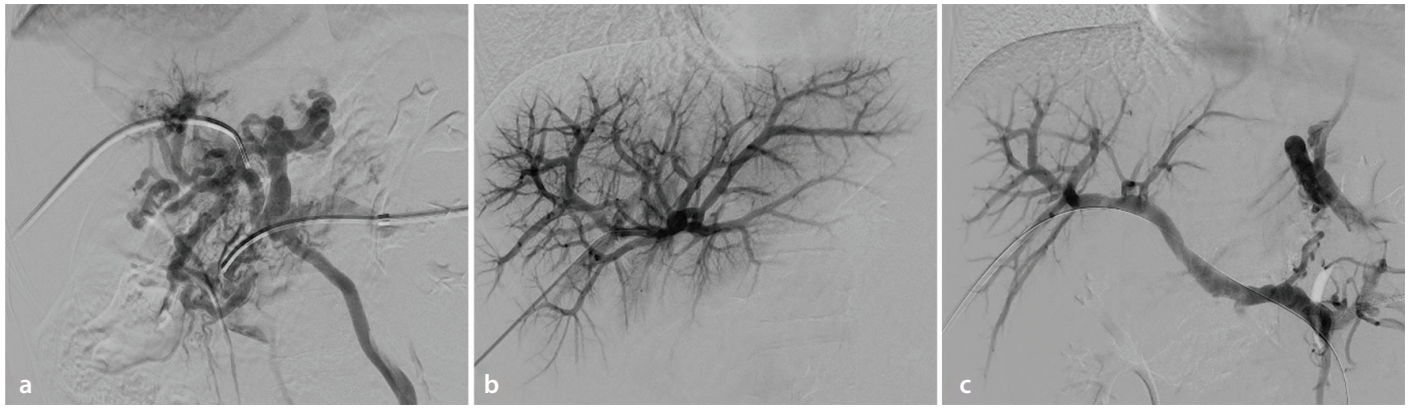


Figure 5. Combined transsplenic and transhepatic approach in a pediatric patient with chronic extrahepatic portal vein obstruction successfully recanalized using dual access. **(a)** Portogram obtained via the transsplenic approach demonstrates markedly dilated and tortuous collateral veins without opacification of the intrahepatic portal branches at this stage. **(b)** Portogram from the transhepatic access shows patent and unaffected intrahepatic portal veins. **(c)** Following successful recanalization, collateral filling has been resolved, and normal opacification of the main and intrahepatic portal veins is restored. Both access tracts were successfully embolized (images not shown).

hematocrit was 31.5% (range, 25.0%–39.0%) before the procedure and 32.0% (range, 22.0%–40.0%) after the procedure. The median platelet count was 77.5 $\times 10^9$/L (range, 46.0–558.0) pre-procedure and 80 $\times 10^9$/L (range, 55.0–560.0) post-procedure. The pre-procedural median international normalized ratio was 1.1 (range, 1.1–1.5), and the median activated partial thromboplastin time was 26.5 seconds (range, 15.4–31.9). A 0–1 g/dL decrease occurred in 4/18 (22.2%) patients, a 1-2 g/dL decrease in 5/18 (27.8%) patients, and a >2-g/dL decrease in 1/18 (5.6%) patients; hemoglobin increased in 6/18 (33.3%) patients and remained unchanged in 2/18 (11.1%) patients. No patient met the 24-hour hemorrhage endpoint. The pre- to postprocedural hemoglobin changes are summarized in Table 2.

Among the patients with postprocedural hemoglobin increases (n = 6), five received one peri-procedural unit of packed red blood cells (PRBCs), and the observed increase (0.2–2.1 g/dL; median, 0.7 g/dL) was therefore largely transfusion related; in the remaining patient, the 0.2-g/dL increase likely reflected hemoconcentration rather than true erythrocyte gain. The single patient with a > 2-g/dL hemoglobin decline required two units of PRBCs a few hours after the intervention for hematochezia. Consequently, this decline was attributable to gastrointestinal bleeding rather than procedure-related hemorrhage. No other patients received peri- or postprocedural PRBC transfusion. A small amount of perisplenic or perihepatic fluid was observed in 16 (88.9%) patients immediately after the procedure, with no subsequent increase on serial ultrasonography. At the approximately 1-month outpatient evaluation, no delayed access-tract complications were identified through clinical assessment or Doppler ultrasound, including no hemorrhage, pseudoaneurysm, abscess, or new intraperitoneal free fluid.

Six patients (age 1–8 years; median 3 years; five boys, 83.3%) were excluded, comprising five sheath dislodgments (83.3%) and one wire perforation (16.7%). In the six

excluded patients, portal vein recanalization was technically successful in four (66.7%), who subsequently underwent percutaneous transluminal angioplasty, whereas two (33.3%) had failed recanalization attempts. Hemoglobin decreased by a median of 1.6 g/dL (range, 0.8–2.4). Transfusion was required in three patients (50.0%), and no additional hemostatic interventions were necessary.

Discussion

In this retrospective cohort of children with native-liver EHPVO undergoing portal vein recanalization via transsplenic and/or transhepatic access, portal vein recanalization was technically successful in 14 of the 18 patients (77.8%), and tract embolization with AGS torpedoes, as described, was technically successful in all 28 access tracts; no patient experienced clinically significant access-tract hemorrhage within 24 hours. Cases in which the sheath was dislodged before embolization developed access-tract hemorrhage, underscoring the importance of performing tract closure whenever technically feasible.

AGS is a temporary, inexpensive, and widely available embolic agent that liquefies within around 7 days and is fully resorbed in 4–6 weeks. By absorbing several times its weight in water and concentrating platelets and clotting factors, the swelling gelatin matrix enhances hemostasis through mechanical compression while preserving the possibility of repeat percutaneous access through or near the prior tract.[16] This is particularly relevant in pediatric EHPVO, where distorted portal venous anatomy may leave a limited number of targetable vessels for percutaneous access. However, the use of AGS as a slurry may have two important drawbacks. First, uncontrolled injections, particularly in pediatric patients, carry the risk of non-target (including paradoxical) embolization.[17,18] Second, in cases with wide sheath tracts, the high-pressure flow in the portal vein after successful recanalization may displace the AGS slurry into the peritoneal cavity, leading to inadequate tract occlusion.[19] Our torpedo-based technique was designed to allow controlled, layered deployment of AGS torpedoes tailored to the sheath lumen, which may improve the stability of the access tract.

In an adult cohort, Tc et al.[18] reported AGS torpedo plugging of the transsplenic access tract after portal vein interventions in adults to be feasible and safe, with no cases requiring interventional or surgical treatment. Previous pediatric studies using various tract embolization materials have reported access-tract hemorrhage rates ranging from 0% to 27%, and most of these studies, particularly in recipients of liver transplant, have described AGS as a tract-embolization material used either as a slurry or as pledgets deployed directly within the tract (Table 3). Uller et al.[8] reported 11 tract closures in 10 pediatric patients, predominantly recipients of liver transplant, using eight transhepatic and three transsplenic accesses with 4F to 6F sheaths. Tracts were closed with AGS slurry, and one procedure was complicated by bleeding requiring a single transfusion, with no re-bleeding during follow-up. Monroe et al.[9] reported 26 children undergoing transsplenic portal venous access. Tract embolization with AGS was performed in 13/26 procedures, whereas ≤ 4F access tracts were not embolized and were not associated with hemorrhage. Intraperitoneal bleeding occurred in 2/26 procedures.[9] Similarly, Patel et al.[20] reported 42 percutaneous portal vein interventions in 21 pediatric recipients of liver transplant, performed via transhepatic portal venous access with a 5F sheath. Transhepatic tracts were plugged with AGS pledgets, and no major procedure-related hemorrhagic complications were reported. Consistent with these experiences, AGS torpedoes achieved successful tract closure in our cohort. By contrast, Pimpalwar et al.[7] reported a higher access-tract hemorrhage rate in 44 transsplenic portal interventions in 30 children, including 13 procedures for native-liver chronic portal vein thrombosis. Tracts were embolized with AGS pledgets, and intraperitoneal bleeding occurred in 12 of the 44 procedures, with all cases managed conservatively; anticoagulation was iden-

Table 2. Distribution of pre-to-postprocedural hemoglobin change in the study cohort

Periprocedural laboratory values		
Measure	Preprocedure, median (range)	Postprocedure, median (range)
Hemoglobin, g/dL	10.4 (7.1–12.5)	10.3 (6.1–12.6)
Hematocrit, %	31.5 (25.0–39.0)	32.0 (22.0–40.0)
Platelet count, $\times 10^9$/L	77.5 (46.0–558.0)	80.0 (55.0–560.0)
INR	1.1 (1.1–1.5)	—
[a]PTT, s	26.5 (15.4–31.9)	—
Distribution of pre-to-postprocedural hemoglobin change (ΔHb)		
ΔHb category	n	Percent of cohort
0–1 g/dL decrease	4	22.2%
1–2 g/dL decrease	5	27.8%
> 2 g/dL decrease	1	5.6%
Increase (ΔHb > 0)	6	33.3%
No change (ΔHb = 0)	2	11.1%
Total	18	100%

ΔHb, hemoglobin change; INR, international normalized ratio; [a]PTT, activated partial thromboplastin time.

Table 3. Summary of studies reporting tract embolization and access-tract hemorrhage in pediatric patients

Study	Closure technique	n patients/tracts	Access-tract hemorrhage
Uller et al.[8]	AGS slurry	9/11	1/11 (9%)
Monroe et al.[9]	AGS slurry, pledgets	26/13	2/26 (7.7%)
Patel et al.[20]	AGS pledgets	21/42	0/42 (0%)
Pimpalwar et al.[7]	AGS pledgets, microfibrillar collagen	30/44	12/44 (27%)
Marra et al.[13]	NBCA	11/15	1/15 (7%)
Our study	AGS torpedoes	18 /28	0/18 (0%)

AGS, absorbable gelatin sponge; NBCA, N-butyl cyanoacrylate.

tified as a significant risk factor for hemorrhage. Intraprocedural anticoagulation was routinely used in all cases in our cohort. A procedural factor that might contribute to hemorrhage is the brief interval during long-to-short sheath exchange; this potential window was avoided in the present study by clamping and cutting the sheath in the desired position, thereby eliminating the need for sheath exchange and minimizing the risk of hemorrhage even when long sheaths were used.

One of the most employed tract-embolization methods in adults is embolization with an ethiodized oil–N-butyl cyanoacrylate (NBCA) mixture, but published pediatric experience remains limited. Marra et al.[13] reported 15 percutaneous portal vein interventions, in which the tract was embolized with this technique in 11 children with non-cirrhotic EHPVO, performed via transhepatic, transsplenic, or combined access. Hemoperitoneum occurred in one procedure, which was managed conservatively.[13] Adoption of an ethiodized oil–NBCA mixture is a potential option for tract embolization; however, its use is technically demanding, requires meticulous flow control, and the risk of inadvertent embolization is of particular concern in pediatric patients. However, to prevent non-target embolization, a combination of coils and an ethiodized oil–NBCA mixture may be employed. Pediatric data on coil-based tract embolization remains limited to isolated cases;[21] Ohm et al.[22] reported no access-tract hemorrhage using this technique in adults. Permanent metallic embolic materials such as coils and vascular plugs may be less desirable in children, as they can produce artifacts on follow-up magnetic resonance imaging, carry a risk of foreign-body reaction in immunosuppressed patients, and impede repeat access when reintervention is required.[8,12,18] Although studies describing tract embolization in adults using vascular closure devices as an alternative are available, their routine use for portal or splenic parenchymal tract closure may not be feasible due to the relatively high cost.[23] Therefore, AGS torpedoes may offer a cost-effective and widely available alternative to ethiodized oil–NBCA embolization, coils, and device-based options such as vascular plugs or closure devices.[19]

Our study has several limitations. First, it is a single-center, retrospective study with a small sample size and no comparator arm using other widely used tract-embolization techniques. Our results should be interpreted as feasibility and safety data for AGS torpedoes rather than definitive evidence of superiority; adequately powered multicenter studies with standardized endpoints and matched or randomized comparators are needed. Accordingly, our results are intended to inform tract-closure techniques in this pediatric setting and were not designed to assess recanalization efficacy or comparative effectiveness. Second, we excluded procedures in which tract embolization could not be attempted because the access sheath was dislodged before closure; although consistent with our efficacy-focused objective, this may bias hemorrhage estimates downward and restrict generalizability to cases in which tract closure is technically feasible. In addition, access profiles in our cohort were limited to 5F and 6F sheaths; therefore, extrapolation to larger sheath sizes (e.g., 8F and 9F, used for stent delivery in other settings) should be performed cautiously. When tract embolization cannot be performed, close hemodynamic and laboratory monitoring, prompt correction of coagulopathy, and a low threshold for transfusion are essential to mitigate hemorrhagic risk. In exceptional cases, surgical management may be considered in a multidisciplinary setting. Finally, selection bias was unavoidable given the heterogeneous etiologies of portal vein obstruction, although most chronic cases were related to prior umbilical venous catheterization.

In conclusion, this preliminary study suggests that torpedo-based tract closure with AGS using a transsplenic and/or transhepatic approach appears feasible and was not associated with clinically significant hemorrhagic complications after recanalization of EHPVO, particularly in procedures requiring dual access and sheaths of up to 6F performed under routine intraprocedural anticoagulation. These findings should be interpreted as technique-focused feasibility and early safety data, rather than evidence of superiority, and warrant verification in larger comparative studies.

Footnotes

Conflict of interest disclosure

The authors declared no conflicts of interest.

References

1. de Franchis R, Bosch J, Garcia-Tsao G, Reiberger T, Ripoll C; Baveno VII Faculty. Baveno VII - Renewing consensus in portal hypertension. *J Hepatol*. 2022;76(4):959-974. [Crossref]
2. Lautz TB, Keys LA, Melvin JC, Ito J, Superina RA. Advantages of the meso-Rex bypass compared with portosystemic shunts in the management of extrahepatic portal vein obstruction in children. *J Am Coll Surg*. 2013;216(1):83-89. [Crossref]
3. Hoevels J, Lunderquist A, Tylén U. Percutaneous transhepatic portography. *Acta Radiol Diagn (Stockh)*. 1978;19(4):643-655. [Crossref]
4. Gayed A, Bridges PH, Johnson DT. A Review of transsplenic access for portal vein interventions. *Semin Intervent Radiol*. 2022;39(4):441-445. [Crossref]
5. Lucey BC, Boland GW, Maher MM, Hahn PF, Gervais DA, Mueller PR. Percutaneous nonvascular splenic intervention: a 10-year review. *AJR Am J Roentgenol*. 2002;179(6):1591-1596. [Crossref]
6. Rigsby CK, Superina R, Alonso EM, Mueller PR, Donaldson JS. Interventional radiology in the pediatric liver transplant patient. *Semin Intervent Radiol*. 2002;19(1):59-72. [Crossref]
7. Pimpalwar S, Chinnadurai P, Hernandez A, Kukreja K, Siddiqui S, Justino H. Trans-splenic access for portal venous interventions in children: do benefits outweigh risks? *Cardiovasc Intervent Radiol*. 2018;41(1):87-95. [Crossref]
8. Uller W, Müller-Wille R, Grothues D, et al. Gelfoam for closure of large percutaneous transhepatic and transsplenic puncture tracts in pediatric patients. *Rofo*. 2014;186(7):693-697. [Crossref]
9. Monroe EJ, Speir EJ, Hawkins CM, Shivaram G, Koo KSH, Gill AE. Transsplenic splenoportography and portal venous interventions in pediatric patients. *Pediatr Radiol*. 2018;48(10):1441-1450. [Crossref]
10. Howie SR. Blood sample volumes in child health research: review of safe limits. *Bull World Health Organ*. 2011;89(1):46-53. [Crossref]
11. Saad WE, Madoff DC. Percutaneous portal vein access and transhepatic tract hemostasis. *Semin Intervent Radiol*. 2012;29(2):71-80. [Crossref]
12. Grosse U, Brechtel K, Ketelsen D, et al. Portal vein recanalization and embolization of the transsplenic puncture tract using an Amplatzer® vascular plug: a case report. *BMC Res Notes*. 2015;8:193. [Crossref]
13. Marra P, Franchi-Abella S, Hernandez JA, et al. Percutaneous recanalization of non-cirrhotic extrahepatic portal vein obstruction in children: technical considerations in a preliminary cohort. *Eur Radiol*. 2025;35(6):3262-3269. [Crossref]
14. Marra P, Carbone FS, Augello L, et al. Embolisation of the parenchymal tract after percutaneous portal vein catheterization: a retrospective comparison of outcomes with different techniques in two centres. *CVIR Endovasc*. 2022;5(1):48. [Crossref]
15. Gultekingil A, Teksam O, Gulsen HH, Ates BB, Saltık-Temizel İN, Demir H. Risk factors associated with clinically significant

gastrointestinal bleeding in pediatric ED. *Am J Emerg Med*. 2018;36(4):665-668. [Crossref]

16. Whalen S, Tanious M. Temporary Embolic Agents. *Semin Intervent Radiol.* 2024;41(2):226-232. [Crossref]
17. Lord DJ, Chennapragada SM. Embolization in neonates and infants. *Tech Vasc Interv Radiol*. 2011;14(1):32-41. [Crossref]
18. Tc M, N K, Ss Y, Fk W, Bc M, Jb H. Transsplenic tract closure after transsplenic portal venous access using gelfoam-based tract plugging. *CVIR Endovasc*. 2023;6(1):37. [Crossref]
19. Nota T, Kageyama K, Yamamoto A, et al. Feasibility of gel-like radiopaque embolic material using gelatin sponge and contrast agent for tract embolization after percutaneous treatment. *PLoS One.* 2023;18(2):e0281384. [Crossref]
20. Patel R, Mahaveer J, Tahir N, Rajwal S, McClean P, Patel JV. Outcomes of percutaneous portal vein intervention in a single UK paediatric liver transplantation programme. *Cardiovasc Intervent Radiol*. 2018;41(1):96-103. [Crossref]
21. Bertram H, Pfister ED, Becker T, Schoof S. Transsplenic endovascular therapy of portal vein stenosis and subsequent complete portal vein thrombosis in a 2-year-old child. *J Vasc Interv Radiol*. 2010;21(11):1760-1764. [Crossref]
22. Ohm JY, Ko GY, Sung KB, Gwon DI, Ko HK. Safety and efficacy of transhepatic and transsplenic access for endovascular management of portal vein complications after liver transplantation. *Liver Transpl*. 2017;23(9):1133-1142. [Crossref]
23. Karluka I, Mazıcan M. Single Angio-Seal™ Device as a Simplified and technically feasible alternative for tract closure in percutaneous portal vein access: a retrospective study. *Diagnostics (Basel)*. 2025;15(10):1266. [Crossref]

Diagn Interv Radiol 2026; DOI: 10.4274/dir.2026.263745

INTERVENTIONAL RADIOLOGY

ORIGINAL ARTICLE

©Copyright 2026 Author(s) - Available online at dirjournal.org.
Content of this journal is licensed under a Creative Commons Attribution-NonCommercial 4.0 International License.

Image-guided, urethra-sparing transperineal radiofrequency ablation for benign prostatic hyperplasia: a prospective bicenter outpatient study

Thiago Franchi Nunes[1]
Denis Szejnfeld[2]
Públio Cesar Cavalcante Viana[3]
Flávio Scavone Stefanini[1]
Vinicius Adami Vayego Fornazari[4]
Túlio Fabiano de Oliveira Leite[5]
Alvaro Sadek Sarkis[6]
Hugo Alexandre Socrates de Castro[1]

[1]Interventix, Rua Dr. Antônio Alves Arantes, Campo Grande, Brazil

[2]Paulista School of Medicine – Federal University of São Paulo (UNIFESP), Department of Diagnostic Imaging, São Paulo, Brazil

[3]Hospital Sírio-Libanês, Clinic of Radiology, São Paulo, SP, Brazil

[4]University of Florida Faculty of Medicine, Department of Radiology, Division of Vascular and Interventional Radiology, Jacksonville, United States of America

[5]Uberlandia Medical Center, Clinic of Radiology, Uberlândia, Brazil

[6]Associate Professor Hospital das Clínicas, University of São Paulo Medical School (HC-FMUSP), Urologist and Medical Director, Hospital Sírio-Libanês, São Paulo, Brazil

PURPOSE

To evaluate the feasibility, reproducibility, and clinical outcomes of an image-guided, urethra-sparing transperineal radiofrequency ablation (TPTA) strategy for benign prostatic hyperplasia (BPH) in an outpatient interventional radiology setting.

METHODS

This was a prospective, bicenter, non-randomized study of consecutive men with moderate-to-severe lower urinary tract symptoms (LUTS) refractory or intolerant to medication treated with ultrasound-guided, urethra-sparing TPTA. Outcomes included the International Prostate Symptom Score (IPSS), quality of life, maximum urinary flow rate (Qmax), post-void residual volume (PVR), prostate volume, prostate-specific antigen (PSA), and ejaculatory function [assessed using the Male Sexual Health Questionnaire–Ejaculatory Dysfunction Short Form (MSHQ-EjD-SF)]; complications were graded using the Clavien–Dindo classification. The primary endpoint was a 12-month change in ejaculatory function; secondary endpoints included composite clinical response (≥ 30% IPSS reduction without retreatment) and urinary and structural changes.

RESULTS

At 12 months, clinically meaningful improvements were observed across patient-reported symptoms and concordant objective functional and anatomical parameters in a carefully selected outpatient cohort. The median IPSS decreased from 19.5 at baseline to 5.0 at 6 months and 4.0 at 12 months ($P < 0.001$), accompanied by sustained increases in the Qmax and reductions in PVR, prostate volume, and PSA (all $P < 0.001$). Among sexually active men, MSHQ-EjD-SF function scores remained stable during the follow-up period, and antegrade ejaculation was preserved in 90% of patients. The composite clinical response rate (≥ 30% IPSS reduction without retreatment) was 97.1% at both 6 and 12 months, with no device-related Clavien–Dindo ≥ III complications observed.

CONCLUSION

These findings suggest that image-guided, urethra-sparing TPTA is a reproducible outpatient interventional radiology procedure capable of achieving clinically meaningful symptom relief while preserving ejaculatory function, supporting further comparative and multicenter evaluation.

CLINICAL SIGNIFICANCE

Urethra-sparing TPTA has proven to be a safe, feasible, and effective treatment for LUTS and may represent a minimally invasive and effective alternative for BPH.

KEYWORDS

Benign prostatic hyperplasia, minimally invasive surgical therapy, transperineal radiofrequency ablation, urethra-sparing technique, ejaculatory function preservation, outpatient procedure

Handling editor: Barbaros Çil

Corresponding author: Túlio Fabiano de Oliveira Leite

E-mail: tuliofabiano@gmail.com

Received 29 December 2025; revision requested 28 January 2026; accepted 12 February 2026.

Epub: 02.03.2026

Publication date: 02.11.2026

DOI: 10.4274/dir.2026.263745

You may cite this article as: Nunes TF, Szejnfeld D, Cavalcante Viana PC, et al. Image-guided, urethra-sparing transperineal radiofrequency ablation for benign prostatic hyperplasia: a prospective bicenter outpatient study. *Diagn Interv Radiol*. 2026;32(6):818-827.

Benign prostatic hyperplasia (BPH) is a leading cause of lower urinary tract symptoms (LUTS) in aging men, substantially impairing quality of life (QoL) and generating substantial healthcare costs.[1] Although transurethral resection of the prostate remains the gold standard, minimally invasive surgical therapies have been developed to reduce morbidity.[2]

Transurethral options such as prostatic urethral lift and water-vapor thermal therapy (Rezūm) provide symptom relief but require urethral instrumentation, which may contribute to discomfort and ejaculatory dysfunction (EjD).[3] By contrast, urethra-sparing approaches aim to preserve periurethral structures and potentially maintain sexual function while ensuring durable outcomes.[4]

However, systematic evaluation of ejaculatory function following urethra-sparing procedures in Western populations is limited, and few studies have incorporated validated tools such as the Male Sexual Health Questionnaire–EjD Short Form (MSHQ-EjD-SF).[5,6] We therefore report the 12-month clinical, functional, and safety outcomes of ultrasound-guided transperineal radiofrequency ablation (TPTA) performed in an outpatient bicenter cohort.

From an interventional radiology perspective, minimally invasive treatments for BPH have progressively shifted toward image-guided, tissue-selective approaches that prioritize procedural safety, anatomical precision, and functional preservation. In this context, transperineal access under real-time ultrasound guidance enables direct targeting of adenomatous tissue while avoiding urethral instrumentation, potentially reducing periurethral injury and preserving ejaculatory pathways. However, prospective data evaluating the reproducibility and functional profile of urethra-sparing, image-guided TPTA in routine outpatient practice remain limited.

Main points

- Urethra-sparing transperineal radiofrequency ablation preserves urological and sexual function.
- This strategy represents a treatment option for benign prostatic hyperplasia.
- This treatment option provides an alternative for patients otherwise ineligible for standard treatments.

Methods

Study design and rationale

This study was conceived as a pragmatic, prospective, bicenter cohort evaluating the feasibility, safety, and functional outcomes of a urethra-sparing, ultrasound-guided TPTA strategy in routine outpatient practice. Given the early clinical adoption phase of this technique, a non-comparative design was intentionally selected to prioritize procedural safety, technical reproducibility, and patient-reported functional outcomes before formal comparative evaluation against established surgical or minimally invasive therapies. All procedures complied with institutional and national standards and the 1964 Declaration of Helsinki, and written informed consent was obtained from all participants. This study was approved by Institutional Review Board of Paulista School of Medicine – Federal University of São Paulo (UNIFESP) (protocol number: CAAE: 74939723.1.0000.5505, date: 20.02.2024)

Participants

Consecutive men aged ≥ 50 years with moderate-to-severe LUTS [International Prostate Symptom Score (IPSS) ≥ 8] who were refractory or intolerant to medication or dissatisfied with α-blockers or 5α-reductase inhibitors (5-ARIs) were included. Additional requirements were a prostate volume of 30–200 mL on transrectal ultrasound or multiparametric magnetic resonance imaging (mpMRI) and a maximum urinary flow rate (Qmax) < 15 mL/s or catheter dependence despite medication. Prostate-specific antigen (PSA) levels were generally < 4 ng/mL, with higher values permitted when prostate cancer was excluded (mpMRI/biopsy). Exclusion criteria included known or suspected prostate cancer, neurogenic bladder, urethral stricture, bladder stones, or uncontrolled systemic disease. Baseline assessment comprised the IPSS, QoL, PSA, uroflowmetry, post-void residual volume (PVR), and prostate imaging. Demographics, American Society of Anesthesiologists class, comorbidities, medication use, and intravesical prostatic protrusion (IPP), when present, were recorded (Figure 1). At baseline, two patients (5.9%) had an indwelling urinary catheter. Given this very small number, no stratified subgroup analysis was prespecified or performed.

Preliminary 3-month outcomes from an earlier phase of this prospective cohort have been reported previously. The present manuscript reports the planned extended follow-up of the same cohort up to 12 months and includes additional longitudinal analyses and outcomes not available in the prior report.

Procedure

After sedation, the patient was placed in the lithotomy position (Figure 2a), and the perineum was prepared and draped under sterile conditions. The Aplio A ultrasound system (Canon Medical Systems Co., Ltd., Otawara, Tochigi, Japan) with a high-frequency biplanar end-fire probe was used in all procedures. With the patient under sedation, the probe was gently inserted into the anal canal for continuous prostate visualization, and the gland was assessed for morphology, echogenicity, capsule integrity, prostate volume, and its relationship with the bladder wall. After ultrasound documentation, a 20G × 20 cm needle was advanced under transperineal ultrasound guidance to perform bilateral perineal nerve block with 5 mL of 1% lidocaine per side, followed by an additional 5 mL per side for periprostatic nerve block. A 17G radiofrequency ablation (RFA) probe with a 10-mm active tip (Amica, HS Hospital Service S.p.A., Italy) was then positioned in the anterosuperior transition zone unilaterally (Figure 2b). For safety, ablation was always performed at a distance of at least 5 mm from the urethra and bladder floor to reduce the risk of stenosis, retrograde ejaculation, and cystitis. The RFA probe was powered at 40 W, and the needle was slowly pulled caudally, allowing real-time visualization of tissue vaporization. After completing ablation on one side of the transition zone, the procedure was repeated contralaterally. The device parameters, periprocedural medications, and discharge criteria are summarized in Table 1.

Postprocedure and follow-up

Routine catheterization was avoided. Acute urinary retention (AUR) was defined as the inability to void within 2 h with discomfort or PVR > 300 mL and was managed with temporary catheterization. Patients were discharged the same day per standard ambulatory criteria. Follow-up at 1, 3, 6, and 12 months included the IPSS, QoL, Qmax, PVR, PSA, prostate volume, ejaculatory function, adverse events, and medication changes. Complications were graded using the modified Clavien–Dindo classification.

Postprocedural contrast-enhanced ultrasound (CEUS) was performed to assess early ablation-related perfusion changes. CEUS

FLOWCHART

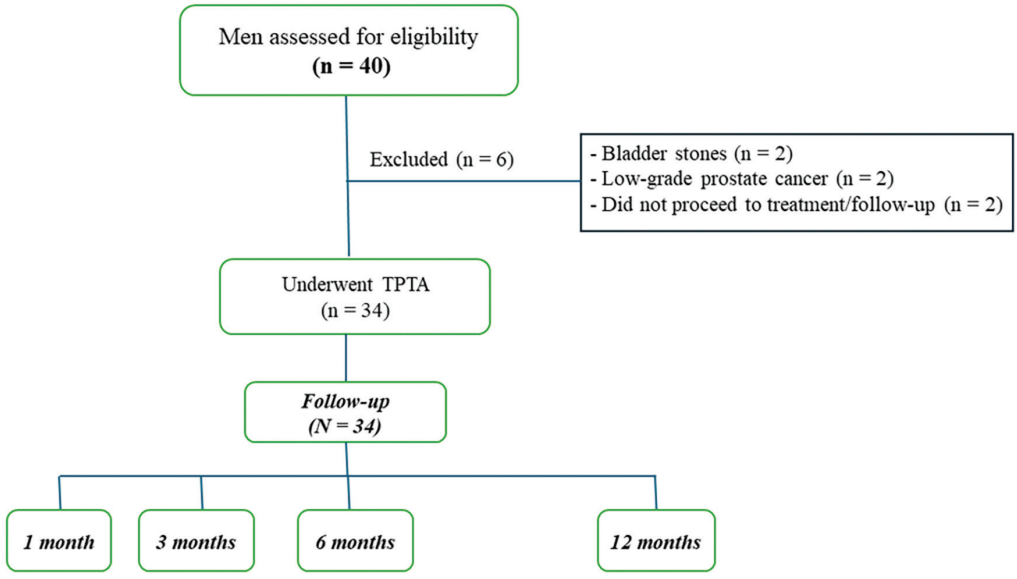


Figure 1. Flowchart of study population selection. TPTA, transperineal radiofrequency ablation.

Table 1. Periprocedural devices, medications, and parameters by center

Item	Center 1	Center 2	Notes
TRUS platform/probe	Aplio A-series, biplanar end-fire	Aplio A-series, biplanar end-fire	Equivalent resolution and needle-tracking workflow
Access needle	17G transperineal introducer	17G transperineal introducer	
RF generator	Commercial unit (HS Hospital Service Amica RF)	Commercial unit (STARmed)	Both temperature-controlled
RF electrode	Internally cooled monopolar, 10-mm active tip	Internally cooled monopolar, 10-mm active tip	Same geometry across centers
Irrigation/pump	Peristaltic pump (continuous saline)	Peristaltic pump (continuous saline)	Maintains tip temperature < 60 °C
Typical power range	70–150 W	35–70 W	Tailored to gland size and tissue response
Urethral safety margin	≥ 5 mm from urethra/bladder neck	≥ 5 mm from urethra/bladder neck	Mandatory criterion for adequacy
Sedation	Midazolam 1–3 mg IV + fentanyl 25–100 µg IV	Same	Titrated to moderate sedation
Local anesthesia	1% lidocaine 10–20 mL/side periprostatic	Same	Field block
Antimicrobial prophylaxis (cohort)	Levofloxacin 750 mg PO q24h from −48 h to +7 d	Same	Legacy regimen used in this series
Current prophylaxis (policy)	Cefazolin 1–2 g IV single dose (± ≤ 48 h extension per risk)	Same	Preferred for future cases; culture-guided
Ancillary meds (cohort)	Tamsulosin 0.4 mg qd + prednisone 20 mg qd × 7 d	Same	Started 48 h pre-procedure
CEUS availability	Yes (routine when feasible)	Yes (selective)	SonoVue® 2.4 mL + 5 mL saline
Trial-of-void	Attempt within 2 h	Same	AUR: PVR > 300 mL or discomfort → Foley 16F 48–72 h
Discharge criteria	Aldrete ≥ 9, PVR < 100 mL, stable vitals, oral analgesia	Same	Same-day discharge intended

AUR, acute urinary retention; CEUS, contrast-enhanced ultrasound; MCID, minimal clinically important difference; PVR, post-void residual; QoL, quality of life; RF, radiofrequency; TRUS, transrectal ultrasound.

enabled real-time visualization of non-perfused ablation zones and facilitated identification of any residual enhancing tissue suggestive of incomplete treatment, thereby providing an early functional assessment of ablation adequacy beyond morphological imaging alone.

Outcomes

The prespecified primary endpoint was a 12-month change in ejaculatory function using the validated MSHQ-EjD-SF (3 items on function, 1 item on bother). Preservation of antegrade ejaculation was captured by a structured patient-reported item and considered alongside the MSHQ domains. Secondary endpoints were the 12-month composite responder rate (≥ 30% IPSS reduction without BPH retreatment) and absolute and percentage changes in the IPSS, Qmax, PVR, prostate volume, and PSA. Minimal clinically important differences (MCIDs) were IPSS ≥ 3 points, QoL ≥ 1 point, and Qmax ≥ 3 mL/s; proportions were reported with exact 95% confidence intervals (CIs).

Follow-up visits were scheduled at 1, 3, 6, and 12 months after the procedure. The 1- and 3-month visits were primarily intended to assess early safety and recovery parameters, including adverse events, voiding status, catheter dependence, and medication discontinuation. The 6- and 12-month visits were prespecified as the main timepoints for evaluation of sustained efficacy outcomes, including symptom scores, functional parameters, prostate volume changes, and patient-reported sexual and ejaculatory outcomes.

Database lock and handling of missing data

All treated participants completed the scheduled 12-month clinical follow-up. Therefore, no attrition-related sensitivity analyses were required. For outcomes not measurable at baseline in catheter-dependent patients (e.g., uroflowmetry or PVR), analyses were conducted on an observed-case basis with explicit denominators reported for each endpoint.

Statistical analysis

Continuous variables are summarized as the median [interquartile range (IQR)] and categorical variables as a number (percentage). Paired comparisons were performed using the Wilcoxon signed-rank test, as appropriate. Between-group comparisons were assessed using the Mann–Whitney U test. Proportions are presented with exact 95% CIs. A two-sided P value < 0.05 was considered statistically significant.

Responder analyses were additionally reported using MCID thresholds commonly applied in BPH/LUTS research. For the IPSS, an improvement of ≥ 3 points was used as a clinically meaningful change. For the Qmax, a ≥ 2 mL/s increase was used as a pragmatic clinically relevant threshold. Because a formally established MCID for the MSHQ-EjD-SF has not been clearly defined, changes in ejaculatory scores were interpreted cautiously and complemented by reporting the clinically intuitive endpoint of antegrade ejaculation preservation.

Results

Patient flow and baseline

Of the 40 men screened, 6 were excluded (bladder stones, n = 2; low-grade prostate cancer, n = 2; did not proceed to treatment or follow-up, n = 2), leaving 34 treated patients, who comprised the analysis cohort. Follow-up was completed at 6 and 12 months for 34/34 patients (100%) (Table 2).

Primary endpoint

Of the 34 men included, 30 were sexually active. On the MSHQ-EjD function domain (higher scores indicate better function), mean scores were 9.66 ± 1.59 at baseline (n = 29), 9.59 ± 2.34 at 6 months, and 9.48 ± 2.26 at 12 months. Paired two-sided tests showed no evidence of change from baseline to 6 months [Δ(6m–BL): −0.07; 95% CI: −0.86 to 0.72; $P = 0.860$] or to 12 months [Δ(12m–BL): −0.17; 95% CI: −1.09 to 0.75; $P = 0.704$]. For the MSHQ-EjD bother domain (lower scores indicate less bother), the baseline mean was 2.63 ± 0.71 (n = 32), increasing to 2.78 ± 0.75 at 6 months [Δ(BL–6m): −0.16; 95% CI: −0.49 to 0.18; $P = 0.344$] and to 2.86 ± 0.64 at 12 months among participants with available data [n = 22; Δ(BL–12m): −0.32; 95% CI: −0.78 to 0.14; $P = 0.167$]. Ejaculatory outcomes were assessed using the validated MSHQ-EjD-SF. Although antegrade ejaculation was preserved in 27/30 (90%) sexually active patients at 12 months, we observed a small reduction in the mean MSHQ-EjD-SF score from baseline to 12 months. This change was numerically modest and occurred in the context of concurrent improvements in urinary symptom burden and functional parameters.

Secondary endpoints

The composite responder rate (≥ 30% IPSS reduction without BPH retreatment) was 33/34 (97.1%; 95% CI: 84.7–99.9) at both 6 and 12 months. The median IPSS decreased from 19.5 (IQR: 14.0–30.3) at baseline to 5.0 (5.0–6.0) at 6 months and 4.0 (4.0–5.0) at 12 months (n = 34) ($P < 0.001$). The median Qmax increased from 9.6 (7.6–10.9) to 18.0 (17.0–20.5) mL/s at 6 months and 20.0 (18.0–21.3) mL/s at 12 months ($P < 0.001$). Two patients (5.9%) were catheter dependent at baseline.

Table 2. Baseline demographic and clinical characteristics of the study population (n = 34). Values are presented as mean ± standard deviation or number (percentage), as appropriate

Characteristic	n = 34
Age (years), mean ± SD	69.7 ± 5.8
BMI (kg/m^2), mean ± SD	27.5 ± 2.5
ASA score ≤ 2, n (%)	19 (55.9)
Comorbidities, n (%)	
Hypertension	22 (64.7)
Diabetes mellitus	13 (38.2)
Cardiovascular disease	5 (14.7)

ASA, American Society of Anesthesiologists; BMI, body mass index; SD, standard deviation.

PVR volume decreased from 34.5 (25.3–52.0) mL at baseline to 10.0 (5.0–12.0) mL at 6 months and 9.0 (7.0–11.0) mL at 12 months ($P < 0.001$). Prostate volume was reduced from 70.0 (52.5–101.0) to 43.5 (27.8–62.8) mL at 6 months and 40.0 (24.8–61.0) mL at 12 months ($P < 0.001$). Median PSA declined from 3.8 (2.0–7.4) ng/mL at baseline to 1.5 (0.8–2.5) ng/mL at both 6 and 12 months ($P < 0.001$) (Table 3).

Importantly, symptom improvement was accompanied by concordant objective changes, including increased urinary flow (Qmax), reduced PVR, and sustained reductions in prostate volume and PSA, supporting a physiological treatment effect beyond symptom perception alone.

In stratified analyses according to baseline prostate volume (< 80 vs. ≥ 80 mL), significant within-group improvements were observed at 6 months across all functional and anatomical outcomes, whereas no statistically significant between-group differences were identified, indicating comparable early efficacy across gland size categories (Table 4).

At baseline, 19/34 (55.9%) patients were receiving alpha-blockers and 7/34 (20.6%) were receiving 5-ARIs, including 6/34 (17.6%) on combination therapy; 2/34 (5.9%) were not receiving prostate-related medications. Per protocol, prostate-related medications were discontinued at 1 month whenever clinically feasible. By 12 months, 32/34 (94.1%) patients had discontinued prostate-related medications completely; 2/34 (5.9%) remained on a single medication despite marked symptom improvement (both had received dual therapy preprocedure).

Adverse events and reinterventions

No Clavien–Dindo ≥ III events occurred. Within 30 days, transient urinary morbidity (AUR/urinary tract infection/dysuria) was common, along with less frequent gross hematuria, perineal pain, and hematoma; all events were non-device-related and managed conservatively. Emergency department visits and readmissions were infrequent. Between 31 and 365 days, reinterventions and retreatments were uncommon (Table 5).

Sensitivity to missing data

Because all treated participants completed the 12-month clinical follow-up assessment, sensitivity analyses for follow-up attrition were not required. For endpoints with baseline measurements unavailable in catheter-dependent patients, analyses were conducted using observed-case denominators, with explicit denominators (n) reported per endpoint.

Percentages are shown with exact 95% CIs (Clopper–Pearson) for proportions. Continuous outcomes are summarized as the median (IQR); *P* values and effect-size estimates are provided in Tables 3 and 4.

Table 3. Comparison of functional and anatomical outcomes before treatment and at the 6 month and 1-year follow-up after transperineal radiofrequency ablation

Outcomes	Baseline	6 months	1 year	% change 6 months	% change 1 year	*P*
IPSS	19.5 (14.0–30.3)†	5.0 (5.0–6.0)	4.0 (4.0–5.0)	72.1 (66.1–80.6)	74.2 (69.1–83.9)	< 0.001
PVR (mL)	34.5 (25.3–52.0)	10.0 (5.0–12.0)	9.0 (7.0–11.0)	77.0 (61.8–84.6)	78.6 (60.4–84.1)	< 0.001
Qmax (mL/s)	9.6 (7.6–10.9)	18.0 (17.0–20.5)	20.0 (18.0–21.3)	94.0 (68.2–167.4)	111.0 (70.1–168.8)	< 0.001
QoL	5.0 (4.0–5.0)	1.0 (1.0–1.0)	1.0 (1.0–1.0)	80.0 (66.7–80.0)	80.0 (75.0–80.0)	< 0.001
Prostate volume (mL)	70.0 (52.5–101.0)	43.5 (27.8–62.8)	40.0 (24.8–61.0)	42.5 (33.3–51.1)	47.7 (38.5–54.1)	< 0.001
PSA (ng/mL)	3.8 (2.0–7.4)	1.5 (0.8–2.5)	1.5 (0.9–2.5)	63.9 (49.9–70.5)	61.5 (50.2–71.8)	< 0.001

†Baseline IPSS available for 32 patients; follow-up IPSS available for 34 patients. IPSS, International Prostate Symptom Score; PVR, post-void residual volume; Qmax, maximum urinary flow rate; QoL, quality of life; PSA, prostate-specific antigen.

Table 4. Comparison of functional and anatomical outcomes before treatment and at 6 month follow-up after transperineal radiofrequency ablation according to baseline prostate volume. Values are presented as median (interquartile range)

Outcome	Prostate volume < 80 mL (n = 20)			Prostate volume ≥ 80 mL (n = 14)			*P*†
	Baseline	6 months	% change	Baseline	6 months	% change	
IPSS	22.0 (16.0–30.0)	2.0 (1.0–2.3)	90.9 (86.2–93.6)	17.0 (14.0–30.0)	2.0 (2.0–2.0)	89.5 (85.7–92.9)	0.759
PVR (mL)	35.0 (30.0–52.0)	10.0 (5.0–10.8)	77.8 (66.7–85.7)	32.0 (25.0–54.0)	10.0 (7.3–15.0)	68.0 (53.1–84.3)	0.343
Qmax (mL/s)	10.0 (7.9–12.9)	18.0 (17.0–22.0)	80.0 (63.6–120.8)	8.5 (6.8–10.2)	18.0 (16.8–19.3)	110.5 (76.5–181.3)	0.099
QoL	5.0 (5.0–5.0)	1.0 (1.0–1.0)	80.0 (75.0–80.0)	4.0 (3.0–5.0)	1.0 (1.0–1.0)	75.0 (66.7–80.0)	0.217
Prostate volume (mL)	55.0 (42.8–63.5)	29.0 (22.0–39.8)	44.1 (30.4–53.7)	111.5 (89.3–167.8)	70.0 (52.5–101.0)	41.6 (33.3–50.7)	0.769
PSA (ng/mL)	2.7 (1.3–4.0)	1.1 (0.5–1.7)	55.2 (45.2–69.6)	7.6 (6.1–9.4)	2.4 (1.6–3.3)	66.1 (62.3–78.0)	0.071

†*P* value for between-group comparison of percentage change at 6 months (Mann–Whitney U test). IPSS, International Prostate Symptom Score; PVR, post-void residual volume; Q_{max}, maximum urinary flow rate; QoL, quality of life; PSA, prostate-specific antigen.

Table 5. Adverse events, healthcare utilization, and reinterventions up to 12 months after urethra-sparing, ultrasound-guided transperineal radiofrequency ablation

Event	Definition	0–30 d n/N (%)	Management	Clavien–Dindo
Acute urinary retention	Inability to void for ≤ 2 h with discomfort or PVR > 300 mL; managed with temporary catheterization.	5/34 (14.7%)	Temporary catheterization (typically 48–72 h)	1
Urinary tract infection	New urinary symptoms accompanied by a positive urine culture requiring antibiotic therapy; culture obtained when available.	4/34 (11.7%)	Oral antibiotics (10–14 days), guided by urine culture when available; no hospitalizations (length of stay 0 days)	1
Dysuria (clinically significant)	New/worse dysuria lasting ≥ 7 d or requiring unplanned contact/analgesic escalation.	12/34 (35%)	Oral analgesics/anti-inflammatories	1
Gross hematuria	Visible blood in urine; assess for clot retention and Hb drop.	3/34 (8%)	Hydration/observation; bladder irrigation if needed	1
Perineal pain (significant)	Pain NRS ≥ 5 beyond 48 h or requiring opioid prescription.	3/34 (8%)	Oral analgesics ± short opioid course	1
Skin/perineal hematoma	Clinically evident subcutaneous hematoma; intervention if expanding or symptomatic.	3/34 (8%)	Observation/ice	1

Discussion

In this bicenter outpatient cohort, urethra-sparing, ultrasound-guided TPTA was associated with clinically meaningful improvements in LUTS and objective functional parameters through 12 months of follow-up. This report extends our previously published 3-month findings[5] by providing a planned 12-month follow-up with additional longitudinal outcome assessments; the prior publication is cited to ensure full transparency regarding the cohort.

Rather than establishing comparative efficacy against existing surgical or minimally invasive therapies, the present study was designed to assess the reproducibility, safety, and functional profile of an image-guided, urethra-sparing TPTA strategy when performed in a real-world interventional radiology setting (Figure 3).

Real-time ultrasound guidance, combined with predefined safety margins from the urethra and bladder neck, allowed consistent anatomical targeting across centers. When available, immediate CEUS served as a quality-assurance step to confirm treatment coverage and exclude early complications, reinforcing procedural reproducibility without compromising periurethral perfusion (Figure 4). The addition of postoperative CEUS provided clinically meaningful functional information by allowing early assessment of ablation perfusion patterns. Unlike grayscale ultrasound, CEUS enabled confirmation of devascularized tissue and identification of residual perfused areas that may not be apparent on conventional imaging. This early functional evaluation supports procedural adequacy, enhances safety surveillance, and may help explain interindividual variability in subsequent symptom improvement and volume reduction. Although CEUS findings were not used to mandate immediate retreatment in this study, their use may inform future protocols incorporating early response assessment and tailored follow-up strategies.

Within this framework, improvements were internally consistent across both patient-reported outcomes and objective measures, including the Qmax, PVR, prostate volume, and PSA.

When positioned within the contemporary minimally invasive surgical therapy landscape, the present outcomes appear directionally consistent with reports of other urethra-sparing and non-transurethral approaches. However, differences in study design, patient selection, and outcome definitions preclude direct comparisons or claims of superiority. Accordingly, the present findings should be viewed as complementary, contributing prospective evidence on functional and ejaculatory outcomes in a real-world outpatient setting.[4,6]

Mean scores on the MSHQ-EjD-SF function domain remained statistically stable during the follow-up period, with no significant changes observed at either 6 or 12 months. Although a slight numerical decline was noted at the latter timepoint, this finding should be interpreted in the context of two consistent signals: the bother domain did not worsen significantly, and 90% of sexually active men reported preservation of antegrade ejaculation. Taken together, these results suggest that symptom relief was achieved without a proportional increase in patient-perceived ejaculatory burden, indicating that ejaculatory function was largely maintained following ultrasound-guided, urethra-sparing TPTA.[5]

In our cohort, only one patient did not achieve an adequate clinical response, with only a 20% reduction in IPSS and a continued need for prior BPH medications. Multiparametric MRI demonstrated a marked increase in IPP, suggesting a possible valvular mechanism. Post-contrast sequences showed enhancement of the periurethral tissue and IPP. A second TPTA session was performed, specifically targeting the IPP region. Thirty days later, the patient reported marked improvement, with a decrease in IPSS from 14 to 2 and discontinuation of all BPH medications. Follow-up endocavitary ultrasound also confirmed a reduction in IPP from 14 to 2 mm. No other patients required retreatment or medication adjustments during follow-up (Figure 5).

Although the absolute magnitude of IPSS reduction was substantial, these findings should be interpreted in the context of a non-randomized study conducted in a carefully selected population with moderate-to-severe baseline symptoms. The ob-

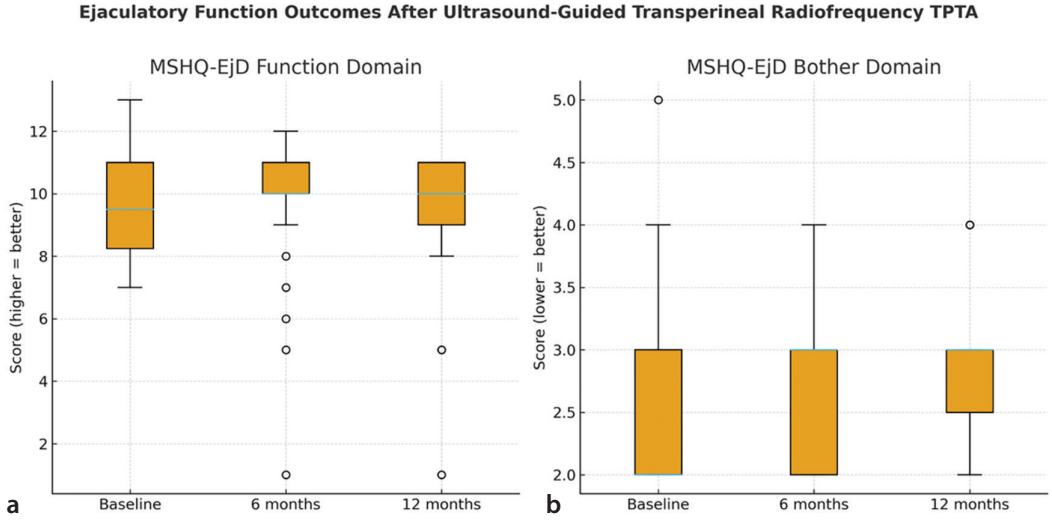


Figure 2. Boxplot comparison of Male Sexual Health Questionnaire–Ejaculatory Dysfunction scores (MSHQ-EjD). **(a)** Ejaculatory function domain. **(b)** Ejaculatory bother domain. Values are shown at baseline, 6 months, and 12 months after ultrasound-guided transperineal radiofrequency ablation for benign prostatic hyperplasia. Horizontal lines within the boxes represent the median, boxes represent interquartile ranges, and whiskers indicate the minimum and maximum values. TPTA, transperineal radiofrequency ablation.

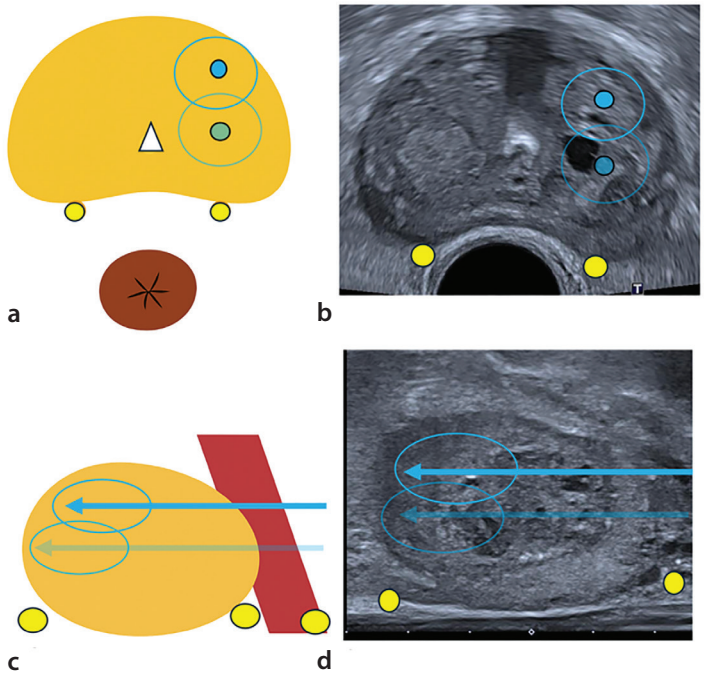


Figure 3. Figure self-designed by authors; no copyright restrictions. Schematic and ultrasound views of the prostate (orange), rectum (brown), and levator ani muscle (red) in axial (**a, b**) and paramedian sagittal (**c, d**) acquisitions. The two yellow dots (**a-d**) indicate the periurethral and periprostatic sites for regional nerve block. The positions of the radiofrequency probes (blue circles and arrows) are shown in both planes, with ablation initiated anteriorly and subsequently performed posteriorly, maintaining a minimum 5-mm distance from the urethra and distal to the verumontanum. Hollow blue circles represent the expected ablation zones surrounding each probe (blue arrows).

served symptom improvement exceeded established MCIDs and was paralleled by concordant objective changes, which argues against symptom fluctuation alone.

Several non-procedural factors may account for the subtle downward drift in function scores over time. Aging across the study interval, the burden of comorbidities such as diabetes or cardiovascular disease, and concomitant use of medications known to affect emission or expulsion (including alpha-blockers, 5-ARIs, selective serotonin reuptake inhibitors, or antihypertensives) may all plausibly contribute.[7-11] Additionally, regression to the mean and survivorship bias among men who remained sufficiently sexually active to complete questionnaires may have influenced the observed trends. These considerations argue against overinterpreting small changes within a single patient-reported outcome domain, particularly when convergent measures such as bother and self-reported antegrade preservation remain favorable.

From a clinical perspective, the consistent preservation of antegrade ejaculation observed in our cohort has practical implications for shared decision-making.[12] Many men with BPH place a high value on maintaining sexual function when selecting among treatment options. By providing validated evidence that a urethra-sparing, non-transurethral approach can achieve robust LUTS relief while minimizing sexual compromise, our findings may help physicians engage patients in more informed discussions and align therapeutic choices with individual priorities.

The overall pattern—meaningful IPSS/Qmax improvements with high rates of antegrade ejaculation—appears directionally consistent with reports from urethra-sparing approaches, but differences in the inclusion criteria and outcome definitions preclude claims of superiority or non-inferiority.[13-17] Where possible, we provide effect sizes and CIs to facilitate evidence synthesis by future systematic reviews rather than making indirect comparative assertions.

Immediate CEUS after ablation served as a real-time quality-assurance step to confirm coverage and exclude periprocedural complications, potentially improving reproducibility without jeopardizing urethral perfusion. Future studies should test whether systematic CEUS integration standardizes outcomes.[18-20]

Although we observed a modest decline in MSHQ-EjD-SF scores, the clinical relevance of this numerical change is uncertain and should be interpreted cautiously. First, antegrade ejaculation was preserved in the vast majority of sexually active men, suggesting that urethra-sparing treatment planning may mitigate clinically overt ejaculatory dysfunction. Second, patient-reported ejaculatory scores can fluctuate over time due to factors not directly attributable to the procedure, including variability in sexual activity, aging, comorbidities, relationship factors, and medication adjustments.[21,22] Third, an established MCID for the MSHQ-EjD-SF in this specific context is not well defined; therefore, small between-timepoint differences may not translate into clinically meaningful impairment. Future comparative studies with larger samples, standardized assessment of sexual activity, medication changes, and broader sexual-function instruments are warranted to better characterize the trajectory and clinical significance of ejaculatory outcomes after transperineal urethra-sparing ablation.[23] Recent studies evaluating contemporary minimally invasive BPH therapies have emphasized the importance of preserving sexual and ejaculatory function alongside symptom relief, reinforcing the clinical relevance of patient-centered outcome measures used in the present study.[24-26]

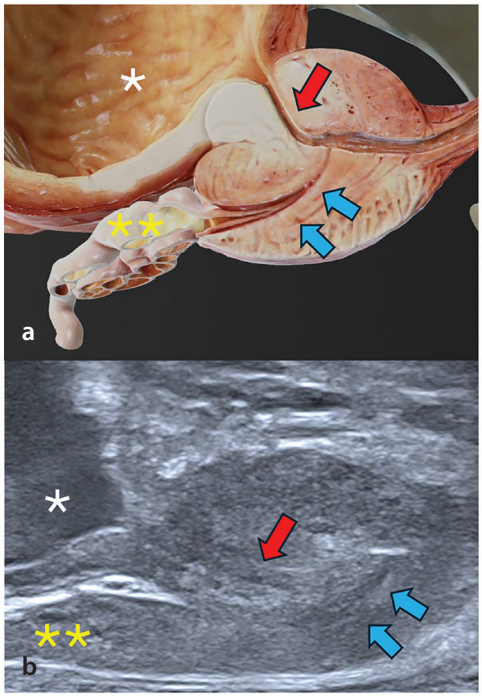


Figure 4. Schematic correlation of the ejaculatory duct pathway between an anatomical illustration **(a)** and transrectal ultrasound imaging obtained with a high-frequency transperineal linear transducer **(b)**. This view is critical as it demonstrates the relationship between the seminal vesicle (double asterisk), bladder (single asterisk), prostatic urethra (red arrow), and ejaculatory duct entering the urethra at the level of the verumontanum (blue arrows). Inadvertent ablation of this region may result in ejaculatory dysfunction.

Several limitations should be acknowledged. Although the sample size (n = 34) is appropriate for a prospective feasibility and safety evaluation, the single-arm design and modest cohort limit causal inference and preclude definitive comparisons with other minimally invasive BPH therapies; thus, these findings should be considered exploratory and hypothesis-generating. Ejaculatory outcomes were assessed using a validated

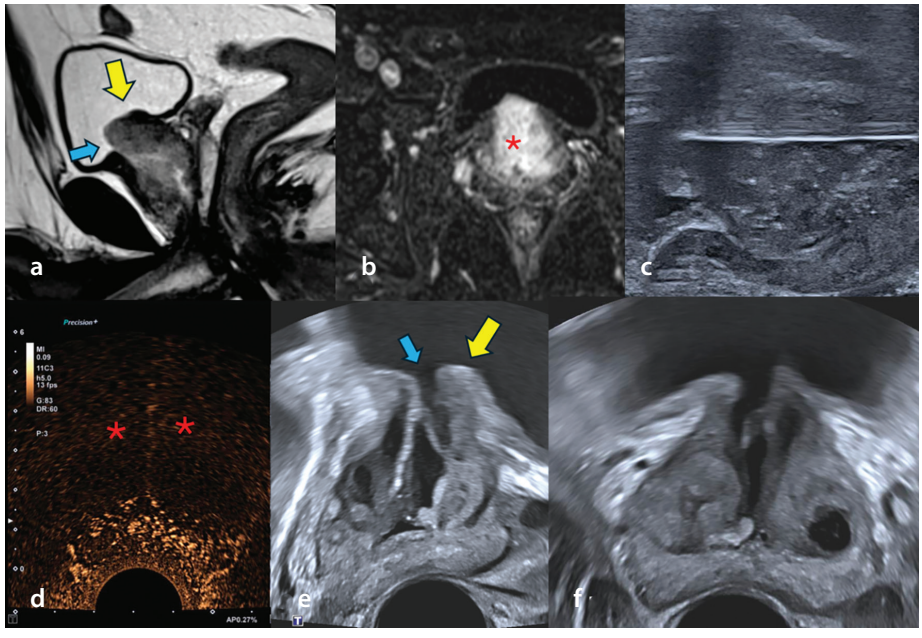


Figure 5. Patient with inadequate initial response requiring retreatment. **(a, b)** Multiparametric prostate magnetic resonance imaging at 6 months post-ablation, sagittal **(a)** and axial post-contrast **(b)**, demonstrates an intravesical prostatic protrusion [intravesical prostatic protrusion (IPP), yellow arrow] measuring 12 mm, consistent with a possible valvular mechanism compressing the proximal urethral lumen (blue arrow). Hyperenhancement of the periurethral tissue and IPP is also noted (red asterisk). **(c)** Repeat transperineal radiofrequency ablation was performed with direct probe placement into the IPP and periurethral zone. **(d)** Immediate contrast-enhanced ultrasound confirmed devascularization of the transition zone and IPP. **(e, f)** Follow-up transrectal ultrasound at 30 days demonstrated marked IPP reduction, opening of the urethral channel, and likely resolution of the valvular mechanism. Clinically, International Prostate Symptom Score improved from 18 pre-retreatment to 2 at 30 days, with complete discontinuation of benign prostatic hyperplasia medications.

instrument (MSHQ-EjD-SF) and antegrade ejaculation preservation, but the study was not powered to define clinically meaningful change thresholds, and an established MCID for the MSHQ-EjD-SF in this setting is lacking; therefore, responder analyses and longitudinal score changes should be interpreted cautiously. In addition, medication discontinuation beyond the planned 1-month withdrawal attempt was not fully protocolized and may have influenced sexual outcomes, and erectile function was not prospectively assessed with the International Index of Erectile Function questionnaire (IIEF-5). Larger, adequately powered multicenter comparative studies with longer follow-up and standardized patient-centered sexual and ejaculatory endpoints are warranted to confirm durability and better define the role of this technique in contemporary BPH care.

Prospective multicenter registries or randomized pragmatic trials are needed to confirm durability and generalizability, ideally using standardized urethra-sparing protocols, independent outcome adjudication, and a core set for sexual function. Given the outpatient setting, a formal health economic analysis (cost-utility, return to usual activities, resource use) is also warranted and may guide adoption by healthcare systems.[18-23] Future prospective studies should incorporate a broader sexual-function battery, including the IIEF-5, to better characterize erectile outcomes alongside ejaculatory preservation after urethra-sparing TPTA. Regarding clinical implications, in the stratified analysis, urethra-sparing TPTA achieved similar symptom relief in men with prostates < 80 and ≥ 80 mL, with consistent improvements across urinary and structural outcomes, supporting its feasibility even in larger glands that are often more challenging to treat.

In summary, a carefully selected outpatient population, urethra-sparing TPTA was associated with clinically meaningful improvements in LUTS and urinary flow at 12 months, with preservation of antegrade ejaculation in the majority of sexually active patients.

Footnotes

Conflict of interest disclosure

The authors declared no conflicts of interest.

References

1. Wei H, Zhu C, Huang Q, et al. Global, regional, and national burden of benign prostatic hyperplasia from 1990 to 2021 and projection to 2035. *BMC Urol*. 2025;25(1):34. [Crossref]
2. Sandhu JS, Bixler BR, Dahm P, et al. Management of lower urinary tract symptoms attributed to benign prostatic hyperplasia (BPH): AUA guideline amendment 2023. *J Urol*. 2024;211(1):11-19. [Crossref]
3. Roehrborn CG, Barkin J, Gange SN, et al. Five-year results of the prospective randomized controlled prostatic urethral L.I.F.T. study. *Can J Urol*. 2017;24(3):8802-8813. [Crossref]
4. Bertolo R, Iacovelli V, Cipriani C, et al. Ejaculatory function following transperineal laser ablation vs TURP for benign prostatic obstruction: a randomized trial. *BJU Int*. 2023;132(1):100-108. [Crossref]
5. Nunes TF, Rocha RD, Ilgenfritz BRW, et al. Ultrasound-guided transperineal prostate thermal ablation (TPTA) for benign prostatic hyperplasia: feasibility of an outpatient procedure using radiofrequency ablation. *Cardiovasc Intervent Radiol*. 2025;48(10):1455-1466. [Crossref]
6. Rosen RC, Catania JA, Althof SE, et al. Development and validation of four-item version of Male Sexual Health Questionnaire to assess ejaculatory dysfunction. *Urology*. 2007;69(5):805-809. [Crossref]
7. Fertig RM, Gamret AC, Darwin E, Gaudi S. Sexual side effects of 5-α-reductase inhibitors finasteride and dutasteride: a comprehensive review. *Dermatol Online J*. 2017;23(11):13030/qt24k8q743. [Crossref]
8. Gandhi J, Weissbart SJ, Smith NL, et al. The impact and management of sexual dysfunction secondary to pharmacological therapy of benign prostatic hyperplasia. *Transl Androl Urol*. 2017;6(2):295-304. [Crossref]
9. Zeiss R, Malejko K, Connemann B, Gahr M, Durner V, Graf H. Sexual dysfunction induced by antidepressants-a pharmacovigilance study using data from VigiBase™. *Pharmaceuticals (Basel)*. 2024;17(7):826. [Crossref]
10. Manolis A, Doumas M, Ferri C, Mancia G. Erectile dysfunction and adherence to antihypertensive therapy: focus on β-blockers. *Eur J Intern Med*. 2020;81:1-6. [Crossref]
11. Barnett AG, van der Pols JC, Dobson AJ. Correction to: regression to the mean: what it is and how to deal with it. *Int J Epidemiol*. 2015;44(5):1748. [Crossref]
12. Vennedey V, Holling H, Steiner T, Schrader M, Grossmann H, Hoenig C. Patient preferences for surgical treatments for benign prostatic hyperplasia: a discrete choice experiment. *JU Open Plus*. 2024;2(11):e00116. [Crossref]
13. McVary KT, Gittelman MC, Goldberg KA, et al. Final 5-year outcomes of the multicenter randomized sham-controlled trial of a water vapor thermal therapy for treatment of moderate to severe lower urinary tract symptoms secondary to benign prostatic hyperplasia. *J Urol*. 2021;206(3):715-724. [Crossref]
14. Patelli G, Altieri VM, Ierardi AM, Carnevale A, et al. Transperineal laser ablation of the prostate for symptomatic benign prostatic hyperplasia: long-term follow-up in 40 patients. *J Vasc Interv Radiol*. 2024;35(8):1187-1193. [Crossref]
15. Franco JVA, Jung JH, Imamura M, et al. Minimally invasive treatments for benign prostatic hyperplasia: a Cochrane network meta-analysis. BJU Int. 2022;130(2):142-156. [Crossref]
16. de Rienzo G, Lorusso A, Minafra P, et al. Transperineal interstitial laser ablation of the prostate: a novel option for minimally invasive treatment of benign prostatic obstruction. *Eur Urol*. 2021;80(1):95-103. [Crossref]
17. Alloussi SH, Lang C, Eichel R, Alloussi S. Ejaculation-preserving transurethral resection of prostate and bladder neck: short- and long-term results of a new innovative resection technique. *J Endourol*. 2014;28(1):84-89. [Crossref]
18. van Kollenburg RAA, van Riel LAMJG, Oddens JR, de Reijke TM, van Leeuwen TG, de Bruin DM. Contrast-enhanced ultrasound imaging following transperineal laser ablation for lower urinary tract symptoms. *Urology*. 2025;198:141-147. [Crossref]
19. van Riel LAMJG, van Kollenburg RAA, Freund JE, et al. Reliable visualization of the treatment effect of transperineal focal laser ablation in prostate cancer patients by magnetic resonance imaging and contrast-enhanced ultrasound imaging. *Eur Urol Open Sci*. 2023;54:72-79. [Crossref]
20. Sidhu PS, Cantisani V, Dietrich CF, et al. The EFSUMB guidelines and recommendations for the clinical practice of contrast-enhanced ultrasound (CEUS) in non-hepatic applications: update 2017 (short version). *Ultraschall Med*. 2018;39(2):154-180. [Crossref]
21. von Elm E, Altman DG, Egger M, et al. The Strengthening the Reporting of Observational Studies in Epidemiology (STROBE) statement: guidelines for reporting observational studies. *PLoS Med*. 2007;4(10):e296. [Crossref]
22. Sahakyan Y, Erman A, Bhojani N, et al. Cost-utility of minimally invasive therapies vs pharmacotherapy as initial therapy for benign prostatic hyperplasia: a Canadian healthcare payer perspective. *Can Urol Assoc J*. 2023;17(4):103-110. [Crossref]

23. Patel N, Yung N, Vigneswaran G, et al. 1-year cost-utility analysis of prostate artery embolization (PAE) versus transurethral resection of the prostate (TURP) in benign prostatic hyperplasia (BPH). *BMJ Surg Interv Health Technol*. 2021;3(1):e000071. [Crossref]

24. Pacini M, Lambertini L, Avesani G, et al. Single-port transvesical simple prostatectomy for the surgical treatment of benign prostatic hyperplasia: functional and continence outcomes. *Prostate Cancer Prostatic Dis*. 2025;28:451-456. [Crossref]

25. Zucchi A, Bartoletti R, Antonov P, et al. Preserving erectile and ejaculatory function in patients undergoing minimally invasive techniques: the first randomized clinical trial comparing convective water vapor ablation and transperineal laser ablation. *J Sex Med*. 2025;22(8):1447-1454. [Crossref]

26. Pacini M, Zucchi A, Salonia A, et al. Short term results after minimally invasive treatments for benign prostatic enlargement: the first randomized trial comparing transperineal laser ablation and water vapor ablation. *Prostate Cancer Prostatic Dis.* 2025;28(4):978-984. [Crossref]

Diagn Interv Radiol 2026; DOI: 10.4274/dir.2026.263802

INTERVENTIONAL RADIOLOGY

ORIGINAL ARTICLE

©Copyright 2026 Author(s) - Available online at dirjournal.org.
Content of this journal is licensed under a Creative Commons Attribution-NonCommercial 4.0 International License.

Safety and efficacy of combined ethanol and bleomycin sclerotherapy via percutaneous pigtail catheter for benign cervical cystic lesions: a single-center retrospective study

Sang Lim Choi[1]
Woosun Choi[2]
Byung Kook Kwak[2]
Jinyoung Choi[2]

[1]Chung-Ang University Gwangmyeong Hospital, Chung-Ang University College of Medicine, Department of Radiology, Gwangmyeong, Republic of Korea

[2]Chung-Ang University Hospital, Chung-Ang University College of Medicine, Department of Radiology, Seoul, Republic of Korea

PURPOSE

To evaluate the safety and efficacy of combined ethanol lavage and bleomycin sclerotherapy administered via a percutaneous pigtail catheter for the treatment of benign cervical cystic lesions.

METHODS

This retrospective study included 29 patients (mean age, 30 years; range, 4–60 years; male-to-female ratio, 16:13) who underwent bleomycin sclerotherapy following ethanol lavage via a pigtail catheter for benign cervical cystic lesions, including branchial cleft cysts, ranulas, thyroglossal duct cysts, lymphatic malformations, and epidermoid cysts, between March 2009 and September 2022. To explore potential predictors of treatment response, clinical diagnosis, baseline cyst size, and the total volume of injected sclerosant were evaluated. Statistical analyses included the paired t-test, chi-square test, and Mann–Whitney U test.

RESULTS

All patients were followed up for a mean duration of 18.2 months (range, 3–72 months) after the final treatment session. Complete cyst resolution was achieved in 17 of the 29 patients (59%), 8 patients (27%) demonstrated a volume reduction greater than 75%, and 2 patients (7%) exhibited a reduction of less than 75%; recurrence occurred in 2 patients (7%) despite repeated sclerotherapy. There were no significant differences between responders and nonresponders with respect to clinical diagnosis, baseline cyst volume, or total sclerosant dose. Minor procedure-related complications occurred in three patients (10.34%); no major complications were observed.

CONCLUSION

Combined ethanol lavage and bleomycin sclerotherapy administered via a percutaneous pigtail catheter is a safe and feasible treatment option for benign cervical cystic lesions.

CLINICAL SIGNIFICANCE

Combined ethanol and bleomycin sclerotherapy represents a safe, minimally invasive treatment option for benign cervical cystic lesions in routine clinical practice, with favorable outcomes and potential to reduce the need for surgical intervention.

KEYWORDS

Sclerotherapy, bleomycin, ethanol, neck, cysts

Handling editor: Barbaros Çil

Corresponding author: Woosun Choi

E-mail: radiochoi527@gmail.com

Received 17 December 2025; revision requested 13 January 2026; accepted 21 February 2026.

Epub: 18.03.2026

Publication date: 02.11.2026

DOI: 10.4274/dir.2026.263802

You may cite this article as: Choi SL, Choi W, Kwak BK, Choi J. Safety and efficacy of combined ethanol and bleomycin sclerotherapy via percutaneous pigtail catheter for benign cervical cystic lesions: a single-center retrospective study. *Diagn Interv Radiol*. 2026;32(6):828-834.

Benign neck cysts are non-neoplastic cystic lesions of the neck that are typically congenital or developmental in origin. They are pathologically characterized by an epithelial or endothelial lining with a benign clinical course and have traditionally been managed with surgical excision. Surgical treatment offers definitive resolution with very low recurrence rates.[1] However, open surgery is associated with inherent risks, including injury to adjacent neurovascular structures, infection, and bleeding, particularly in lesions that are poorly defined or demonstrate expansile growth.[2] Therefore, increasing attention has been directed toward non-surgical, minimally invasive treatment strategies for benign neck cysts. Sclerotherapy has emerged as a promising alternative to surgical excision, employing chemical ablation agents such as OK-432 (Picibanil), tetracycline, doxycycline, bleomycin, and ethanol.[2] Of these, OK-432 is the most frequently reported sclerosant for this procedure.[2,3] Although intracystic injection of OK-432 is generally considered safe, recurrence rates of up to 47% have been reported, and routine clinical access to OK-432 remains limited in many settings.[3,4] These limitations highlight the need for effective and readily available alternative sclerosants.

Ethanol is widely used in sclerotherapy and exerts its effects through cellular dehydration and protein denaturation, leading to coagulation, vascular wall necrosis, thrombosis, and eventual vascular occlusion.[5] Ethanol ablation has demonstrated safety and efficacy in the treatment of cystic thyroid nodules, thyroglossal duct cysts, and lymphatic malformations.[6-8] Standard ethanol sclerotherapy typically involves aspiration of cyst contents followed by instillation of ethanol without lavage, patient repositioning, and subsequent aspiration of the sclerosant after a predefined dwell time. In most prior reports, this procedure has been performed using a single percutaneous needle puncture, without placement of a pigtail catheter to allow continuous irrigation or drainage.

Bleomycin represents another commonly used sclerosant with broad availability and a favorable safety profile, with reported adverse effects generally mild and transient.[9] However, ethanol may demonstrate limited efficacy in mucus-filled cysts due to insufficient contact with the cyst wall, and bleomycin often necessitates repeated treatment sessions to achieve adequate sclerosis.[10,11] From a mechanistic standpoint, ethanol induces chemical denudation of the cystic epithelium and facilitates evacuation of viscous intracystic contents, whereas bleomycin promotes endothelial injury and subsequent fibrosis. Accordingly, the sequential application of ethanol lavage followed by bleomycin instillation was conceived to offer theoretical complementarity between these agents rather than proven therapeutic superiority.

To our knowledge, the safety and efficacy of this combined sclerotherapy approach for benign neck cysts have not been previously evaluated. The present study therefore aimed to assess the therapeutic efficacy and safety profile of combined ethanol lavage and bleomycin sclerotherapy administered via a percutaneous pigtail catheter.

Main points

- Combined ethanol lavage and bleomycin sclerotherapy administered via a percutaneous pigtail catheter is a safe and feasible minimally invasive treatment option for benign cervical cystic lesions.
- This approach was applied to patients with symptomatic benign cervical cystic lesions, particularly in cases where surgical excision was unsuitable, declined by the patient, or when a minimally invasive alternative was preferred.
- Clinical outcomes were evaluated based on cyst volume reduction and recurrence during follow-up.

Methods

Patients

This retrospective study was approved by the Institutional Review Board of Chung-Ang University Hospital (IRB number: 2507-014-2741, date: July 22, 2025), which waived the requirement for written informed consent. Between March 2009 and September 2022, 44 patients underwent bleomycin sclerotherapy following ethanol lavage for benign neck cysts at our institution. Of these, 15 patients were excluded because follow-up imaging was unavailable to assess treatment response. The final study cohort therefore comprised 29 patients (mean age, 30 years; range, 4–60 years; male-to-female ratio, 16:13). The diagnosis of benign neck cyst was established on the basis of characteristic clinical presentation and imaging findings obtained using ultrasonography (US) and computed tomography (CT). Routine histopathologic confirmation was not performed, given the minimally invasive nature of the treatment strategy. An overview of patient selection and cohort characteristics is provided in Figure 1 and Table 1.

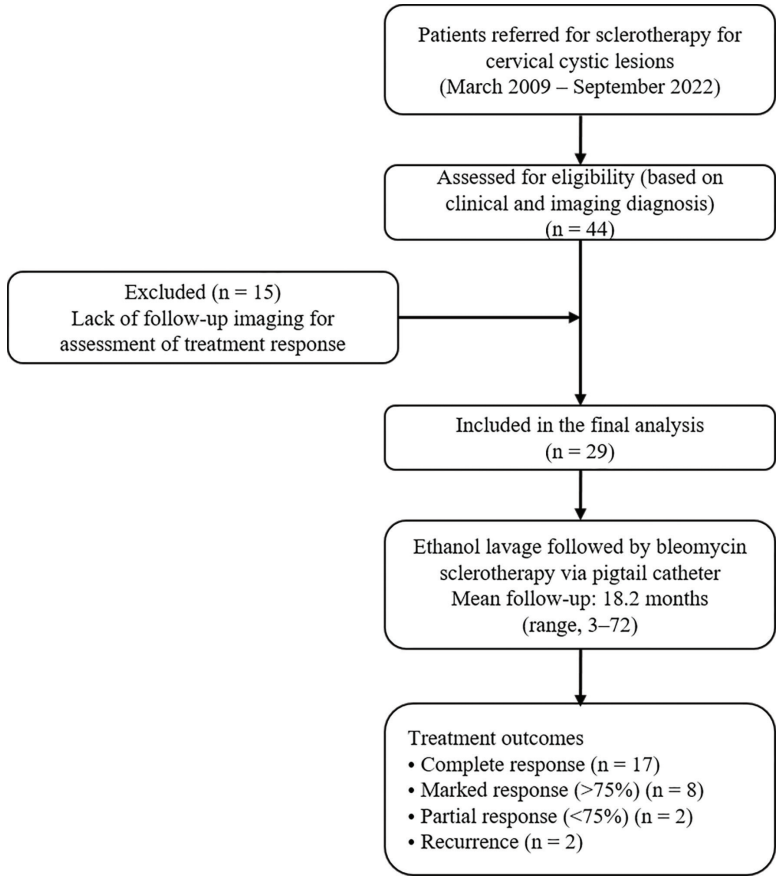


Figure 1. Study flow diagram illustrating patient selection and clinical outcomes.

Table 1. Patient characteristics and treatment outcomes of sclerotherapy for benign cervical cystic lesions

Case	Sex	Age (y)	Clinical diagnosis	Prior treatment	Measured volume (mL)	Number of treatments	Follow-up duration (months)	Outcome
1	F	38	BCC		8.8		3	PR
2	M	30	Plunging ranula	SMG excision	9.9	3	72	NR
3	M	32	Ranula		10.4	2	8	NR
4	F	27	Ranula		7.4		9	CR
5	M	39	Lymphangioma		162.0		18	MR
6	M	19	Ranula		18.0		22	CR
7	M	48	Lymphangioma		30.4		4	MR
8	M	25	Ranula		4.1		6	MR
9	F	33	Epidermoid cyst		2.2		4	PR
10	F	28	BCC		7.7		9	CR
11	M	25	Plunging ranula		34.9		9	CR
12	M	35	BCC		18.0		48	CR
13	M	35	Epidermoid cyst		6.1		9	MR
14	F	13	BCC		10.1		44	CR
15	F	29	Lymphangioma		60.5		12	MR
16	F	4	Ranula		5.9		12	CR
17	M	7	Plunging ranula		6.3		16	CR
18	M	14	Lymphangioma		30.6		20	CR
19	M	24	Plunging ranula		14.1	2	31	CR
20	F	60	BCC		14.0		32	CR
21	F	24	BCC		29.3	2	36	CR
22	M	20	Plunging ranula		8.8		4	CR
23	F	35	BCC		29.7		18	CR
24	M	36	BCC		69.7		15	MR
25	F	38	TGDC		32.9		24	CR
26	M	49	TGDC		13.3		6	CR
27	F	28	Ranula		6.9		6	MR
28	F	52	BCC		17.4		18	CR
29	M	24	Plunging ranula		27.2		12	MR

CR, complete response; MR, marked response; PR, partial response; NR, no response; TGDC, thyroglossal duct cyst; BCC, branchial cleft cyst; F, female; M, male; SMG, submandibular gland.

Technique

All procedures were performed by a board-certified interventional radiologist with 30 years of clinical experience in an interventional radiology suite. Cyst size and anatomical location were confirmed using US, and local anesthesia was administered at the puncture site with 2% lidocaine. Initial cyst access was achieved using a 21-gauge needle, followed by placement of a 7-Fr or 8.5-Fr pigtail catheter (Cook Medical, Bloomington, IN, USA) within the cystic cavity. Ultrasound guidance was used for initial cyst puncture, whereas fluoroscopic guidance was employed for pigtail catheter placement and contrast injection to confirm appropriate intracystic positioning and exclude extravasation. Cyst contents were aspirated as completely as possible. Alcohol lavage using 99% ethanol was then performed between the syringe and the cyst lumen for 3–5 cycles to remove mucinous components, with syringe contents discarded after each cycle. Lavage was considered complete once visual and tactile feedback indicated the absence of highly viscous mucus in the aspirate. The volume of ethanol instilled corresponded to one-third of the aspirated cyst volume, with a maximum volume of 100 mL.

Bleomycin (Hikma Pharmaceuticals, Berkeley Heights, NJ, USA) was prepared by reconstituting one or two vials in 1–2 mL of normal saline and diluting the solution to a total volume of 10 or 20 mL. Each vial contained 15 mg of bleomycin, and one or two vials were used per treatment session at the operator's discretion. When the aspirated cyst volume was less than 10 mL, an equivalent volume of bleomycin solution was instilled; when the aspirated volume was 10 mL or greater, up to 20 mL was instilled. Bleomycin was subsequently instilled into the cyst without aspiration, and the procedure was completed (Figures 2 and 3). The pigtail catheter was routinely removed the following day.

Data collection and follow-up

The following variables were extracted from the electronic medical record for each patient: age, sex, lesion location, presenting

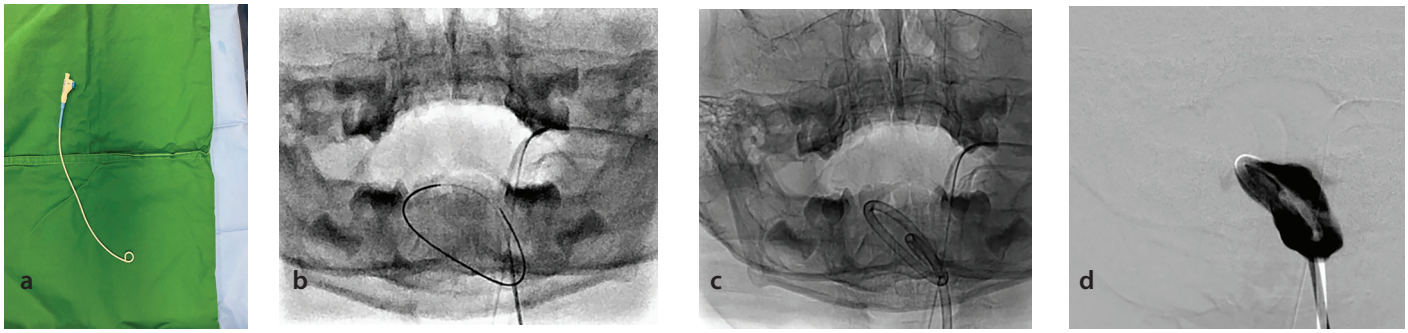


Figure 2. Procedural steps: **(a)** placement of a 7-Fr pigtail catheter; **(b, c)** catheter insertion into a left sublingual ranula under ultrasonographic and fluoroscopic guidance with aspiration of cyst fluid as completely as possible; **(d)** contrast injection to confirm the absence of extravasation into adjacent soft tissues, followed by sequential ethanol lavage and bleomycin sclerotherapy.

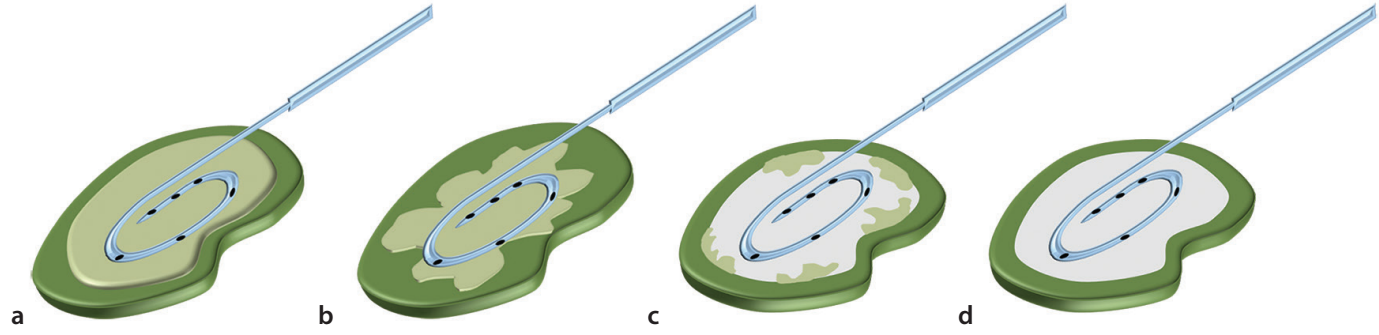


Figure 3. Illustrations of ethanol lavage: **(a)** insertion of a 7-Fr pigtail catheter into a benign neck cyst; **(b)** aspiration of cyst contents as completely as possible; **(c, d)** ethanol lavage demonstrating clearance of residual adherent fluid from the cyst wall.

symptoms, injected volumes (mL) of ethanol and bleomycin, number of bleomycin treatment sessions, and cumulative bleomycin dose. Procedure-related complications were classified as major or minor in accordance with the Society of Interventional Radiology Standards of Practice guidelines.[12] Major complications were defined as events requiring major therapy, prolonged hospitalization exceeding 48 hours, or unplanned escalation of care. Minor complications were defined as events requiring only nominal therapy or no therapy and could include overnight admission for observation.

Induration and erythema at the injection site were assessed on the day following the procedure. Patients were subsequently followed up in the outpatient setting. At each follow-up visit, a focused clinical history and physical examination were performed. If recurrence of a benign neck cyst was suspected based on symptoms or examination findings, follow-up imaging with US or CT was obtained. Treatment response was assessed by calculating the percentage of volume reduction using cyst measurements obtained from baseline and post-sclerotherapy US or CT scans. Lesion volume was calculated using the prolate ellipse formula (V = 0.5 × length × width × thickness). Complete response was defined as complete disappearance of the lesion, marked response as a reduction greater than 75%, and partial response as a reduction of less than 75%. Recurrence was defined as any clinically meaningful increase in lesion volume during follow-up.

Statistical analysis

Pre- and post-sclerotherapy cyst volumes were compared using the paired t-test. Categorical variables stratified by etiology were analyzed using the chi-square test. Differences in baseline cyst volume and injected sclerosant dose between the complete-response and noncomplete-response groups were evaluated using the independent t-test or the Mann–Whitney U test, as appropriate. All statistical analyses were performed using MedCalc Statistical Software (version 18.6, MedCalc Software Ltd., Ostend, Belgium). A two-sided *P* value < 0.05 was considered statistically significant.

Results

A total of 29 patients were followed up for a mean duration of 18.2 months (range, 3–72 months); 4 patients (13.8%) had a follow-up period of less than 6 months. Complete response was achieved in 17 patients (59%), and 8 patients (27%) demonstrated a marked response, defined as a volume reduction greater than 75%. Partial response, defined as a volume reduction of less than 75%, was observed in two patients (7%). Recurrence despite repeated sclerotherapy occurred in two patients (7%). The two cases with recurrence were clinically diagnosed as a plunging ranula and a simple ranula. Overall, cyst volume decreased significantly following combined ethanol lavage and bleomycin sclerotherapy administered via a percutaneous pigtail catheter, from a mean baseline volume of 24.03 [95% confidence interval (CI) 12.23–35.82] to 1.25 mL (95% CI: 0.22–2.28) after treatment (*P* = 0.0005). No major complications were observed. Minor procedure-related symptoms occurred in three patients and included fever (n = 1) and pain (n = 2); all symptoms resolved within 3 days.

The mean number of procedures per patient was 1.17. When stratified by clinical diagnosis, the mean number of procedures was 1.11 for branchial cleft cysts, 1.00 for epidermoid cysts, 1.33 for ranulas, 1.00 for thyroglossal duct cysts, and 1.00 for lymphangiomas. Among the 17 patients who achieved a complete response, 15 responded after a single procedure (Figure 4) and 2 required two procedures. Two patients experienced relapse despite repeated sclerotherapy (Figure 5). One patient in the cohort had previously undergone surgical excision as an initial treatment.

To evaluate outcomes according to clinical diagnosis, patients were dichotomized into a complete-response group and a non-complete-response group and compared statistically. Among the 17 patients with complete response, 7 (41%) were diagnosed with ranula, 7 (41%) with branchial cleft cyst, 2 (12%) with thyroglossal duct cyst, 1 (6%) with lymphangioma, and none with epidermoid cyst. Among the 12 patients with non-complete response, diagnoses included ranula in 5 patients (42%), lymphatic malformation in 3 (25%), thyroglossal duct cyst in 2 (17%), and epidermoid cyst in 2 (17%). The distribution of diagnoses did not differ significantly between the complete-response and non-complete-response groups ($P = 0.745$; Table 2).

The potential impact of cyst size on treatment response was also evaluated. Baseline cyst volume did not differ significantly between the complete-response and non-complete-response groups ($P = 0.790$). Similarly, there was no significant difference in the injected sclerosant dose between the groups ($P = 0.655$). Across the entire cohort, the mean cumulative intralesional bleomycin dose was 16.84 ± 11.56 mg per patient.

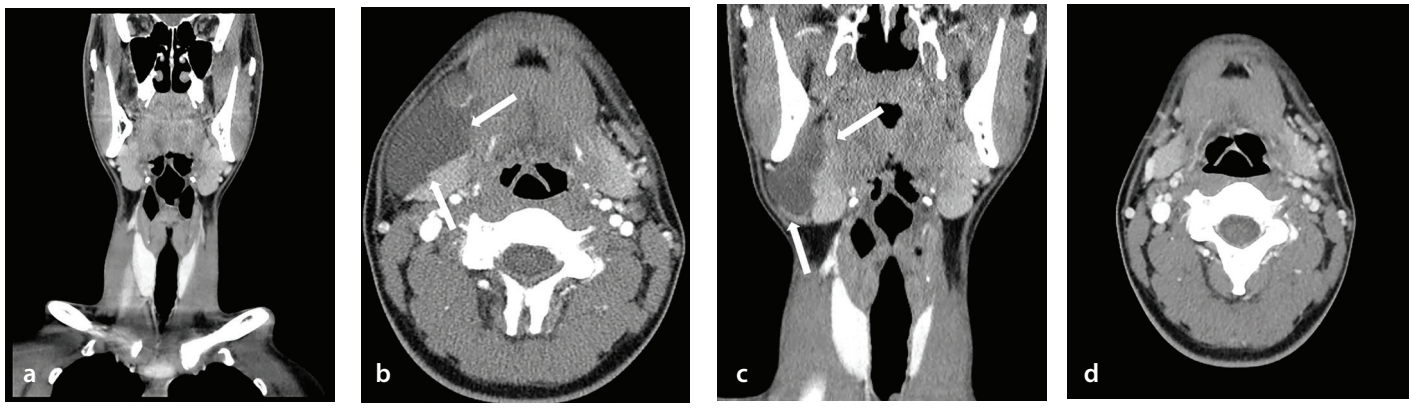


Figure 4. (a, b) Initial computed tomography (CT) images demonstrating a 5.8 × 4.3 × 2.7-cm plunging ranula (arrows) in the right submandibular space on axial and coronal views, respectively. **(c, d)** Follow-up CT obtained 1 year after ethanol lavage and bleomycin sclerotherapy showing complete resolution of the plunging ranula.

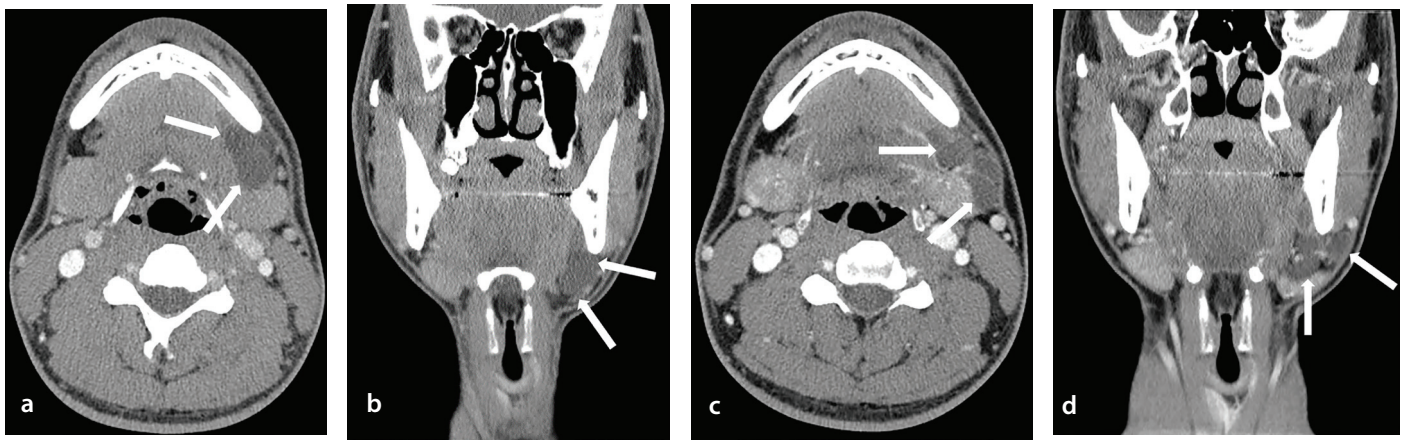


Figure 5. (a, b) Initial computed tomography (CT) images demonstrating a 3.2 × 2.0 × 3.1-cm cystic lesion (arrows) in the left submandibular space on axial and sagittal views, respectively. **(c, d)** Follow-up CT obtained 2 years after two sessions of ethanol lavage and bleomycin sclerotherapy showing recurrence of the cystic lesion (arrows).

Table 2. Treatment response according to cyst type

Cyst type	Complete response (n = 17)	Other response (n = 12)	Total (n = 29)
Ranula	7 (41%)	5 (42%)	12
BCC	7 (41%)	0	7
TGDC	2 (12%)	2 (17%)	4
Lymphangioma	1 (6%)	3 (25%)	4
Epidermoid cyst	0	2 (17%)	2
Total	17	12	29

$P = 0.745$. BCC, branchial cleft cyst; TGDC, thyroglossal duct cyst.

Discussion

Surgical excision remains the standard treatment for benign neck cysts. However, complete resection can be technically challenging, and the risk of recurrence is not negligible. In addition, surgical management carries the potential for complications, including muscle weakness, neurovascular injury, infection, and unfavorable cosmetic outcomes such as scarring and stitch granuloma.[13,14] These considerations have contributed to growing interest in minimally invasive alternatives. Sclerotherapy is now widely accepted in this context. Among available sclerosants, OK-432 (Picibanil) has been commonly used; however, access to this agent can be limited, and recurrence as well as inflammatory reactions following OK-432 sclerotherapy have been reported.

In the present study, combined ethanol lavage and bleomycin sclerotherapy administered via a percutaneous pigtail catheter demonstrated favorable clinical outcomes with an acceptable safety profile. The observed response rates were comparable to those reported for commonly used sclerosants, including OK-432, ethanol, and bleomycin monotherapy, as described in previous studies.[2,3,15-18] Notably, sustained treatment responses were observed over a relatively long mean follow-up period of 18.2 months, whereas prior reports have primarily emphasized short-term outcomes.[1,15]

The absence of major complications and the low incidence of minor, self-limited adverse events in this cohort are consistent with the established safety profiles of intralesional bleomycin and ethanol sclerotherapy.[9,11] Treatment failure occurred in a patient with a history of surgical excision and subsequent recurrence, suggesting that altered anatomy or postoperative fibrosis may adversely affect the efficacy of subsequent sclerotherapy. Collectively, these findings support the feasibility of this minimally invasive approach as an alternative treatment option in selected patients while acknowledging that direct comparisons with other techniques require prospective, controlled evaluation.

Although reported outcomes vary across studies, ethanol or bleomycin monotherapy has generally yielded favorable responses in the treatment of benign cystic lesions of the head and neck.[2,9,15] The outcomes observed in the present study fall within the range reported in the existing literature. Importantly, the relatively long follow-up period provides additional insight into the durability of treatment response beyond the early post-treatment phase.

In many cases, cyst contents were dense and adhesive, limiting effective evacuation using the standard 16- or 18-gauge needles typically employed for sclerotherapy. To address this limitation, a 7-Fr or 8.5-Fr pigtail catheter was inserted, allowing more effective aspiration of viscous intracystic material. Ethanol irrigation was subsequently performed through the catheter to clear residual thick contents and facilitate closer contact between the sclerosant and the cyst wall. Bleomycin was then instilled and left *in situ* without drainage in accordance with the procedural protocol.

Bleomycin is a sclerosing agent associated with a low rate of complications. However, large cumulative doses exceeding 400 mg or 5 mg/kg have been associated with an increased risk of pulmonary fibrosis.[19,20] This risk is greatest among older adults, patients with renal dysfunction, and individuals receiving systemic bleomycin therapy for malignancy.[21] In the present study, the mean cumulative intralesional bleomycin dose was 16.84 ± 11.56 mg per patient, well below thresholds associated with pulmonary toxicity. No cases of pulmonary complications were observed. Nevertheless, larger cohorts with longer follow-up durations are needed to more precisely estimate the incidence of rare adverse events.

Alcohol lavage may play a supportive role in the management of mucus-filled cysts by reducing intracystic viscosity and removing adherent contents, thereby potentially allowing closer contact between the sclerosant and the cyst wall. In sclerotherapy performed without lavage, residual mucinous material may act as a physical barrier that limits effective interaction between the sclerosant and the cyst intima. Although the present study was not designed to evaluate the incremental benefit of lavage, this technical step may be considered a feasible adjunct in selected cystic lesions characterized by thick intracystic contents.

Several limitations of this study should be acknowledged. First, the retrospective design spanning an extended period resulted in some missing data, although the sclerotherapy technique itself did not change over time. Second, diagnoses of benign cervical cystic lesions were based on clinical and imaging findings rather than histopathologic confirmation, reflecting an inherent limitation of minimally invasive treatment strategies that aim to avoid surgical excision. Third, the sample size was insufficient to identify factors associated with treatment effectiveness, and no direct comparison with other sclerosants was performed. In addition, all patients underwent routine next-day removal of the pigtail catheter, and the necessity of overnight catheter retention was not systematically evaluated. As a result, the impact of catheter retention on recurrence rates and procedural invasiveness could not be assessed. Prospective, adequately powered studies with head-to-head comparisons are therefore warranted.

In conclusion, combined ethanol lavage and bleomycin sclerotherapy administered via a percutaneous pigtail catheter represents a safe and feasible treatment option for benign cervical cystic lesions.

Footnotes

Conflict of interest disclosure

The authors declared no conflicts of interest.

References

1. Manna S, Bageac DV, Berenstein A, Sinclair CF, Kirke D, De Leacy R. Bleomycin sclerotherapy following doxycycline lavage in the treatment of ranulas: a retrospective analysis and review of the literature. *Neuroradiol J*. 2021;34(5):449-455. [Crossref]
2. Talmor G, Nguyen B, Mir G, Badash I, Kaye R, Caloway C. Sclerotherapy for benign cystic lesions of the head and neck: systematic review of 474 cases. *Otolaryngol Head Neck Surg*. 2021;165(6):775-783. [Crossref]
3. Rho M, Kim D, Kwon J, et al. OK-432 sclerotherapy of plunging ranula in 21 patients: it can be a substitute for surgery. *AJNR Am J Neuroradiol*. 2006;27(5):1090-1095. [Crossref]
4. Valle Rodríguez E, Villanueva San Vicente V, González R, Segarra Fenoll D, García Mateos M, Méndez-Trujillo S. Linfangioma cervical: manejo terapéutico con OK-432 (Picibanil). *Rev Esp Cir Oral Maxilofac*. 2007;29(6):399-403. [Crossref]
5. Mason KP, Michna E, Zurakowski D, Koka BV, Burrows PE. Serum ethanol levels in children and adults after ethanol embolization or sclerotherapy for vascular anomalies. *Radiology*. 2000;217:127-132. [Crossref]
6. Koo H, Lee J, Kim G, et al. Ethanol and/or radiofrequency ablation to treat venolymphatic malformations that manifest as a bulging mass in the head and neck. *Clin Radiol*. 2016;71(10):1070. [Crossref]

7. Zingrillo M, Torlontano M, Chiarella R, et al. Percutaneous ethanol injection may be a definitive treatment for symptomatic thyroid cystic nodules not treatable by surgery: five-year follow-up study. *Thyroid*. 1999;9(8):763-767. [Crossref]
8. In HS, Kim DW, Choo HJ, Jung SJ, Kang T, Ryu JH. Ethanol ablation of benign thyroid cysts and predominantly cystic thyroid nodules: factors that predict outcome. *Endocrine*. 2014;46(1):107-113. [Crossref]
9. Nevesny F, Chevallier O, Falvo N, et al. Bleomycin for percutaneous sclerotherapy of venous and lymphatic malformations: a retrospective study of safety, efficacy and mid-term outcomes in 26 patients. *J Clin Med*. 2021;10(6):1302. [Crossref]
10. Kim JH, Jeon UB, Jang JY, et al. Efficacy of single-session 99.5% ethanol sclerotherapy for incidentally found simple renal cysts. *Medicine (Baltimore)*. 2022;101(50):e32114. [Crossref]
11. Upadhyaya VD, Bhatnagar A, Kumar B, Neyaz Z, Kishore JS, Sthapak E. Is multiple session of intralesional bleomycin mandatory for complete resolution of macrocystic lymphatic malformation? *Indian J Plast Surg*. 2018;51(1):60-65. [Crossref]
12. Sacks D, McClenny TE, Cardella JF, Lewis CA. Society of Interventional Radiology clinical practice guidelines. *J Vasc Interv Radiol*. 2003;14(9 Pt 2):S199-202. [Crossref]
13. Kim MG, Kim SG, Lee JH, Eun YG, Yeo SG. The therapeutic effect of OK-432 (picibanil) sclerotherapy for benign neck cysts. *Laryngoscope*. 2008;118:2177-2181. [Crossref]
14. Colbert SD, Seager L, Haider F, Evans BT, Anand R, Brennan PA. Lymphatic malformations of the head and neck-current concepts in management. *Br J Oral Maxillofac Surg*. 2013;51(2):98-102. [Crossref]
15. Lee E, Park I, Elzomor A, et al. Efficacy of ethanol ablation as a treatment of benign head and neck cystic lesions. *Am J Otolaryngol*. 2021;42(6):103082. [Crossref]
16. Erikçi V, Hoşgör M, Yıldız M, et al. Intralesional bleomycin sclerotherapy in childhood lymphangioma. *Turk J Pediatr*. 2013;55(4):396-400. [Crossref]
17. M A, Nishad RK, Gupta S, Yadav Y. Role of bleomycin sclerotherapy as a non-surgical method for the treatment of cystic hygroma of head and neck region-an institutional study. *Indian J Otolaryngol Head Neck Surg*. 2022;74(Suppl):2553-2559. [Crossref]
18. Pan P. Ultrasound guided intralesional bleomycin therapy for cystic lymphangioma in childhood. *Int J Contemp Pediatr*. 2017;4(4):1496-1500. [Crossref]
19. Samuel M, Spitz L. Klippel-Trenaunay syndrome: clinical features, complications and management in children. *Br J Surg*. 1995;82:757-761. [Crossref]
20. Muir T, Kirsten M, Fourie P, Dippenaar N, Ionescu GO. Intralesional bleomycin injection (IBI) treatment for haemangiomas and congenital vascular malformations. *Pediatr Surg Int*. 2004;19(12):766-773. [Crossref]
21. O'Sullivan JM, Huddart RA, Norman AR, Nicholls J, Dearnaley DP, Horwich A. Predicting the risk of bleomycin lung toxicity in patients with germ-cell tumours. *Ann Oncol*. 2003;14:91-96. [Crossref]

Diagn Interv Radiol 2026; DOI: 10.4274/dir.2026.263808

INTERVENTIONAL RADIOLOGY

ORIGINAL ARTICLE

©Copyright 2026 Author(s) - Available online at dirjournal.org.
Content of this journal is licensed under a Creative Commons Attribution-NonCommercial 4.0 International License.

Pleural and intra-abdominal long-term drainage: comparison of a novel double-loop and a conventional single-loop catheter

Su Ho Kim
Jung Suk Oh
Ho Jong Chun

Seoul St. Mary's Hospital, College of Medicine, The Catholic University of Korea, Department of Radiology, Seoul, South Korea

PURPOSE

To evaluate the efficacy and advantages of a novel double-loop drainage catheter (nDLC) compared with a conventional single-loop catheter (cSLC) in overcoming dysfunctional retraction for pleural and intra-abdominal drainage.

METHODS

A retrospective review of 356 patients who underwent drainage procedures between January and October 2023 was conducted. Of these, 221 received cSLC and 135 received nDLC, all using 8-F catheters. Complicated collections (e.g., empyema, pneumothorax, bile, pancreatic secretions, bloody collection, urine, or air) were excluded. The complication-free catheter indwelling time was analyzed using the Kaplan–Meier method. Patient characteristics and complications were compared using paired t-tests and Fisher's exact tests.

RESULTS

The nDLC group demonstrated a significantly longer mean complication-free catheter indwelling time [70.3 days, 95% confidence interval (CI): 52.8–87.9] than the cSLC group (19.6 days, 95% CI: 17.9–21.2; $P < 0.05$). Subgroup analysis showed superior indwelling times with nDLC for both intra-abdominal (77.5 vs. 18.7 days) and pleural drainage (35.9 vs. 19.7 days) ($P < 0.05$). Dysfunctional retraction occurred in 10 cases in the cSLC group but in no cases in the nDLC group ($P < 0.001$).

CONCLUSION

The nDLC significantly reduces dysfunctional retraction and provides a longer complication-free catheter indwelling time than the cSLC for both pleural and intra-abdominal drainage.

CLINICAL SIGNIFICANCE

The nDLC design effectively prevents catheter retraction and eliminates the need for suture anchoring, potentially reducing suture-related complications and improving long-term catheter performance in patients requiring prolonged pleural or intra-abdominal drainage.

KEYWORDS

Double-loop catheter, pleural effusion, ascites, abdominal drainage, catheter occlusion

Handling editor: Bahri Üstünsöz

Corresponding author: Jung Suk Oh

E-mail: medof99@catholic.ac.kr

Received 16 December 2025; revision requested 07 January 2026; last revision requested 04 February 2026; accepted 15 February 2026.

Epub: 23.03.2026

Publication date: 02.11.2026

DOI: 10.4274/dir.2026.263808

The use of pigtail catheters has become the preferred minimally invasive treatment modality for draining pleural or intra-abdominal fluids.[1] Compared with conventional large-bore chest tubes, pigtail catheters, which are made from smaller and more flexible materials, are equally effective but cause less pain and are better tolerated by patients.[2] However, a smaller bore increases the risk of catheter blockage.[2]

Maintaining the correct position of an indwelling pigtail catheter is crucial for the successful drainage of pleural or intra-abdominal fluids.[3] Despite being securely fixed to the skin with sutures, a long-term catheter can still be inadvertently pulled out, leading to catheter dysfunction. To overcome this, the development of a double-pigtail catheter, which features additional coiling in the middle section, has been reported.[2] This design not only facilitates

You may cite this article as: Kim SH, Oh JS,, Chun HJ. Pleural and intra-abdominal long-term drainage: comparison of a novel double-loop and a conventional single-loop catheter. *Diagn Interv Radiol*. 2026;32(6):835-840.

drainage but also helps prevent complete dislodgement and maintains catheter function by resisting retraction. However, we observed that although the double-pigtail catheter helps prevent displacement, blockages can still occur if any side holes near the chest wall in the second loop become obstructed (Figures 1a and b).

Consequently, we designed a novel double-loop drainage catheter (nDLC) that lacks side holes along the proximal coiling segment. Drainage occurs exclusively through the side holes located in the distal loop, whereas the proximal loop, which has no drainage holes, functions primarily as a mechanical anchor against retraction. This design aims to address specific clinical issues, with particular emphasis on preventing catheter occlusion due to side-hole blockage in the second loop. Omitting side holes in the proximal loop was intended to reduce the risk of blockage by preventing debris accumulation at the wall interface, and retraction resistance is provided by the proximal loop's mechanical anchoring. Therefore, this study aims to compare the survival and effectiveness of conventional single-loop catheters (cSLCs) with those of nDLC.

Methods

Characteristics of a novel double-loop drainage catheter

The pigtail catheters used in this study were designed as follows: (1) the cSLC was an 8-F/21-cm multipurpose drainage catheter made of polyurethane, with a hydrophilic-coated distal segment (5 cm, five side holes with pigtail formation; Sungwon Medical, Cheongju, Republic of Korea, and UreSil LLC, Skokie, IL, USA); and (2) the nDLC was an 8-F/21-cm catheter made of polyurethane, with hydrophilic-coated proximal and distal segments (5 cm, five side holes only in the distal pigtail coiling, no side holes in the mid-shaft, and proximal coiling), a distal pigtail loop size of 2 cm, and a proximal loop of 1 cm (EQ drainage catheter, Hepato, Seoul, Republic of Korea) (Figure 2).

Main points

- The novel double-loop drainage catheter (nDLC) completely prevented dysfunctional retraction (0 cases vs. 10 cases in conventional single-loop catheters; $P < 0.001$) and did not require suture anchoring, potentially avoiding suture-related complications such as infection or tissue damage.
- The mean indwelling time without dysfunction was significantly longer with the nDLC (70.3 vs. 19.6 days; $P < 0.05$), with consistent benefits in both pleural (35.9 vs. 19.7 days) and intra-abdominal (77.5 vs. 18.7 days) drainage.
- The clinical success rate was higher with the nDLC (91.9% vs. 80.5%; $P = 0.004$), suggesting it is particularly advantageous for patients needing prolonged drainage of uncomplicated pleural effusions or ascites.

Patient characteristics

The need for informed consent from participants was waived due to the study's retrospective design. The protocol for this study was approved by the Institutional Review Board of the Catholic Medical Center of The Catholic University of Korea (approval number: KC25RISI0353, date: June 4, 2025). All consecutive drainage procedures performed between January and October 2023 were reviewed. The inclusion criteria focused on patients who underwent pleural or intra-abdominal drainage using 8-F catheters. Patients were excluded from the study if they had complicated intra-abdominal collections, such as bile, pancreatic secretions, bloody collections, urine, or air (n = 16), or complicated pleural collections, such as empyema or pneumothorax (n = 11). To focus

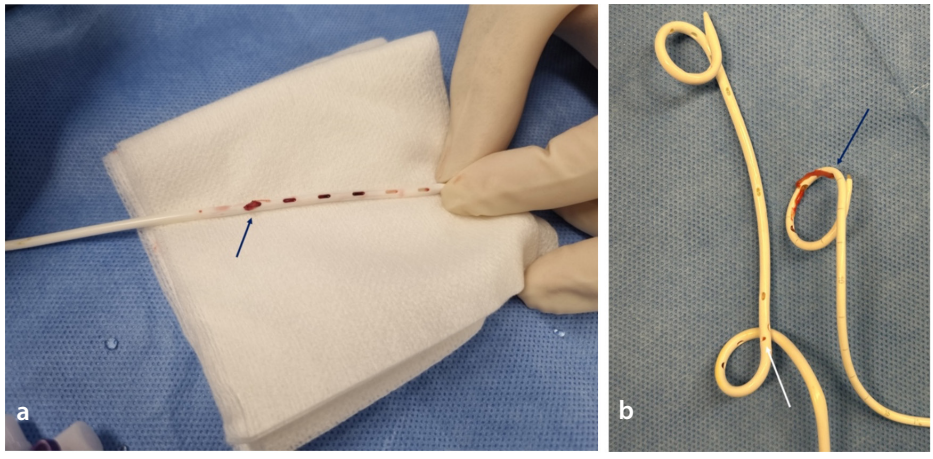


Figure 1. Occlusion pattern of the pigtail catheter. **(a)** Substantial amount of debris accumulation in the last side hole, potentially causing progressive catheter blockage (black arrow). **(b)** Similarly, in the case of double-loop catheters, debris starts to accumulate at the last side hole of the second loop adjacent to the chest or abdominal wall (white arrow).

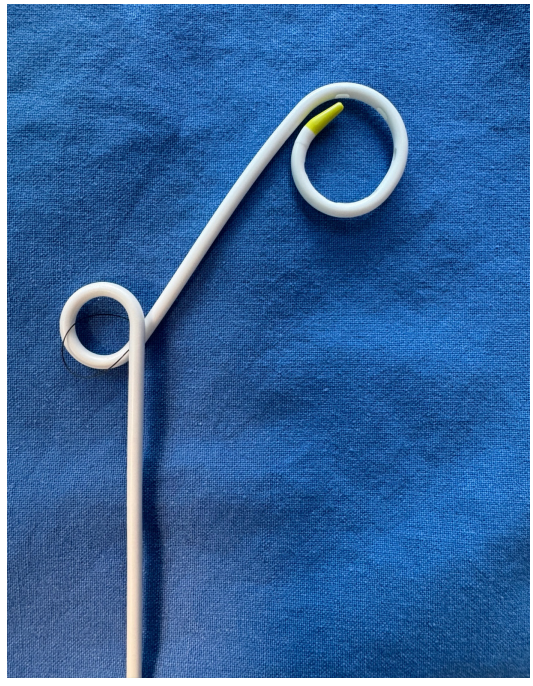


Figure 2. Detailed structure of the novel double-loop catheter. The multipurpose drainage catheter features two pigtail coiling segments spaced at 5-cm intervals. Side holes facing the centripetal direction inside the loop were only present in the distal pigtail coiling—the mid-shaft and proximal coiling segments have no side holes. Suture fixation was only applied to the proximal coil.

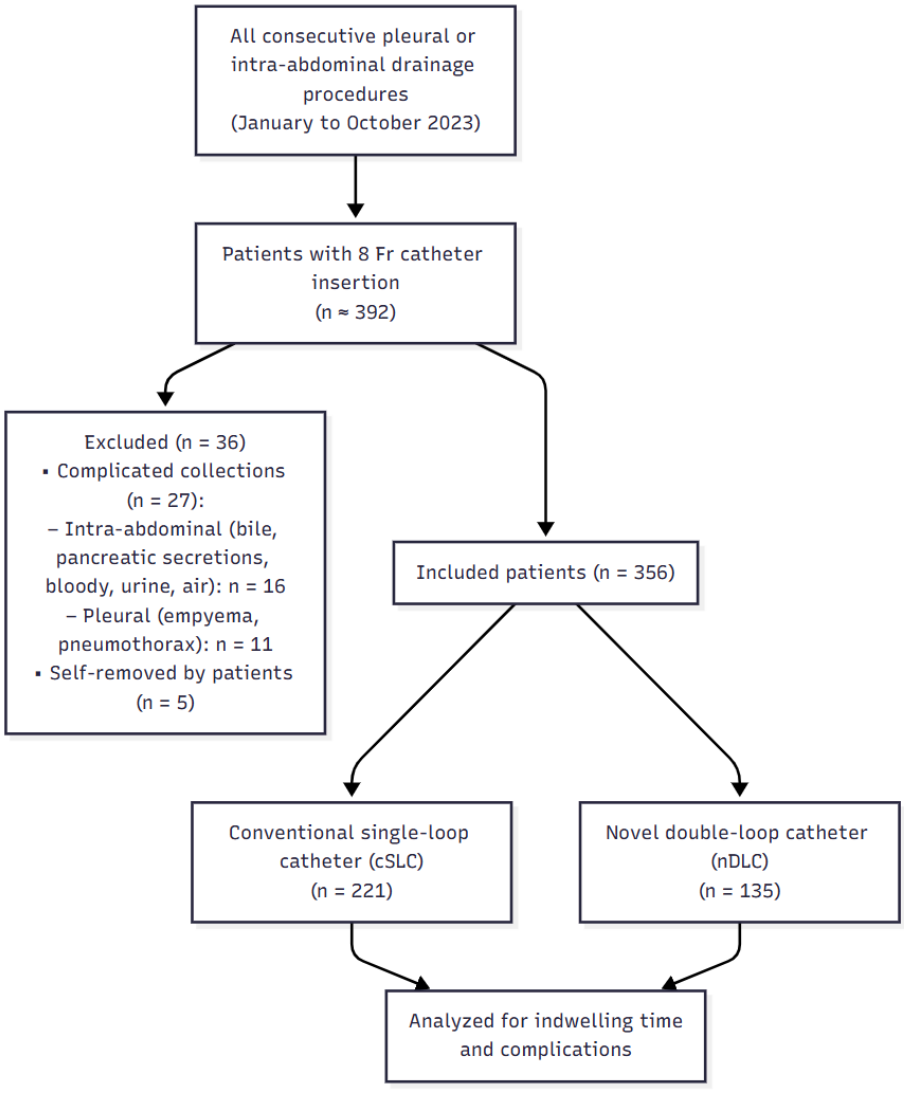


Figure 3. Flowchart of patient selection for the study.

on the analysis of the catheter's inherent anchoring efficacy and patient outcomes, catheters that were self-removed by patients (n = 5) were excluded from the study.

A total of 356 patients met these criteria and were divided into two groups based on the catheter design employed. The nDLC group comprised 135 patients, and the cSLC group included 221 patients. Demographic information, including age and sex, as well as clinical characteristics such as fluid location (ascites or pleural effusion), underlying etiology (e.g., cardiac or renal failure, infection, portal hypertension, pneumoconiosis, or malignancy), and fluid type (transudate or exudate), were gathered (Figure 3).

Procedures

Four interventional radiologists performed all the pleural or intra-abdominal drainage procedures in the interventional radiology suite. All four interventional radiologists had over 5 years of procedural experience. Drainage catheter placement was performed under fluoroscopy and ultrasound guidance using the Seldinger technique as follows: (1) after confirmation of fluid collection in the lower thorax or dependent position in the supine (intra-abdominal fluid drainage) or lateral decubitus position (pleural drainage), 1% lidocaine hydrochloride was locally administered at the skin surface of the prepared puncture site. Under ultrasound guidance, the fluid collection was punctured with an 18-gauge Angiocath needle, and a few milliliters of fluid were aspirated. After dilation, an 8-F pigtail catheter was inserted over the introduced 0.035-inch guidewire (Radifocus; Terumo, Tokyo, Japan) under fluoroscopic control. No suture anchoring was performed in the nDLC group because the second loop of the catheter was expected to prevent retraction effectively. However, all catheters in the cSLC group were secured with suture anchoring to ensure proper placement and prevent displacement.

Catheter survival and complications

Clinical success was defined as an improvement in intra-abdominal or pleural fluid collection on follow-up radiographs without catheter dysfunction. The complication-free catheter indwelling time was defined as the catheterization period without catheter dysfunction. If a catheter was exchanged or removed due to catheter dysfunction or catheter-related complications, it was treated as an uncensored event. If the patient was either discharged with the catheter or lost to follow-up without catheter dysfunction, the catheter indwelling time was determined as the period up to the last follow-up radiograph or the most recent assessment of drainage volume, and it was treated as a censored event.

Major complications included dysfunctional retraction, simple blockage, and complete dislodgement. Dysfunctional retraction is characterized by the outward pulling of the pigtail loop, causing it to retract toward the chest or abdominal wall. This results in blockage of the last side hole of the drainage catheter, ultimately leading to catheter dysfunction. Simple blockage refers to an obstruction within the drainage catheter without any displacement despite substantial residual fluid collection evident on simple radiographs or ultrasound. Complete dislodgement is defined as full displacement of the catheter tip outside the pleural or peritoneal cavity.

Statistical analysis

No formal a priori sample size calculation was conducted in this retrospective observational study. Post-hoc power analysis showed that the achieved sample sizes (n = 221 for cSLC, n = 135 for nDLC) provided > 95% power to detect the observed difference in the complication-free indwelling time (log-rank test) and > 90% power to detect the difference in dysfunctional retraction rates (Fisher's exact test) at α: 0.05. Continuous variables are reported as mean ± standard deviation, and categorical variables are presented as numbers (percentages). Comparisons between the novel and conventional catheter groups were conducted using the chi-square test or Fisher's exact test for categorical variables and Student's t-test for continuous variables. Kaplan–Meier survival

analysis was used to calculate the indwelling time of each group. Statistical significance was set at $P < 0.05$.

Results

Demographic data, including patient characteristics and fluid composition, showed no significant differences between the two groups (Table 1). In the nDLC group, 23.1% of patients had transudative fluids and 76.9% had exudative fluids, whereas in the cSLC group, 25.9% had transudative fluids and 74.1% had exudative fluids; these differences were not statistically significant ($P = 0.372$). Catheter dysfunction was observed in 28 cases (12.7%) in the cSLC group and in 9 cases (6.7%) in the nDLC group. A significant difference was noted in the incidence of dysfunctional retraction, with 10 occurrences in the cSLC group and none in the nDLC group ($P < 0.05$). Simple blockages were observed in 18 cases (8.1%) with the cSLC and 9 cases (6.7%) with the nDLC; however, this difference was not statistically significant ($P = 0.609$).

In total, 124 of the 135 patients in the nDLC group and 178 of the 221 patients in the cSLC group demonstrated improvement in intra-abdominal or pleural fluid collection on follow-up radiographic evaluations without catheter dysfunction. The clinical success rates for the nDLC and cSLC groups were 91.9% and 80.5%, respectively, with a statistically significant difference between the two groups ($P < 0.05$). The mean catheter indwelling time before the occurrence of an event (catheter dysfunction, catheter-related complications, discharge with a functioning catheter, or loss to follow-up) was 13 days in the nDLC group and 8.7 days in the cSLC group when the censored data were not considered. Kaplan–Meier survival analysis, which accounted for both censored and uncensored data, demonstrated a significant difference in the complication-free catheter indwelling time between the two groups ($P < 0.05$; Figure 4a). The nDLC group showed a markedly longer mean indwelling time [72.1 days, 95% confidence interval (CI): 54.0–90.1] than the cSLC group (20.4 days, 95% CI: 18.8–22.0). This result indicates a substantial improvement in catheter function duration with the nDLC. (Table 2).

Subgroup analyses further confirmed the superiority of the nDLC in both drainage settings ($P < 0.05$ for both comparisons). In the pleural drainage subgroup, the mean indwelling time was 36.9 days with the nDLC versus 20.7 days with the cSLC (Figure 4b). In the intra-abdominal drainage subgroup, the corresponding values were 77.5 vs. 19.1 days, respectively (Figure 4c).

Table 1. Baseline characteristics of the study patients

	Single loop	Double loop	*P* value
No. of patients	221	135	
Sex			
Men	107	67	0.733
Women	114	68	
Age (years), mean ± SD	66.5 ± 15.6	69.9 ± 14.8	0.233
Fluid location			
Ascites	31 (14.0%)	24 (17.7%)	0.095
Pleural effusion	190 (86.0%)	111 (82.3%)	
Etiology			
Cardiac or renal failure	49	32	
Infection	32	25	
Portal hypertension	3	4	0.057
Pneumoconiosis	0	1	
Malignancy	137	73	
Nature of fluid			
Transudate	51 (23.1%)	35 (25.9%)	0.372
Exudate	170 (76.9%)	101 (74.1%)	

SD, standard deviation.

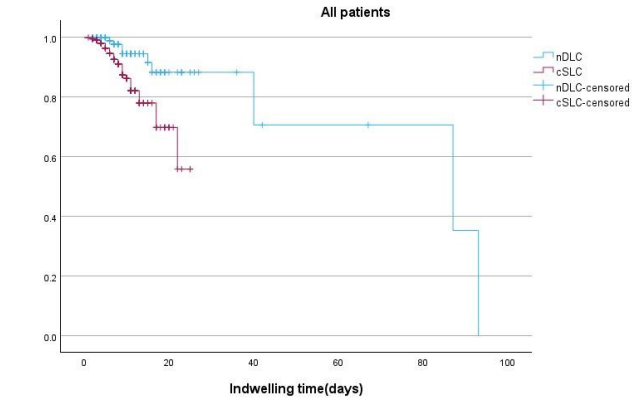
Table 2. Summary of study outcomes

	Single loop (n = 221)	Double loop (n = 135)	*P* value
Catheter dysfunction	28	9	
Dysfunctional retraction	10	0	< 0.001
Simple blockage	18	9	0.295
Complete dislodgement	1	0	0.411
Clinical success	178 (80.5%)	124 (91.9%)	0.004
Complication-free catheter (days) **Indwelling time** (days)	20.4	72.1	0.012
Pleural	20.7	36.9	0.048
Intra-abdominal	19.1	77.5	0.007

Discussion

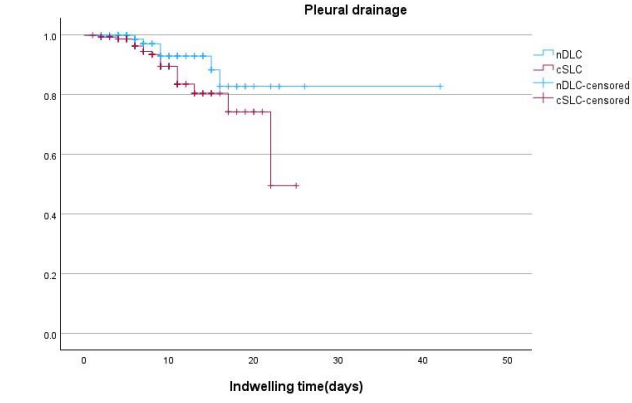
The average indwelling time for drainage catheters used in the management of ascites or pleural effusion varies according to patient factors, the type of effusion, and catheter characteristics. For ascitic fluid drainage catheters, the mean indwelling time typically ranges from 5 to 14 days. Some studies have reported longer durations, with safe usage documented for up to 30 days in certain cases.[4] Pleural drainage catheters exhibit a mean indwelling time of 3–14 days. However, in cases of chronic pleural effusion requiring long-term management, indwelling times may extend to several weeks or months.[5] Therefore, the selection and development of drainage catheters with improved performance for long-term use is necessary.

The main causes of catheter dysfunction can be categorized as catheter retraction, simple blockage, or complete dislodgement. Catheter retraction is one of the most common types of catheter malfunction.[4,6] Catheter migration can occur due to respiratory motion and routine movement even when the catheter is securely anchored to the skin.[7,8] This phenomenon is more prevalent in newly inserted catheters without an established tract formation, potentially leading to a relatively high incidence of relatively short-term intra-abdominal or pleural drainage catheters. In addition, suture-mediated anchoring can lead to various complications, including tissue damage caused by exces-



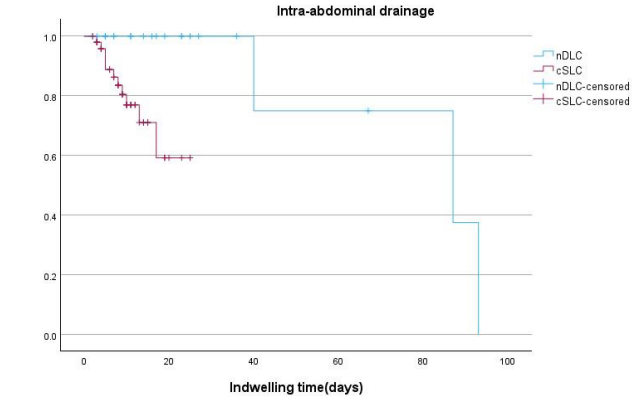
a

	0 days	20 days	40 days	60 days	80 days	93 days
Novel (nDLC)	130	14	5	3	2	1
Conventional (cSLC)	197	9	0	0	0	0



b

	0 days	10 days	20 days	30 days	40 days	42 days
Novel (nDLC)	111	40	6	1	1	1
Conventional (cSLC)	170	53	6	0	0	0



c

	0 days	20 days	40 days	60 days	80 days	93 days
Novel (nDLC)	24	9	4	3	2	1
Conventional (cSLC)	51	3	0	0	0	0

Figure 4. Kaplan–Meier curves showing the indwelling catheter survival time.

(a) Comparison between the novel double-loop catheter and conventional single-loop catheter in the overall cohort. **(b)** Subgroup analysis of the indwelling time for pleural drainage cases. **(c)** Subgroup analysis of the indwelling time for intra-abdominal drainage cases. nDLC, novel double-loop drainage catheter; cSLC, conventional single-loop catheter.

sive tension, leakage from improper track angles, catheter dislodgement (particularly in patients with obesity), and an increased risk of infection at suture sites.[8] Considering these issues, Huang et al.[8] proposed the use of internal pigtail loops for fixation instead of suture-mediated anchoring for long-term catheter use. In the present study, the nDLC group demonstrated significantly lower catheter retraction rates than the cSLC group despite the absence of suture-mediated anchoring. Moreover, no complete dislodgement was observed in the nDLC group. These findings suggest that the proximal coil of the nDLC effectively inhibited catheter retraction. Additionally, by eliminating the need for suture-based fixation, as typically required in conventional catheters, the nDLC design potentially reduces the risk of suture-related complications.

In this study, the cSLC group exhibited a higher blockage rate than the nDLC group (8.1% vs. 5.1%). Catheter obstruction can occur due to the accumulation of biological materials, including proteins, fibrin, and cellular debris, within the catheter lumen or drainage ports, progressively narrowing or completely occluding the inner diameter of the catheter. In our experience, a substantial amount of debris lodged only in the last hole of the pigtail coiling was frequently observed during the exchange of dysfunctional drainage catheters. Fibrin and cellular debris accumulation appears to accelerate when the catheter is retracted, causing the last hole in the pigtail coil to be occluded by the chest wall. To address this, we designed a dual-loop catheter without side holes in the proximal coil. This design effectively reduced the catheter retraction rate while preventing the last side hole from contacting the chest wall, thereby eliminating the risk of fibrin and cellular debris accumulation and potentially reducing the simple blockage rate. Although the difference in the simple blockage rate did not achieve statistical significance in this study, we hypothesize that catheter blockage may still occur due to the accumulation of biological materials when the drainage fluid volume decreases and the catheter contacts the pleura or peritoneum. Further systematic and detailed observational studies are needed to investigate this phenomenon.

This study has some limitations. First, it was retrospective in nature. However, to minimize bias, we compared consecutive cases of ascites and pleural drainage that were performed during the same period. To overcome the limitations of this retrospective study, a prospective randomized controlled

trial comparing the nDLC and the cSLC is being planned. Second, this study focused solely on uncomplicated fluid drainage. The nDLC has a fixed 5 cm interval between the proximal and distal pigtail coils. This interval might potentially reduce drainage efficacy in multiseptate complicated fluid collections. As catheter use continues to expand to various conditions and indications, further evidence-based studies are warranted to improve our understanding of this nDLC. Third, owing to the consecutive patient comparison during the same period, a high proportion of censored data was present (discharges with functioning catheters or loss to follow-up). This censoring can bias the simple mean indwelling time downward; therefore, we relied primarily on Kaplan–Meier estimates, which appropriately handle censoring, to compare catheter survival between groups. Another limitation is the lack of a subgroup comparison between the non-sutured nDLC and the non-sutured cSLC, which could have better delineated the role of suturing. This should be explored in future prospective studies. Furthermore, although simple blockage showed a numerical reduction with the nDLC, the difference was not statistically significant; thus, the proposed mechanism remains suggestive and requires confirmation in larger studies. Moreover, multivariable adjustment was not performed due to the retrospective design and standardized approach. However, the numerical difference in malignancy prevalence warrants multivariable regression in future prospective studies to exclude confounding.

In conclusion, this nDLC effectively improved the chronic issue of dysfunctional retraction associated with single-loop catheters. Notably, despite the absence of sutures, there were no instances of dysfunctional retraction or complete dislodgement, which suggests a lack of anchoring-related complications. These characteristics indicate that this nDLC may be suitable for long-term use.

Footnotes

Conflict of interest disclosure

The authors declared no conflicts of interest.

References

1. Mehra S, Heraganahally S, Sajkov D, Morton S, Bowden J. The effectiveness of small-bore intercostal catheters versus large-bore chest tubes in the management of pleural disease with the systematic review of literature. *Lung India*. 2020;37(3):198-203. [Crossref]
2. Cho Y, Lee HN, Shin JH, Park SJ, Lee S, Song JS. Double-pigtail drainage catheter: a new design for efficient pleural drainage. *Medicina (Kaunas)*. 2023;59(6):1089. [Crossref]
3. Roberts JS, Bratton SL, Brogan TV. Efficacy and complications of percutaneous pigtail catheters for thoracostomy in pediatric patients. *Chest*. 1998;114(4):1116-1121. [Crossref]
4. Jayawardena T, Vekaria S, Krivinskas S, Sidhu C, Chakera A, Lee YCG. Antibiotic administration via indwelling peritoneal catheter to treat infected malignant ascites. *Respirol Case Rep*. 2022;10(11):e01055. [Crossref]
5. Türk Y, Devecioğlu İ, Yıldızhan İ, Arslan BC, Arıbaş BK. Tunneled uncuffed pigtail drainage catheter placement in patients with refractory ascites or pleural effusion: a single-center experience. *Cardiovasc Intervent Radiol*. 2022;45(11):1735-1741. [Crossref]
6. Oviedo Flores K, Kaltenegger L, Eibensteiner F, et al. Assessing mechanical catheter dysfunction in automated tidal peritoneal dialysis using cycler software: a case control, proof-of-concept study. *Sci Rep*. 2022;12(1):5657. Erratum in: *Sci Rep*. 2022;12(1):7623. [Crossref]
7. Zhao L, Yang J, Bai M, Dong F, Sun S, Xu G. Risk factors and management of catheter malfunction during urgent-start peritoneal dialysis. *Front Med (Lausanne)*. 2021;8:741312. [Crossref]
8. Huang SY, Engstrom BI, Lungren MP, Kim CY. Management of dysfunctional catheters and tubes inserted by interventional radiology. *Semin Intervent Radiol*. 2015;32(2):67-77. [Crossref]

Diagn Interv Radiol 2026; DOI: 10.4274/dir.2026.263734

INTERVENTIONAL RADIOLOGY

ORIGINAL ARTICLE

©Copyright 2026 Author(s) - Available online at dirjournal.org.
Content of this journal is licensed under a Creative Commons Attribution-NonCommercial 4.0 International License.

Reduction of hemorrhagic complications after non-focal renal biopsy with pre-procedure desmopressin administration

Bradford Dugan[1]
Christine A. Welch[2]
Asif Rahman[3]
Michael V. Korona[4]
Amy R. Deipolyi[1,4]

[1]West Virginia School of Medicine, Charleston Division, West Virginia, United States of America

[2]Institute of Academic Medicine, Charleston Area Medical Center, West Virginia, United States of America

[3]Charleston Area Medical Center Nephrology, West Virginia, United States of America

[4]Charleston Area Medical Center, Interventional Radiology, Department of Surgery, West Virginia, United States of America

PURPOSE

Ultrasound-guided non-focal renal biopsy (NFRB), which is performed to assess systemic renal processes, is associated with a 1.5%–14% bleeding risk. The goal of this study is to evaluate the safety and efficacy of 1-deamino-8-D-arginine vasopressin (DDAVP, or desmopressin) in mitigating bleeding risk when administered prior to NFRB.

METHODS

This retrospective observational study includes 158 patients who underwent NFRB between March 2022 and June 2025 at the study hospital before and after the implementation of a DDAVP administration protocol. Beginning in July 2023, every patient at the study site received intravenous DDAVP immediately before biopsy, regardless of renal function. Ultimately, 79 patients received DDAVP (the DDAVP group), and 79 did not receive the intervention (the non-DDAVP group). This study's primary endpoint was clinically significant bleeding (resulting in unplanned admission; intervention for bleeding, such as angiography or surgery; and/or death) within 1 week of biopsy. Secondary endpoints were hyponatremia or a thromboembolic event within 1 week of biopsy. The data from patients in the two groups were compared using Mann–Whitney U tests for non-parametric data, Student's t-tests for parametric data, and chi-squared tests for categorical data (with an alpha level of $P < 0.05$).

RESULTS

Six of the 79 patients (8%) in the non-DDAVP group experienced a clinically significant hemorrhage, compared with 0 in the DDAVP group ($P = 0.03$). Sodium levels were not significantly different between the two groups post-procedure ($P = 0.43$). There was no significant difference in the rate of thromboembolic events between the two groups [2/79 (2.5%) in the non-DDAVP group vs. 3/79 (3.8%) in the DDAVP group; $P = 1.00$]. The 5 patients (out of 158; 3.2%) who experienced a thromboembolic event within 1 week of NFRB had been on anticoagulants or antiplatelet agents that were held for biopsy.

CONCLUSION

DDAVP is associated with a reduction in unplanned hospitalizations and bleeding interventions (angiography and embolization) after NFRB, without an observed increase in thromboembolic events.

CLINICAL SIGNIFICANCE

Routine DDAVP administration before NRFB significantly reduces clinically significant bleeding, supporting its potential role as a simple prophylactic strategy.

KEYWORDS

Non-focal renal biopsy, desmopressin, hemorrhage

Handling editor: Bahri Üstünsöz

Corresponding author: Amy Deipolyi

E-mail: amy.deipolyi@camc.org

Received 04 November 2025; revision requested 14 December 2025; accepted 20 January 2026.

Epub: 23.03.2026

Publication date: 02.11.2026

DOI: 10.4274/dir.2026.263734

You may cite this article as: Dugan B, Welch CA, Rahman A, Korona MV, Deipolyi AR. Reduction of hemorrhagic complications after non-focal renal biopsy with pre-procedure desmopressin administration. *Diagn Interv Radiol*. 2026;32(6):841-845.

Ultrasound-guided percutaneous non-focal renal biopsy (NFRB) is performed to assess systemic processes affecting the kidneys, such as nephropathies.[1] The Society of Interventional Radiology (SIR) considers NFRB to carry a high bleeding risk, with a threshold adverse event rate of 5%.[2] Bleeding after NFRB has been reported in up to 14% of cases,[3] with risk factors including a low estimated glomerular filtration rate (eGFR), hypertension, prolonged bleeding time, acute tubular necrosis, vasculitis, systemic lupus erythematosus, female sex, younger age, abnormal coagulation factors, anticoagulant or antiplatelet agent use, and anemia.[4-7] Hemorrhage after NFRB is particularly concerning, since anemia and a low eGFR yield a high risk of contrast-induced nephropathy, should contrast angiography be required.[8]

The administration of 1-deamino-8-D-arginine vasopressin (DDAVP, or desmopressin), a synthetic analogue of vasopressin that increases blood plasma levels of the von Willebrand factor and clotting factor VIII, has been proposed to minimize bleeding risk. Theoretically, DDAVP could reverse uremia-mediated prolonged bleeding times, impaired platelet aggregation, and von Willebrand factor dysfunction.[9] Systematic reviews suggest that there is insufficient high-quality evidence to support the routine use of DDAVP before NFRB.[10] Additionally, DDAVP may cause adverse events resulting from hypercoagulable states, including thromboembolic events and metabolic derangements (e.g., hyponatremia).[11] There is controversy in the literature regarding the use of DDAVP, with some studies showing a benefit and others showing none.[10] A recent randomized study demonstrated that DDAVP administration in patients undergoing biopsy resulted in fewer and smaller perirenal hematomas, regardless of baseline renal function,[12] though there were no differences in the need for interventions such as arterial embolization or hospital admission in this study. Based on this paper, a DDAVP administration protocol was initiated at our academic institution for all patients undergoing NFRB, and data were collected on all biopsies performed before and after the instatement of this protocol to assess the safety and efficacy of DDAVP in lowering bleeding risk.

Main points

- Non-focal renal biopsy (NFRB), performed to evaluate systemic renal disease, carries a bleeding risk that may be reduced by the administration of desmopressin (DDAVP or 1-deamino-8-D-arginine vasopressin) immediately before the procedure.
- A clinically significant hemorrhage occurred in 8% of the patients who did not receive DDAVP, compared with 0% of those who received DDAVP.
- No differences in the rates of hyponatremia or thromboembolic events were observed between the two groups.
- Routine DDAVP administration before NFRB may improve patient safety by preventing major bleeding.

Methods

This single-center retrospective observational study, conducted at Charleston Area Medical Center in Charleston, West Virginia, complies with the Health Insurance Portability and Accountability Act and was approved by the Charleston Area Medical Center Institutional Review Board (protocol number: #23-935, date: 03.06.2023). One-hundred fifty-eight patients who underwent ultrasound-guided NFRB, performed by two interventional radiologists with 11 and 31 years of experience, between March 2022 and June 2025 were included (Figure 1). Due to its retrospective nature, informed consent was not required for this study. Initially, DDAVP was not administered to any patient peri-procedurally. Beginning in July 2023, every patient was administered DDAVP intravenously (0.3 mcg/kg) within 1–2 hours before biopsy, regardless of renal function. Ultimately, 79 patients received DDAVP (the DDAVP group), and 79 did not receive the intervention (the non-DDAVP group). One operator who joined the practice in May 2023 performed NFRPs under both computed tomography and ultrasound guidance. For consistency across cases and to allow for meaningful comparisons, this analysis was limited to procedures performed with ultrasound guidance.

Biopsies were performed using a 17-gauge coaxial guide to obtain 18-gauge cores, with the on-site assessment of specimen adequacy performed by trained cytotechnologists. The obtained tracts were embolized with an absorbable gelatin sponge. Anticoagulants and antiplatelet agents were always held, according to SIR practice guidelines.[13] Blood pressure was controlled such that systolic blood pressure (SBP) was maintained below 140 mmHg. Inpatients were not accepted for biopsy unless their SBP was < 140 mmHg. If a patient's pressure was elevated upon arrival to the interventional radiology unit, 10 mg of intravenous hydralazine was administered. If their SBP was < 150 mmHg, the patient was placed in a prone position, and intravenous midazolam and fentanyl were administered. If their SBP was still > 140 mmHg, a second dose of hydralazine was administered. If the patient's SBP was still not < 140 mmHg, the procedure was aborted and rescheduled with anesthesiologic support. Patients were recovered for ≥ 2 hours on strict bedrest in a supine position, either in their inpatient beds or in a recovery space, prior to discharge.

Patients who underwent biopsies were identified by a search of the institution's picture archiving and communication system. Demographic characteristics, laboratory information, vital signs, hospitalization status, and other interventions were gleaned from medical charts. The primary endpoint of this

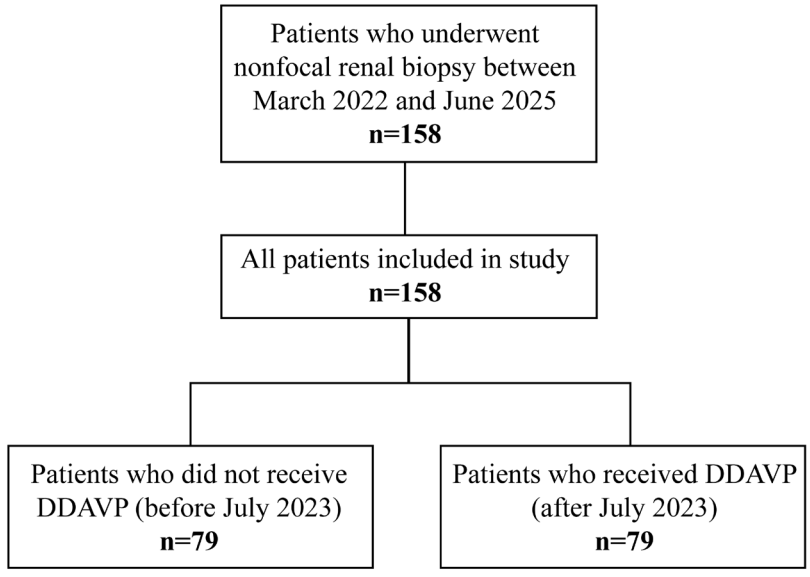


Figure 1. Study flowchart. DDAVP, 1-deamino-8-D-arginine vasopressin (desmopressin).

study was clinically significant hemorrhage. Given the high rate of transfusions for anemia in patients with renal failure, clinically significant hemorrhage was defined as hospital admission, angiography with or without embolization, and surgery to control bleeding within 1 week of biopsy. Secondary endpoints were a thromboembolic event within 1 week of biopsy and hyponatremia. Thromboembolic events were defined as stroke, myocardial infarction, and other embolic complications and were determined based on their documentation in consultation notes. Sodium and hemoglobin levels were observed within 24 hours before and after biopsy.

Statistical analysis

Data analysis was performed using SAS version 9.4 (SAS Institute Inc., Cary, NC, USA). Comparisons of continuous variables were conducted using Mann–Whitney U tests for abnormally distributed data and represented as median (interquartile range; range), and Student's t-tests were used for normally distributed data and represented as (mean ± standard deviation; range). Categorial data were compared using chi-squares tests and Wilson confidence intervals (CIs)—or Fisher's exact test and a Clopper–Pearson for CIs (for binomial variables)—and presented as number (n), proportion (%), and CI, as dictated by the data. Alpha was set to $P < 0.05$ for all tests. Multivariate analysis was completed using Firth's bias-reduced logistic regression.

Results

The patients in the non-DDAVP group were older on average than their counterparts in the DDAVP group but matched them in terms of baseline renal function (Table 1). Most often, three core biopsies were obtained. The median dose of DDAVP administered was 25 (13.6; 12–43.7) mcg in the DDAVP group. Sodium and hemoglobin levels did not differ between the two groups before or after the procedure (Table 2). Blood transfusion within 48 hours of biopsy was the same for both groups (Table 2).

Six of the 79 patients (8%) in the non-DDAVP group experienced a clinically significant hemorrhage within 1 week of biopsy, compared with 0 patients in the DDAVP group ($P = 0.03$) (Table 2). Among these 6 patients (Table 3), the median pre-procedure eGFR was 29.5 (14; 6–83), compared with 30 (34; 6–100) among the patients in the non-DDAVP group who did not experience clinically significant bleeds ($P = 0.82$). No patient required surgery to stop bleeding after biopsy, and there were no deaths. In both groups, there were patients who experienced a stroke or myocardial infarction, but the odds of thromboembolic events were not significantly different between the two groups (odds ratio: 1.52; 95% CI: 0.25–9.35).

Table 1. Baseline characteristics

Characteristic	w/o DDAVP	w/ DDAVP	*P* value
Number of patients (n)*	79	79	
Mean age (years)	59 ± 14	54 ± 18	0.04
Male gender (n [%])	38 (48.1%)	43 (54.4%)	0.43
Performed on inpatient basis (n [%])	29 (36.7%)	44 (55.7%)	0.02
Number of cores (median [IQR; range])	3 (1; 2–11)	3 (1; 2–7)	0.10
Maximum SBP during biopsy (mmHg) (mean ± SD)	123.8 ± 13.0	120.6 ± 15.6	0.16
DBP during biopsy (mmHg) (mean ± SD)	69.1 ± 10.1	67.1 ± 12.9	0.30
Hemoglobin before biopsy (g/dL) (median [IQR; range])	n = 45, 9.5 (2.4; 6.7–17.7)	n = 57, 9.4 (2.9; 7.2–19.4)	0.50
eGFR before biopsy (mL/min) (median [IQR; range])*	n = 76, 30.0 (33; 6–100)	23.0 (38; 4–128)	0.39
Sodium before biopsy (mmol/L) (mean ± SD; range)	n = 44, 136.8 ± 4.3; 126–145)	n = 57, 137.19 ± 3.3; 130–144	0.61

*n = 79, except where otherwise noted.
DDAVP, 1-deamino-8-D-arginine vasopressin (desmopressin); IQR, interquartile range; SBP, systolic blood pressure; SD, standard deviation; DBP, diastolic blood pressure; eGFR, estimated glomerular filtration rate; w/o, without; w/, with.

Table 2. Adverse events and laboratory changes after biopsy

Characteristic	w/o DDAVP	w/ DDAVP	*P* value
Number of patients (n)*	79	79	
Sodium after biopsy (mmol/L) (mean ± SD; range)	n = 36, 136 ± 3.81; 130–147	n = 46, 137 ± 3.96; 130–146	0.43
Hemoglobin after biopsy (g/dL) (median [IQR; range])*	n = 36, 9.2 (2.0; 6.7–16.6)	n = 46, 8.8 (2.9; 6.5–15.8)	0.28
Blood transfusion within 48 h	8 (10.1%)	8 (10.1%)	1.00
Clinically significant hemorrhage within 1 week (n [%; 95% CI])	6 (7.6%; 0.03–0.16)	0 (0%; 0.95–1.00)	0.03**
Unplanned admission only (n [%; 95% CI])	2 (2.5%; 0.003–0.089)	0 (0%; 0.95–1.00)	0.50**
Angiography only (already admitted) (n [%; 95% CI])	1 (1.3%; 0.0003–0.069)	0 (0%; 0.95–1.00)	1.00**
Unplanned admission and angiography (n [%; 95% CI])	3 (3.8%; 0.008–0.107)	0 (0%; 0.95–1.00)	0.25**
Surgery for bleeding control (n [%; 95% CI])	0 (%; 0.95–1.00)	0 (0%; 0.95–1.00)	
Thromboembolic event within 1 week (n [%; 95% CI])	2 (2.5%; 0.003–0.089)	3 (3.8%; 0.008–0.107)	1.00**
Myocardial infarction (n [%; 95% CI])	1 (1.3%; 0.0003–0.069)	2 (2.5%; 0.003–0.089)	1.00**
Stroke/transient ischemic attack (n [%; 95% CI])	1 (1.3%; 0.0003–0.069)	1 (1.3%; 0.0003–0.069)	1.00**

*n = 79, except where otherwise noted; **Fisher's exact test.
DDAVP, 1-deamino-8-D-arginine vasopressin (desmopressin); SD, standard deviation; IQR, interquartile range; CI, confidence interval; w/o, without; w/, with.

Table 3. Characteristics of patients with clinically significant hemorrhage after biopsy

Patient	1	2	3	4	5	6
Age (years)	66	29	61	75	75	39
Gender	M	F	M	F	F	F
Number of cores	3	5	4	6	3	5
Maximum SBP (mmHg)	146	120	132	108	114	120
eGFR	20	6	32	27	34	83
Hemoglobin (g/dL) before	13.4	6.7	11.8	12.3	9.7	13.5
Hemoglobin (g/dL) after	14	8.5	10	11.4	7.1	8.8
Blood transfusion	No	Yes	Yes	No	Yes	Yes
Unplanned admission	Yes	Yes	Yes	Yes	No*	Yes
Angiography	No	Yes	Yes	No	Yes	Yes
Embolization		Yes	No		No	Yes

*Already admitted.
SBP, systolic blood pressure; eGFR, estimated glomerular filtration rate.

All 5 patients who experienced thromboembolic events within 1 week of biopsy had been on an anticoagulant or antiplatelet therapy that was held, as per SIR guidelines, for biopsy. A regression model that evaluated covariates—including 1) the use or nonuse of DDAVP; 2) eGFR levels, broken into three ranges (≥ 45, ≥ 15 to < 45, and < 15); 3) the number of cores obtained (≤ 4 or > 4); 4) age (≥ 65 or < 65 years); and 5) visit status (inpatient or outpatient)—and considered 155 patients showed that those who did not receive DDAVP were 13.8 times (95% CI: 1.0–185.0) more likely to experience a clinically significant hemorrhage ($P = 0.048$). No other covariates were significant.

Discussion

In this single-center retrospective study, DDAVP administration before NFRB was associated with a significant reduction in the risk of clinically significant hemorrhage. The patients who received DDAVP were administered the intervention regardless of baseline renal function. No differences in thromboembolic events or hyponatremia were observed between the two groups in this cohort. Our findings suggest that the routine administration of DDAVP before NFRB may prevent hemorrhagic complications, which are associated with worse outcomes and increased healthcare costs.

This study differs from prior literature in two ways. First, this study focused on clinically significant bleeds, whereas prior research investigated hematomas after biopsy, which are common but do not necessarily result in a need for intervention.[12] Second, DDAVP administration in this study proceeded regardless of baseline eGFR, unlike prior reports.[14] Low eGFR is a risk factor for bleeding after NFRB due to uremic platelet dysfunction, which may be reversed by DDAVP. For patients with no coagulopathies or uremia, DDAVP may lower bleeding risk by stimulating the release of the von Willebrand factor, improving platelet adhesion and aggregation, and enhancing clotting activity.[15]

The lack of an observed increase in thromboembolic events or hyponatremia provides reassurance for the broader use of DDAVP prior to biopsy. DDAVP is an antidiuretic agent that promotes water retention, potentially leading to hyponatremia, though this was not observed in the current study. DDAVP also has thrombogenic properties that could cause major thromboembolic events, including stroke and myocardial infarction. It may be that the holding of anticoagulants and antiplatelet agents itself leads to the observed risk of stroke and myocardial infarction, regardless of DDAVP administration. The finding that NFRB is associated with a 3%–5% risk of stroke or myocardial infarction is important to note when counseling patients who are on antiplatelet or anticoagulant medications and who are planning to undergo NFRB.

This study has several limitations. Its retrospective, non-randomized design inherently limits our ability to establish causality and is subject to incomplete data and unmeasured confounders. Patients who received DDAVP were not matched to those who did not, which may have resulted in selection bias. In particular, biopsies performed without DDAVP administration were more commonly performed on an outpatient basis and on older patients. Additionally, the study was conducted over a 3-year period, during which time an evolution in procedural techniques, operator experience, and institutional practice patterns may have occurred, potentially introducing temporal and procedural biases. As a single-center study, these findings may not be generalizable to other settings. Data on potential confounders, such as platelet and clotting function, which may influence bleeding outcomes, were not consistently available. Finally, this study was not adequately powered to detect a difference in very rare observations, such as thromboembolic events. Given the low absolute difference in the rate of stroke and myocardial infarction between the two groups (1.3%), approximately 4,000 patients per group would be required to achieve 90% power at an alpha level of 0.05. Future prospective randomized studies with larger and more diverse cohorts would help confirm these findings and clarify the role of DDAVP in reducing bleeding complications after NFRB in all patients, regardless of renal function.

In conclusion, DDAVP administration immediately before NFRB is associated with a decrease in unplanned hospitalizations and angiographic procedures, with no observed increase in thromboembolic events or hyponatremia. The routine administration of DDAVP prior to NFRB may mitigate hemorrhagic complications.

Footnotes

Conflict of interest disclosure

Dr. Deipolyi is a paid consultant for Boston Scientific, Inc., and Varian, Medical. The other authors have no conflicts of interest.

References

1. Uppot RN, Harisinghani MG, Gervais DA. Imaging-guided percutaneous renal biopsy: rationale and approach. *AJR Am J Roentgenol*. 2010;194(6):1443-1449. [Crossref]
2. Sheth RA, Baerlocher MO, Connolly BL, et al. Society of Interventional Radiology Quality improvement standards on percutaneous needle biopsy in adult and pediatric patients. *J Vasc Interv Radiol*. 2020;31(11):1840-1848. [Crossref]
3. Corapi KM, Chen JL, Balk EM, Gordon CE. Bleeding complications of native kidney biopsy: a systematic review and meta-analysis. *Am J Kidney Dis*. 2012;60(1):62-73. [Crossref]
4. Deipolyi A, Leonardo F, Hahn PF, et al. Predictors of hemorrhagic complications after ultrasound-guided nonfocal renal biopsy. *J Prev Epidemiol*. 2016;1(2):e11. [Crossref]
5. Manno C, Strippoli GF, Arnesano L, et al. Predictors of bleeding complications in percutaneous ultrasound-guided renal

biopsy. *Kidney Int*. 2004;66(4):1570-1577. [Crossref]

6. Shidham GB, Siddiqi N, Beres JA, et al. Clinical risk factors associated with bleeding after native kidney biopsy. *Nephrology (Carlton)*. 2005;10(3):305-310. [Crossref]
7. Whittier WL, Korbet SM. Timing of complications in percutaneous renal biopsy. *J Am Soc Nephrol*. 2004;15(1):142-147. [Crossref]
8. Haber ZM, Charles HW, Erinjeri JP, Deipolyi AR. Predictors of active extravasation and complications after conventional angiography for acute intraabdominal bleeding. *J Clin Med*. 2017;6(4):47. [Crossref]
9. Cattaneo M, Mannucci PM. Desmopressin (DDAVP). In: Michelson AD, Cattaneo M, Frelinger AL, Newman PJ, editors. Platelets. 4th ed. Cambridge (MA): Academic Press; 2019. p. 1111-1120. [Crossref]
10. Lim CC, Tan HZ, Tan CS, Healy H, Choo J, Franca Gois PH. Desmopressin acetate to prevent bleeding in percutaneous kidney biopsy: a systematic review. *Intern Med J*. 2021;51(4):571-579. [Crossref]
11. Goad N, Levesque M. Role of desmopressin in the critical care setting. *AACN Adv Crit Care*. 2020;31(1):5-11. [Crossref]
12. Sattari SA, Shahoori A, Shahbazian H, et al. Desmopressin acetate in percutaneous ultrasound-guided native kidney biopsy in patients with reduced kidney function: a double-blind randomized controlled trial. *Iran J Kidney Dis*. 2022;16(4):238-245. [Crossref]
13. Patel IJ, Rahim S, Davidson JC, et al. Society of Interventional Radiology Consensus Guidelines for the periprocedural management of thrombotic and bleeding risk in patients undergoing percutaneous image-guided interventions-part II: recommendations: endorsed by the Canadian Association for Interventional Radiology and the Cardiovascular and Interventional Radiological Society of Europe. *J Vasc Interv Radiol*. 2019;30(8):1168-1184.e1. [Crossref]
14. Ho QY, Lim CC, Thangaraju S, et al. Bleeding complications and adverse events after desmopressin acetate for percutaneous renal transplant biopsy. *Ann Acad Med Singap*. 2020;49(2):52-64. [Crossref]
15. Wang C, Lebedeva V, Yang J, et al. Desmopressin to reduce periprocedural bleeding and transfusion: a systematic review and meta-analysis. *Perioper Med (Lond)*. 2024;13(1):5. [Crossref]

Diagn Interv Radiol 2026; DOI: 10.4274/dir.2026.263960

INTERVENTIONAL RADIOLOGY

ORIGINAL ARTICLE

©Copyright 2026 Author(s) - Available online at dirjournal.org.
Content of this journal is licensed under a Creative Commons Attribution-NonCommercial 4.0 International License.

Comparative evaluation of two resorbable microparticles in a porcine kidney model: angiographic and pathologic outcomes

Won Seok Choi[1]
Kun Yung Kim[1]
Chong-ho Lee[1]
Young-Min Han[2,3]
Minuk Kim[4]
Sung-hwan Yoon[5]
Chang Jin Yoon[1,6]
Jae Hwan Lee[1,6]

[1]Seoul National University Bundang Hospital, Department of Radiology, Seongnam, Republic of Korea

[2]Jeonbuk National University Faculty of Medicine, Department of Radiology, Jeonju, Republic of Korea

[3]Research Institute of Clinical Medicine of Jeonbuk National University, Biomedical Research Institute of Jeonbuk National University Hospital, Jeonju, Republic of Korea

[4]Seoul Metropolitan Government, Seoul National University Boramae Medical Center, Department of Radiology, Seoul, Republic of Korea

[5]Seoul National University Bundang Hospital, Department of Plastic and Reconstructive Surgery, Seongnam, South Korea

[6]Seoul National University College of Medicine, Department of Radiology, Seoul, Republic of Korea

PURPOSE

This study aimed to compare the safety and efficacy of two resorbable microparticles in a porcine kidney model, focusing on recanalization and tissue injury outcomes over a 7-day follow-up period.

METHODS

This exploratory proof-of-concept study included 10 pigs, each undergoing embolization of the upper polar arteries in both kidneys, resulting in 20 treated kidneys (10 per group). Angiographic evaluations were performed on all 20 treated kidneys (10 per group) across the 10 animals at immediate, 2-hour, 1-day, and 7-day post-embolization time points. Histopathologic evaluations were performed on 5 animals per group (5 kidneys per group). The primary endpoint was complete angiographic recanalization at 7 days. Secondary endpoints included early recanalization at 2 hours and 1 day and histopathologic tissue injury. In Group A, the right upper polar artery was embolized with spherical gelatin microparticles (Nexsphere-F®), whereas in Group B, the left upper polar artery was embolized with irregular microparticles (KIPZA®). Approximately 5–10 mL of microparticle suspension was injected per kidney; the mean embolization time per kidney was 30 ± 5 minutes.

RESULTS

At 2 hours post-embolization, complete recanalization was observed in all Nexsphere-F kidneys and in 9 of 10 KIPZA kidneys; 1 KIPZA kidney showed partial recanalization. Full recanalization was observed in all kidneys by day 7. Histopathologic evaluation (5 kidneys per group) revealed no residual emboli or parenchymal infarction in Group A. In Group B, minimal microparticle residue and focal infarction (mean infarcted area 2.78% ± 1.33%) were observed, along with endothelial proliferation in arcuate and interlobular arteries.

CONCLUSION

In this exploratory pilot study, embolization with both Nexsphere-F and KIPZA microparticles resulted in early recanalization and minimal tissue injury. These proof-of-concept findings suggest that both microparticles may be suitable for temporary embolization when organ preservation is paramount, although larger powered studies with disease models and longer follow-up are needed.

CLINICAL SIGNIFICANCE

These preliminary data support the potential of resorbable microparticles for temporary embolization, emphasizing their use in scenarios requiring parenchymal preservation and underscoring the need for further research.

KEYWORDS

Microparticles, organ preservation, angiography, embolization, therapeutic, embolic agent

Handling editor: Onur Taydaş

Corresponding author: Jae Hwan Lee

E-mail: lzhwanmd@gmail.com

Received 26 February 2026; revision requested 11 March 2026; last revision requested 23 March 2026; accepted 24 March 2026.

Epub: 21.04.2026

Publication date: 02.11.2026

DOI: 10.4274/dir.2026.263960

Transarterial embolization (TAE) is a cornerstone technique in interventional radiology, widely used to manage hemorrhage, target tumor vasculature, and treat vascular disorders.[1-5] Permanent embolic agents, such as polyvinyl alcohol particles and tris-acryl microparticles, have been the standard for achieving sustained occlusion.[6] However, their pro-

You may cite this article as: Choi WS, Kim KY, Lee C, et al. Comparative evaluation of two resorbable microparticles in a porcine kidney model: angiographic and pathologic outcomes. *Diagn Interv Radiol*. 2026;32(6):846-851.

longed presence can cause ischemic injury to non-target tissues, particularly in sensitive regions, such as the kidneys, liver, or reproductive organs, where ischemia may impair function or limit future therapeutic options.[7] These limitations highlight the need for temporary embolization agents that provide effective occlusion while minimizing long-term tissue damage.

Resorbable microparticles have recently emerged as promising alternatives for TAE, offering controlled, temporary occlusion with predictable degradation.[8-11] These agents have shown therapeutic benefits across diverse applications. For example, resorbable microparticles have been used in uterine artery embolization to treat fibroids while preserving fertility.[11] In genicular artery embolization for osteoarthritis, temporary occlusion reduces inflammation without causing permanent vascular damage.[9] Additionally, in transarterial chemoembolization for liver tumors, resorbable microparticles enhance chemotherapy delivery and reduce surrounding tissue injury by aligning with drug pharmacokinetics.[10]

Despite their growing use, the unique characteristics of resorbable microparticles, such as composition and morphology, remain underexplored. These features influence their safety, efficacy, and suitability for different clinical contexts. Detailed evaluations are essential to optimize their use for temporary embolization, particularly in organ-preserving interventions.

In this study, we compare the angiographic and histopathological outcomes of two distinct resorbable microparticles, Nexsphere-F (Nextbiomedical, Incheon, Republic of Korea) and KIPZA (Engain, Hwaseong, Republic of Korea), in a porcine kidney model. The findings provide insights into their potential applications and limitations for temporary embolization, addressing the critical need for informed selection of embolic agents in clinical settings requiring organ preservation.

Main points

- Embolization with Nexsphere-F and KIPZA resorbable microparticles in porcine kidneys demonstrated early recanalization, minimal inflammatory reaction, and no significant tissue injury.
- Effective, safe, and temporary vascular occlusion with minimal tissue injury is possible with both microparticles.
- Our findings suggest that Nexsphere-F and KIPZA resorbable microparticles are suitable for temporary embolization applications, in which preservation of the organ parenchyma is essential.

Methods

Animal model

This study was approved by the Institutional Animal Care and Use Committee of Seoul National University Bundang Hospital (protocol number: BA-2007-301-085, date: 30.01.2025) and was conducted in compliance with the Animal Research: Reporting of *In Vivo* Experiments 2.0 guidelines to ensure ethical and accurate reporting of animal research.[12] Ten male farm pigs (30–40 kg) were housed under standard conditions with free access to food and water and received veterinary oversight throughout the study.

This investigation was an exploratory proof-of-concept study; therefore, no formal sample size calculation was performed. Ten pigs were selected to allow bilateral within-animal comparisons, and the findings should be interpreted as hypothesis-generating. Following embolization, the animals were monitored for welfare, analgesia, and post-procedural complications. Analgesia was provided via intramuscular ketoprofen (3 mg/kg) as needed. The animals were evaluated hourly for appetite, behavior, and signs of distress by veterinary staff using predefined welfare assessment criteria. On day 7, after the final angiography and under deep anesthesia, the animals were humanely euthanized by intravenous potassium chloride injection.

Renal arteriography and embolization

All procedures were performed by a board-certified interventional radiologist. On the day of the experiment, the animals were pretreated with an injection of atropine (Jeil Pharmaceutical, Seoul, Republic of Korea) 0.05 mg/kg and the antibiotic 'Baytril (Bayer, Leverkusen, Germany) 5 mg/kg, and then anesthesia was induced with intramuscular injections of Zoletil 50 (Virbac, Carros, France) 5 mg/kg and Rompun (Bayer, Leverkusen, Germany) 2 mg/kg. After induction, the animals were transferred to the laboratory, and tracheal intubation was performed. Respiratory anesthesia was maintained at 5–10 mL/kg/min with FORANE (JW Pharmaceutical, Seoul, Republic of Korea) and O_2 in a ratio of 1-1.5 using a Primus respiratory anesthesia machine (Drager, Lübeck, Germany). The pigs were positioned supine in a dedicated angiography suite (Axiom Artis Zee, Siemens, Forchheim, Germany). Right femoral artery access was obtained through ultrasound-guided puncture, followed by insertion of a 5-F angiographic guide catheter (Davis, Cook Medical, Bloomington, IN, USA) and a 1.7-F microcatheter (Progreat Lambda, Terumo, Tokyo, Japan). Bilateral renal and upper polar angiograms were then performed.

Each animal underwent embolization of the upper polar arteries in both kidneys. For procedural consistency, the right upper polar artery was embolized with resorbable gelatin microparticles (100–300 μm; Nexsphere-F®, Nextbiomedical, Incheon, Republic of Korea), and the left upper polar artery was embolized with resorbable microparticles of the same size range (100–300 μm; KIPZA®, Engain, Hwaseong, Republic of Korea). Follow-up angiography was performed immediately and at 2 hours, 1 day, and 7 days post-embolization to assess recanalization. After the final angiography on day 7, 5 of the 10 pigs were randomly selected for histopathologic evaluation to minimize animal sacrifice while enabling robust comparative analysis; these animals were euthanized under deep anesthesia, and both treated renal segments were harvested for pathologic analysis (5 kidneys per group) (Figure 1).

Nexsphere-F® consists of uniform spherical gelatin-based microparticles (100–300 μm) with smooth surfaces, whereas KIPZA® comprises irregularly shaped gelatin-based microparticles (100–300 μm) with rough surfaces. All microparticles were prepared by hydration with 2 mL of normal saline, followed by the addition of approximately 8 mL of contrast medium and thorough mixing. Subsequently, 5–10 mL of the suspension was injected per kidney until near stasis was achieved. The mean procedure time per kidney (from catheter placement to completion of embolization) was 30 ± 5 minutes.

Angiographic recanalization was graded by two independent interventional radiologists using a modified Thrombolysis in Myocardial Infarction (TIMI) scale (0: no perfusion; 1: minimal perfusion; 2: partial recanalization; 3: complete recanalization). Reviewers were blinded to group allocation; disagreements were resolved by consensus.

Endpoints

The primary endpoint was complete angiographic recanalization at 7 days post-embolization. Secondary endpoints included early angiographic recanalization at 2 hours and 1 day and histopathologic parameters, including the presence of residual micropar-

ticles, infarcted area percentage, inflammatory cell infiltration, and endothelial proliferation.

Histopathological analysis

To minimize bias, kidney specimens from each pig were sent to an independent laboratory (HLB BioStep, Incheon, Republic of Korea) for blinded analysis. Each kidney was bisected longitudinally and transversely sectioned to produce 12 slides per specimen. The pathological evaluation focused on parenchymal infarction and inflammatory cell infiltration, and the infarcted area was quantified as a percentage of the total cross-sectional area using ImageJ software (Bethesda, Maryland, USA). Prior to histological processing, each kidney was visually inspected for surface discoloration and textural changes as indicators of infarction. Tissue samples were stained with hematoxylin and eosin to detect residual embolic agents, lymphocyte and macrophage infiltration, and reactive endothelial cell proliferation.

The histopathologic assessment was independently performed by two board-certified pathologists blinded to group allocation. They quantified infarcted tissue and inflammation and noted endothelial proliferation.

Statistical analysis

Because this was an exploratory pilot study without a formal sample size calculation, statistical analyses were descriptive and hypothesis-generating. Inter-rater reliability for histopathologic assessments was evaluated using Cohen's κ statistic.

Given the exploratory pilot design and small sample size, the analyses were primarily descriptive, focusing on effect sizes and paired comparisons without prespecified hypothesis testing. The normality of continuous variables was evaluated using the Shapiro–Wilk test. Paired comparisons (right vs. left kidney) used paired t-tests for normally distributed outcomes and Wilcoxon signed-rank tests otherwise to generate exploratory *P* values; however, these should be interpreted cautiously and without strict significance thresholds.

Results

Angiographic evaluation

Pre-embolization angiography showed no significant variations in the renal vasculature of any pig. Immediately after embolization, angiography confirmed complete occlusion of the arteries supplying the embolized upper poles of the kidneys. At the 2-hour follow-up, restored blood flow and full parenchymal staining were observed in the right kidneys of all animals treated with Nexsphere-F (TIMI 3) (Figure 2). Among the left kidneys treated with KIPZA, partial recanalization (TIMI 2) was observed in 1 animal, whereas the remaining animals showed complete recanalization (TIMI 3) at this time point (Figure 3). Follow-up angiograms at 1 and 7 days post-embolization revealed full recanalization with restored parenchymal staining in all pigs.

Qualitative and quantitative histopathological analysis

On day 7, after bilateral renal angiography, all animals were sacrificed, and the kidneys were harvested. Gross examination revealed no significant abnormalities in the kidneys treated with either product. Histological evaluation revealed no residual emboli and no lymphocyte or macrophage infiltration in the Nexsphere-F group, with no evidence of parenchymal infarction. The inter-rater reliability for assessing parenchymal infarction and endothelial proliferation was excellent (Cohen's κ: 0.92).

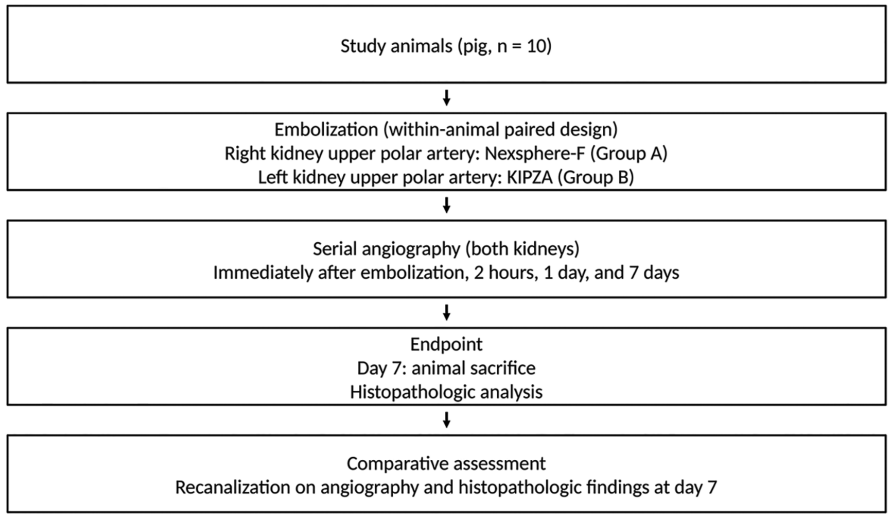


Figure 1. Flowchart of experimental procedure. The flowchart illustrates the embolization procedure performed on the upper polar artery in both groups.

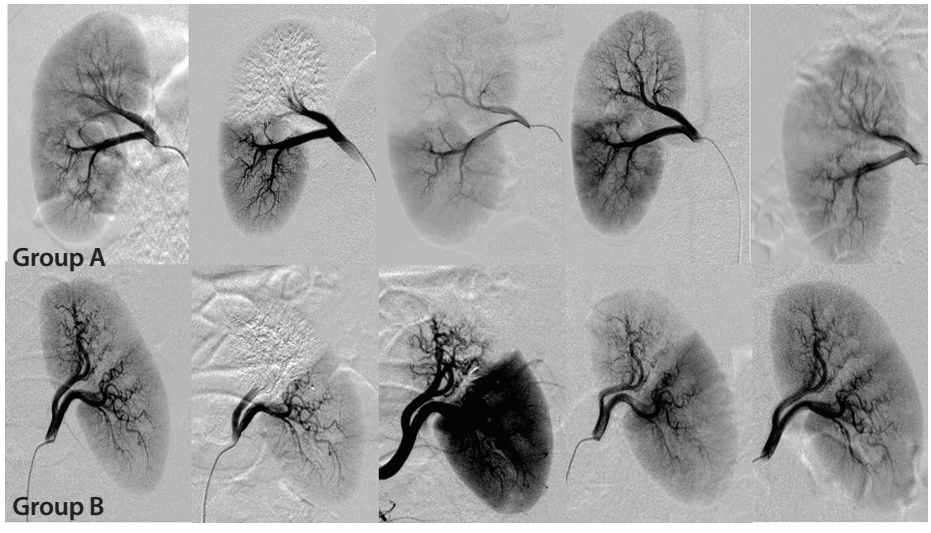


Figure 2. Baseline and follow-up angiography post-embolization of Groups A and B. Serial angiographic images display blood flow in treated renal segments at baseline, immediately post-embolization, 2 hours post-embolization, 1 day post-embolization, and 7 days post-embolization (arranged chronologically from left to right). The top row (Group **A**) and bottom row (Group **B**) represent representative cases chosen to illustrate typical recanalization patterns; all animals demonstrated similar findings. Full recanalization with restored perfusion was observed at the 2-hour mark and maintained through day 7 in Group A. Partial recanalization was observed at 2 hours post-embolization in Group B, with flow fully restored by day 7.

In the KIPZA group, 1 kidney (1/5) exhibited minimal microparticle residue in the dorsal glomerulus and interlobular arteries, along with multifocal lymphocyte infiltration in a single lobule. Additionally, endothelial cell proliferation in the arcuate and interlobular arteries was observed in all kidneys in the KIPZA group, as shown in Table 1. A focal infarction area was observed in 3 of the 5 kidneys in the KIPZA group (60%). The mean infarction percentage area was 2.78% ± 1.33% (95% confidence interval: 1.2%–4.3%), whereas no infarctions were observed in Group A. Although the sample size precludes definitive statistical comparison, this effect size suggests a difference in tissue response between the two microparticles (Figure 4).

Discussion

In this study, we evaluated the angiographic and histopathologic characteristics of two resorbable microparticles—Nexsphere-F and KIPZA—in a porcine kidney model, focusing on their potential for controlled, temporary embolization. Both microparticle types demonstrated favorable safety profiles, with full recanalization of embolized vessels and minimal tissue injury observed by day 7 post-embolization. Because this was an exploratory pilot study, our findings should be interpreted descriptively rather than as definitive comparative efficacy. The

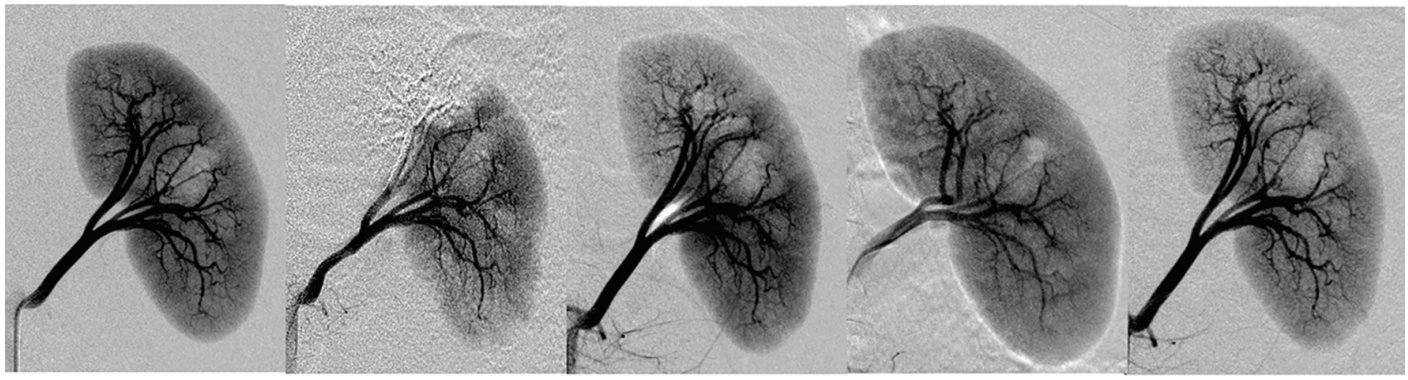


Figure 3. Baseline and follow-up angiography post-embolization in an additional representative case of Group B. Serial angiographic images display blood flow in treated renal segments at baseline, immediately post-embolization, 2 hours post-embolization, 1 day post-embolization, and 7 days post-embolization (arranged chronologically from left to right). This case was selected to represent the typical angiographic response in Group B; all other Group B animals exhibited similar recanalization patterns with full restoration by day 7.

Table 1. Histopathologic evaluation of two groups

	Right kidney upper pole (Nexsphere-F)			Left kidney upper pole (KIPZA)		
Individual number	Residual emboli in renal vessels	Lymphocyte/ macrophage infiltration	Endothelial cell proliferation	Residual emboli in renal vessels	Lymphocyte/ macrophage infiltration	Endothelial cell proliferation
1	No (0/12)	No (0/12)	No (0/12)	No (0/12)	Yes (12/12)	Yes (9/12)
2	No (0/12)	No (0/12)	No (0/12)	No (0/12)	Yes (3/12)	Yes (1/12)
3	No (0/12)	No (0/12)	No (0/12)	Yes (2/12)	Yes (2/12)	Yes (5/12)
4	No (0/12)	No (0/12)	No (0/12)	No (0/12)	Yes (9/12)	Yes (3/12)
5	No (0/12)	No (0/12)	No (0/12)	No (0/12)	Yes (12/12)	Yes (2/12)

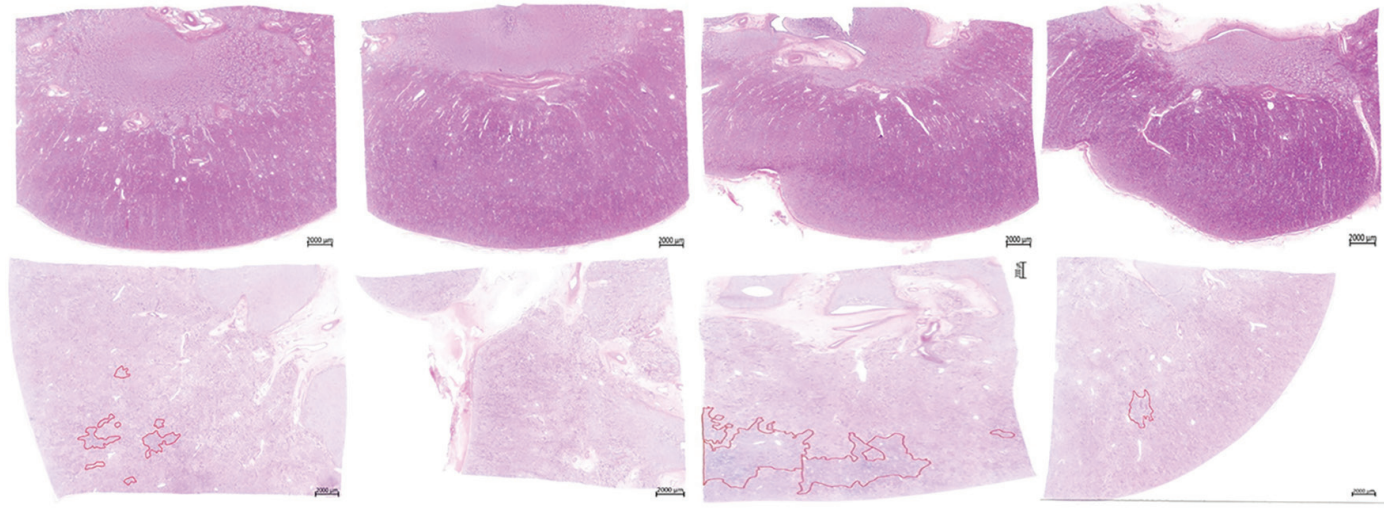


Figure 4. Infarction area analysis in both groups. Quantitative analysis of infarcted tissue in the right kidney (top row) and left kidney (bottom row) post-embolization. Red-shaded areas indicate areas of infarction.

observed effect sizes highlight trends that warrant further investigation in larger, powered studies. Our claims regarding organ preservation reflect structural observations only; functional renal outcomes were not assessed, so organ preservation must be interpreted cautiously.

Resorbable microparticles have shown promising applications in settings that require temporary vascular occlusion. For instance, Han et al.[11] demonstrated the effectiveness of resorbable microparticles in uterine artery embolization, achieving outcomes comparable with those of permanent agents while preserving options for future interventions due to recanalization. In addition, Verret et al.[13] reported transient uterine artery occlusion using a resorbable embolization microparticle in a sheep model. Similarly, Min et al.[9] reported effective pain relief in osteoarthritis using resorbable microparticles for genicular artery occlusion, minimizing long-term tissue damage. Wang and Rao[10] highlighted their alignment with chemotherapy in transarterial chemoembolization for liver tumors, enhancing therapeutic effects while reducing liver injury.

Despite these advances, detailed *in vivo* characterization of resorbable microparticles is limited, particularly in differentiating their effects across diverse clinical contexts that require specific properties. Factors such as particle shape and surface structure influence microparticle behavior and outcomes. Laurent et al.[14] observed that irregular microparticles penetrate more distally within vascular networks, promoting more durable occlusions due to enhanced deformation and thrombotic retention. Another study reported that irregularly shaped particles tend to aggregate and occlude vessels larger than their own diameter, unlike spherical embolics with smooth surfaces.[15] This aligns with the present findings, as differences between Nexsphere-F and KIPZA highlight how microparticle morphology impacts recanalization. These findings may have implications for real-world embolization practice: agents with rapid recanalization may be preferable for temporary hemostasis or fertility-preserving interventions, whereas KIPZA may be more suitable when temporary but relatively more durable occlusion is desired, particularly in embolization of relatively high-flow vascular channels, such as transarterial microembolization for shoulder pain.

In this study, serial angiography post-embolization showed complete recanalization and restored parenchymal enhancement in all individuals of Group A by 2 hours, likely owing to its rapid hydrolytic degradation and smooth, spherical structure, which promotes efficient resorption and timely recanalization. In contrast, 1 animal in Group B showed partial recanalization with reduced parenchymal enhancement at the 2-hour follow-up, with full restoration by day 7. Rapid recanalization may be desirable in contexts where quick restoration of perfusion is critical (e.g., fertility-sparing uterine artery embolization); however, in situations requiring durable occlusion, such early recanalization could indicate insufficient durability of the embolic material. The irregular shape of KIPZA likely enhances deep penetration, aggregation, and thrombotic occlusion, leading to a delayed recanalization response.[6,14,16]

Histopathologic analysis supported these angiographic findings, showing no ischemic damage or inflammatory cell infiltration in Group A. The fast resorption of Nexsphere-F was not associated with any structural alteration of the arterial walls. Conversely, Group B exhibited minimal ischemia (2.78% ± 1.33%) and endothelial cell proliferation in the arcuate and interlobular arteries, likely due to KIPZA's irregular surface, which promotes platelet adhesion and more durable thrombosis.[6,14,17,18] In this context, the endothelial proliferation observed in Group B may represent a reparative response to transient ischemia rather than pathologic neointimal formation; however, further mechanistic studies are needed to clarify this finding.

This study contributes to the literature by comparing the differential effects of Nexsphere-F and KIPZA *in vivo*. Although both achieved full recanalization, KIPZA's irregular shape may be beneficial for temporary embolization in high-flow areas or lesions with multiple connections where more durable occlusion is needed. Nexsphere-F's uniform spherical shape appears more suitable for end organs or tissues vulnerable to ischemia. These findings underscore the impact of microparticle morphology on embolization outcomes, highlighting the importance of selecting embolic agents based on specific clinical needs.

This study had several limitations. It was an exploratory pilot study with a small sample size (angiography n = 10, histopathology n = 5 per group) and no formal power calculation. The healthy porcine model lacks underlying disease and functional endpoints (e.g., serum creatinine) to assess renal function. Therefore, conclusions regarding organ preservation are limited to structural findings rather than functional outcomes. The follow-up duration was limited to 7 days, preventing evaluation of long-term outcomes or delayed recanalization. Furthermore, extrapolation of these results to human pathology should be undertaken with caution.

In this exploratory pilot study, both Nexsphere-F and KIPZA demonstrated temporary vascular occlusion with early recanalization and minimal structural tissue injury in a porcine kidney model. However, the observed differences in recanalization pattern and histopathologic response should be interpreted descriptively rather than as evidence of definitive comparative efficacy. Rapid recanalization may be advantageous in clinical settings requiring temporary embolization and parenchymal preservation, although its implications for embolic durability depend on the intended therapeutic use. Because organ preservation in this study was assessed only by structural findings in a healthy animal model over short-term follow-up, larger studies with functional endpoints, disease models, and longer observation are needed.

Footnotes

Conflict of interest disclosure

J.H.L. received a donation of experimental microparticles from Nextbiomedical Co., Ltd. and Engain Co., Ltd., the manufacturers of the microparticles studied. All other authors declare no conflicts of interest related to this work.

Funding

This study was supported by the Seoul National University Bundang Hospital research fund (02-2021-0011, 14-2022-0001) and the Seoul National University research program (800-20210520). The sponsors did not initiate the study, nor did they participate in the study design, data collection, analysis, or interpretation. Furthermore, the sponsors did not contribute to the writing of the first draft of the manuscript, nor did they provide any writing assistance beyond copy editing. The decision to submit the manuscript for publication was made independently of the sponsors.

References

1. Comploj E, Pycha A, Trenti E, et al. Transarterial embolization in the management of intractable haemorrhage. *Urol Int*. 2021;105(1-2):95-99. [Crossref]

2. Pech M, Serafin Z, Fischbach F, et al. Transarterial embolization of acute iatrogenic hemorrhages: predictive factors for mortality and outcome. *Br J Radiol*. 2020;93(1110):20190413. [Crossref]
3. Ochiai D, Nakatsuka S, Abe Y, et al. The efficacy of transarterial embolization for postpartum hemorrhage complicated with disseminated intravascular coagulation: a single-center experience. *J Clin Med*. 2021;10(18):4082. [Crossref]
4. Kaya V, Tahtabasi M. Efficacy and safety of transarterial embolization in patients with intraabdominal hemorrhage: experience from two centers. *Ann Med Res*. 2023;30(8):945-951. [Crossref]
5. Ma X, Chen H, Luo X, Wang J, Zhou B, Liu X. The clinical application of transarterial embolization via radial artery in hemorrhagic diseases in obstetrics and gynecology. *Front Med (Lausanne)*. 2023;10:1273179. [Crossref]
6. Lee S, Ghosh A, Xiao N, et al. Embolic agents: particles. *Semin Intervent Radiol*. 2023;40(3):315-322. [Crossref]
7. Wolanske KA, Gordon RL, Wilson MW, Kerlan RK Jr, LaBerge JM, Jacoby AF. Coil embolization of a tuboovarian anastomosis before uterine artery embolization to prevent nontarget particle embolization of the ovary. *J Vasc Interv Radiol*. 2003;14(10):1333-1338. [Crossref]
8. Choi H, Choi B, Yu B, et al. On-demand degradable embolic microspheres for immediate restoration of blood flow during image-guided embolization procedures. *Biomaterials*. 2021;265:120408. [Crossref]
9. Min J, Park SW, Hwang JH, et al. Evaluating the safety and effectiveness of quick-soluble gelatin sponge particles for genicular artery embolization for chronic knee pain associated with osteoarthritis. *J Vasc Interv Radiol*. 2023;34(11):1868-1874. [Crossref]
10. Wang D, Rao W. Bench-to-bedside development of multifunctional flexible embolic agents. *Theranostics*. 2023;13(7):2114-2139. [Crossref]
11. Han K, Kim SY, Kim MD, et al. Resorbable microspheres versus trisacryl gelatin microspheres for uterine artery embolization: a randomized controlled trial. *Radiology*. 2024;312(3):e231525. [Crossref]
12. Percie du Sert N, Hurst V, Ahluwalia A, et al. The ARRIVE guidelines 2.0: updated guidelines for reporting animal research. *PLoS Biol*. 2020;18(7):e3000410. [Crossref]
13. Verret V, Pelage JP, Wassef M, et al. A novel resorbable embolization microsphere for transient uterine artery occlusion: a comparative study with trisacryl-gelatin microspheres in the sheep model. *J Vasc Interv Radiol*. 2014;25(11):1759-1766. [Crossref]
14. Laurent A, Wassef M, Namur J, Ghegediban H, Pelage JP. Arterial distribution of calibrated tris-acryl gelatin and polyvinyl alcohol embolization microspheres in sheep uterus. *Cardiovasc Intervent Radiol*. 2010;33(5):995-1000. [Crossref]
15. Yamamoto A, Imai S, Kobatake M, Yamashita T, Tamada T, Umetani K. Evaluation of tris-acryl gelatin microsphere embolization with monochromatic X Rays: comparison with polyvinyl alcohol particles. J Vasc *Interv Radiol*. 2006;17(11 Pt 1):1797-1802. [Crossref]
16. Nakamura H, Yamamoto A, Watanabe H, et al. Microembolization effects of imipenem/cilastatin in vivo depicted by monochromatic synchrotron X-Ray microangiography. *J Vasc Interv Radiol*. 2025;36(2):340-346. [Crossref]
17. Luo Y, Ma Y, Chen Z, et al. Shape-anisotropic microembolics generated by microfluidic synthesis for transarterial embolization treatment. *Adv Healthc Mater*. 2022;11(10):e2102281. [Crossref]
18. Jang TS, Lee JH, Kim S, et al. Ta ion implanted nanoridge-platform for enhanced vascular responses. *Biomaterials*. 2019;223:119461. [Crossref]

Diagn Interv Radiol 2026; DOI: 10.4274/dir.2026.263969

INTERVENTIONAL RADIOLOGY

LETTER TO THE EDITOR

©Copyright 2026 Author(s) - Available online at dirjournal.org.
Content of this journal is licensed under a Creative Commons Attribution-NonCommercial 4.0 International License.

Letter to the Editor: Methodological considerations in the analysis of multiphase computed tomography angiography findings for outcome prediction in middle cerebral artery M1 occlusion

Yakup Ozbay

University of Health Sciences Türkiye, Ankara Etlik City Hospital, Clinic of Radiology, Ankara, Türkiye

Dear Editor,

I read with great interest the recent article titled "Analysis of the baseline multiphase computed tomographic angiography findings to predict clinical outcomes in patients with middle cerebral artery M1 occlusion treated with mechanical thrombectomy," published by Çıvgın and Bayındır.[1] The authors are to be commended for studying a homogeneous cohort and for focusing on imaging biomarkers that may assist early risk stratification. I would like to raise several points for clarification in the spirit of strengthening the interpretability of the findings.

First, important clinical confounders (such as age, sex, comorbidities, and National Institutes of Health stroke score) were not included in the logistic regression analysis. Age, in particular, is a well-established independent predictor of functional outcomes after mechanical thrombectomy;[2,3] even though the age difference between outcome groups did not reach statistical significance in this cohort, the approximately 6-year mean difference may still be clinically meaningful. In prognostic modeling, adjustment for known determinants (such as age and sex) is generally recommended regardless of univariate significance. Omission of these variables raises the possibility of confounding, especially if thrombus characteristics correlate with patient age or biological reserve.

Second, an interesting observation in this study is that thrombus density did not demonstrate a statistically significant difference between outcome groups ($P = 0.053$) in the group comparison, yet it emerged as an independent predictor in the logistic regression model ($P = 0.022$). Such findings are not uncommon in prognostic research and may reflect several underlying mechanisms, including collinearity among imaging variables, adjustment effects related to thrombus length, or model sensitivity associated with the relatively small sample size. In particular, when correlated predictors are entered simultaneously into a multivariable model, statistical adjustment can alter the apparent strength and direction of associations observed in the group comparison.

Third, the number of predictors entered into the logistic regression model appears relatively high given the sample size and number of outcome events. With 24 patients experiencing poor outcomes, inclusion of multiple imaging variables simultaneously may approach the limits recommended for stable multivariable modeling. Although the reported goodness-of-fit measures are reassuring, clarification of the variable selection strategy would enhance confidence in the robustness of the reported independent associations.

Finally, thrombus density was evaluated using absolute Hounsfield unit (HU) values. Because attenuation measurements may vary according to scanner characteristics and patient-specific factors such as the hematocrit, consideration of normalization (such as relative thrombus density compared with the contralateral artery or adjacent vascular structures) could potentially improve reproducibility. Future studies incorporating normalized HU metrics may further clarify the biological and prognostic relevance of thrombus composition.

Corresponding author: Yakup Ozbay

E-mail: docofrad@gmail.com

Received 01 March 2026; accepted 02 March 2026.

Epub: 07.04.2026

Publication date: 02.11.2026

DOI: 10.4274/dir.2026.263969

You may cite this article as: Ozbay Y. Letter to the editor: methodological considerations in the analysis of multiphase computed tomography angiography findings for outcome prediction in middle cerebral artery M1 occlusion. *Diagn Interv Radiol*. 2026;32(6):852-853.

Overall, this study contributes valuable data on the potential prognostic role of thrombus length and density in a carefully selected population. Addressing the points above would further strengthen the conclusions and facilitate broader clinical applicability.

Footnotes

Conflict of interest disclosure

The author declared no conflicts of interest.

References

1. Çıvgın E, Bayındır H. Analysis of the baseline multiphase computed tomographic angiography findings to predict clinical outcomes in patients with middle cerebral artery M1 occlusion treated with mechanical thrombectomy. *Diagn Interv Radiol*. 2025. **[Crossref]**
2. Rhiner N, Thut MZ, Thurner P, et al. Impact of age on mechanical thrombectomy and clinical outcome in patients with acute ischemic stroke. *J Stroke Cerebrovasc Dis*. 2023;32(9):107248. **[Crossref]**
3. Forti P, Maioli F, Procaccianti G, et al. Independent predictors of ischemic stroke in the elderly: prospective data from a stroke unit. *Neurology*. 2013;80(1):29-38. Erratum in: *Neurology*. 2013;81(21):1882. **[Crossref]**

Diagn Interv Radiol 2026; DOI: 10.4274/dir.2026.264007

INTERVENTIONAL RADIOLOGY

LETTER TO THE EDITOR

©Copyright 2026 Author(s) - Available online at dirjournal.org.
Content of this journal is licensed under a Creative Commons Attribution-NonCommercial 4.0 International License.

Letter to the Editor: Pleural tail sign in computed tomography–guided lung biopsy: insights and considerations for clinical practice

Andrea Carolina Munive
Nicolás Guerrero Acosta
Isabella Andrea Bolaños Bermúdez
David Fernando Torres Cortés

Fundación Santa Fe de Bogotá, Department of Radiology, Bogotá, Colombia

Dear Editor,

We read with great interest the recent article by Hassan et al.[1] titled "Pleural tail sign in computed tomography–guided lung biopsy: an imaging predictor of severe pneumothorax requiring chest tube placement." The authors address a clinically relevant question and propose a practical refinement of the pleural tail sign (PTS), distinguishing between thin and triangular subtypes. This approach adds depth to the existing literature and reflects the increasing interest in imaging biomarkers as practical tools for improving preprocedural risk stratification in computed tomography (CT)–guided percutaneous transthoracic needle biopsy.[1]

The observation that the triangular PTS subtype is associated with a higher risk of severe pneumothorax requiring chest tube placement is particularly relevant. By focusing on clinically significant complications rather than overall pneumothorax rates, the study provides information that is directly applicable to daily practice.[1,2]

However, some aspects deserve further consideration. In particular, the potential role of patient-related factors is not fully explored. Although the analysis appropriately includes several technical variables, there is limited information on relevant comorbidities such as emphysema or other chronic lung diseases, which are well-known risk factors for pneumothorax following CT–guided biopsy.[3] In this setting, it is difficult to determine whether the association between triangular PTS and severe pneumothorax reflects a true imaging biomarker or, instead, an indirect indicator of underlying pulmonary vulnerability. Including more detailed clinical variables could help clarify this relationship.

Another aspect worth considering is how the main outcome was defined. Although the need for chest tube placement is clinically meaningful, it can also be influenced by operator judgment, local protocols, and individual patient factors. As such, it may not fully represent a standardized measure of pneumothorax severity, which could affect the interpretation of the results.

In addition, although the proposed subclassification of PTS is interesting and adds nuance, its application in everyday practice may be less straightforward. The reported interobserver agreement suggests only moderate consistency, raising the possibility that distinguishing between the thin and triangular subtypes may vary across readers, particularly outside specialized settings.

In conclusion, this study provides valuable insight into PTS and its potential role in identifying patients at higher risk of clinically significant complications. However, further information incorporating both imaging and clinical variables, along with standardized outcome definitions, would be helpful to better define its role in clinical practice.

Handling editor: Bahri Üstünsöz

Corresponding author: Andrea Carolina Munive

E-mail: andrecmunive@gmail.com

Received 24 March 2026; accepted 30 March 2026.

Epub: 08.05.2026

Publication date: 02.11.2026

DOI: 10.4274/dir.2026.264007

You may cite this article as: Munive AC, Guerrero Acosta N, Bolaños Bermúdez IA, Torres Cortés DF. Letter to the editor: pleural tail sign in computed tomography–guided lung biopsy: insights and considerations for clinical practice. *Diagn Interv Radiol*. 2026;32(6):854-855.

Footnotes

Conflict of interest disclosure

The authors declared no conflicts of interest.

References

1. Hassan JJ, Leonhardi J, Denecke T, et al. Pleural tail sign in computed tomography-guided lung biopsy: an imaging predictor of severe pneumothorax requiring chest tube placement. *Diagn Interv Radiol*. 2026;32(2):228-232. **[Crossref]**
2. Heerink WJ, de Bock GH, de Jonge GJ, Groen HJ, Vliegenthart R, Oudkerk M. Complication rates of CT-guided transthoracic lung biopsy: meta-analysis. *Eur Radiol*. 2017;27(1):138-148. **[Crossref]**
3. Ozturk K, Soylu E, Gokalp G, Topal U. Risk factors of pneumothorax and chest tube placement after computed tomography-guided core needle biopsy of lung lesions: a single-centre experience with 822 biopsies. *Pol J Radiol*. 2018;83:e407-e414. **[Crossref]**

Diagn Interv Radiol 2026; DOI: 10.4274/dir.2026.264079

INTERVENTIONAL RADIOLOGY

LETTER TO THE EDITOR

©Copyright 2026 Author(s) - Available online at dirjournal.org.
Content of this journal is licensed under a Creative Commons Attribution-NonCommercial 4.0 International License.

Reply: "Pleural tail sign in computed tomography–guided lung biopsy: insights and considerations for clinical practice"

Jacob Jalil Hassan
Hans-Jonas Meyer

University of Leipzig Faculty of Medicine, Department of Diagnostic and Interventional Radiology, Leipzig, Germany

Dear Editor,

We thank the authors for their thoughtful comments on our study investigating the pleural tail sign (PTS) as a predictor of severe pneumothorax following computed tomography (CT)–guided lung biopsy.[1]

We agree that pneumothorax following CT–guided lung biopsy is a multifactorial complication dependent on established patient-related and procedural factors, including emphysema and other chronic lung diseases.[2,3] We acknowledge that an important limitation of our study is that chronic lung parenchymal changes were not systematically assessed and, therefore, could not be included in the multivariable analysis. Given their known impact, residual confounding cannot be excluded.

Regarding the definition of the primary endpoint, we acknowledge that the need for chest tube placement may be influenced by operator judgment. However, we deliberately selected this outcome because it represents a clinically meaningful endpoint reflecting complications that require active intervention.

We also appreciate the comment on interobserver variability. Although the observed agreement was moderate, the proposed two-tier classification was intentionally designed as a simplified and pragmatic approach to facilitate clinical applicability. Moreover, we believe that interobserver agreement could be improved with minimal training and a clear definition of the PTS groups.

Given the study's retrospective design and the potential for confounding, the findings should be considered hypothesis-generating. Future studies integrating imaging and clinical variables with standardized outcome definitions are needed to better define its role in clinical practice.

We thank the authors once more for their insightful comments and for contributing to the discussion on this topic.

Corresponding author: Jacob Jalil Hassan

E-mail: Jacob.Hassan@medizin.uni-leipzig.de

Received 24 March 2026; accepted 30 March 2026.

Epub: 08.05.2026

Publication date: 02.11.2026

DOI: 10.4274/dir.2026.264079

You may cite this article as: Hassan JJ, Meyer HJ. Reply: "pleural tail sign in computed tomography–guided lung biopsy: insights and considerations for clinical practice". *Diagn Interv Radiol*. 2026;32(6):856-857.

Footnotes

Conflict of interest disclosure

The authors declared no conflicts of interest.

References

1. Hassan JJ, Leonhardi J, Denecke T, et al. Pleural tail sign in computed tomography-guided lung biopsy: an imaging predictor of severe pneumothorax requiring chest tube placement. *Diagn Interv Radiol*. 2026;32(2):228-232. [Crossref]
2. Heerink WJ, de Bock GH, de Jonge GJ, Groen HJ, Vliegenthart R, Oudkerk M. Complication rates of CT-guided transthoracic lung biopsy: meta-analysis. *Eur Radiol*. 2017;27(1):138-148. [Crossref]
3. Huo YR, Chan MV, Habib AR, Lui I, Ridley L. Pneumothorax rates in CT-Guided lung biopsies: a comprehensive systematic review and meta-analysis of risk factors. *Br J Radiol*. 2020;93(1108):20190866. [Crossref]

Diagn Interv Radiol 2026; DOI: 10.4274/dir.2026.263875

NEURORADIOLOGY

INVITED COMMENTARY

©Copyright 2026 Author(s) - Available online at dirjournal.org.
Content of this journal is licensed under a Creative Commons Attribution-NonCommercial 4.0 International License.

Standardizing neuroradiological ancillary testing in brain death determination: a national clinical protocol from Türkiye

Gul Hatipoglu[1]
Kamil Karaali[2]
Burak Kocak[3]
Derya Bako[4]
Mehmet Fatih Erbay[5]

[1]Ankara Bilkent City Hospital, Clinic of Radiology, Ankara, Türkiye

[2]Akdeniz University Faculty of Medicine, Department of Radiology, Antalya, Türkiye

[3]Başakşehir Çam and Sakura City Hospital, Department of Radiology, İstanbul, Türkiye

[4]Ondokuz Mayıs University Faculty of Medicine, Department of Radiology and Pediatric Radiology, Samsun, Türkiye

[5]İnönü University Faculty of Medicine, Department of Radiology, Malatya, Türkiye

Corresponding author: Burak Kocak

E-mail: drburakkocak@gmail.com

Received 15 February 2026; revision requested 02 March 2026; accepted 16 March 2026.

Epub: 27.03.2026

Publication date: 02.11.2026

DOI: 10.4274/dir.2026.263875

ABSTRACT

This commentary introduces Türkiye's national clinical protocol for neuroradiological ancillary testing in brain death determination, which was developed to address persistent variability in imaging-based practice; it was first published in Turkish (2025) and subsequently translated into English (2026). It outlines a pragmatic national framework for the standardized use, interpretation, and reporting of computed tomography angiography, digital subtraction angiography, and transcranial Doppler ultrasonography while reaffirming that brain death remains a clinical diagnosis. By emphasizing practical examples, structured reporting, common pitfalls, and pediatric considerations, the protocol aims to improve consistency and interpretive reliability while contributing to the broader international discussion on ancillary testing.

KEYWORDS

Brain death, death by neurologic criteria, ancillary testing, computed tomography angiography, neuroradiology, clinical guidelines, pediatric brain death

The determination of death by neurologic criteria (DNC), commonly referred to as brain death, is fundamentally a clinical diagnosis based on the irreversible cessation of all brain functions.[1,2] Ancillary tests for diagnosis are not intended to replace the clinical examination, although they are often used in specific circumstances.[1] These include situations where the clinical examination is confounded by severe craniofacial trauma, pre-existing ocular or cranial nerve abnormalities, or when the apnea test cannot be safely performed due to hemodynamic instability or severe hypoxemia. Furthermore, ancillary tests are utilized to facilitate timely diagnosis when legal requirements necessitate a single clinical examination followed by a confirmatory objective test. Despite broad agreement on these principles, the type, role, and interpretation of ancillary tests, particularly imaging-based methods, vary substantially across countries and guidelines.[2,3]

In response to this variability, the Republic of Türkiye Ministry of Health released the Clinical Protocol for Neuroradiological Diagnostic Criteria in Brain Death in Turkish in 2025 and in English in 2026.[4,5] The protocols can also be accessed through the following link: https://osf.io/fej34/overview. The protocol was developed through a structured review of the literature and a series of regularly scheduled multidisciplinary meetings involving the authors, with participation from representatives of the Ministry of Health. The protocol was originally prepared in the Turkish language to support national implementation and was subsequently translated into English to facilitate broader international accessibility and knowledge sharing. It was developed within the framework of the National Organ Transplantation and Donation Coordination System and reviewed by the Turkish Society of Radiology. It primarily aims to standardize neuroradiological ancillary testing practices at a national level.

This commentary summarizes the scope, rationale, and structure of the protocol, situating it within the broader international context while staying within the evidence base on which it is founded.

You may cite this article as: Hatipoglu G, Karaali K, Kocak B, Bako D, Erbay MF. Standardizing neuroradiological ancillary testing in brain death determination: a national clinical protocol from Türkiye. *Diagn Interv Radiol*. 2026;32(6):858-861.

Rationale for a neuroradiology-focused protocol

Although international consensus documents have clarified many aspects of DNC determination, neuroradiological ancillary tests remain an area of persistent heterogeneity.[2,3] Differences are evident in (i) which imaging modalities are accepted, (ii) how they should be performed, and (iii) which radiological criteria should be used for interpretation. Computed tomography angiography (CTA), for example, is recommended as a standard ancillary test in some countries,[6] whereas current United States guidelines cite insufficient evidence to recommend its use.[7] A simplified comparative overview of prominent international guideline approaches to ancillary neuroradiological testing is summarized in Table 1.

Within Türkiye, as in many healthcare systems, CTA, digital subtraction angiography (DSA), and transcranial Doppler ultrasonography (TCD) are widely available and frequently used in practice. Before this protocol, however, uniform imaging acquisition parameters, interpretation criteria, and reporting standards were not formally defined at the national level. The protocol, therefore, focuses not on endorsing a single modality but on standardizing how commonly used neuroradiological tests are applied and interpreted when used as ancillary support to a clinical diagnosis of brain death.

Scope and general principles

The protocol explicitly reaffirms that brain death is a clinical diagnosis, consistent with national legislation. Neuroradiological tests are positioned as supportive tools rather than confirmatory substitutes. Importantly, the document avoids ranking ancillary tests or mandating a preferred modality. Instead, test selection is left to institutional resources, patient-specific factors, and clinical judgment.

The scope is limited to neuroradiological imaging methods. Nuclear medicine techniques and electroencephalography are intentionally excluded, reflecting both practical considerations and the protocol's focus on radiological workflows. Separate sections address adult and pediatric populations, recognizing the substantial physiological and anatomical differences that influence imaging interpretation.

A distinguishing characteristic of the protocol is its deliberate emphasis on practical interpretation, supported by numerous illustrative case examples and an explicit discussion of common pitfalls. This case-based approach is intended to complement existing guideline documents, many of which primarily focus on high-level recommendations and provide limited guidance on real-world imaging interpretation challenges.

Adult neuroradiological ancillary tests

Digital subtraction angiography

DSA is formally presented as a reference or gold standard ancillary neuroradiological method. This designation is based on the modality's ability to provide a definitive demonstration of the arrest of cerebral blood flow at a certain level. The protocol provides detailed guidance on catheterization strategies, contrast volumes, acquisition duration, and minimum imaging requirements. Interpretation criteria emphasize the absence of antegrade intracranial arterial flow and the lack of venous drainage. Potential sources of false-negative results, such as insufficient intracranial pressure elevation or stasis filling, are explicitly discussed.

Transcranial Doppler ultrasonography

TCD is described as a noninvasive option for adult patients when performed by experienced operators. The protocol standardizes insonation windows, hemodynamic prerequisites, and waveform interpretation. Diagnostic patterns, such as oscillatory flow, systolic spikes, and complete flow absence, are defined, alongside common pitfalls, including decompressive craniectomy, preserved collateral circulation, and systemic hypotension.

Computed tomography angiography

CTA receives particular attention due to its widespread availability and variable international acceptance. Rather than proposing new criteria, the protocol adopts previously published CTA scoring systems, with emphasis on the 4-point scale assessing bilateral cortical middle cerebral artery branches (M4) and internal cerebral veins.[8] Acquisition timing, contrast dosing, and interpretation steps are specified in detail to minimize technical and interpretative variability.

In short, the examination requires adequate physiologic conditions, including a confirmed mean arterial pressure >60 mmHg and a body temperature >35°C, together with the administration of non-ionic iodinated contrast material (100–120 mL in adults; 1–2 mL/kg in children) with a minimum iodine concentration of 340 mg/mL. A three-phase acquisition is mandated: (i) a non-contrast phase, to identify pre-existing hyperdensities (e.g., previous contrast, thrombosis) that could lead to false-negative interpretations; (ii) an early phase (20 s), used

Table 1. Simplified comparative overview of major international guideline approaches to ancillary neuroradiological testing

Guideline/protocol	Year	DSA	CTA	TCD
Republic of Türkiye (Ministry of Health Clinical Protocol)[4,5]	2025	Accepted	**Accepted.** Focuses on 4-point scoring system (M4 + ICV)	Accepted (adults only)
United Kingdom Consensus Guideline[6]	2023	-	**Preferred.** Accepted as a standard ancillary investigation for adults	-
Canada Clinical Practice Guideline[9]	2023	Not recommended	**Accepted (adults only).** 10-point scoring system discussed	Accepted (adults only)
American Academy of Neurology; American Academy of Pediatrics[7]	2023	Accepted	Not recommended	Accepted (adults only)
World Brain Death Project[10]	2020	Accepted	Not recommended	Accepted (adults only)

CTA, computed tomography angiography; DSA, digital subtraction angiography; ICV, internal cerebral vein; M4, cortical segment of the middle cerebral artery; TCD, transcranial Doppler ultrasound.
Note #1: "Accepted" denotes acceptance as an ancillary test rather than as a primary diagnostic test or a preferred method.
Note #2: This table does not encompass the nuanced, age-specific pediatric recommendations within each framework. As diagnostic criteria in children vary substantially according to patient age and cranial development (e.g., status of fontanelles and sutures), readers are advised to consult the specific pediatric sections of the referenced guidelines or the Türkiye protocol.[4,5]

exclusively to confirm successful contrast delivery by visualizing opacification of the superficial temporal arteries; and (iii) a delayed phase (60 s), the definitive phase for assessing the intracranial vascular opacification.

The protocol places special emphasis on side-by-side comparison of non-contrast and 60-s post-contrast images, supported by multiple example cases demonstrating both supportive and non-supportive findings. The diagnosis of brain death can be supported only if there is a complete absence of contrast opacification in all four vessels (i.e., M4 and internal cerebral veins). Conversely, the presence of contrast in any of these four landmarks does not support the diagnosis.

An example of a CTA assessment for suspected brain death is provided in Figure 1. For more detailed evaluation guidance and a wide range of practical example cases, readers are referred to the full protocol.[4,5]

Pediatric considerations

Ancillary testing in children presents additional challenges due to open sutures and fontanelles, which can prevent the rise in intracranial pressure required to arrest cerebral blood flow. The protocol acknowledges the limited pediatric evidence base and the absence of international consensus, explicitly cautioning against the direct application of adult criteria to children.

Both CTA and DSA are discussed cautiously, recognizing that adult-derived CTA scoring systems may yield false-negative results in pediatric patients; persistent, non-functional perfusion may be observed even when clinical criteria for brain death are met. Where CTA is used, the protocol highlights the potential value of supplemental venous assessment, including superior petrosal veins, as supportive rather than definitive findings. The pediatric section includes numerous case examples illustrating scenarios in which perfusion may remain preserved despite severe injury, thereby reducing the risk of misinterpretation.

Reporting templates and standardization

A distinctive feature of the protocol is the inclusion of structured reporting templates for each imaging modality. These templates are designed to (i) ensure documentation of technical adequacy, (ii) standardize terminology, and (iii) clearly separate descriptive findings from interpretive conclusions. Reports are limited to stating whether imaging findings support or do not support the clinical diagnosis of brain death, avoiding absolute or determinative language. A brief reporting template example for CTA is provided in Box 1. For detailed reporting templates for all modalities, readers are referred to the full protocol.[4,5]

Strengths and limitations

The primary strength of this protocol lies in its pragmatic standardization of imaging practice, supported by detailed protocols, checklists, and a substantial collection of illustrative cases. By explicitly addressing pitfalls and sources of misinterpretation, it aims to complement existing guidelines that may offer limited practical imaging guidance.

At the same time, the protocol does not attempt to resolve international disagreements regarding ancillary testing, nor does it propose new diagnostic criteria. Its limitations include reliance on heterogeneous and, in some areas, limited evidence, particularly within pediatric populations.

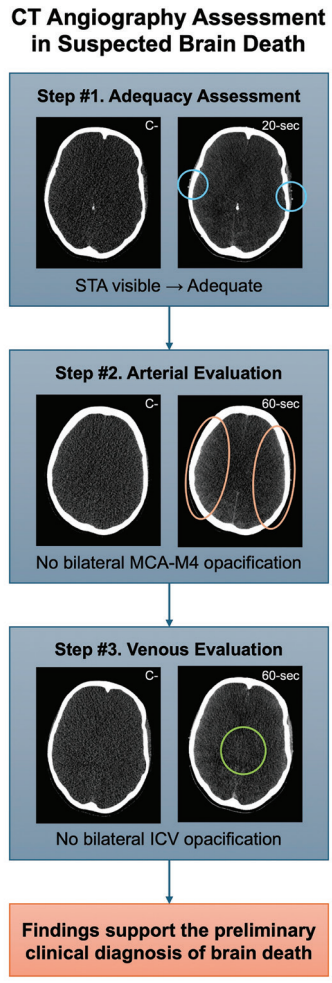


Figure 1. Computed tomography angiography (CTA) assessment example in suspected brain death, according to the 4-point system. Adequate scan quality is confirmed by visualization of the superficial temporal artery (STA; blue circles). Absence of opacification in the bilateral middle cerebral artery (MCA) cortical (M4) branches (orange ellipses) and bilateral internal cerebral veins (ICVs; green circle) supports the preliminary clinical diagnosis of brain death.

Box 1. Concise reporting template example

Examination: Computed tomography angiography for brain death determination.

Clinical information: [age]-year-old patient with a history of [relevant condition or event]; apnea test [positive/could not be performed].

Technique: Non-contrast phase followed by early (20 s) and delayed (60 s) post-contrast phases after intravenous administration of non-ionic iodinated contrast material (100 mL; iodine concentration 340 mg/mL).

Findings:
- **Quality check:** Opacification of the superficial temporal arteries confirmed on the 20-s phase, indicating successful contrast delivery.
- **Intracranial vascular evaluation (60-s phase):**
  - **M4 segments of right MCA:** [Opacified/not opacified]
  - **M4 segments of left MCA:** [Opacified/not opacified]
  - **Right internal cerebral vein:** [Opacified/not opacified]
  - **Left internal cerebral vein:** [Opacified/not opacified]

Impression:
- [Choice A]: Findings **SUPPORT** the clinical diagnosis of brain death (complete absence of opacification in the 4-point landmarks).
- [Choice B]: Findings **DO NOT SUPPORT** the clinical diagnosis of brain death (persistence of opacification in one or more landmarks).

MCA, middle cerebral artery.

Final remarks

This national clinical protocol represents an effort to operationalize neuroradiological ancillary testing within a clearly defined clinical and legal framework while maintaining consistency with international evidence. By combining standardized imaging protocols with extensive case-based illustration, it seeks to support accurate interpretation in routine clinical practice.

The protocol is intended as a living document, adaptable to future evidence and evolving international standards. Its contribution lies not in redefining brain death criteria but in providing a transparent and reproducible approach to neuroradiological support of a fundamentally clinical diagnosis.

Acknowledgement

The language of this manuscript was refined with assistance from ChatGPT 5.2 and Gemini 3 Pro. All uses of these tools were performed under strict author supervision.

Footnotes

Conflict of interest disclosure

All co-authors are also authors of the clinical protocol that is the subject of this commentary. Burak Kocak, MD, served as Section Editor for Diagnostic and Interventional Radiology (Section: Artificial Intelligence and Informatics; 2023-2025) during the conduct of this commentary. He had no involvement in the peer-review of this article and had no access to information regarding its peer-review.

References

1. Duvuru S, Sanker V, Mishra RK, et al. Ancillary tests for brain death. *Front Neurol*. 2025:1491263. [Crossref]
2. Iacobellis G, Leggio A, Salzillo C, Solenne M, Marzullo A. The role of neuroimaging in brain death diagnosis: a review of radiological protocols and the need for standardization. *Eur J Radiol*. 2025;190:112247. [Crossref]
3. Lewis A, Liebman J, Kreiger-Benson E, et al. Ancillary testing for determination of death by neurologic criteria around the world. *Neurocrit Care*. 2021;34(2):473-484. [Crossref]
4. T.C. Sağlık Bakanlığı. Beyin ölümünde nöroradyolojik tanı kriterleri klinik protokolü. Ankara: T.C. Sağlık Bakanlığı, Sağlık Hizmetleri Genel Müdürlüğü, Araştırma Geliştirme ve Sağlık Teknolojisi Değerlendirme Daire Başkanlığı; 2025. 50 p. [Crossref]
5. Republic of Türkiye, Ministry of Health. Clinical protocol for neuroradiological diagnostic criteria in brain death. Ankara: General Directorate of Health Services, Department of Research, Development and Health Technology Assessment; 2026. 50 p. [Crossref]
6. Thomas EO, Manara A, Dineen RA, et al. The use of cerebral computed tomographic angiography as an ancillary investigation to support a clinical diagnosis of death using neurological criteria: a consensus guideline. *Anaesthesia*. 2023;78(3):330-336. [Crossref]
7. Greer DM, Kirschen MP, Lewis A, et al. Pediatric and adult brain death/death by Neurologic Criteria Consensus Guideline. *Neurology*. 2023;101(24):1112-1132. Erratum in: *Neurology*. 2024;102(3):e208108. [Crossref]
8. Frampas E, Videcoq M, de Kerviler E, et al. CT angiography for brain death diagnosis. *AJNR Am J Neuroradiol*. 2009;30(8):1566-1570. [Crossref]
9. Shemie SD, Wilson LC, Hornby L, et al. A brain-based definition of death and criteria for its determination after arrest of circulation or neurologic function in Canada: a 2023 clinical practice guideline. *Can J Anaesth*. 2023;70(4):483-557. [Crossref]
10. Greer DM, Shemie SD, Lewis A, et al. Determination of brain death/death by neurologic criteria: the world brain death project. *JAMA*. 2020;324(11):1078-1097. [Crossref]

Diagn Interv Radiol 2026; DOI: 10.4274/dir.2026.260001

CORRIGENDUM

©Copyright 2026 Author(s) - Available online at dirjournal.org.
Content of this journal is licensed under a Creative Commons Attribution-NonCommercial 4.0 International License.

In the article entitled "Vascularity Assessment in Hashimoto's Thyroiditis: A Prospective Comparative Study with Power Doppler and Superb Microvascular Imaging" (Diagnostic and Interventional Radiology. 2026;32(3):315-321; DOI: 10.4274/dir.2025.253311), errors were identified in the Results section of the Abstract and in Table 4.

Correction 1: Abstract–Results

The following sentence:

"The SMI VI values were recorded at 8.85 [interquartile range (IQR): 25%–75%, 6.55–12.6] for patients with HT and 8.40 (IQR: 25%–75%, 6.70–12.8) for the control group, indicating a statistically significant increase in the HT cohort ($P < 0.001$)."

should read as follows:

"The SMI VI values in patients with HT were recorded at 8.85% [interquartile range (IQR): 25%–75%, 6.55–12.6%] for the right lobe and 8.40% (IQR: 25%–75%, 6.70–12.8%) for the left lobe, indicating a statistically significant increase compared to the control group values of 3.75% (IQR: 25%–75%, 2.82–5.16%) for the right lobe and 3.97% ± 1.34% for the left lobe ($P < 0.001$)."

Correction 2: Table 4

Table 4 contained typographical and layout errors. The corrected version of Table 4 is presented below. In addition, the "Euthyroid vs. Control" comparison has been included.

Table 4. Diagnostic performance of cSMI VI

Group (cut-off value)	Sensitivity (CI) %	Specificity (CI) %	PPV (CI) %	NPV (CI) %	PLR (CI)	NLR (CI)	Accuracy (CI) %
Hashimoto's thyroiditis vs. Control (6.75)*	75.34 (63.86-84.68)	100 (94.56-100)	100	78.57 (71.06-84.56)	-	0.25 (0.16-0.37)	87.05 (80.31-92.14)
Hypothyroid vs. Euthyroid (8.825)**	89.47 (75.20-97.06)	94.29 (80.84-99.30)	94.44 (81.50-98.50)	89.19 (76.49-95.44)	15.66 (4.06-60.41)	0.11 (0.04-0.28)	91.78 (82.96-96.92)
Euthyroid vs. Control (4.99)***	81.58 (65.67-92.26)	77.27 (65.3-86.69)	67.39 (56.37-76.78)	87.93 (78.65-93.51)	3.59 (2.24-5.74)	0.24 (0.12-0.47)	78.85 (69.74-86.24)

*AUC: 0.933, CI% (0.894-0.973), Youden's index: 0.753
**AUC: 0.959, CI% (0.913-1), Youden's index: 0.838
***AUC: 0.872, CI% (0.802-0.942), Youden's index: 0.589
cSMI, color superb microvascular imaging; VI, vascularity index; CI, confidence interval; PPV, positive predictive value; NPV, negative predictive value; PLR, positive likelihood ratio; NLR, negative likelihood ratio; AUC, area under curve.

The authors apologize for these errors and any inconvenience they may have caused.